



Lluís Artús Suàrez

Computational Study on the Deaminative Hydrogenation of Amides Catalyzed by Base Metal Complexes.

Thesis submitted for the degree of Philosophiae Doctor

Department of Chemistry
Faculty of Mathematics and Natural Sciences

Hylleraas Centre for Quantum Molecular Sciences



2021

© Lluís Artús Suàrez, 2021

*Series of dissertations submitted to the
Faculty of Mathematics and Natural Sciences, University of Oslo*

ISBN XXX-XX-XXXX-XXX-X

All rights reserved. No part of this publication may be reproduced or transmitted, in any form or by any means, without permission.

Cover: Hanne Badsgaard Utigard.

Print production: Reprosentralen, University of Oslo.

Contents

<u>I.</u> <u>Preface</u>	I
<u>II.</u> <u>Abstract</u>	III
<u>III.</u> <u>List of Papers and Manuscripts</u>	V
<u>IV.</u> <u>Symbols and Abbreviations</u>	VII

1. Introduction	1
1.1. Hydrogenation Reactions.....	1
1.1.1. Hydride vs molecular hydrogen	1
1.1.2. Homolytic vs heterolytic cleavage of H ₂	3
1.1.3. Mono-vs Bi-functional catalysts	6
1.2. Reactivity of Amides	8
1.2.1. Electronic properties.....	9
1.2.2. C-N vs C-O cleavage.....	11
1.3. Deaminative hydrogenation of amides with bifunctional catalysts.....	12
1.3.1. Fe-PNP Catalyzed	16
1.3.2. Mo ^{Cl} -PN ^H P Catalyzed	20

2. Methods	25
2.1. Density Functional Theory (DFT)	25
2.1.1. Kohn-Sham Equations.....	27
2.1.2. M06	29
2.2. Implicit solvent modelling	30
2.3. Microkinetic modelling.....	34
3. Objectives	39
4. Synopsis of Results	41
4.1. Reaction mechanisms of deaminative hydrogenation of amides	45
4.1.1. Catalyst hydrogenation and catalyst inhibition	45
4.1.2. Amide and aldehyde C=O hydrogenation	49
4.1.3. Hemiaminal C-N bond protonolysis.....	51
4.2. Comparison between experimental and computational results	58
4.3. Reaction optimization	69
5. Summary and concluding remarks	77

Appendix	81
Computational details.....	81
Method benchmarking	86
Bibliography	87
Papers	
I. The Key Role of the Hemiaminal Intermediate in the Iron-Catalyzed Deaminative Hydrogenation of Amides	99
II. Rational Selection of co-Catalysts for the Deaminative Hydrogenation of Amides	127
III. Highly Selective Hydrogenation of Amides Catalyzed by a Molybdenum Pincer Complex: Scope and Mechanism	149

Preface

The thesis is submitted in partial fulfilment of the requirements for the degree of Philosophiae Doctor at the University of Oslo. The research here presented is the result of my studies, from August 2015 until March 2021, under the supervision of Ainara Nova, David Balcells and Mats Tilset, in the Centre for Theoretical and Computational Chemistry of the Kjemisk institutt, Universitet I Oslo.

I want to thank my supervisors for their guidance and perseverance. I am sure the education I received from them will influence my working life from now onwards, independently of the field of work. I know I have not been an easy nor regular student, and therefore, my supervision required a lot of patience. Thank you.

I also want to emphasize the importance of my friends Marius and The Pinnipeds, as well as my PhD and Master colleagues. Your moral support and scientific advice have been essential and helped me go back to the chair to keep writing.

Finally, I want to thank my family, friends from Palafrugell and Wietske, that offered unconditional sentimental support and love in the darkest times. This period of my life has been a rollercoaster, and you managed to put me back in the rails after I derailed.

Standing on the shoulders of giants

Oslo August 2020

Lluís Artús Suàrez

II. Abstract

The thesis describes my investigations on the reaction mechanisms of the **Fe^H-PN^HP-** or **Mo^H-PN^HP-**catalyzed deaminative hydrogenation of amides (see Figure I). Here I propose reaction mechanisms that can explain the experimental behaviour of these reactions. The proposed reaction mechanisms have also been used for the optimization and design of more efficient systems, and the qualitative prediction of reaction-rate changes caused by several additives (proton-shuttle molecules and alkaline countercations). The reaction was studied using Density Functional Theory (DFT) calculations, and the results were later inputted in microkinetic models to be compared against experimental measures.

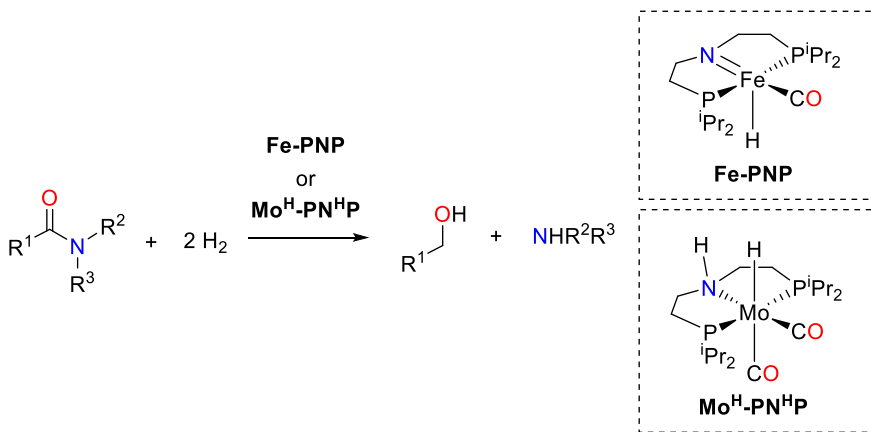


Figure I Deaminative hydrogenation of amides catalyzed by **Fe-PNP** or **Mo^H-PN^HP**

III. List of Papers and Manuscripts

The thesis is comprised of results included in the following papers.

Paper 1: *The key role of the Hemiaminal Intermediate in the Iron-Catalyzed Deaminative Hydrogenation of Amides*

Artús Suàrez, L.; Culakova, Z.; Balcells, D.; Bernskoetter, W. H.; Eisenstein O.; Goldberg, K. I.; Hazari, N.; Tilset, M.; Nova, A.

ACS Catalysis, **2018**, 8, 8751-8762

Paper II: *Rational Selection of co-Catalysts for the Deaminative Hydrogenation of Amides*

Artús Suàrez, L.; Jayarathne, U.; Balcells, D.; Bernskoetter, W. H.; Hazari, N.; Jaraiz M.; Nova A.

Chemical Science, **2020**, 11, 2225-2230

Paper III: *Highly Selective Hydrogenation of Amides Catalyzed by a Molybdenum Pincer Complex: Scope and Mechanism*

Leischner, T.; **Artús Suàrez, L.**; Spannenberg, A.; Junge, K.; Nova A.; Beller M.

Chemical Science, **2019**, 10, 10566-10576

IV. Symbols and Abbreviations

Symbols

n = number of electrons

\vec{r}_i = spatial coordinates of electron i

s_i = spin of electron i

\hat{H} = Hamiltonian of a system

\hat{h}_i = monoelectronic Hamiltonian of electron i

Ψ = system wave function

ψ_i = monoelectronic wave function of electron i

E = Expectation value of the energy of a system

K = Expectation value of the electronic kinetic energy of a system

J = Expectation value of the Coulomb potential energy of a system

E_{ne} = Expectation value of the nuclei-electron potential energy of a system

T = Temperature

R = Ideal gas constant

h = Planck constant

k_B = Boltzmann constant

TS = Transition state

G = Free energy

v_{ne} = Nuclei-electron potential field felt by a single electron.

Abbreviations

B.O. = Born-Oppenheimer approximation

COPASI = COmplex PAthway SImulator

D = DMF = Dimethylformamide

DFT = Density Functional Theory

F = Formanilide

HF = acronym for Hartree-Fock

IEF-PCM = Integral Equation Formalism of PCM (*vide-infra*)

KS = Acronym for Kohn-Sham

LSODA = Livermore Solver for Ordinary Differential Equations “Automatic”

M = Morpholidine

MF = Methylformanilide

MA = Methylacetanilide

ODE = Ordinary Differential Equation

PCM = Polarized Continuum Model

SASA = Solvent Accessible Surface Area

SCF = Self-Consistent Field

SCRF = Self-Consistent Reaction Field

SMD = Solvent Model based on Density

TBD = Triazabicyclodecene

THF = Tetrahydrofuran

1 Introduction

1.1 Hydrogenation Reactions

The addition of hydrogen atoms to unsaturated C=X or C≡X bonds (X = C, N, O) is a widespread and routine reaction in the synthesis of both commodity and fine chemicals. The importance of hydrogenation reactions is highlighted by its broad use as an efficient method for inducing chirality: readily available prochiral olefins, ketones, imines and amides, can be transformed into high-value high-demand products, using an inexpensive reagent (hydrogen).^{1,2} Furthermore, in 2001, the Royal Swedish Academy of Sciences, recognized the importance of this reaction by awarding the Nobel Prize in Chemistry to W.S. Knowles and R. Noyori for their contributions to enantioselective hydrogenation. As the thesis focusses on the hydrogenation of amides, I will introduce some general topics of hydrogenation reactions: the nature and origin of the hydrogen atoms (1), the reaction mechanisms for hydrogen activation (2) and the reaction mechanisms for hydrogen transfers (3).

1.1.1 Hydride vs molecular hydrogen

The source of hydrogen atoms will determine the reaction hazard, cost, and reaction conditions. Hydrogen sources can be classified into two main groups: hydride or molecular hydrogen sources.^{3–6}

INTRODUCTION

Hydrogenation reactions with hydride sources are those that use already activated hydrogen. However, they require of an external source of protons for completing hydrogenation. Some examples of hydride sources are LiAlH₄, LiBH₄ and NaBH₄. Their advantage over molecular hydrogen is that they are solid and they can hydrogenate at low temperatures. However, they are less selective, and LiAlH₄ and LiBH₄ are very aggressive reducing agents that can cause severe damage if mishandled. Alternatively, some organic molecules (e.g. iPrOH)⁷ can be catalytically reduced in order to use them as hydrogen sources.

Molecular hydrogen can be used directly as hydrogen source. Therefore, it is often a cheaper substrate if compared to hydride sources. Molecular hydrogen is also a greener alternative to hydride sources due to its atom efficiency. However, molecular hydrogen requires heterogeneous or homogeneous catalysts for its activation, the cost and toxicity of which may surpass those of hydride sources.

Examples of heterogeneous catalysts for hydrogenation reactions are those made of solid or supported palladium and platinum (e.g. Adam's catalyst) or nickel and aluminium (e.g. Raney nickel). These catalysts split molecular hydrogen on their surface into two hydrides via oxidative addition. They offer high catalyst reuse and easy product separation. However, their lack of selectivity and the necessary harsh reaction conditions are not suitable for many applications, including the synthesis of fine chemicals.

Homogeneous catalysts, instead, usually operate under milder conditions, are highly tunable, may be selective in respect to their reactants and/or induce chirality in their products. Their main disadvantages are their often-high production price and the need of catalyst separation from products. Some classic examples of catalyst for molecular hydrogen activation are the widely known $[\text{Rh}(\text{PPh}_3)_3\text{Cl}]$ Wilkinson's catalyst (developed by Geoffrey Wilkinson, 1973 Nobel Prize of Chemistry) or the stereoselective $[\text{Rh}(\text{COD})(\text{BINAP})^*]$ and $[\text{Rh}(\text{COD})(\text{DIPAMP})^*]$ catalysts (developed by R. Noyori and W. S. Knowles, 2001 Nobel Prize of Chemistry). Popular newer catalysts for hydrogen activation are $[\text{Ru}(\text{Triphos})(\text{TMM})]$, frustrated Lewis pairs^{8–10} and the bi-functional Shvo-, Milstein- and Noyori-type catalysts (see Chapter 1.1.2).¹¹

1.1.2 Homolytic vs heterolytic cleavage of H₂

Reaction mechanisms for catalytic molecular hydrogen activation are generally classified in two groups: those involving a homolytic cleavage of H₂ and those with a heterolytic cleavage.

The homolytic cleavage of H₂ consists of a hydrogen oxidative addition to one (e.g. Wilkinson's catalyst) or two metallic centres (e.g. Iguchi's catalyst), thus oxidizing the metal centres and producing two hydrides. (see Figure 1.1).^{3,5} Both homogeneous and heterogeneous catalysts can utilize this mechanism.

INTRODUCTION

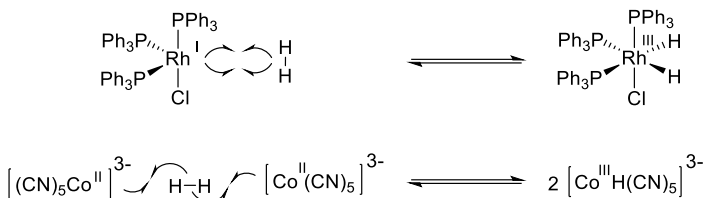


Figure 1.1 Homolytic cleavage of H_2 by Wilkinson's catalyst (above) and by Iguchi's catalyst (below).

In the heterolytic cleavage of H_2 , a metal centre forms a hydride while a nucleophile generates a $H^{\delta+}$ (Figure 1.2).^{3,5} Some catalysts contain nucleophilic ligands that facilitate the reaction due to their proximity to the metal centre.¹² Heterolytic cleavage of H_2 does not change the oxidation state of the metal.

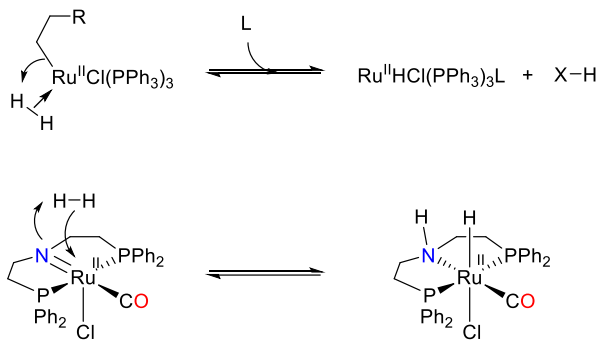


Figure 1.2 Examples of heterolytic cleavage with a $[RuCl(PPh_3)_3R]$ catalyst (above) or a Noyori-type Ru catalyst (below).

The hydrogenations studied in the thesis utilize molecular hydrogen activated by bi-functional tridentate Noyori-type catalysts, with iron or molybdenum centres (see Figure 1.3). Bi-functional catalysts are catalysts with two active centres that can perform elementary steps of different nature, i.e. nucleophilic attacks and electrophilic additions. The active sites of bi-functional catalysts for hydrogenation reactions are

placed in a disposition favouring the reversible heterolytic cleavage of hydrogen, yielding a hydride for nucleophilic attack and a proton for electrophilic addition (see Figure 1.3). This charge separation resembles the concept of frustrated Lewis pairs.^{8–10} The most popular bi-functional catalysts for multiple-bond hydrogenation can be categorized in three families that involve different nucleophilic centres: nitrogen for Noyori-type bifunctional catalysts, carbon for Milstein-type bifunctional catalysts and oxygen for Shvo-type bifunctional catalysts (see Figure 1.3). Rigid ligands are often used to set an appropriate arrangement of the catalyst active site. In the case of Noyori- and Milstein-type catalysts, these ligands are multidentate chelating ligands. The large variety of non-innocent multidentate chelating ligands gives modularity to these catalysts.^{13–15}

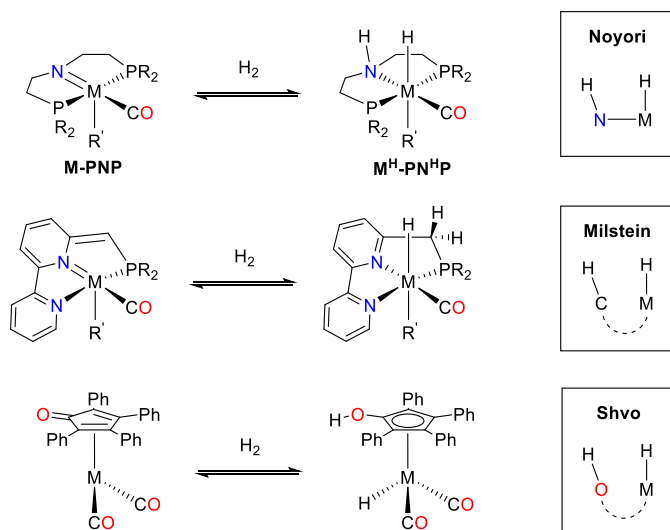


Figure 1.3 Heterolytic hydrogen cleavage assisted by Noyori-, Milstein- and Shvo-type bifunctional catalysts. Most popular metallic centres (M) are Ru, Rh or Mn. Dashed lines indicate an indirect bond between the transition metal centre and the nucleophilic centre.

INTRODUCTION

1.1.3 Hydrogen transfer mechanisms. Inner- vs outer -sphere mechanisms.

Two main reaction mechanisms exist for homogeneous hydrogenation reactions, and they are differentiated by the presence or absence of a substrate-metal bond: inner-sphere and outer-sphere hydrogenation mechanisms, respectively (see Figure 1.4 and Figure 1.5).^{3,5}

In the inner-sphere hydrogenations mechanisms, the reaction begins with a ligand decoordination to facilitate the coordination of the double-bond (see Figure 1.4). The following step is a hydride insertion to the double-bond and the formation of a substrate-metal bond. Finally, the hydrogenated molecule is eliminated either by a reductive elimination or a σ -bond metathesis (depending on the metal facility to change its oxidation state).¹⁶ The rate of inner-sphere mechanisms strongly depends on the lability of the decoordinated ligand.

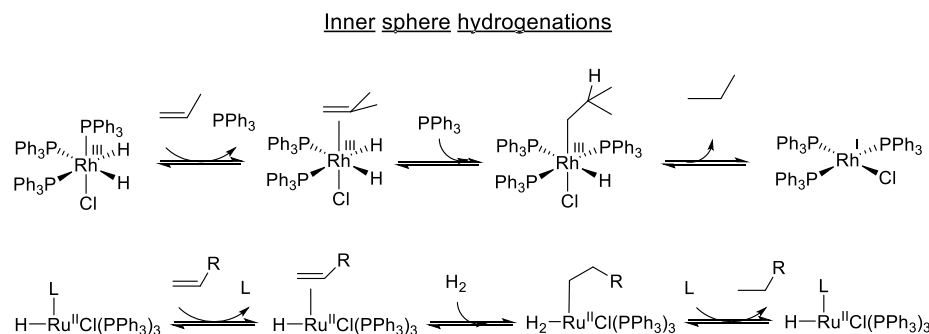


Figure 1.4 Examples of inner sphere reaction mechanisms for homogeneous catalytic double-bond hydrogenations.

INTRODUCTION

In the other hand, outer-sphere hydrogenation mechanisms do not require the coordination of the substrate, neither a ligand dissociation. This mechanism consists of a hydride nucleophilic attack and a $\text{H}^{\delta+}$ electrophilic addition. There are two classes of outer-sphere mechanisms, differentiated by the order of the steps (see Figure 1.5), and none of them involve a change in the metal oxidation state. Hydrogenation of highly nucleophilic substrates (such as quinolines or acridines) will prefer outer-sphere mechanisms where there is first a $\text{H}^{\delta+}$ electrophilic addition, followed by a hydride nucleophilic attack.³ In the other hand, Shvo-, Noyori- and Milstein-type catalysts are known to favour first a hydride nucleophilic attack, followed by a $\text{H}^{\delta+}$ electrophilic addition.^{13,14}

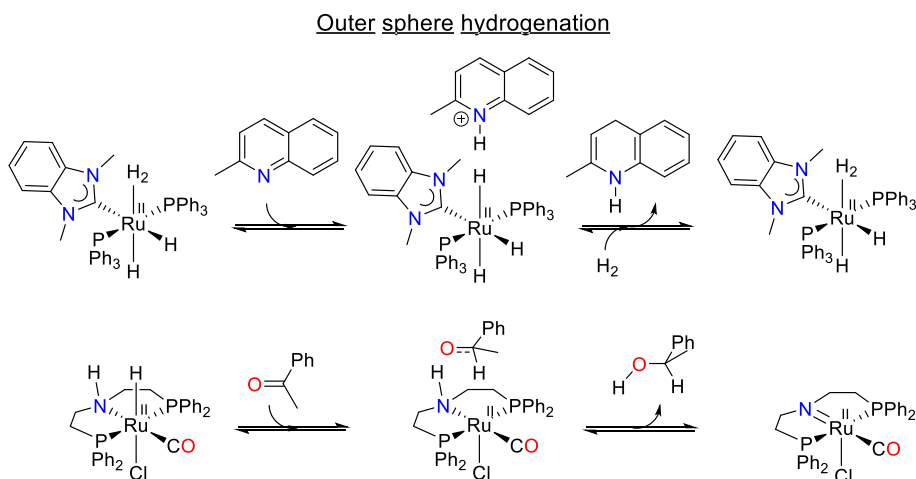


Figure 1.5 Examples of outer sphere reaction mechanisms for homogeneous catalytic double-bond hydrogenations.

1.2 Amides as a substrate.

Amides and carboxamides are the names given to molecules containing the functional group $R^1C(=O)NR^2R^3$. Due to their natural abundance and synthetic accessibility, amides play prominent roles in several contexts, such as biochemistry, synthesis of industrial and fine chemicals,^{17–22} in processes of CO_2 conversion to methanol^{23–26} as well as amine precursors. Amides belong to the family of carboxylic acid derivatives: electron-rich carbonyl groups of the form $RC(=O)Y$, which are susceptible to be hydrolyzed to carboxylic acids (Figure 1.6). Amides are the most stable within that family, which is a desired feature for example in their biological role in protein's peptide bonds. However, amides relative high stability is a drawback when they are used as a substrate since their reactivity is more challenging and slower than that of carboxylic acid derivatives.

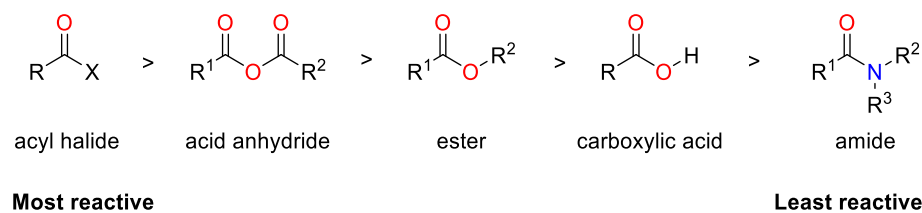


Figure 1.6 Relative reactivity and electron affinity of carboxylic acid derivatives.

Traditionally, methods for amide reduction relied on the consumption of stoichiometric amounts of strong reducing agents, such as $LiAlH_4$ or $LiBH_4$ and/or heterogeneous catalysts that demand very high pressures (>100 atm).^{27–30} To date, only a small number of homogenous catalysts can directly hydrogenate amides to amines.^{23,31–36} The thesis presents

our efforts to understand and improve the deaminative hydrogenation of amides by **M^H-PN^HP** catalysts. Therefore, it is important to contextualize the origin of amides low activity, as well as the reactions in which they can get involved.

1.2.1 Amides reactivity

Although amides are the least reactive of the carboxylic acid derivatives, they still do react under appropriate conditions. Amides can undergo nucleophilic addition (Figure 1.7) via a nucleophilic attack to the carbonyl carbon, and formation of an alkoxide molecule, which will later undergo either an oxygen protonation or an amine elimination.

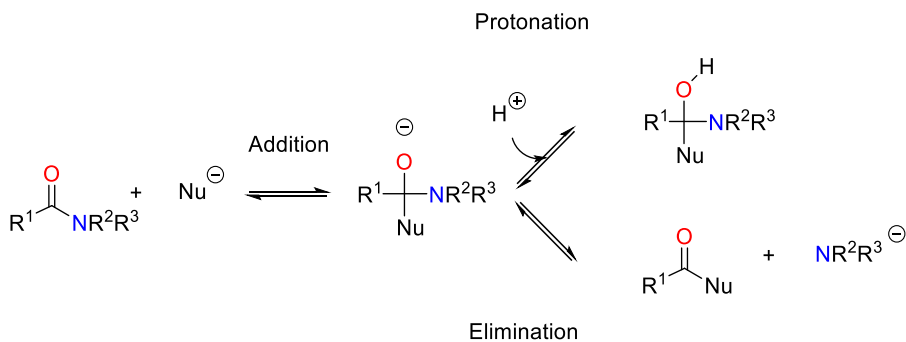


Figure 1.7 General amide reactivity.

Most of amides main reactions (see Figure 1.8) result from the combination of these fundamental steps with different nucleophiles and reaction conditions. We can differentiate two amide reaction families: those which involve C-N cleavage (with amine elimination), and those which involve C=O cleavage (with water elimination). C-N cleavage reactions can proceed with five different nucleophiles (alcohols, water,

INTRODUCTION

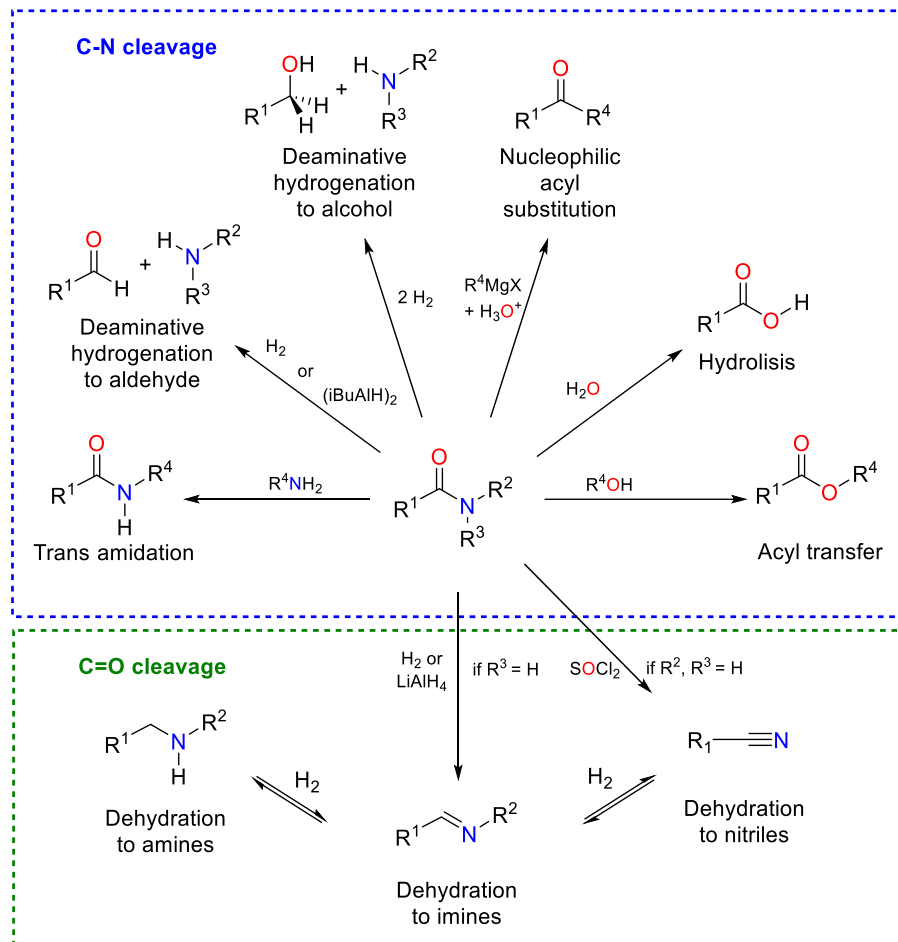


Figure 1.8 Schematic summary of amide reaction types. In blue: reactions involving C-N cleavage. In green: reactions involving C=O cleavage.

amines, Grignard reagents and hydrogen), leading to six different reaction types: acyl transfer, hydrolysis, trans amidation, nucleophilic acyl substitution, deaminative hydrogenation to aldehyde³⁷ (similar to the Vilsmeier-Haack reaction) and deaminative hydrogenation to alcohol.^{37,38} In the case of C=O cleavage, the reaction can lead to three different products (amine, imine and nitrile) depending on the amide, the

catalyst or the reaction conditions. In some cases, mixed products can be formed.

Though all those reaction types are worth a chapter by themselves, they fall out of the scope of the thesis. Extensive reviews on amides C-N and C=O cleavage were written by J. Blanchet,³⁹ A. Y. Khalimon et al.⁴⁰ and A. Smith and R. Whyman.²⁷

1.2.2 Electronic properties

Amides stability is often associated with their multiple resonance forms (see Figure 1.9). In terms of Lewis theory, amides possess six conjugated electrons over the O-C-N moiety, resulting in the formation of three possible resonant forms. Such electron delocalization gives planarity and rigidity to the O-C-N moiety while contributing to amide's stability.

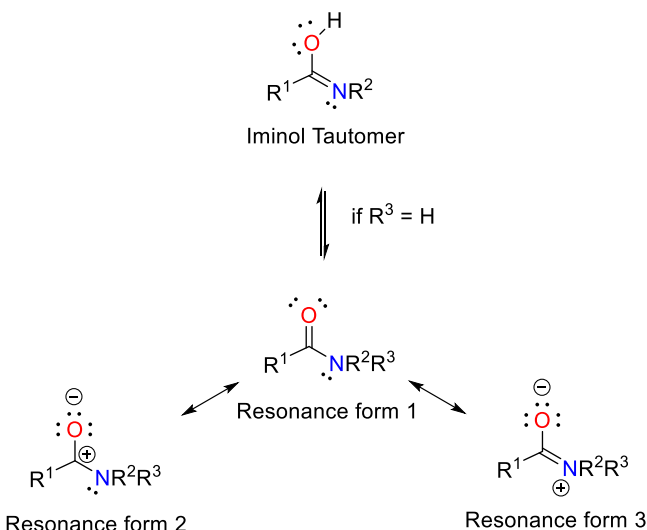


Figure 1.9 Amides resonance and tautomeric forms. Iminol tautomerization is only accessible from primary and secondary amides ($R^3 = H$).

INTRODUCTION

Resonance forms 2 and 3 play an important role in the reactivity of amides. Nucleophilic additions to amides formally proceed through the resonance form 2 (see Figure 1.9). However, resonance form 3 (see Figure 1.9) strengthens the C-N bond reducing the C electrophilicity, and thus, depending on their weight in the electronic structure, can hamper nucleophilic additions. Amides with electron-withdrawing groups will have a stronger contribution of resonance form 2. Therefore, they will undergo nucleophilic additions faster than amides with electron donor groups, which have a stronger contribution of resonance form 3. The same rule applies to amides C-N cleavage reactions.

Alternatively, secondary and tertiary amides can transfer a proton from their N to their O to form an iminol tautomer (see Figure 1.9). The iminol tautomer hampers nucleophilic additions and C-N cleavages similarly to resonance form 3: it strengthens the C-N bond and reduces the C electrophilicity. The negative contribution of iminol tautomers can be reduced with the use of non-polar solvents, which disfavor their formation.

1.3 Deaminative hydrogenation of amides with bifunctional catalysts

The increasing pollution, and the necessity of renewable energies during the 21st century, has enforced a boost to green chemistry. Daily, new synthetic methods are being developed for the synthesis of industrial and fine chemicals with atom efficient reactions, renewable chemical

reagents, and mild reaction conditions. Deaminative hydrogenation of amides, the reaction studied in this work, is an example of such evolution. First attempts of deaminative hydrogenation of amides to alcohols without aggressive reagents were documented in 2003 within a patent.^{41,42} That work was the first to use molecular hydrogen as hydrogen source instead of hydride sources like LiAlH₄ or hydroboranes. The hydrogenation reaction was achieved by using the ruthenium triphos catalyst [Ru(triphos)CO(H)₂] (see Figure 1.10). However, ruthenium is a precious metal, high temperatures and pressures were required and only modest Turn Over Number (TON) and Turn Over Frequency (TOF) were achieved (600 and 43 h⁻¹ respectively).

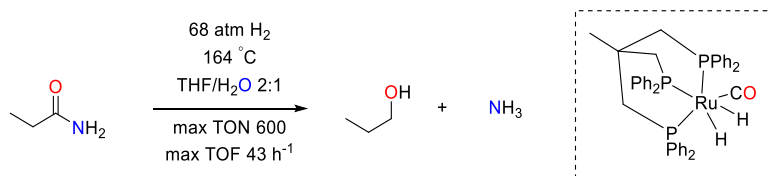


Figure 1.10 First homogeneous catalyzed deaminative hydrogenation of amides to alcohols with molecular hydrogen

INTRODUCTION

Seven years later, in 2010, the Milstein group used for the first time a bifunctional catalyst for this reaction and it drastically reduced the required temperatures and pressures from 68 atm and 164 °C to 10 atm and 110 °C (entry **1** in Figure 1.11).³³ From then onward, bifunctional catalysts gained popularity and rapidly dominated the homogeneous catalysis of deaminative hydrogenation of amides to alcohols: bidentate Noyori- and Milstein-type catalysts were introduced in this reactions in 2011 and 2013 (entries **2** and **3** in Figure 1.11),^{34,43–46} tridentate Noyori-type catalysts were reported in 2015 (entry **4** in Figure 1.11)^{25,35,47} and base metal tridentate Milstein- and Noyori-type catalysts in 2016 (entries **5** and **6** in Figure 1.11).^{36,48,49} This was the state of the art when this project started in the second half of 2016.

More recently, during the course of this research, deaminative hydrogenation of amides by Noyori-type catalysts has been expanded from ruthenium⁵⁰ and iron^{31,51–53} to molybdenum⁵⁴ and manganese^{23,55} with modest TONs and TOFs (entries **1** and **2** in Figure 1.12). Ruthenium and iron catalysis went through reaction optimization, emerging as the most active catalysts for this reaction, with maximum TONs up to 19600 and 5180, and TOFs up to 980 and 1108 h⁻¹, respectively (entries **3** and **4** in Figure 1.12).

INTRODUCTION

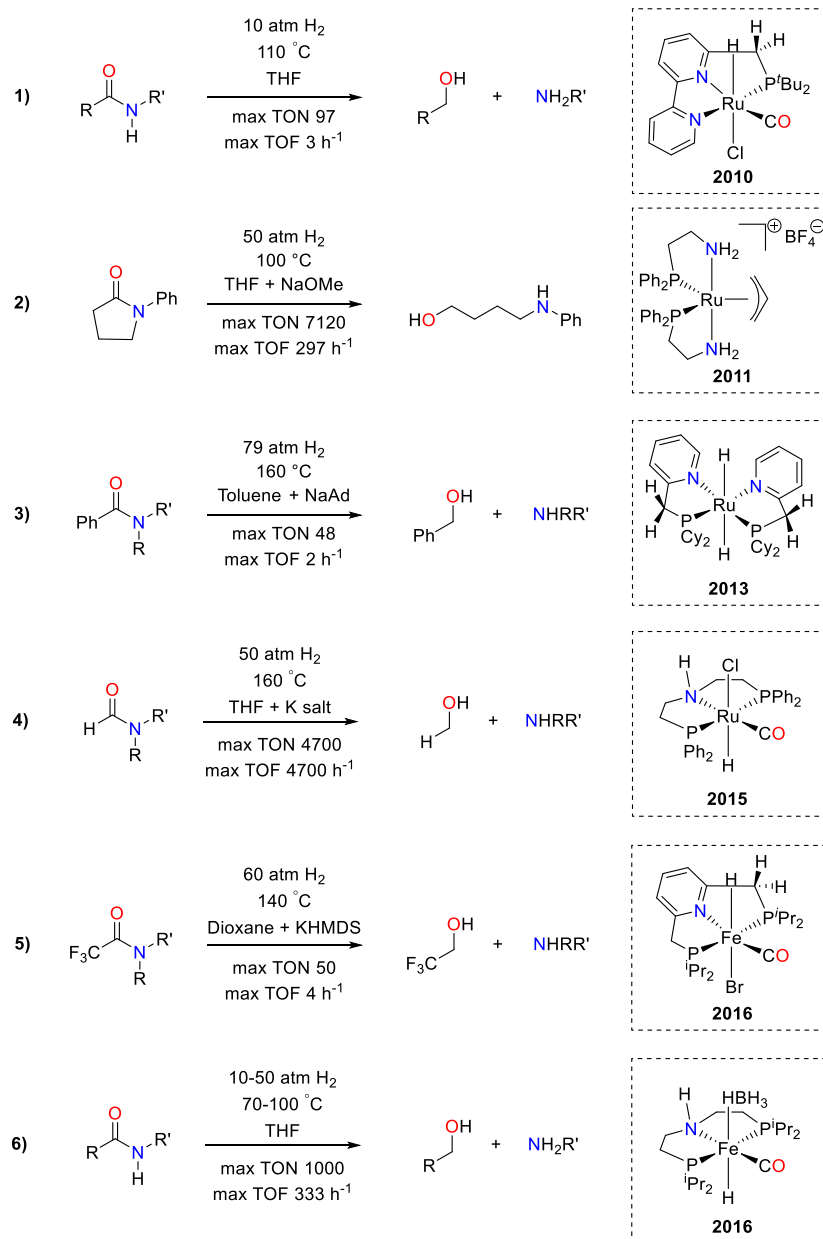


Figure 1.11 Historical evolution of bifunctional catalyst utilization in the deaminative hydrogenation of amides to alcohol until 2016.

INTRODUCTION

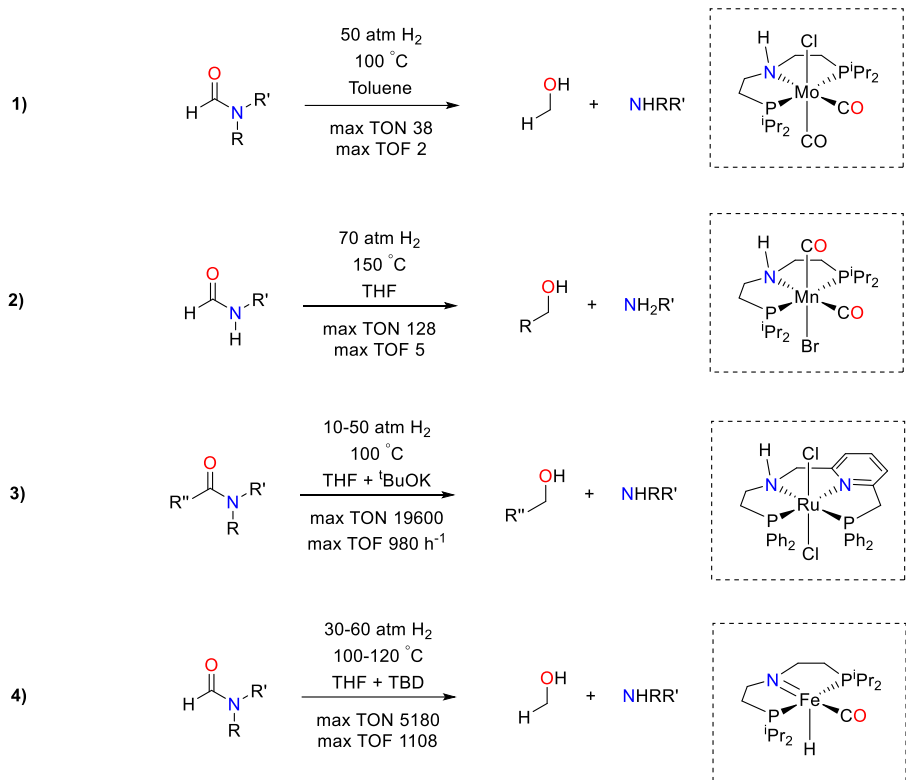


Figure 1.12 State of the art of amide deaminative hydrogenation catalyzed by Noyori-type catalysts in 2020.

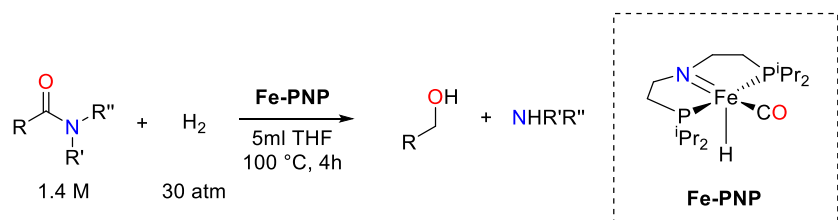
1.3.1 Fe-PNP Catalyzed Deaminative Hydrogenation of Amides

In 2020, the Noyori-type bifunctional catalyst **Fe-PNP** (see Table 1.1) was the non-noble metal homogeneous catalysts with the best performance at the time for the deaminative hydrogenation of amides. The first iron Noyori-type catalyst was first synthesized in 2013 by M. Beller and co-workers, who used it as a catalyst for methanol dehydrogenation.⁵⁶ This catalyst strongly gained popularity in the next

two years for its ability to hydrogenate the double bonds of a wide variety of substrates, including esters, carbon dioxide, alkenes, heterocycles and nitriles.^{57–62} In 2016, iron Noyori-type catalysts was used for the first time for deaminative hydrogenation of amides, by Langer and coworkers⁴⁸ and by Sanford and co-workers.⁴⁹ The catalyst exhibited selectivity towards the reduction of aryl formamides and benzamides with promising activities: TONs and TOFs up to 177 and 59 h⁻¹ respectively, under mild conditions of 110 °C and 20 bar; and TONs and TOFs up to 1080 and 100 h⁻¹ in the presence of K₃PO₄, temperature of 110 °C and H₂ pressure of 60 bar.

A key milestone for the project came in 2017 in a new study published by Hazari, Bernskoetter and co-workers.³¹ This paper presented three main results: (I), they presented a catalyst optimization: utilization of the dehydrogenated catalyst **Fe-PNP** reached TONs and TOFs up to 4430 and 1108 h⁻¹ (see Table 1.1); (II), they reported that the conversion of alkyl formamides and benzamides is enhanced by the presence of secondary aryl amides or LiOTf (see Table 1.2); and (III), they reported the formation of adducts between **Fe-PNP** and secondary amides in the absence of hydrogen (see Figure 1.13), similar to those observed between **Fe-PNP** and methanol or formic acid.⁶³ Interestingly, secondary amides and/or LiOTf had no catalytic effect on secondary amides.

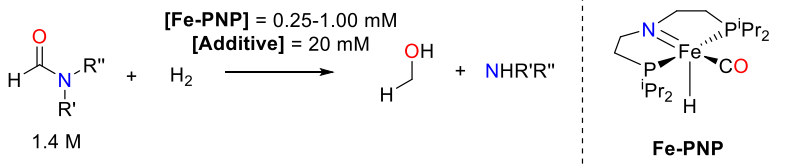
INTRODUCTION



Amide/substrate	[Fe-PNP]	Conv. (%)	TON // TOF (h ⁻¹)
	1 mM 0.25 mM	>99 79	>1400 // >350 4430 // 1108
	1 mM 0.25 mM	>99 58	> 1400 // > 350 3240 // 810
	1 mM 0.25 mM	97 36	1360 // 340 2000 // 500
	1 mM	9	130 // 33
	1 mM	4	60 // 15
	1 mM	0	-- // --

Table 1.1 Summary of the results reported by Hazari, Bernskoetter *et al.* on the **Fe-PNP**-catalyzed deaminative hydrogenation of different secondary and tertiary amides.³¹

INTRODUCTION



Amide/substrate	Additive	Conv. (%)	TON // TOF (h ⁻¹)
a 	4'-Trifluoromethylformanilide	> 99	> 1390 // 348
	Formanilide	93	1305 // 326
	4'-Methoxyformanilide	78	1098 // 275
	Aniline	24	335 // 84
	Benzanilide	12	168 // 42
	-----	4	60 // 15
b 	Formanilide + LiOTf	24	340 // 21
	Formanilide	14	190 // 12
	-----	4	50 // 3
c 	Formanilide + LiOTf	54	3010 // 188

Table 1.2 a) 30 atm H₂, 100 °C, 1 mM of **Fe-PNP**, 4h. b) 60 atm H₂, 120 °C, 1 mM of **Fe-PNP**, 16h. c) 60 atm H₂, 120 °C, 0.25 mM of **Fe-PNP**, 16h.

INTRODUCTION

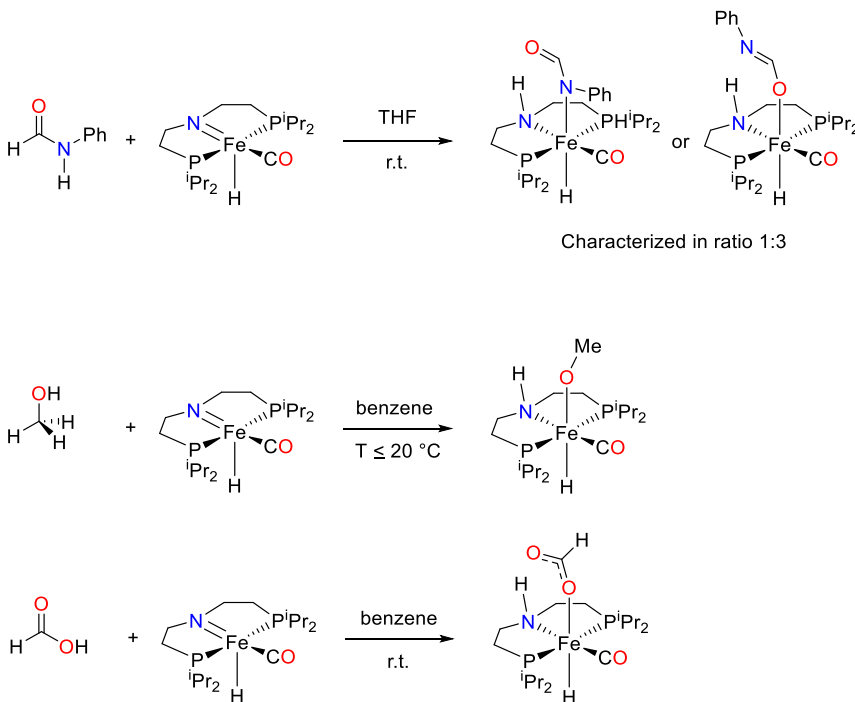


Figure 1.13 Experimentally observed adducts of **Fe-PNP** when treated with stoichiometric amounts of formanilide, methanol and formic acid (in the absence of hydrogen).^{31,63,64}

1.3.2 **Mo^{Cl}-PN^HP** Catalyzed Deaminative Hydrogenation of Amides

Mo^{Cl}-PN^HP (see Table 1.3) was first synthesized in 2018 by M. Beller and co-workers, as an alternative of **Fe-PNP**.^{54,65} **Mo^{Cl}-PN^HP** could hydrogenate ketones, olefines, amides, though it had modest TONs and TOFs when compared to **Fe-PNP**. Still, it exhibited an opposite selectivity within amides: **Mo^{Cl}-PN^HP** performance was good in the deaminative hydrogenation of tertiary aryl amides, but it was barely active for acetamides or secondary aryl amides, and inert for aliphatic

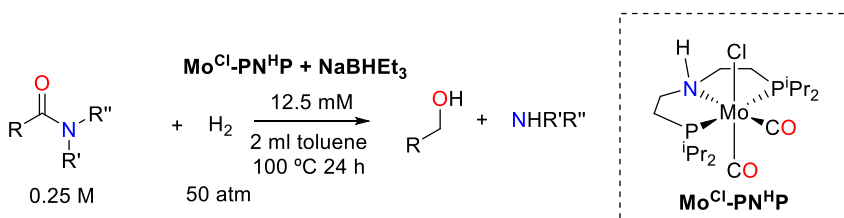
INTRODUCTION

formamides. Similarly to **Fe-PNP**, **Mo^{Cl}-PN^HP** favoured the deaminative hydrogenation of formamides, or amides with electron-withdrawing groups, over other amide types with electron-donor groups.

The activation of **Mo^{Cl}-PN^HP** pre-catalyst formally requires the elimination of HCl to allow the addition of H₂. This reaction was performed using NaBHEt₃, yielding Mo(0) d⁶ **Mo-PNP** and hydrogen elimination (Figure 1.14). The formation of **Mo-PNP** was supported by HR-ESI-MS (High-Resolution Electron Spray Ionization Mass Spectroscopy), and by an inactive Electron Paramagnetic Resonance (EPR).

Mo^{Cl}-PN^HP was reported to form adducts in the presence of formanilide and NaBHEt₃ (Figure 1.14), in a similar fashion to **Fe-PNP**. The resulting compound was characterized by single-crystal X-ray diffraction, as a Mo(0) dimeric complex. The formed adduct catalyzed the deaminative hydrogenation of amides in the absence of NaBHEt₃, reinforcing the hypothesis that Mo(0) d⁶ **Mo-PNP** is the active catalyst.

INTRODUCTION



Amide/substrate	Conv. (%)	TON // TOF (h ⁻¹)
	>99	20 // 1
	>99 94 ^a	20 // 1 38 ^a // 2 ^a
	83	17 // 1
	20	4 // 0
	13	3 // 0
	<1 ^b	0 ^b // 0 ^b

Table 1.3 Brief summary of the experimental results reported by M. Beller and co-workers on the **Mo^{Cl}-PN^HP** catalyzed deaminative hydrogenation of amides.⁵⁴ a) [Mo^{Cl}-PN^HP + NaBHET₃] = 6.25 mM. b) T = 130 °C.

INTRODUCTION

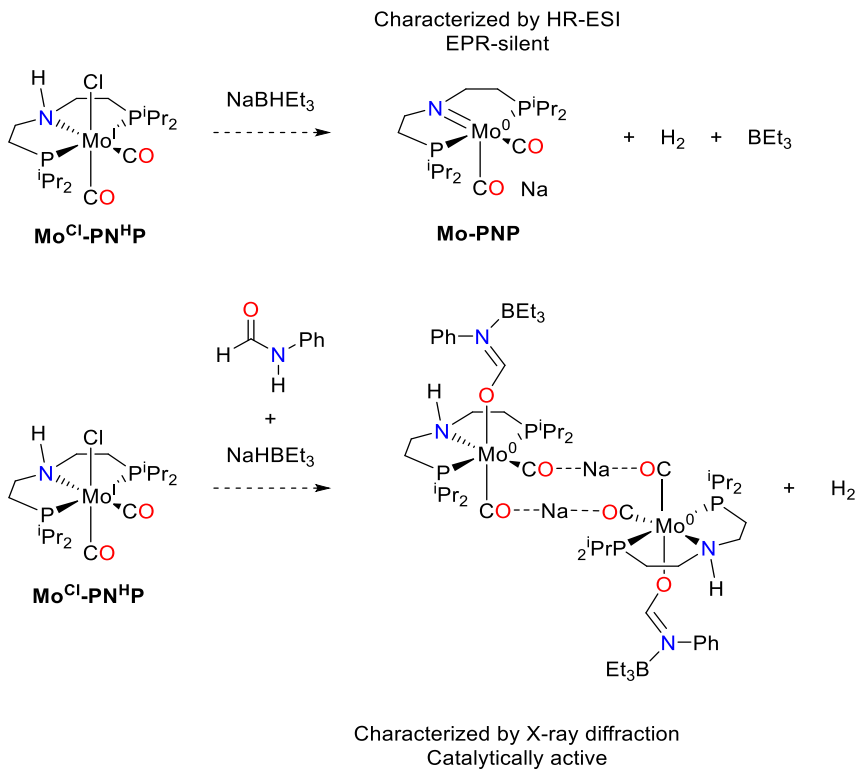


Figure 1.14 **Mo^{Cl}-PN^{HP}** activation by **NaBHET₃** (above) and by **NaBHET₃** plus formanilide.⁵⁴ The dashed arrow indicates the lack of experimental information to have reaction mass balance.

2 Methods

The workflow used in this study (see Figure 2.1) consisted on (I) benchmarking different methods to experimental and theoretical references (described in Appendix) to select a density functional that accurately described our system, (II) computing reaction mechanism guesses, by Density Functional Theory (DFT) calculations, (III) using the computed energies to generate a microkinetic model of the reaction mechanism, (IV) comparing the results of the microkinetic model against experimental measures. New reaction mechanisms were calculated in case of discrepancies between calculations and experiments.

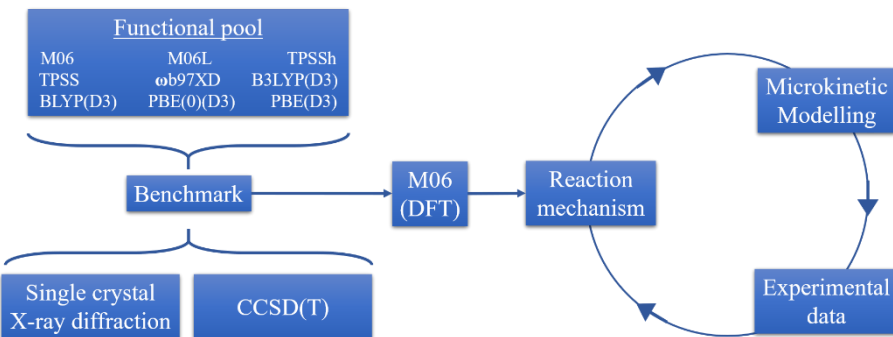


Figure 2.1 Work-flow chart used in this research.

2.1 Density Functional Theory (DFT)

DFT is the method used in this research for the calculation of ground-energies and geometries. DFT, was selected among other computational methods because its accuracy *vs* computational-cost ratio allowed for the

METHODS

calculation of free energies with sufficient accuracy and within a reasonable time span.

DFT was first proposed in 1927 by Thomas and Fermi, and its bases were founded in 1964 by Hohenberg and Kohn, who enunciated and proved their two theorems:^{66,67} (I) an electron density function $\rho(\vec{r})$ (see Eq 2-1 and Eq 2-2) can adopt the role of a “function that defines the state of a system” and hence define all the properties of the ground state; and (II) the functional $F_{HK}[\rho]$ delivers the ground state energy of the system if and only if the input $\rho(\vec{r})$ and potential field $v(\vec{r})$ match those of the real ground state (see Eq 2-3).

Eq 2-1

$$\rho(\vec{r}) = n \int \dots \int |\Psi(\vec{r}_1, s_1, \vec{r}_2, s_2, \dots \vec{r}_n, s_n)|^2 ds_1 d\vec{r}_2 ds_2 \dots d\vec{r}_n ds_n$$

$$\int \rho(\vec{r}) d\vec{r} = n \quad \text{Eq 2-2}$$

$$E[\rho] = \int \rho(\vec{r}) v(\vec{r}) d\vec{r} + F_{HK}[\rho] \quad \text{Eq 2-3}$$

Although the Hohenberg-Kohn theorems are rigorously correct, they do not yield an analytical expression for $F_{HK}[\rho]$, which remains unknown. Therefore, further approximations were needed to make DFT applicable to computational chemistry.

2.1.1 Kohn-Sham Equations

In 1965, Kohn and Sham reformulated Hohenberg and Kohn's theory into a computationally implementable DFT approximation. Kohn and Sham proved that the solution of an ideal system with non-interacting electrons and with a density function ρ_{KS} , can reproduce the energy of a real system if ρ_{KS} is equal to that of the real system.⁶⁸

The advantages of using an ideal system are that it can be defined with a kinetic energy operator \hat{T}_{el} , and an external potential V^{KS} that artificially simulates the real electron-electron repulsion (see Eq 2-4). This ideal system can be expressed in terms of the one-electron operator $\hat{h}^{KS}(\vec{r})$, similar to the Fock operator.

$$\hat{H}^{KS} = \hat{K}_{el} + V^{KS} = \sum_{i=1}^n \left(-\frac{\nabla_i}{2} + v^{KS}(\vec{r}_i) \right) = \sum_{i=1}^n \hat{h}^{KS}(\vec{r}_i) \quad \text{Eq 2-4}$$

v^{KS} in Eq 1-4 is the potential field that a single electron feels from the ideal nuclei-electron interaction, $v_{ne}(\vec{r})$, the ideal electron-electron interaction, $\int \frac{\rho_{KS}(r')}{|r-r'|} dr'$, and the non-ideal electron-electron repulsion, $\frac{\delta E_{xc}[\rho_{KS}]}{\delta \rho_{KS}}$ (see Eq 2-5). Kohn and Sham named E_{xc} the exchange-correlation energy.

$$v^{KS}(\vec{r}) = v_{ne}(\vec{r}) + \int \frac{\rho_{KS}(r')}{|r-r'|} dr' + \frac{\delta E_{xc}[\rho_{KS}]}{\delta \rho_{KS}} \quad \text{Eq 2-5}$$

METHODS

An exact mathematical expression of $E_{xc}[\rho_{KS}]$ is unknown and all further DFT methods focus on finding an approximation of E_{xc} . Once a E_{xc} approximation has been selected, an initial guess wavefunction Ψ^{HF} can be used as an input in Eq 2-1 to obtain a ρ_{KS} guess, which can be input in Eq 2-5 to calculate a ψ^{KS} guess, which at the same time can built a \hat{h}^{KS} guess. Then $\hat{h}^{KS}(\vec{r})\psi^{KS}(\vec{r}) = \epsilon^{KS}\psi^{KS}(\vec{r})$ can be solved iteratively to find all ψ^{KS} until a self-consistent $\rho_{KS}(\vec{r})$ is found. It is at this point when $\rho_{KS}(\vec{r})$ can be used to calculate the energy of the system (see Eq 2-6) whose components are: kinetic energy $T^{KS}[\rho_{KS}]$, Coulomb energy $J^{KS}[\rho_{KS}]$, nuclei-electron potential energy $E_{ne}[\rho_{KS}]$ and exchange-correlation energy $E_{xc}[\rho_{KS}]$.

$$\begin{aligned} \rho_{KS}^0 &\rightarrow \psi^{KS\ 0} \rightarrow (\hat{h}^{KS})^0 \rightarrow \{\psi_1^{KS\ 0}, \psi_2^{KS\ 0}, \dots \psi_n^{KS\ 0}\} \\ \hookrightarrow \rho_{KS}^1 &\rightarrow \psi^{KS\ 1} \rightarrow (\hat{h}^{KS})^1 \rightarrow \{\psi_1^{KS\ 1}, \psi_2^{KS\ 1}, \dots \psi_n^{KS\ 1}\} \\ \hookrightarrow \dots &= \dots \rightarrow \dots \rightarrow \dots \\ \hookrightarrow \rho_{KS} &= \rho_{real} \end{aligned}$$

$$E[\rho_{KS}] = K^{KS}[\rho_{KS}] + J^{KS}[\rho_{KS}] + E_{ne}[\rho_{KS}] + E_{xc}[\rho_{KS}] \quad \text{Eq 2-6}$$

The fundamental difficulty in DFT is that we do not know the exact expression of the exchange-correlation energy $E_{xc}[\rho_{KS}]$. Many approximations of $E_{xc}[\rho_{KS}]$ have been proposed since Kohn and Sham published their computable implementation of DFT. However, there is not a $E_{xc}[\rho]$ approximation that generally outperforms all the others.

Therefore, a benchmark of methods against an experimental or computational reference is recommended.

In the thesis, the hybrid *meta*-GGA M06⁶⁹ functional was selected on the basis of geometry and energy benchmarks (see Appendix), using X-ray crystal structures and CCSD(T) (also known as the golden standard method to obtain accurate bond energies),⁷⁰ with basis set cc-pVTZ.⁷¹

2.1.2 M06

M06, the functional used in the thesis for the calculation of molecular ground energies, is a hybrid meta-exchange-correlation functional created in 2008 by Truhlar and co-workers. It belongs to the family of the so-called Minnesota functionals.⁶⁹ M06 is a highly parametrized functional, specifically optimized to reproduce the thermochemistry of main group elements and organometallic compounds. M06 was also optimized to reproduce non-covalent interactions of main group elements. A total of 36 parameters were fitted against databases with empirical measures and highly accurate calculations of both transition metals and non-metal elements. These databases contained over 403 energetic data points of thermochemistry, kinetics, non-covalent and metallic bonding and excitation energies. M06 accurately describe dispersion forces thanks to the inclusion of second derivatives of the density function.

METHODS

M06 energies can be decomposed in three components: 27% of Hartree-Fock exchange energy, 73% of pure M06 exchange energy, and 100 % of M06 correlation functional (see Eq 2-7).

$$E_{xc}^{M06}[\rho, x_\sigma, \tau_\sigma] = 0.27E_x^{HF} + 0.73E_x^{M06} + E_C^{M06} \quad \text{Eq 2-7}$$

The inclusion of Hartree-Fock exchange makes M06 a hybrid functional. Also, M06 is classified as a meta-GGA functional because it depends on the variables electron density (ρ_σ), reduced spin density gradient (x_σ), and spin kinetic energy density (τ_σ).

2.2 Solvent Modelling

The free energy of a system, and hence its reactivity, can be severely altered by the presence or absence of a surrounding condensed phase. Inclusion of solvent modelling is critical in systems with relevant interaction between solvent and solute, like those found in ionic solvents or solutes, solvents with the possibility to coordinate or hydrogen bond with the solute, reactions involving proton transfers, etc. The effect of a solvent in the free energy of a system receives the name of solvation free energy, ΔG_S° , and it is divided into three terms (see Eq 2-8):⁷² (1) ΔG_{ENP} which contains the effect of electrostatic interactions between charges on the solute and charges on the solvent molecules (acronym of Electrons and Nuclei Polarization from gas- to liquid-phase); (2) ΔG_{CDS} , which contains the effect of non-electrostatic interactions (acronym of solvent Cavitation energy, Dispersion energy and local Solvent reorganization energy); and (3) ΔG_{conc}° , which contains the change in

free energies due to differences in standard state concentration between gas and liquid-phase (1.89 kcal mol⁻¹ if 1 atm and 1 mol L⁻¹ are used in the gaseous and solvated-phase respectively).

$$\Delta G_S^\circ = \Delta G_{ENP} + \Delta G_{CDS} + \Delta G_{conc}^\circ \quad \text{Eq 2-8}$$

The modelling of a condensed-phase system is not trivial. The most realistic way to construct a model is to surround the solute with a finite number of solvent molecules (explicit solvent modelling) (see left scheme in Figure 2.2). However, the high number of solvent molecules surrounding the solute (which increases as the square of the radius of the simulated cell) implies the computation of an impracticable number of particle interactions and energy minimums, only computable by simulation techniques such as molecular dynamics.

Implicit continuum solvation modelling emerged as an alternative to implicit solvent modelling. The assumptions underlying implicit continuum solvation models are that (I) solvent molecules do not react with the solute, and (II) the huge number of individual solvent molecules may be replaced by a continuous medium with properties consistent with those of the solvent itself (see right scheme in Figure 2.2).^{73,74} Some implicit models are: PCM,⁷⁵ IEF-PCM,⁷⁶ SMD,⁷² SMD12,⁷⁷ COSMO,⁷⁸ MCSCRF⁷⁹ or FEM.⁸⁰

Alternatively to implicit or explicit solvent modelling, hybrid implicit-explicit solvation models can be used (see middle scheme in Figure 2.2). Hybrid solvation models typically consist of a continuous medium that surrounds a solute and few solvent molecules. Such approximation is

METHODS

usually used when solvent reactivity is expected but full explicit solvent simulation is computationally too expensive. It is in these cases when hybrid solvation models shine thanks to their computational cost in between that of implicit and explicit models.

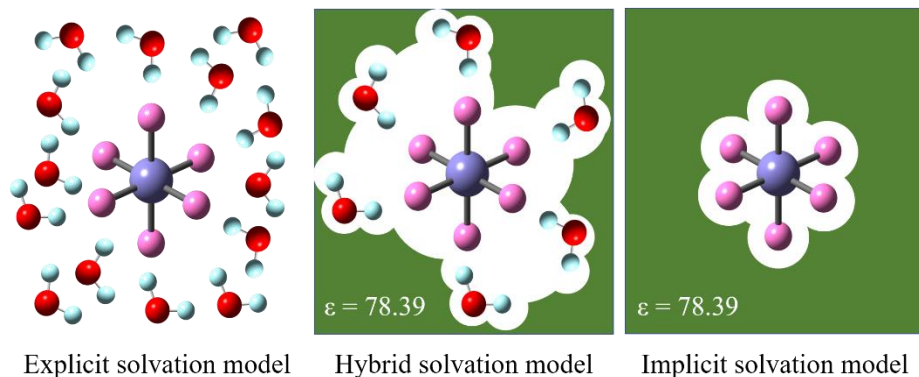


Figure 2.2 Toy systems of explicit, hybrid and implicit solvation models.

In the thesis, implicit models have been used because solvent reactivity was not expected (i.e. the simulated solvent, toluene and thf, are aprotic and non-coordinating molecules), and the big size of our system made the computational cost of explicit solvation modeling not practical for this study. Instead, the method Solvent Modeled Density (SMD) was used to introduce solvation free energy corrections to DFT calculated free energies. SMD is an implicit continuum solvent model developed in 2009 by A. Marenich, C. Cramer and D. Truhlar.⁷² The SMD modelling of ΔG_{ENP} is a parametrized version of the Polarized Continuum Model approximation (PCM) (more specifically the IEF-PCM). In PCM, the Born-Oppenheimer approximation (B.O.) of clamped nuclei is assumed. B.O. implies that the dielectric field of the solvent does not polarize the solvated nuclei, therefore, the system

wavefunction is reduced to the electronic component and ΔG_{ENP} will be treated as ΔG_{EP} which is equal to Eq 2-9,

Eq 2-9

$$\Delta G_{EP} = \left\langle \Psi_{sol.} \left| \hat{H}_{gas} - \frac{e}{2} \phi \right| \Psi_{sol.} \right\rangle + \frac{e}{2} \sum_A^N Z_A \phi_A - \langle \Psi_{gas} | \hat{H}_{gas} | \Psi_{gas} \rangle$$

where ϕ (a.k.a. reaction field) is the electrostatic potential caused by the solute dipole moment and the solvent polarization. ϕ can be calculated with the Poisson equation (see Eq 2-10) which relates the solvent dielectric constant ϵ , and the charge density of the solute ρ_f . ϕ and ρ_f depend reciprocally on each other; hence they must be solved iteratively in a self-consistent process named Self-Consistent Reaction Field (SCRF).

$$\nabla \cdot (\epsilon \nabla \phi) = -4\pi \rho_f \quad \text{Eq 2-10}$$

The SMD modelling of ΔG_{CDS} is a sum of terms that are proportional (with geometry-dependent proportionality constants σ , called atomic surface tensions) to the solvent-accessible surface areas of the individual atoms of the solute (A) (see Eq 2-11, where k and M refer to solute and solvent atoms respectively). Surface tension σ are parameterized constants of atoms k or M , characteristic of the SMD model, and they have no particular connection with conventional surface tension. In the SMD model, the Solvent-Accessible Surface Area is calculated as the area created by the addition spheres centred in the solute atoms, and with

a radius equal to the sum of the atom van der Waals radii plus the solvent radius.⁶

$$\Delta G_{CDS} = \sum_k^N \sigma_k A_k + \sigma^{[M]} \sum_k^N A_k \quad \text{Eq 2-11}$$

2.3 Microkinetic modelling

The prediction of a reaction experimental macroscopic behaviour from its calculated reaction mechanism is often not straight forward. To achieve a deeper understanding of the studied reaction mechanisms, microkinetic models were constructed. Microkinetic modelling is a computational technique directed to solve the apparent rate of a reaction mechanism from the calculation of its elementary step rates. Using microkinetic models, one can obtain a set of concentrations and rates as a function of time (see Figure 2.3) from a complete set of elementary reactions and their rate constants (usually obtained with computational studies), and the initial reaction concentrations and conditions. These models facilitate the interpretation of complex reaction networks, like competing reactions or interconnected reaction cycles.

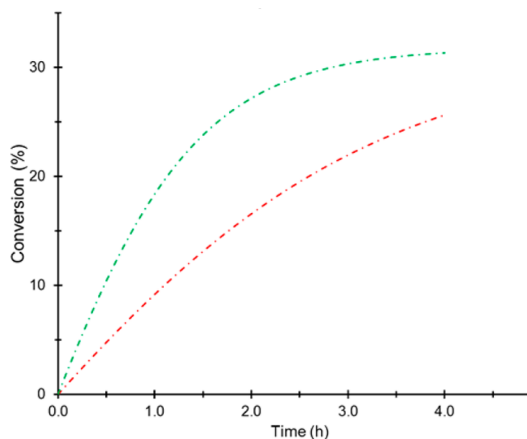


Figure 2.3 Example of a microkinetic model output of a toy reaction were the green and red lines are the conversion of two reactants ($\text{Conversion}_t = 100 * [\text{Reactant}]_t / [\text{Reactant}]_0$).

Microkinetic modelling is based on transition-state theory. Transition-state theory states that reaction mechanisms can be decomposed in elementary reactions: unidirectional reactions of one or more reactants or intermediates in *quasi-equilibrium* with a single activated transition state complex X^\ddagger that irreversibly leads to one or more product or intermediates (see Figure 2.4).^{74,81,82}

METHODS

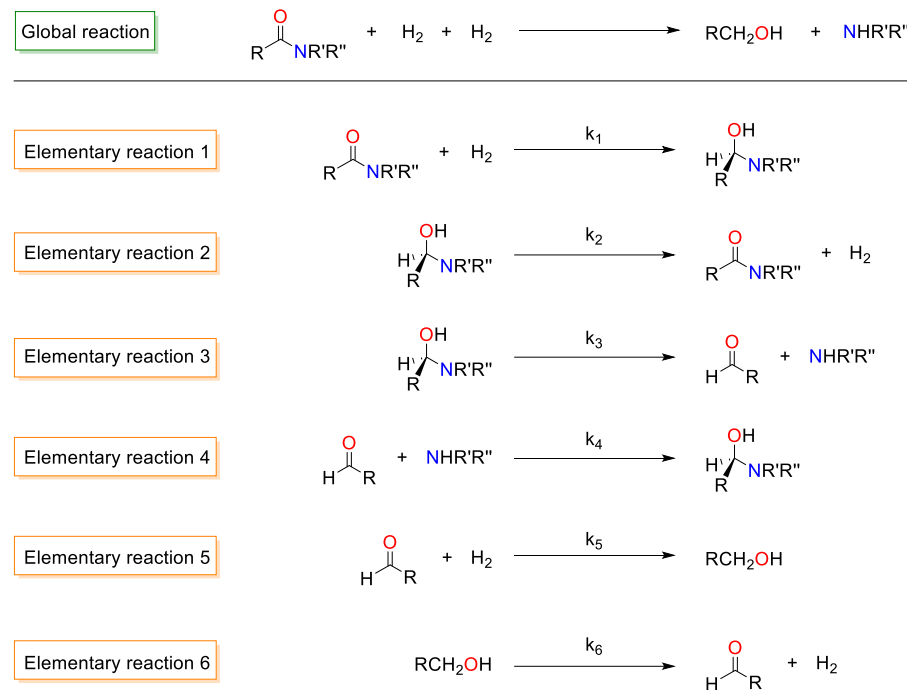


Figure 2.4 Toy example of a fictional reaction mechanism and its elementary reactions.

The velocity of an elementary reaction is proportional to the product of the concentration of its reactants, as described by Eq 2-12,

$$\text{elementary reaction rate} = k \prod_i [R_i] \quad \text{Eq 2-12}$$

$$k = \frac{\kappa k_B T}{h} e^{-\frac{\Delta G^\ddagger}{RT}}$$

where k is a rate constant, k_B is the Boltzmann constant, T the reaction temperature, h the Planck constant, ΔG^\ddagger the free energy barrier of the elementary reaction, R is the ideal gas constant, and κ is transmission

coefficient (accounting for the phenomenons of tunnelling and “re-crossing”).⁸¹ Consequently, the macroscopic behaviour of any molecule R_i in a reaction mechanism is described by an ordinary differential equation (ODE) of the form of Eq 2-13,

$$\frac{\partial [R_i]}{\partial t} = [R_i] \sum_j k_j \prod_{a \neq i} [R_a] - [R_i] \sum_l k_l \prod_{b \neq i} [R_b] \quad \text{Eq 2-13}$$

where j are the elementary reactions in which R_i is a reactant and R_a their reactants, and l are the elementary reactions in which R_i is a product and R_b their reactants.

The ODEs of a reaction mechanism are usually intercorrelated, and their analytical solution is unknown. Microkinetic modelling software offers several algorithms that numerically solve ODEs and allow us to simulate the time-evolution of the concentration of all species involved in the reaction mechanism. COPASI (COPASI (COmplex PAthway SImulator)⁸³ is the software package used in the thesis for microkinetic modelling. COPASI solves ODE with the algorithm LSODA (Livermore Solver for Ordinary Differential Equations “Automatic”).^{84–87} LSODA automatically detects the stiffness of the evaluated ODE and determines which numerical method should be used to solve it: the Adam method for non-stiff ODEs and the Backward Differentiation Formula (BDF) for stiff ODEs.⁸⁴

3 Objectives

The main goal of the thesis was the computational determination of the reaction mechanisms of the deaminative hydrogenation of amides by base metal Noyori-type catalysts. The secondary objective was the improvement of the reaction activity using the information given by the proposed mechanisms.

The reaction was studied with two catalysts, **Fe-PNP** and **Mo^H-PN^HP**. The different selectivity of these catalysts moulded the objective details of each reaction. While the **Fe-PNP**-catalyzed reaction mechanism should explain the different reactivity of secondary and tertiary amides, the **Mo^H-PN^HP**-catalyzed reaction mechanism should explain the different reactivity of formamides and acetamides. Despite their different selectivity, both catalysts were reported to form stable adducts with secondary amides such as formanilide. The thesis also aims to understand the formation of these adducts as well as their impact on the reaction outcome.

4 Results

This chapter summarizes the main findings obtained in the included papers. The central theme throughout this chapter is the computational mechanistic study on the deaminative hydrogenation of amides by either catalyst **Fe-PNP** or **Mo^{Cl}-PN^HP** (see Figure 4.1).

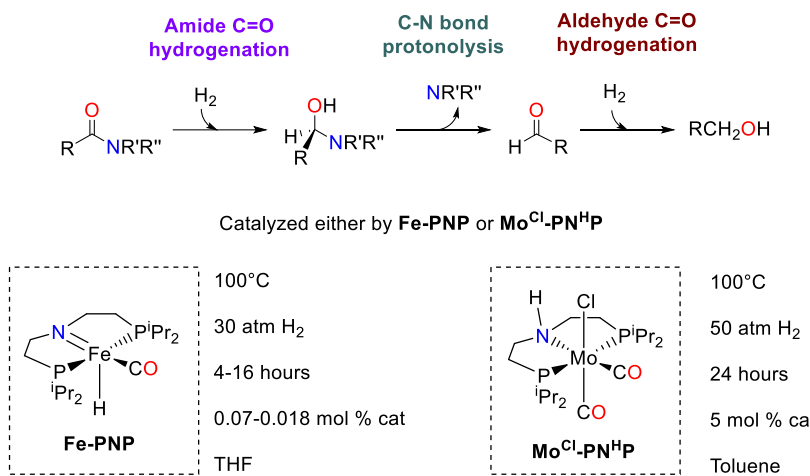


Figure 4.1 Above, commonly proposed elementary reaction steps on the deaminative hydrogenation of amides when in the presence of **Fe-PNP** or **Mo^{Cl}-PN^HP** catalysts. Below, studied catalysts and experimental conditions.

The overall reaction mechanism is based in three consecutive reaction steps (see Figure 4.1 and Figure 4.2):⁶⁴ amide C=O hydrogenation, C-N bond protonolysis and aldehyde C=O hydrogenation. This division is a proposal consistent with the ability of Noyori- and Milstein-type catalysts to hydrogenate carbonyl groups.^{88,89} Although **M-PNP** catalysts are known to be involved in C=O hydrogenations, their role in C-N bond protonolysis remained unclear prior to the thesis. Hence, we considered adequate to investigate its role in C-N protonolysis too. We

RESULTS

have also studied the role of secondary amides, alcohols and other proton relay molecules. These species have been observed both to bind to the dehydrogenated catalysts and to co-catalyze the hydrogenation of some tertiary amides and esters.^{31,63,64,88–91} Therefore, we included proton relay mechanisms for competitive catalyst inhibition, co-catalyzed C-N bond protonolysis and co-catalyzed **M-PNP** hydrogenations (see Figure 4.2).

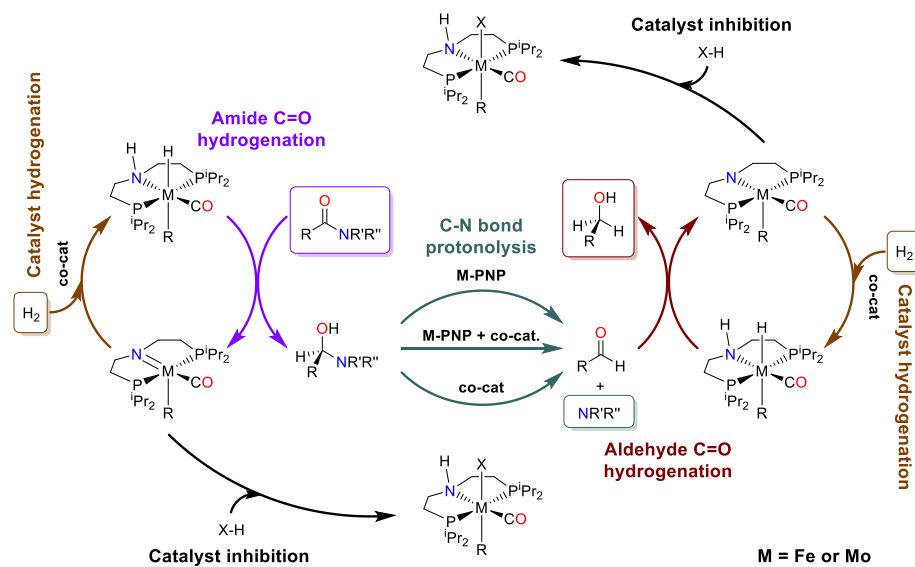


Figure 4.2 Studied interactions of **M-PNP** and co-catalysts in the elementary steps of deaminative hydrogenation of amides.

The amides used for this study are shown in Figure 4.3. The amides have been selected to cover a range of reactivity, substituents and steric hindrance. The selected amides for the **Fe-PNP**-catalyzed deaminative hydrogenation of amides are formanilide, morpholidine and dimethylformamide (DMF), and their experimental conversions are 58%, 36% and 0% respectively. The selected amides for the **Mo^{Cl-}**

RESULTS

PN^HP-catalyzed deaminative hydrogenation of amides are formanilide, N-methylformanilide and N-methylacetanilide, and their experimental conversions are 13%, >99% and 20% respectively. The lack of correlation between experimental conversions and the reaction thermodynamics indicates that deaminative amide hydrogenation behaviour is not thermodynamically but kinetically controlled. Substrate-dependent out-cycle reactions could also account for conversion differences between amides. **Fe-PNP** and **Mo^{Cl}-PN^HP** different selectivity (see the case of formanilide) suggests that their reaction mechanisms are different.

Amide C=O hydrogenation
C-N bond protonolysis
Aldehyde C=O hydrogenation

Fe-PNP	Calculated ΔG _r (kcal mol ⁻¹)			Exp. Conv.	
	0.0	4.7	5.2	-10.1	58%
	0.0	8.8	12.4	-2.8	36%
	0.0	10.5	13.8	-1.5	No conversion

Mo ^{Cl} -PN ^H P	Calculated ΔG _r (kcal mol ⁻¹)			Exp. Conv.	
	0.0	4.0	5.1	-10.1	13%
	0.0	7.6	6.8	-8.5	>99%
	0.0	10.5	0.6	-7.5	20%

Figure 4.3 Calculated free energies (kcal mol⁻¹) of organic key intermediates of selected amides, next to their experimental yields.^{31,54} Experimental reaction conditions for the **Fe-PNP** catalyst are 1.4 M amide, 0.25 mM **Fe-PNP**, 30 atm H₂, 100 °C and 4 hours in tetrahydrofuran (THF). Experimental reaction conditions for the **Mo^{Cl}-PN^HP** catalyst are 0.25 M amide, 12.5 mM **Mo^{Cl}-PN^HP**, 50 atm H₂, 100 °C and 24 hours in toluene.

RESULTS

The hybrid *meta*-GGA M06 functional was selected on the basis of geometry and energy benchmarks,⁶⁹ using X-ray crystal structures and CCSD(T)⁷⁰ (with basis set cc-pVTZ)⁷¹ energies as references. Double-z and triple-z basis sets were used for geometry optimization and energy refinement, respectively. Temperature and pressure and solvent modelling have been selected to match experimental conditions. A more detailed description of the method benchmark and the computational methods utilized is described in the Appendix chapter.

The results chapter is organized using a different structure than in the publications to eliminate redundancy and to maximize the comparisons between **Fe-PNP** and **Mo^{Cl}-PN^HP**. Many different reaction mechanisms have been explored, but only those with the lowest energy are described in the thesis (unless relevant exceptions). All presented energies are free energies (unless contrary stated). In the thesis, the superindexes F, D, M, MF and MA in the nomenclature of reaction intermediates have been used to denote the presence of formanilide, DMF, morpholidine, N-methylformanilide or N-methylacetanilide, respectively. The hydrogenated catalyst form **M^H-PN^HP** has been used as free energy reference (unless stated). Note that the labelling of species in the thesis does not follow the labelling used in the corresponding papers.

4.1 Reaction mechanisms of deaminative hydrogenation of amides

4.1.1 Hydrogen activation and catalyst inhibition

Molecular hydrogen is not sufficiently reactive to reduce amides or aldehyde C=O bonds. Therefore, hydrogen activation is needed before such reactions. When in presence of the Fe catalyst (ⁱPrPNP)Fe(H)(CO) (**Fe-1**), H₂ suffers a concerted heterolytic cleavage, yielding the trans-dihydride complex (ⁱPrPN^HP)Fe(H)₂(CO) (**Fe-2**) (see Figure 4.4). This hydrogenation is a -10.2 kcal mol⁻¹ exergonic reaction with an internal energy barrier of 11.6 kcal mol⁻¹ (**Fe-TS-1-2**). Alternatively, **Fe-1** hydrogenation can be assisted by a proton relay molecule such as methanol (studied by the groups of Wang and Guan)⁸⁸ or formanilide (studied in the thesis, see Figure 4.5). Wang and Guan reported an internal barrier of 17.3 kcal mol⁻¹ for the methanol assisted **Fe-1** hydrogenation. In the thesis we researched the formanilide assisted mechanism, which proceeds through a H₂ binding to the metal centre while formanilide NH protonates the catalyst ligand, thus forming intermediate **Fe-3** at 6.8 kcal mol⁻¹. Then, H₂ is deprotonated by the formanilide N, yielding **Fe-2**. The formanilide-assisted activation of H₂ has an effective energy barrier of 4.0 kcal mol⁻¹, which is 3.1 and 7.6 kcal mol⁻¹ less energetic than the methanol-assisted and the unassisted reactions.

RESULTS

However, hydrogen activation can be inhibited by weak acids such as formanilide or methanol (see Figure 4.4), which can react with **Fe-1**, forming the adducts **Fe-4^F** and **Fe-4^{MeOH}**, respectively. These adducts are not part of the catalytic cycle (off-cycle reactions). The stability of **Fe-4^F** ($\Delta G = -2.0$ kcal mol⁻¹) is consistent with its characterization by NMR and single-crystal X-ray diffraction analysis.³¹ In the other hand, the less stable **Fe-4^{MeOH}** ($\Delta G = 3.3$ kcal mol⁻¹) has only been characterized by NMR analysis at temperatures ≤ 20 °C.^{63,64} As a consequence of Fe catalyst inhibition by **Fe-4^F**, the catalyst activation mechanism has an effective energy barrier of 21.8 kcal mol⁻¹, or 16.2 kcal mol⁻¹ in the presence of formanilide or 14.0 kcal mol⁻¹ in the presence of methanol.

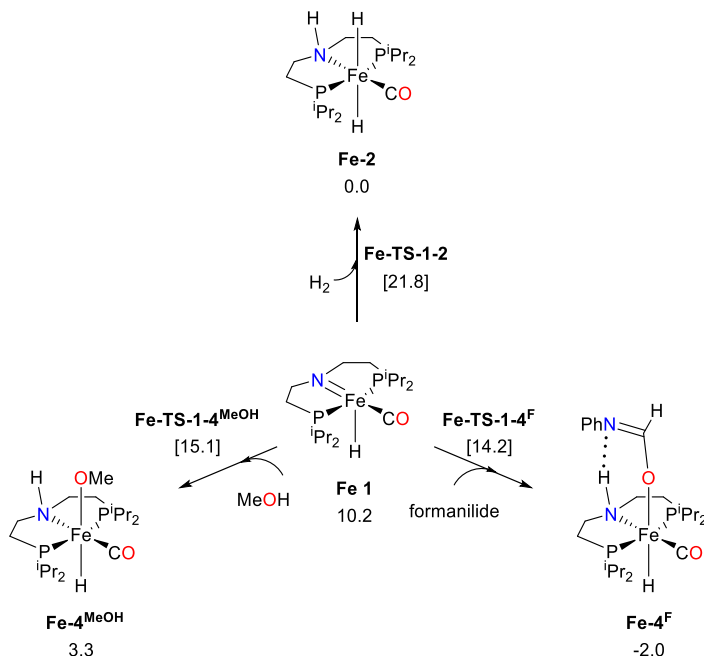


Figure 4.4 Free energies (kcal mol⁻¹) of unassisted **Fe-1** hydrogenation and **Fe-1** off-cycle species.

RESULTS

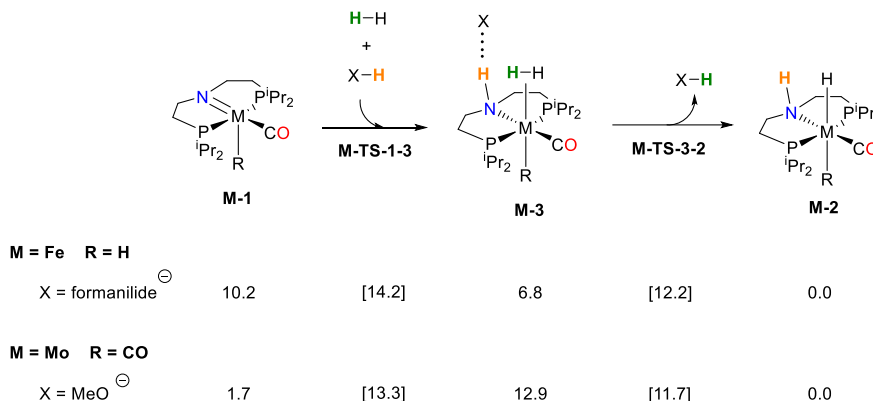


Figure 4.5 Free energies (kcal mol⁻¹) of catalyst hydrogenation assisted by formanilide and methanol.

On the case of Mo, the use of the catalyst precursor **MoCl-PN^HP** requires stoichiometric amounts of NaBH₃ to generate the active [ⁱPrPNP]Mo(CO)₂]Na (**Mo-1**) (see Figure 4.6), in which Mo(I) has been reduced to Mo(0).⁵⁴ The reduction of Mo(I) to Mo(0) is supported by the observation of hydrogen gas, and by HR-ESI mass spectrometry and EPR analysis of **Mo-1**.

Hydrogen activation with **Mo-1** follows the same mechanism than with **Fe-1** (see Figure 4.6), but on Mo case, the reaction is more thermoneutral (-1.7 vs -10.2 kcal mol⁻¹) and its internal barrier is higher (18.6 vs 11.6 kcal mol⁻¹). Furthermore, the Mo-methanol-assisted hydrogen activation has a higher internal barrier than that of the Fe-formanilide-assisted (11.6 kcal mol⁻¹ vs 4.0 kcal mol⁻¹). In the other hand, the formations of adducts **Mo-4^F**, **Mo-4^{MeOH}** and **Mo-4^{EtOH}** (-20.8, -9.7 and -11.6 kcal mol⁻¹) are more exergonic than their Fe counterparts. The higher stability of **Mo-4** adducts might be attributed to a charge stabilization via the Na⁺ counterion, the Lewis acid BEt₃ present in the solution (see Figure 4.5),

RESULTS

and the trans-CO ligand back-donation. As a consequence of Mo catalyst inhibition by **Mo-4^F**, **Mo-4^{MeOH}** and **Mo-4^{EtOH}**, hydrogen activation is not feasible without a proton relay molecule (effective barriers > 30 kcal mol⁻¹). Only the methanol assisted mechanism has a thermally accessible effective energy barrier (21.4 kcal mol⁻¹).

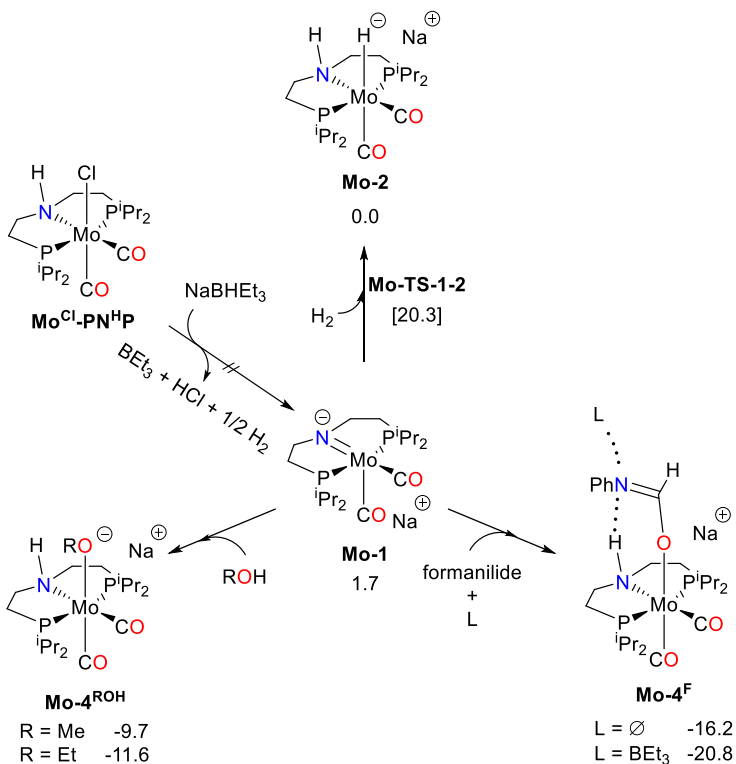


Figure 4.6 Free energies (kcal mol⁻¹) of unassisted **Mo-1** hydrogenation and **Mo-1** off-cycle species.

4.1.2 Amide and aldehyde C=O hydrogenation

The hydrogenation of the amide C=O, as well as the hydrogenation of the aldehyde C=O, is performed by the hydrogenated catalyst species **Fe^H-PN^HP** or **Mo^H-PN^HP** (**Fe-2** or **Mo-2**) (see Figure 4.2). Our calculations indicate that both amide and aldehyde C=O hydrogenation by **Fe-2** or **Mo-2** share a common reaction mechanism (see Table 4.1): The mechanism is a stepwise process, consisting on an outer-sphere hydride transfer from the metal to the carbonyl C (**M-TS-2-5**), followed by a proton transfer from the ligand NH to the carbonyl O (**M-TS-5-1**). This proposal is consistent with other reported mechanistic studies on bifunctional pincer catalysts for (de)hydrogenation reactions.^{11,14,92,93}

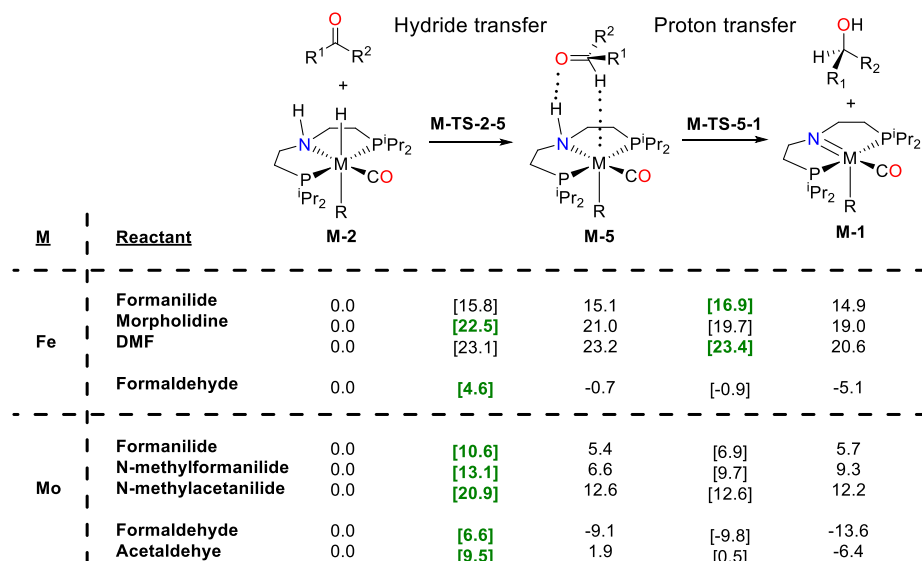


Table 4.1 Free energies (kcal mol⁻¹) for amide and aldehyde C=O hydrogenation by **M^H-PN^HP** catalyst. The most energetic transition states are highlighted in green colour.

On the case of **Fe-2** assisted amide C=O hydrogenation, all the studied reductions are endergonic (from 15 to 20 kcal mol⁻¹), and all their

RESULTS

transition states are thermally accessible (below 24 kcal mol⁻¹). The energy difference between the hydride transfer (**Fe-TS-2-5**) and proton transfer barriers (**Fe-TS-5-1**) is small: (between -1 and 3 kcal mol⁻¹). Therefore, it is difficult to predict whether the hydride or the proton transfer will be the most energetic transition state of amide C=O hydrogenation by **Fe-2**. In the case of formaldehyde C=O hydrogenation, the reduction is exergonic (-5.1 kcal mol⁻¹) and the hydride transfer is significantly more energetic than the proton transfer (4.6 kcal mol⁻¹ vs -0.9 kcal mol⁻¹). The energies associated with formaldehyde reduction are significantly smaller than those of amides as a consequence of formaldehyde C=O lower electron density.

Regarding **Mo-2** assisted amide C=O hydrogenation, all the reductions are endergonic too, and their transition states are also thermally accessible. However, hydrogenation barriers with Mo are significantly lower than Fe barriers (around 10 kcal mol⁻¹ higher). Moreover, contrary to Fe, Mo hydride transfers (**Mo-TS-2-5**) are consistently higher than Mo proton transfers (**Mo-TS-5-1**). Within the studied amides, acetanilide hydride transfer barrier is significantly higher than those of formamides (20.9 vs 10.6 and 13.1 kcal mol⁻¹), as a consequence of acetanilide C=O higher electron density. In Chapter 4.2 we will see that this energy difference is one of the reasons for **Mo^{Cl}-PN^HP** selectivity towards formamides. On the case of aldehydes, **Mo-2** assisted formaldehyde and acetaldehyde C=O hydrogenations follow the same trends as the **Fe-2** assisted: they are exergonic, their most energetic

transition state is the hydride transfer, and their transition states are lower than those of amide C=O hydrogenation.

4.1.3 Hemiaminal C-N bond protonolysis

The hemiaminal C-N bond protonolysis involves the following chemical transformations: hemiaminal OH deprotonation, hemiaminal N protonation and C-N cleavage (Figure 4.7). The simplest reaction mechanism, the intramolecular O-to-N proton transfer followed by C-N cleavage, has prohibitively high energy barriers for any of the tested amides ($> 45 \text{ kcal mol}^{-1}$). Therefore, proton relay molecules are needed, as already proposed in the literature.^{49,88} The candidates to assist the proton transfer are many: the catalyst, secondary amides (substrate), hydrogen (reactant) and alcohols (products). For these reasons, C-N bond protonolysis can proceed through different paths. However, only three paths have been identified to be the most relevant. They differ on which are the assisting molecules and on the order of the reaction steps (Figure 4.7).

Path 1 is catalyzed only by the catalyst (**M-1**). It consists of first the hemiaminal OH deprotonation by the ligand N (**M-TS-1-7**). Then the hemiaminal C-N cleavage (**M-TS-7-8**) forms an amido complex **M-8** and releases an aldehyde molecule, which can rapidly be reduced to alcohol. Finally, **M-8** amido group is protonated by the ligand NH (**M-TS-8-1**), yielding the corresponding amine.

RESULTS

Path 2 is catalyzed by both **M-1** and a proton relay molecule. It consists of first the hemiaminal OH deprotonation by the ligand N (**M-TS-1-9**) and the coordination of the proton relay to the metal centre. Then, the proton relay protonates the hemiaminal N (**M-TS-9-10**), thus liberating the corresponding zwitterion. Finally, the zwitterion will then undergo C-N cleavage (**M-TS-10-4**) and liberate the corresponding amine and aldehyde.

Path 3 is catalyzed by a proton relay molecule only, and the order of the steps depends on the acidity/basicity of the proton relay molecule. **Path 3** with formanilide as proton relay presents first the hemiaminal N protonation (**TS-6-11**), followed by the hemiaminal OH deprotonation (**TS-11-12**), forming a zwitterion that will then undergo C-N cleavage (**TS-12-13**). In the other hand, **Path 3** with methanol as proton relay, presents first a concerted hemiaminal protonation/deprotonation (**TS-6-12**) to a zwitterion, that will then undergo C-N cleavage (**TS-12-13**) to the corresponding aldehyde and amine.

RESULTS

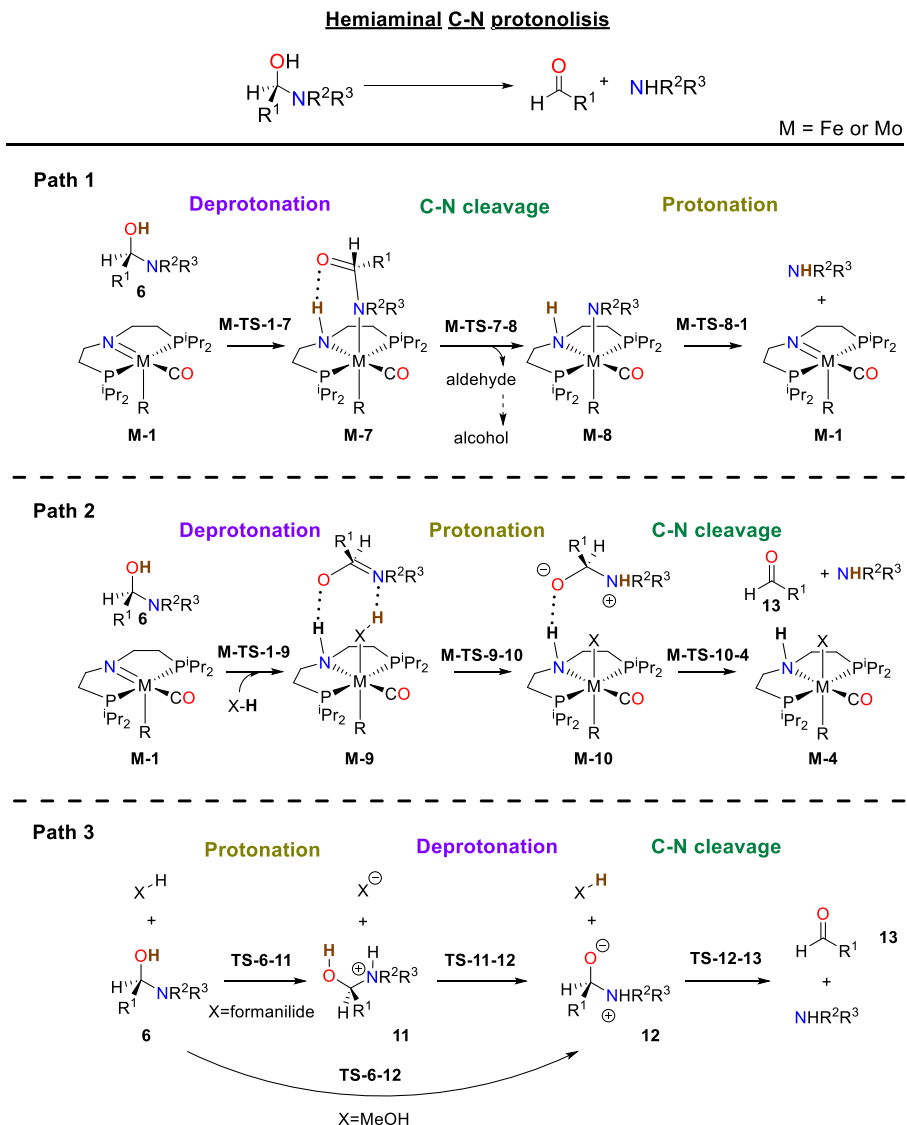


Figure 4.7 Calculated key steps of hemiaminal C-N bond protonolysis when in the presence of an **M-PNP** catalyst.

When in the presence of **Fe-1**, formanilide hemiaminal C-N bond protonolysis is assisted solely by **Fe-1** (**Path 1** in Figure 4.8). This path is almost thermoneutral, $\Delta G = 0.1 \text{ kcal mol}^{-1}$, due to the exergonic (and

RESULTS

fast) reduction of formaldehyde to methanol. Its highest energy barrier **Fe-TS-7-8^F** ($\Delta G^\ddagger = 24.9 \text{ kcal mol}^{-1}$) is associated with the C-N bond cleavage step.

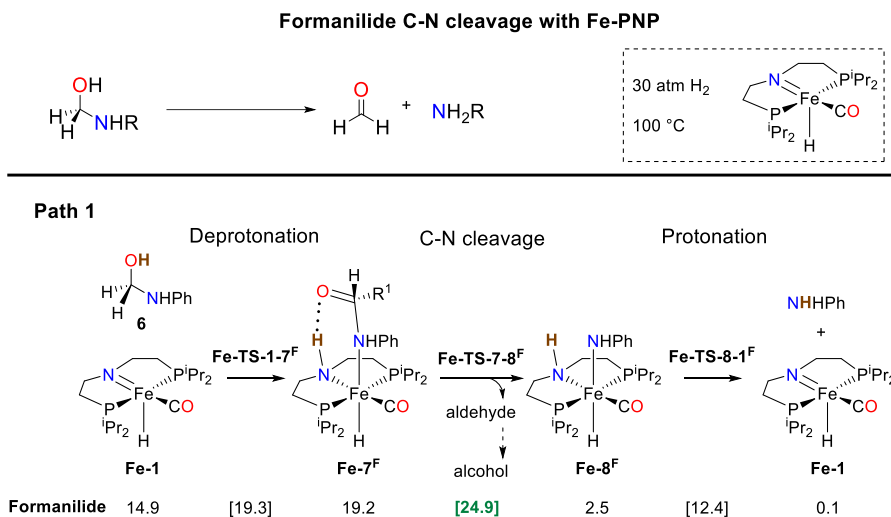


Figure 4.8 Calculated key steps of hemiaminal C-N bond protonolysis of formanilide when in **Fe-1** catalysis experimental conditions.^{31,51} In green, most energetic species.

On the other case, morpholidine and DMF hemiaminal C-N protonolysis prefer **Path 2** and **Path 3** (see Figure 4.9) over **Path 1**, which is disfavoured by morpholidine and DMF more electron-donor substituents ($\Delta G > 40 \text{ kcal mol}^{-1}$). For both amides, the highest energy barrier is the proton transfer, but the methanol-assisted **Path 3** ($\Delta G = 28.1$ and $29.6 \text{ kcal mol}^{-1}$) is slightly less energetic than **Path 2** ($\Delta G = 31.4$ and $30.4 \text{ kcal mol}^{-1}$). However, **Path 3** precise of methanol, which can only be previously produced through **Path 2**. Therefore, one can expect that the reaction will evolve through **Path 2** during the first minutes, and will gradually switch to **Path 3** as methanol concentration increases. **Path 2** becomes unnecessary when formanilide is used as co-

RESULTS

catalyst: In this case, morpholidine and DMF hemiaminal C-N protonolysis proceeds only through the less energetic formanilide-assisted **Path 3** (highest energy barriers of 23.4 and 23.8 kcal mol⁻¹).

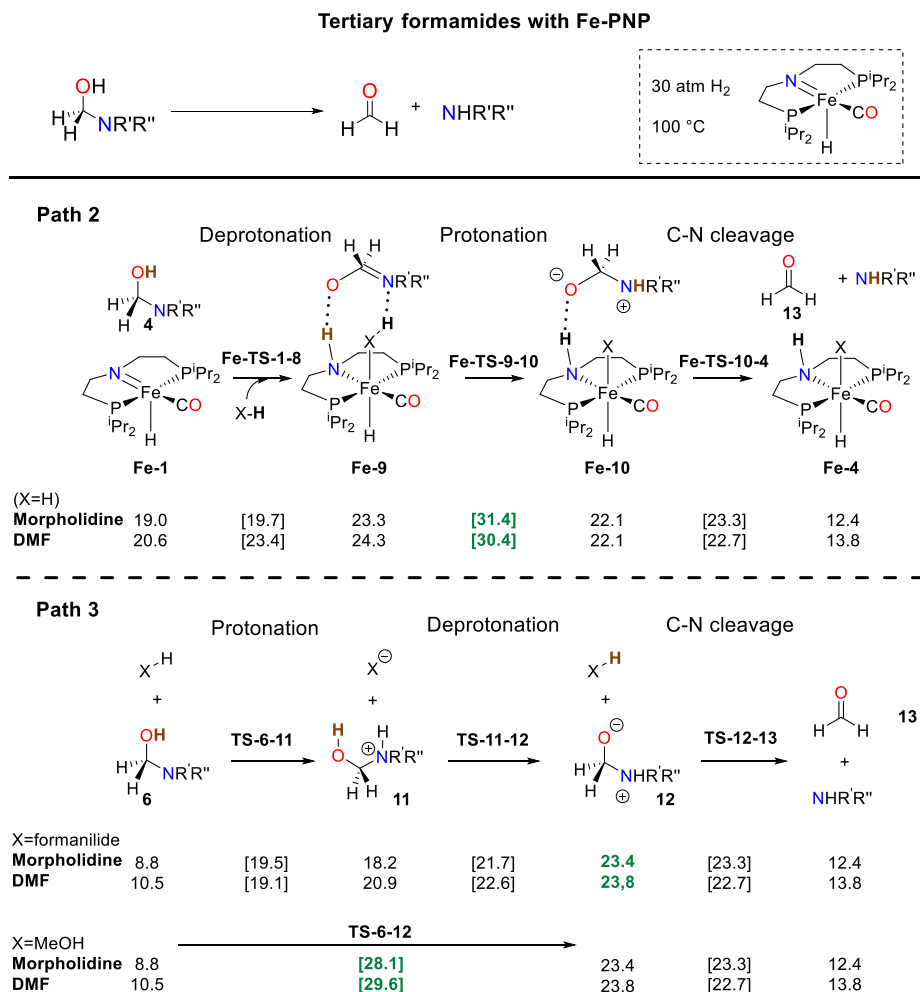


Figure 4.9 Calculated key steps of hemiaminal C-N bond protonolysis of DMF and morpholidine when in **Fe-1** catalysis experimental conditions.^{31,51} In green, most energetic species.

RESULTS

Briefly, formanilide, morpholidine and DMF highest energy barriers for the hemiaminal C-N protonolysis are 24.9, 28.1 and 29.6 kcal mol⁻¹ when unassisted, and 24.9, 23.4 and 23.8 kcal mol⁻¹ when formanilide-assisted. In Chapter 4.2 we will see that these energy barriers are one of the rate-limiting factors in the **Fe-PNP**-catalyzed deaminative hydrogenation of amides.

The reaction pathways for the hemiaminal C-N protonolysis when in the presence of **Mo-1** are shown in Figure 4.10. Formanilide, N-methylformanilide and N-methylacetanilide go through both **Path 1** and the methanol-assisted **Path 2**. The most energetic species of the methanol-assisted **Path 2** ($\Delta G = 12.4, 10.8$ and 11.2 kcal mol⁻¹) are less energetic than those of **Path 1** ($\Delta G = 12.5, 22.9$ and 23.2 kcal mol⁻¹). However, **Path 2** precise of methanol, which can only be previously produced through **Path 1**. Therefore, one can expect that the reaction will evolve through **Path 1** during the first minutes, and will gradually switch to **Path 2** as methanol concentration increases. This situation resembles the cases of Morpholidine and DMF hemiaminal protonolysis when in the presence of **Fe-PNP**, where the methanol assisted paths were preferred over the other mechanisms. Remarkably, transition state **Mo-TS-7-8** with formanilide (12.5 kcal mol⁻¹) is substantially less energetic than with N-methylformanilide, N-methylacetanilide or its Fe analogue **Fe-TS-7-8** (22.9, 23.2 and 24.9 kcal mol⁻¹ respectively). On the cases of N-methylformanilide and N-methylacetanilide, this is because of their more electron-rich C-N bond due to the electron-donating nature of the N methyl.

RESULTS

Hemiaminal C-N protonolysis with Mo-PNP

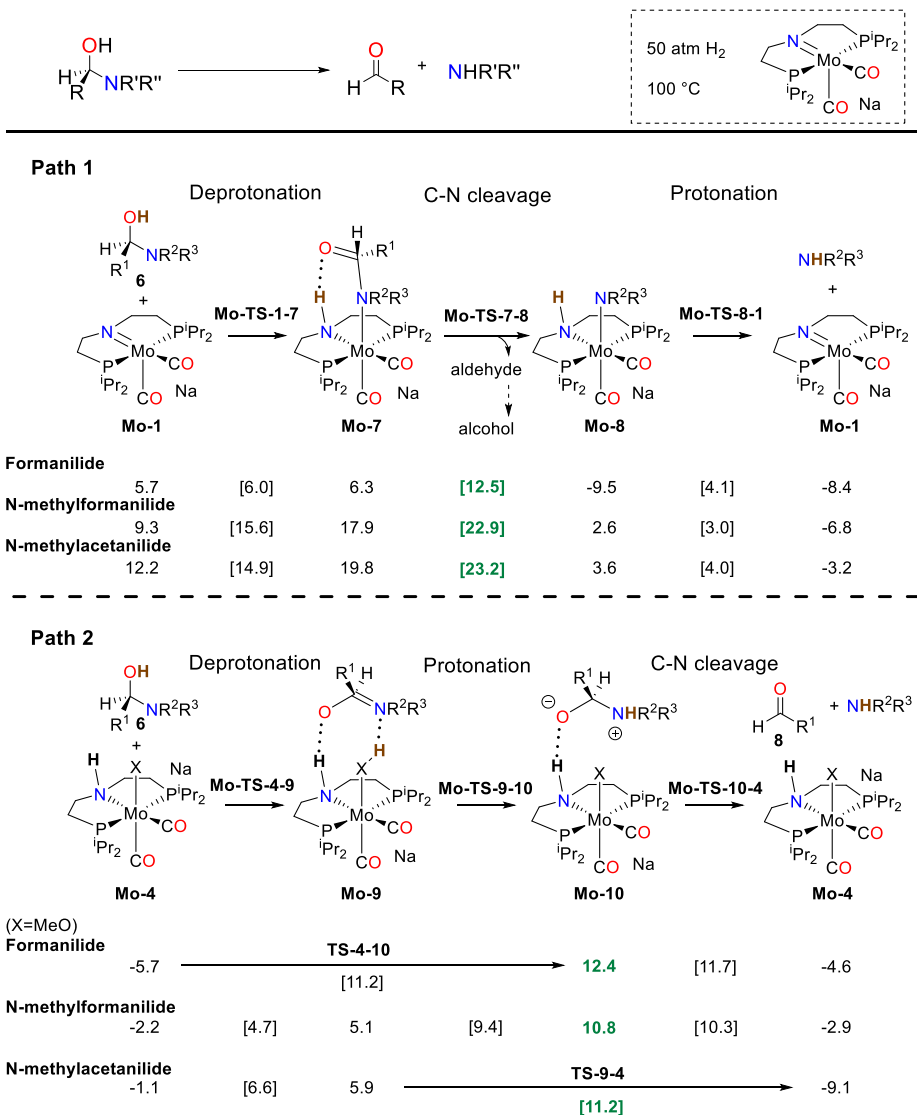


Figure 4.10 Calculated key steps of hemiaminal C-N bond protonolysis when in **Mo-1** catalysis experimental conditions.^{31,51} In green, most energetic species.

4.2 Comparison between experimental and computational results.

Fe-PNP-catalyzed deaminative hydrogenation of amides

The species with the highest and the lowest energies in the reaction mechanisms of the Fe-catalyzed deaminative hydrogenation of amides are shown in Figure 4.11. The rate-limiting step for formanilide is the hemiaminal C-N cleavage (**Fe-TS-7-8^F** with 24.9 kcal mol⁻¹), whereas for morpholidine and DMF, is the hemiaminal proton transfer assisted by methanol (**TS-6-12^M** and **TS-6-12^D** with 28.1 and 29.6 kcal mol⁻¹) (see Figure 4.11). In the other hand, morpholidine and DMF share the same resting state, **Fe-2** with 0.0 kcal mol⁻¹, but not formanilide, which inhibits the catalyst with the formation of **Fe-4^F** with -2.0 kcal mol⁻¹. The formation of the methanol adduct **Fe-4^{MeOH}** is slightly endergonic ($\Delta G = 3.3$ kcal mol⁻¹) but it could also play a role as inhibitor at large concentration of methanol and low temperatures.^{63,64} Therefore, the effective energy barriers of formanilide, morpholidine and DMF hydrogenation are 26.9, 28.1 and 29.6 kcal mol⁻¹ respectively, which are in qualitatively agreement with their experimental conversions of 58%, 36% and 0%.

RESULTS

Key species of Fe-PNP-catalyzed amide deaminative hydrogenation

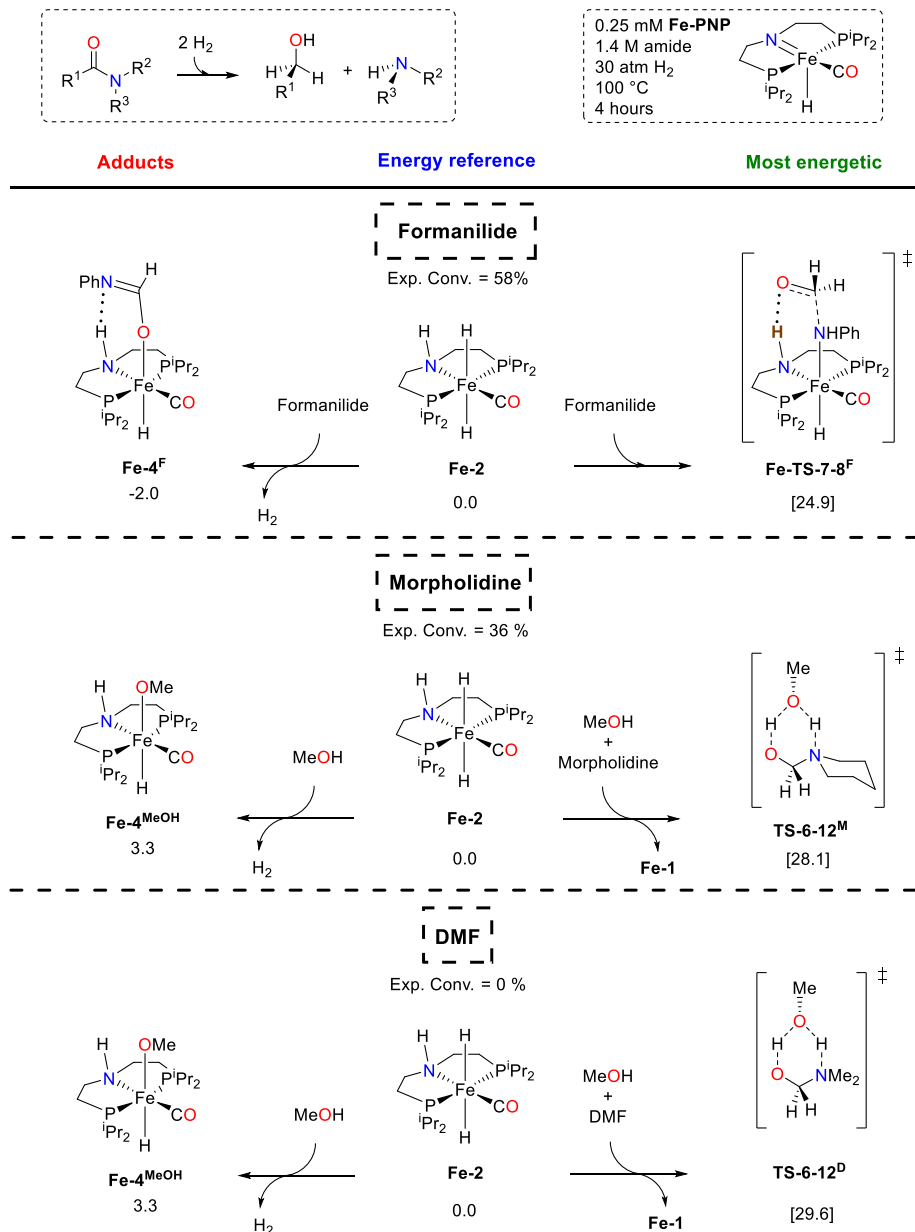


Figure 4.11 Catalyst adducts and most energetic species, in the reaction mechanisms of formanilide, DMF and morpholidine deaminative hydrogenation, when catalyzed by Fe-PNP.

RESULTS

Nevertheless, when formanilide is used as co-catalyst, the resting state and the TS with the highest energy change (see Figure 4.12). In this case, the species with the largest energy are the zwitterions **12^M** and **12^D** for morpholidine and DMF respectively, with energies of 23.4 and 23.8 kcal mol⁻¹. The adduct **Fe-4^F** becomes the least energetic species, at -2.0 kcal mol⁻¹. The effective barriers for morpholidine and DMF are 25.4 and 25.8 kcal mol⁻¹ respectively, which qualitatively match their experimental conversions of >99% and 14%. The low conversion of DMF when compared to morpholidine, can be attributed to the global thermodynamic energy of the DMF reaction, which is close to thermoneutrality ($\Delta G = -1.5$ kcal mol⁻¹, see Figure 4.3) and limits the conversion of DMF to a maximum of 32%.

The use of experimental data to validate and evaluate the precision of our computed mechanisms is not straightforward because of several factors: the multiple roles of formanilide in the reaction (as substrate, co-catalyst and inhibitor), thermoneutrality of the DMF hydrogenation reaction, the difficulty to estimate the real concentration of solved hydrogen, and the large difference in concentration of amide, hydrogen and catalysts in solution. Consequently, microkinetic models were constructed using the computed free energy barriers for the **Fe-PNP**-catalyzed formanilide and DMF deaminative hydrogenation (see Paper I for detailed information about their construction).⁵¹

RESULTS

Key species of Fe^H-PN^HP-catalyzed amide deaminative hydrogenation

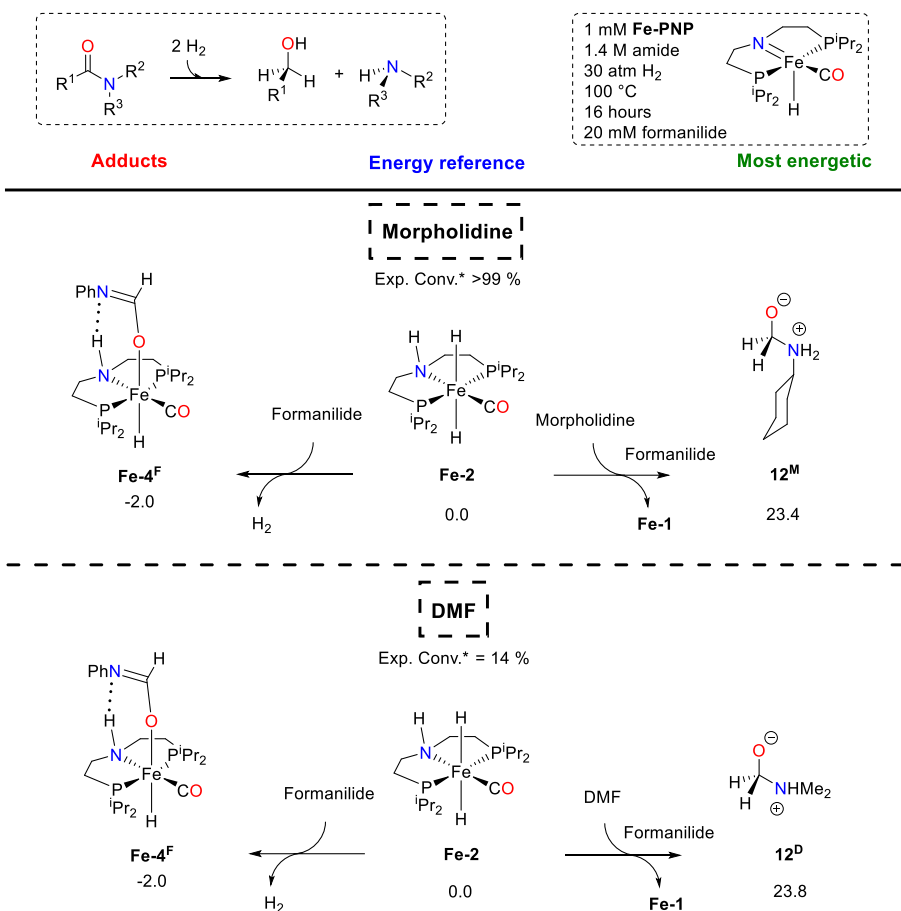


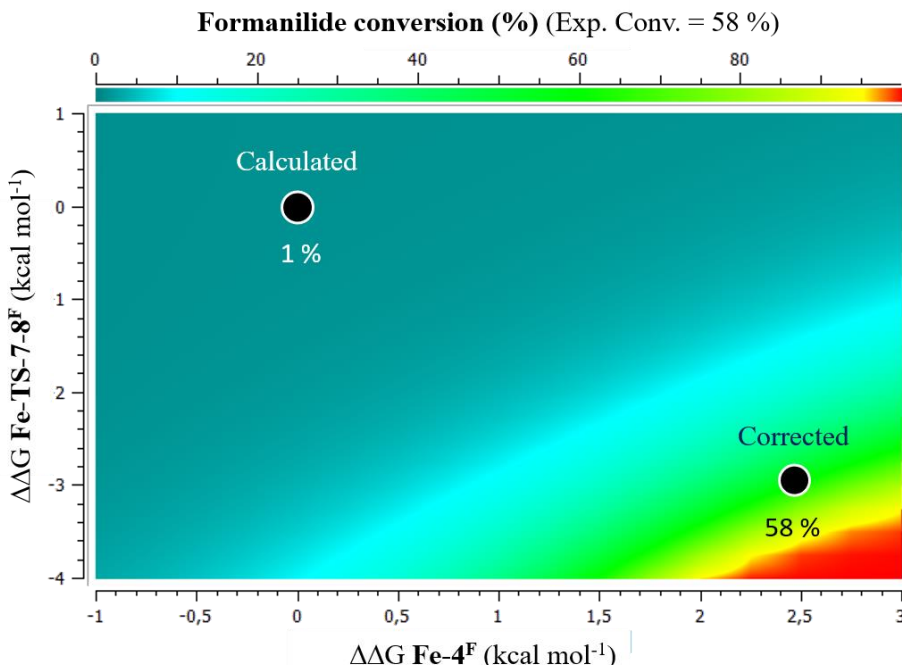
Figure 4.12 Catalyst adducts and most energetic species, in the reaction mechanisms of DMF and morpholidine deaminative hydrogenation when catalyzed by **Fe-PNP** and co-catalyzed by formanilide. * Experimental conversion at 60 atm H₂ and 120 °C.

RESULTS

The microkinetic model for the hydrogenation of formanilide predicted a low conversion of 1 % (see Graph 4.1). Such calculated conversion diverges from the experimental formanilide conversion of 58%. The microkinetic model reproduced the experimental results after adding small corrections in the free energies of **Fe-TS-7-8^F** and **Fe-4^F** ($\Delta\Delta G = -2.9$ and $2.5 \text{ kcal mol}^{-1}$, respectively), which are the stationary points with the highest and lowest energy in the overall reaction profile.

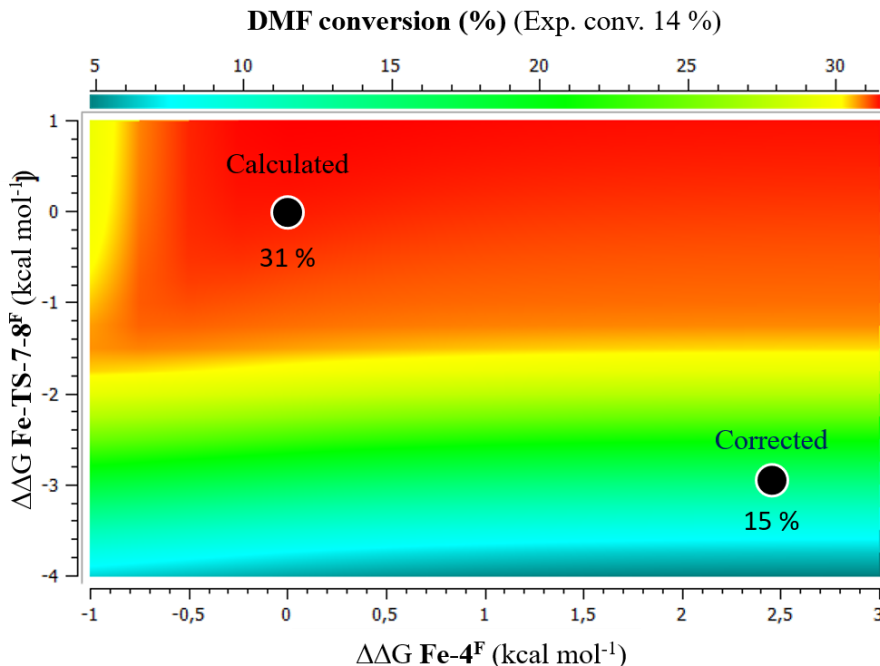
In the other hand, the DMF microkinetic model predicted a DMF conversion of 0 %. Such calculated conversion matched the experimental DMF conversion. However, when 20 eq. of formanilide were added in the microkinetic model (as co-catalyst), the calculated 31 % conversion did not match the experimental 14 % conversion (see Graph 4.2). Incorporation of the corrections done in the formanilide microkinetic model ($\Delta\Delta G = -2.9$ and $2.5 \text{ kcal mol}^{-1}$ to **Fe-TS-7-8^F** and **Fe-4^F**) considerably improved DMF predicted conversion to 15 %.

In conclusion, the mechanism inferred from the DFT calculations accounts for the experimental observations, since the energy deviations derived from the fit are within the error range expected for calculated Gibbs energies,^{95,96} the approach used to calculate the concentration of solved hydrogen, and the standard deviation in experimental measurements.



Graph 4.1 Microkinetic simulations of the formanilide deaminative hydrogenation. Formanilide conversion at 4 hours (%) vs $\Delta\Delta G \text{ Fe-TS } 7-8^F$ vs $\Delta\Delta G \text{ Fe-}4^F$ (kcal mol⁻¹). The simulations were based on the reaction mechanisms shown in Figure 4.4, Figure 4.5, Figure 4.8 and Table 4.1. The initial conditions are set up according to the experiments:³¹ 1.4 M of formanilide, 0.162 M of H₂⁹⁴ and 0.25 mM of **Fe^H-PN^HP**. H₂ concentration was kept constant throughout the kinetic simulations, consistent with the effectively constant pressure of H₂ used in the experiments.

RESULTS



Graph 4.2 Microkinetic simulations of the DMF deaminative hydrogenation. DMF conversion at 16 hours (%) vs $\Delta\Delta G \text{ Fe-TS-7-8}^F$ vs $\Delta\Delta G \text{ Fe-4}^F$ (kcal mol^{-1}). The simulations were based on the reaction mechanisms shown in Figure 4.4Figure 4.5, Figure 4.8 and Figure 4.9 and Table 4.1. The initial conditions are set up according to the experiments:³¹ 1.4 M of formanilide, 0.162 M of H₂ ⁹⁴ 1 mM of **Fe^H-PN^HP** and 20mM of formanilide. H₂ concentration was kept constant throughout the kinetic simulations, consistent with the effectively constant pressure of H₂ used in the experiments.

Mo-PNP-catalyzed deaminative hydrogenation of amides

The most and least energetic species of the reaction mechanism of the **Mo-PNP**-catalyzed deaminative hydrogenation of amides are summarized in Figure 4.13. Using **Mo-2** as energy reference, both the **M-4** adducts and the most energetic species in the molybdenum-catalyzed reaction are more stable than those of the iron-catalyzed reaction ($> 10 \text{ kcal mol}^{-1}$ and $> 3 \text{ kcal mol}^{-1}$ respectively). Two species regulate the reaction rates of formanilide, and N-methylformanilide hydrogenation, due to their similar energies: species **Mo-TS-1-3** and **Mo-10^F** in the case of formanilide ($\Delta G = 13.3$ and $12.4 \text{ kcal mol}^{-1}$), and species **Mo-TS-1-3** and **Mo-TS-2-5^{MF}** in the case of methylformanilide ($\Delta G = 13.3$ and $13.1 \text{ kcal mol}^{-1}$). Species **Mo-TS-2-5^{MA}** ($\Delta G = 20.9 \text{ kcal mol}^{-1}$) is the rate limiting step of N-methylacetanilide hydrogenation by **Mo-PNP**.

The effective barriers of formanilide, N-methylformanilide and N-methylacetanilide (33.2 , 22.8 and $32.5 \text{ kcal mol}^{-1}$) qualitatively match their experimental conversions (13% , $>99\%$ and 20%). Remarkably, N-methylacetanilide has a non-zero conversion despite its prohibitively high $32.5 \text{ kcal mol}^{-1}$ effective barrier: N-methylacetanilide reacts only at the beginning of the reaction, when the low concentration of ethanol makes the contribution of the species **Mo-4^{EtOH}** irrelevant, thus resulting in an initial effective barrier of $20.9 \text{ kcal mol}^{-1}$. Unfortunately, the non-zero conversion of formanilide cannot be explained by the proposed mechanism.

RESULTS

Key species of Mo^H-PN^HP-catalyzed amide deaminative hydrogenation

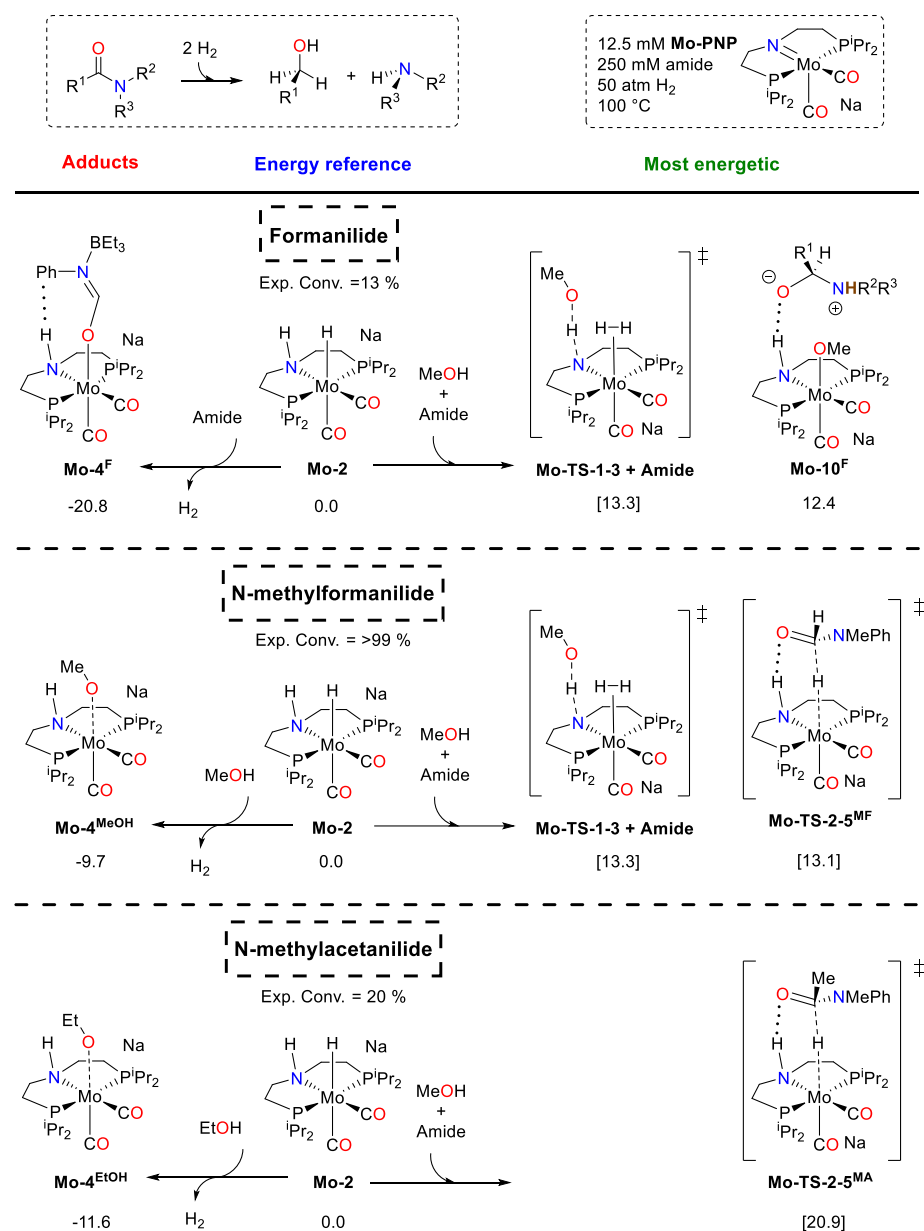


Figure 4.13 Catalyst adducts and most energetic species, in the reaction mechanisms of formanilide, N-methylformanilide and N-methylacetanilide deaminative hydrogenation, when catalyzed by Mo^H-PN^HP.

RESULTS

As in the case of Fe, microkinetic modelling was used to compare the calculated energies with the experimental conversions. In this case we simulated the hydrogenation of N-methylformanilide, and we studied the inhibiting effect of ethanol over this reaction (see Paper III for detailed information about its construction).⁵⁴ The microkinetic model predicted a considerable dependence of amide conversion on ethanol concentration: >99 %, 99 % and 55 % conversion in the presence of 0, 0.5 and 2 eq. of ethanol (straight-lines in Figure 4.14). The calculated conversions qualitatively matched the experimental conversions of >99%, 96 % and 35 % respectively. The microkinetic model was able to reproduce the experimental values after small corrections in the most and least energetic species ($\Delta\Delta G = +0.3, +0.4, -1.8$ and $+0.2$ kcal mol⁻¹ to **Mo-TS-2-5^{MF}**, **Mo-TS-1-3**, **Mo-4^{MeOH}** and **Mo-4^{EtOH}**) (dashed lines in Figure 4.14). An alternative source of error is the catalyst activation mechanism, which fitted the experimental conversions when introduced as a single irreversible reaction with a 25 kcal mol⁻¹ barrier.

RESULTS

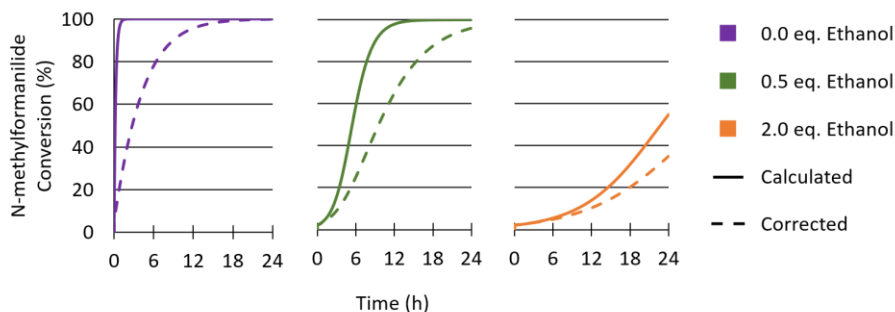


Figure 4.14 Fitted and unfitted microkinetic models of the $\text{Mo}^{\text{Cl}}\text{-PN}^{\text{H}}\text{P}$ catalyzed N-methylformanilide deaminative hydrogenation when in the presence of 0, 0.5 and 2.0 eq. of ethanol. The simulations were based on the reaction mechanisms shown in Figure 4.5, Figure 4.6 and Figure 4.10 and Table 4.1. The initial conditions for the microkinetic model are set up according to the experiments:⁵⁴ 0.25 M of N-methylformanilide, 0.207 M of H_2 ,⁹⁴ 12.5mM of $\text{Mo}^{\text{Cl}}\text{-PN}^{\text{H}}\text{P}$. H_2 concentration was kept constant throughout the kinetic simulations, consistent with the effectively constant pressure of H_2 used in the experiments.

4.3 Reaction optimization.

Fe-PNP - catalyzed deaminative hydrogenation of amides

A rational approach involving DFT calculations has been used to design co-catalysts tailored for the deaminative hydrogenation of tertiary amides (*Paper II*).⁵³ This was possible thanks to the research on **Fe-PNP** catalyzed deaminative amide hydrogenation (*Paper I*),⁵¹ which identified the role of the co-catalyst: proton shuttle for the formation of zwitterion **12**, here named $[\Delta G_{HT}]^\ddagger$ (see Figure 4.15). However, formanilide, the co-catalyst studied in *Paper I*, had the drawbacks of being parallelly hydrogenated by **Fe-2** on the course of the reaction and inhibiting the catalyst by the formation of adducts **Fe-4F**, here named ΔG_{add} (see Figure 4.15).

In *Paper II*, I calculated the ΔG_{add} and $[\Delta G_{HT}]^\ddagger$ of a series of potential organic co-catalysts that could act as a proton shuttle for hemiaminal proton transfer (low $[\Delta G_{HT}]^\ddagger$), without inhibiting the catalyst (**Fe-4** > **Fe-2**), or being hydrogenated by **Fe-2**.

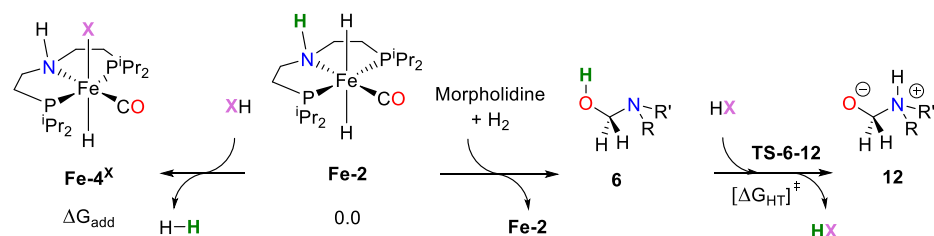


Figure 4.15 Key energies and species of tertiary alkyl amides deaminative hydrogenation when catalyzed by **Fe-1**.

RESULTS

The potential catalysts assessed (see Table 4.2) included molecules with either hydrogen-bond donor single-sites (entries 4, 5 and 8) or with both hydrogen-bond donor and acceptor sites which could act as push-pull proton shuttles (entries 1-3, 6 and 9). In molecules with C=O or C=N functional groups, only electron-rich systems were chosen to minimize the hydrogenation of the co-catalyst.

The calculated $[\Delta G_{HT}]^\ddagger$ and ΔG_{add} of morpholidine deaminative hydrogenation were used to estimate the effective energy barrier of the reaction: $\Delta G_{eff} = ([\Delta G_{HT}]^\ddagger - \Delta G_{add})$ except when $\Delta G_{add} > \textbf{Fe-2}$ and/or **TS-6-12^{MeOH}** $< [\Delta G_{HT}]^\ddagger < \textbf{12}^M$, in which cases **Fe-2**, **TS-6-12^{MeOH}** or **12^M** substituted $[\Delta G_{HT}]^\ddagger$ and ΔG_{add} . The ΔG_{eff} of each potential co-catalyst was then compared to its corresponding experimental performance (see Table 4.2)

ΔG_{eff} qualitatively correlated to experimental TONs, with the exception of 1,2,3-triphenyl guanidine (entry 6), which may react differently as indicated by an immediate colour change upon treatment with **Fe-PNP**. Triazabicyclodecene (TBD, entry 1) and acetanilide (entry 2) experimentally proved to be co-catalysts more active than formanilide, being TBD the best performing co-catalyst among the tested, improving formanilide co-catalyst activity by a 130%.

RESULTS

Entry	Co-catalyst	0.07 mol% [Fe-PNP]		ΔG_{eff}	TON ^a	Conv. ^a
		$[\Delta G_{\text{HT}}]^{\ddagger}$	ΔG_{add}			
1		22.1	8.7	23.4	830	59%
2		25.4	1.9	25.4	780	55%
3		21.7	-2.0	25.4	630	45%*
4		25.5	14.6	25.5	560	40%
5	Me—OH	28.1	3.3	28.1	510	37%
6		21.4	1.4	23.4	440	31%†
7	No additive	28.1	---	28.1	320	22%
8		31.9	18.2	28.1	320	22%
9		35.6	1.4	28.1	90	6%*

Table 4.2 Computational and experimental results on potential co-catalysts for morpholidine deaminative hydrogenation, **Fe-PNP** catalyzed. * co-catalyst is consumed in the course of the reaction. † Immediate colour change was observed upon treatment with **Fe-PNP**. ^aExperimental reaction conditions: 30 atm H₂, 5 μmol of [Fe-PNP] (0.07 mol%), 1.75 mol% of each additive and 7 mmol of morpholidine in 5 mL of THF at 100 °C for 2 h. TON and Conv. were determined by GC-FID analysis of the products and remaining starting material. Each entry is the average of two or more trials.

RESULTS

TBD was later proved to significantly enhance the hydrogenation of other inactive amides (when **Fe-PNP**-catalyzed) (see Table 4.3), and the hydrogenation of morpholidine when catalyzed by **Ru^{HBH₃}**-PN^HP or **Ru^{HBH₃}**-PN^HN (see Table 4.4). TBD could not co-catalyze N-phenylbenzamide deaminative hydrogenation, though acetanilide did (Table 4.3; entry 4c).

Entry	Amide	[TBD]	TON ^b .
			0.07 mol% [Fe-PNP] x mol% [TBD]
1		0	50
		1.75	300
2		0	1150
		0.45	5180
3		0	140
		1.75	230
4		0	120
		1.75	120
		1.75 ^c	250 ^c

Table 4.3 ^a Reaction conditions: 60 atm H₂, 5 μmol of [Fe-PNP] (0.07 mol%), x μmol of TBD, and 7 mmol of substrate in 5 mL of THF at 120 °C for 16 h. ^b TON was determined by GC-FID and NMR analysis of the products and remaining starting material. Each entry is the average of three or more trials. ^c TBD was substituted by N-acetanilide (Table 4.2; entry 2).

RESULTS

1.4 M $0.07 \text{ mol\% } [\text{CAT}]$
 H_2 $1.75 \text{ mol\% } [\text{Co-cat}]$
 30 atm THF
 $2\text{h}, 100^\circ\text{C}$

Entry	Catalyst	Co-catalyst	TON ^b	Conv. ^b
1		None	320	23%
	Fe-PNP	TBD	830	59%
		Formanilide	630	45%
2		None	310	22%
	Ru^{HBH3}-PN^HP	TBD	1200	86%
		Formanilide	0 ^c	0% ^c
3		None	440	31%
	Ru^{HBH3}-PN^HN	TBD	1170	84%
		Formanilide	1040	74%

Table 4.4 ^a Experimental reaction conditions: 30 atm H₂, 5 µmol of [Fe or Ru] (0.07 mol%), 125 µmol co-catalyst and 7 mmol of morpholidine in 5 mL of THF at 100 °C for 2 h. For [Ru] co-catalysts 10 µmol of NEt₃ was added to activate the catalyst. ^b Determined by GC-FID analysis of the products and remaining starting material. Each entry is the average of two or more trials. ^c Formanilide reacts irreversibly with this Ru catalyst to form an adduct (see *Paper II* for details).

RESULTS

Mo^{Cl}-PN^HP - catalyzed deaminative amide hydrogenation

In a similar fashion to the case of **Fe-PNP**, I attempted to optimize the **Mo^{Cl}-PN^HP**-catalyzed amide hydrogenation with the information obtained in its mechanistic study. Mo reaction mechanism shows a clear dependence on the counter-cation type (see Table 4.5) and location (see *Paper III S.I.*):⁵⁴ the energy difference between transition state **Mo-TS-2-5^{MF}** (rate-limiting step) and adduct **Mo-4^{MeOH}** (catalyst resting state) swings from 28.8 kcal mol⁻¹ to 22.9 and 23.0 kcal mol⁻¹ with the alkaline counterions Li⁺, Na⁺ and K⁺, respectively. The extreme case of counterion absence shows an even lower effective energy barrier ($\Delta G_{\text{eff}} = 19.9$ kcal mol⁻¹). These calculations were later tested experimentally: **Mo^{Cl}-PN^HP** was activated with LiHBH₃, NaHBH₃ or KHBH₃, and then used to hydrogenate N-methylformanilide at 80 °C and 50 atm of H₂. The resulting experimental conversions qualitatively agreed with their respective calculated effective energy barriers (see Table 4.5). Unfortunately, none of the tested counter-cations resulted in an improved reaction performance. To approach the limit of counter-cation absence, the sterically hindered counter-cation PPh₄⁺ or the Na⁺-trap crown ether 15-crown-5 were tested experimentally. However, they decreased the reaction yield, contrary to the computational predictions. This unexpected behaviour may be attributed to the probably low solubility of the ion pairs **[Mo^H-PN^HP]⁻/PPh₄⁺** and **[Mo^H-PN^HP]⁻/15-crown-5-Na⁺**.

RESULTS

Counter-cation (M)	ΔG_{eff} (kcal mol ⁻¹)	Yield (%)*
Li ⁺	28.8	9
Na ⁺	22.9	75
K ⁺	23.0	75
Absence of counter-cation	19.9	

Table 4.5 Free energies (kcal mol⁻¹) for the isodesmic reaction between **Mo-4^{MeOH}** and **Mo-TS-2-5^F**. *Yields of **Mo^{Cl}-PN^HP**-catalyzed N-methylformanilide deaminative hydrogenation after 24h at 80 °C with 5 mol% of alkali metal hydrides, 0.25 M of N-methylformanilide, 50 atm of H₂, 12.5mM of **Mo^{Cl}-PN^HP**

5 Conclusions and Future Outlook

The main conclusions of the computational mechanistic study on the **Fe-PNP** catalyzed deaminative hydrogenation of amides were the following:

- Reliable energies and molecular geometries of amides and **Fe-PNP** complexes can be obtained with the use of the M06 functional and double-z basis sets, together with energy refinements with functional M06 and triple-z basis set.
- Deaminative hydrogenation of amides by **Fe-PNP** follows a three-step process consisting of (1) amide C=O hydrogenation, (2) C-N bond protonolysis, and (3) aldehyde C=O hydrogenation. The rate-limiting step of both secondary and tertiary amides is the C-N bond protonolysis, which proceeds by a different pathway for the two substrates. While **Fe-PNP** promotes the cleavage of the C-N bond of secondary amides, the C-N bond of tertiary amides is too electron-rich to be broken by **Fe-PNP**. In the latter case, secondary amides can act as proton-shuttles, and thus assist the C-N bond protonolysis.

CONCLUSIONS AND FUTURE OUTLOOK

- Catalyst **Fe-PNP** can dehydrogenate weak acids such as secondary amides or methanol, which can block the catalyst active-site and prevent its hydrogenation. This reaction is reversible but significant enough to hamper the catalyst activity.
- TBD has proved to co-catalyze the deaminative hydrogenation of tertiary amides thanks to (I) its proton-shuttle abilities, that facilitate the cleavage of tertiary amides C-N bonds, (II) its steric hindrance, that avoid TBD from blocking **Fe-PNP** active site, and (III) its difficult hydrogenation by **Fe-PNP**.

Particular conclusions of the computational mechanistic study on the **Mo^H-PN^HP** catalyzed deaminative hydrogenation of amides were the following:

- Deaminative hydrogenation of amides by **Mo^H-PN^HP** follows the same three-step pathway of **Fe-PNP**: (1) amide C=O hydrogenation, (2) C-N bond protonolysis, and (3) aldehyde C=O hydrogenation. However, in the case of **Mo^H-PN^HP**, the rate-limiting step is amide-dependent: In the case of formamides, their rate-limiting step is the C-N bond protonolysis, which is assisted by **Mo^H-PN^HP** and a methanol molecule; in the case of acetamides, their rate-limiting step is the amide C=O hydrogenation, because their more electron-rich carbonyl is harder to hydrogenate than that of formamides.

CONCLUSIONS AND FUTURE OUTLOOK

- Secondary amides and alcohols can block **Mo-PNP** active site. This inhibition is more significant than in the case of **Fe-PNP**, and therefore, the more energy demanding hydrogenations of acetamides can only be performed by **Fe-PNP**.
- The alkaline counteraction of **Mo^H-PN^HP** stabilizes the catalyst negative charge, while modifying the hydricity of the catalyst. The substitution of the alkaline cation by a larger molecule enhances the catalyst hydricity but it reduces its solubility.

Only three substrates have been computed per catalyst. A broader scope of amides remains to be investigated computationally in future work, as well as a broader scope of base metal Noyori-type catalysts. A broader scope of amides could solidify the conclusions of the thesis, while a broader scope of metals could lead to a rational catalyst design that maximizes the catalyst hydricity while minimizes the formation of adducts between primary or secondary amides and the catalyst. Also, further research on orbital analysis of **Mo^H-PN^HP** interaction with its counteraction would help to understand how it modifies the catalyst hydricity.

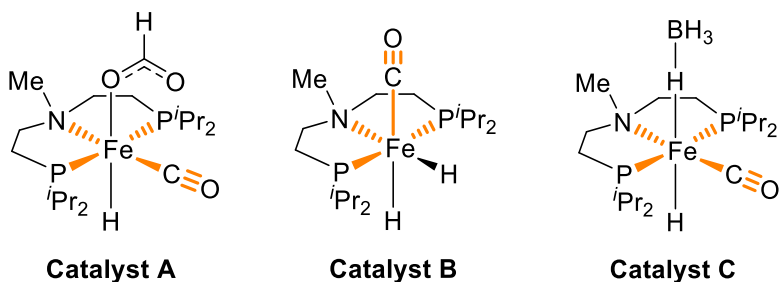
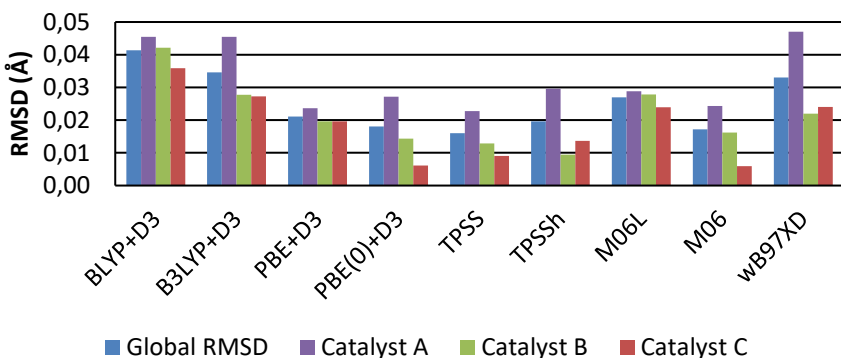
Appendix

Method benchmarking.

In order to select the best method describing the reactivity of **Fe-PNP**, the performance of several density functionals against geometric and energetic benchmarks were tested.

The density functionals used for the study were BLYP, B3LYP, PBE, PBE(0), TPSS, TPSSh, M06-L, M06 and ω B97XD.^{69,97–105} Three parameter Grimme dispersion corrections¹⁰⁶ were used in non-GGA functionals without dispersion corrections: BLYP, B3LYP, PBE and PBE(0). The basis sets used were the double-z quality LANL2DZ¹⁰⁷ on iron and 6-31+G** for all other elements.¹⁰⁸

Catalysts A, B and C were selected for geometric benchmarking since their molecular structure has been resolved by single-crystal X-ray diffraction.⁶⁰ The experimental geometries of **A**, **B** and **C** were compared against DFT gas-phase geometry optimizations (see Graph 0.1). Bonds Fe-P, Fe-N, Fe-C and C≡O were selected for an RMSD analysis because they were the most sensitive to density functional changes. All functionals gave acceptable global RMSD, though functionals PBE(0)+D3, TPSS, TPSSh and M06 were identified as the best candidates, giving global RMSD smaller than 0.02 Å.

**Geometry Benchmark**

Graph 0.1 Geometry benchmark results of **Catalyst A**, **B** and **C**. Experimental bond distances (Exp.) **1**, **2**, **3**, **4** and **5** by single-crystal x-ray diffraction in front of gas-phase density functional theory geometry optimizations with **BLYP+D3**, **B3LYP**, **PBE+D3**, **TPSS**, **TPSSh**, **M06L+D3**, **M06+D3** and **wB97XD** functionals and double-z quality basis set (LANL2DZ on iron and 6-31+G** for all other elements).

Next, an energy benchmark of **Reactions 1**, **2** and **3** (see Figure 0.1) was performed to assess the energy accuracy in the calculation of **Fe^H-PN^{Me}P** and **Fe^H-PN^HP** complexes, and to discriminate between the functionals that performed best in the geometry benchmark. The tested reactions are the isomerizations of the **Fe-PN^HP** and **Fe-PN^{Me}P** complexes (**Reaction 1** and **2** in Figure 0.1) and a hydrogen transfer from a **Fe^H-PN^HP** catalyst to a CO₂ molecule (**Reaction 3** in Figure 0.1).

Geometry optimizations of these reactions complexes were performed with the M06 functional. Then we computed their reaction potential energies (ΔE_r) with single point CCSD(T)/cc-pVTZ calculations as energy benchmarks. The coupled-cluster energies were then compared with ΔE_r calculated with functionals PBE(0)+D3, TPSSh and M06 (LANL2TZ on Fe, 6-311+G** on the rest)^{109,110} (see Graph 0.2). The DFT computed reaction energies for **Reactions 1** and **2** matched the coupled-cluster energies, with a deviation smaller than 1 kcal mol⁻¹. However, the coupled-cluster computed reaction energy for **Reaction 3** could only be reproduced with the M06 functional. Therefore we concluded that, when compared to the other tested density functionals, the M06 functional provide both the most accurate energies and acceptable geometry optimizations of complexes of amides and iron Noyori-type catalysts.

APPENDIX

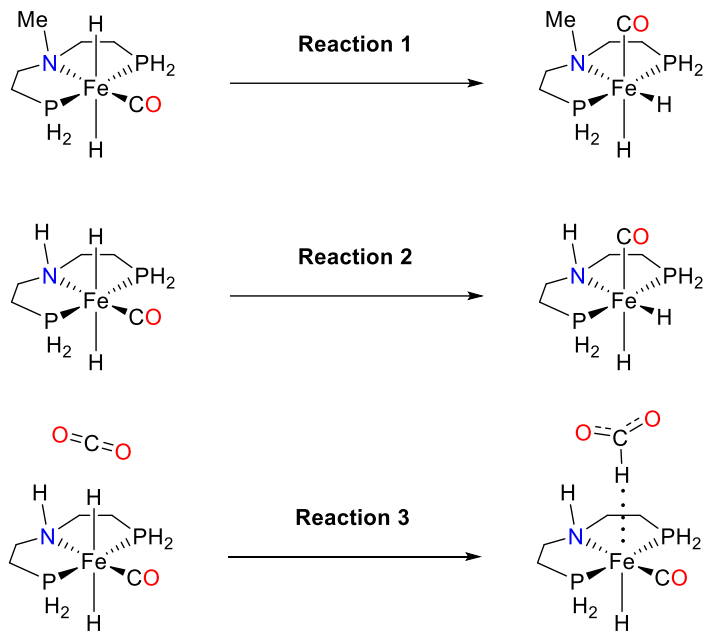
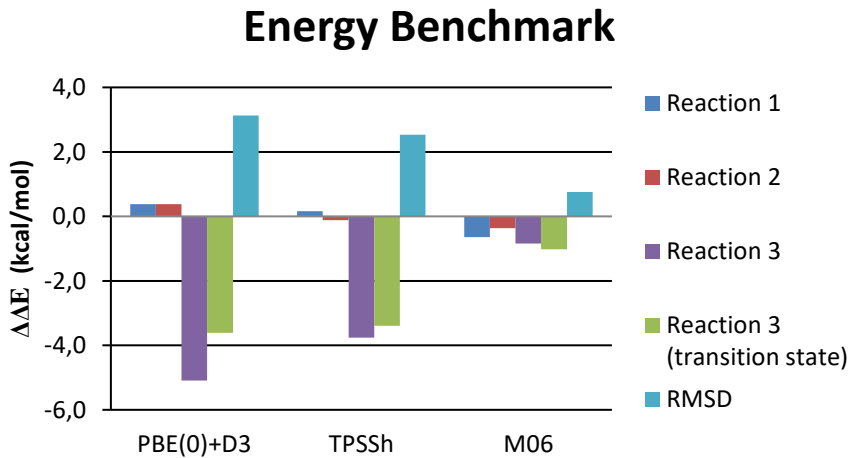
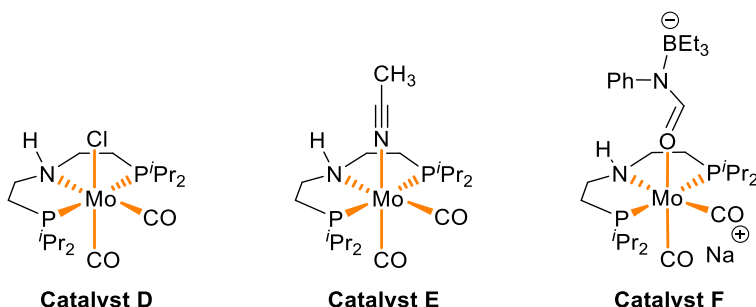
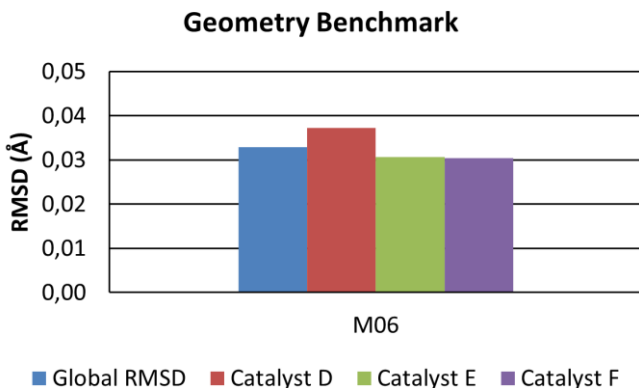


Figure 0.1 Reactions selected for the energy benchmarks. Phosphines iso-propyls were replaced by hydrogens to make CCSD(T) calculations feasible.



Graph 0.2 Quantitative deviation of DFT $\Delta_r E$ and ΔE^\ddagger relative to CCSD(T) energies of reaction 1, 2, 3 and reaction 3 transition state.

Finally, we tested M06 performance in geometry optimizations of molybdenum Noyori-type catalysts. Single-crystal X-ray diffractions of **Catalysts D, E and F** were used as geometry benchmarks, and they were compared against DFT geometry optimizations with the M06 functional and double-z quality basis set (LANL2DZ on iron and 6-31+G** for all other elements). Bonds Mo-P, Mo-N, Mo-Cl, Mo-nitrile and Mo-C constitute molybdenum first coordination sphere; therefore, they were selected for an RMSD analysis. M06 RMSD of 0.03 Å (see Graph 0.3) support the use of M06 for geometry optimizations of molybdenum Noyori-type catalysts.



Graph 0.3 Root mean square deviation (Å) of marked distances of **Catalysts D, E and F** calculated geometries with respect their single-crystal X-ray diffraction geometries.

Selected Methodology

The M06 functional was used for both geometry optimizations (with double-z basis set) and energy refinement (with triple-z basis set). Analytic frequency calculations of stationary points were performed to classify them in either energy minima or saddle points. Free energies were calculated from double-z basis set analytic frequency calculations. Our calculations contain thermal and pressure corrections to emulate the experimental conditions of 373.15 K and 30 atm in the case of **Fe-PNP**-catalyzed reactions, and 373.15 K and 50 atm in the case of **Mo^{Cl}-PN^HP**-catalyzed reactions. Solvent effects of THF were introduced with the continuum SMD model. The ultrafine (99,590) grid was used in all calculations for higher numerical accuracy. All calculations were carried out with the Gaussian09 (RevD.01) software package.¹¹¹

Microkinetic models were constructed with the COPASI (version 4.22) software.⁸³ The models were based on deterministic time course simulations with the LSODA algorithm.⁸⁷ Temperature, reaction times and initial concentrations were adjusted to experimental values and will be specified at each case. Hydrogen pressurized reactions were simulated as a constant hydrogen saturated concentration of 0.162M, calculated using the molar fraction of H₂ in a H₂ saturated solution of THF at 33.4 atm and 100 °C (0.01461 H₂ mol / solution mol), assuming incompressibility of THF and that [H₂] << [THF].⁹⁴ Elementary reactions and their associated reaction energies and barriers are specified in the supporting information of their corresponding articles.

Bibliography

- (1) Boaz, N. W.; Mackenzie, E. B.; Debenham, S. D.; Large, S. E.; Ponasik, J. A. Synthesis and Application of Phosphinoferrocenyl-Aminophosphine Ligands for Asymmetric Catalysis. *J. Org. Chem.* **2005**, *70*, 1872–1880. <https://doi.org/10.1021/jo048312y>.
- (2) Tang, W.; Zhang, X. New Chiral Phosphorus Ligands for Enantioselective Hydrogenation. *Chem. Rev.* **2003**, *103*, 3029–3069. <https://doi.org/10.1021/cr020049i>.
- (3) Crabtree, R. H. Homogeneous Catalysis. In *The organometallic chemistry of the transition metals*; John Wiley & Sons, Inc.: Hoboken, New Jersey, 2014; p 224.
- (4) Crabtree, R. H. Alkyls and Hydrides. In *The organometallic chemistry of the transition metals*; John Wiley & Sons, Inc.: Hoboken, New Jersey, 2014; p 69.
- (5) Hartwig, J. F. Homogeneous Hydrogenation. In *Organotransition metal chemistry: from bonding to catalysis*; Murdzek, J., Ed.; University Science Books: Sausalito, Calif, 2010; p 575.
- (6) Hartwig, J. F. Hydrofunctionalization and Oxidative Functionalization of Olefins. In *Organotransition metal chemistry: from bonding to catalysis*; Murdzek, J., Ed.; University Science Books: Sausalito, Calif, 2010; p 667.
- (7) Dobereiner, G. E.; Crabtree, R. H. Dehydrogenation as a Substrate-Activating Strategy in Homogeneous Transition-Metal Catalysis. *Chem. Rev.* **2010**, *110*, 681–703. <https://doi.org/10.1021/cr900202j>.
- (8) Stephan, D. W. Frustrated Lewis Pairs: From Concept to Catalysis. *Acc. Chem. Res.* **2015**, *48*, 306–316. <https://doi.org/10.1021/ar500375j>.
- (9) Stephan, D. W.; Erker, G. Frustrated Lewis Pair Chemistry: Development and Perspectives. *Angew. Chemie - Int. Ed.* **2015**, *54*, 6400–6441. <https://doi.org/10.1002/anie.201409800>.
- (10) Stephan, D. W. The Broadening Reach of Frustrated Lewis Pair Chemistry. *Science (80-.).* **2016**, *354*, aaf7229. <https://doi.org/10.1126/science.aaf7229>.
- (11) Piccirilli, L.; Pinheiro, D. L. J.; Nielsen, M. Recent Progress with Pincer Transition Metal Catalysts for Sustainability. *Catalysts* **2020**,

BIBLIOGRAPHY

- 10, 1–115. <https://doi.org/10.3390/catal10070773>.
- (12) Kuriyama, W.; Matsumoto, T.; Ogata, O.; Ino, Y.; Aoki, K.; Tanaka, S.; Ishida, K.; Kobayashi, T.; Sayo, N.; Saito, T. Catalytic Hydrogenation of Esters. Development of an Efficient Catalyst and Processes for Synthesising (R)-1,2-Propanediol and 2-(1-Menthoxy)Ethanol. *Org. Process Res. Dev.* **2012**, *16*, 166–171. <https://doi.org/10.1021/op200234j>.
- (13) Filonenko, G. A.; Van Putten, R.; Hensen, E. J. M.; Pidko, E. A. Catalytic (de)Hydrogenation Promoted by Non-Precious Metals-Co, Fe and Mn: Recent Advances in an Emerging Field. *Chem. Soc. Rev.* **2018**, *47*, 1459–1483. <https://doi.org/10.1039/c7cs00334j>.
- (14) Alig, L.; Fritz, M.; Schneider, S. First-Row Transition Metal (De)Hydrogenation Catalysis Based on Functional Pincer Ligands. *Chem. Rev.* **2018**, *119*, 2681–2751. <https://doi.org/10.1021/acs.chemrev.8b00555>.
- (15) Peris, E.; Crabtree, R. H. Key Factors in Pincer Ligand Design. *Chem. Soc. Rev.* **2018**, *47*, 1959–1968. <https://doi.org/10.1039/c7cs00693d>.
- (16) Perutz, R. N.; Sabo-Etienne, S. The σ-CAM Mechanism: σ Complexes as the Basis of σ-Bond Metathesis at Late-Transition-Metal Centers. *Angew. Chemie - Int. Ed.* **2007**, *46*, 2578–2592. <https://doi.org/10.1002/anie.200603224>.
- (17) Pattabiraman, V. R.; Bode, J. W. Rethinking Amide Bond Synthesis. *Nature* **2011**, *480*, 471–479. <https://doi.org/10.1038/nature10702>.
- (18) De Figueiredo, R. M.; Suppo, J. S.; Campagne, J. M. Nonclassical Routes for Amide Bond Formation. *Chem. Rev.* **2016**, *116*, 12029–12122. <https://doi.org/10.1021/acs.chemrev.6b00237>.
- (19) Acosta-Guzmán, P.; Mateus-Gómez, A.; Gamba-Sánchez, D. Direct Transamidation Reactions: Mechanism and Recent Advances. *Molecules* **2018**, *23*, 2382. <https://doi.org/10.3390/molecules23092382>.
- (20) Valeur, E.; Bradley, M. Amide Bond Formation: Beyond the Myth of Coupling Reagents. *Chem. Soc. Rev.* **2009**, *38*, 606–631. <https://doi.org/10.1039/b701677h>.
- (21) Mahesh, S.; Tang, K. C.; Raj, M. Amide Bond Activation of Biological Molecules. *Molecules* **2018**, *23*, 2615. <https://doi.org/10.3390/molecules23102615>.
- (22) Arthur, G. *The Amide Linkage: Selected Structural Aspects in*

BIBLIOGRAPHY

- Chemistry, Biochemistry, and Materials Science.*, 1st ed.; Wiley-Interscience: Hoboken, 2000.
- (23) Kar, S.; Goeppert, A.; Kothandaraman, J.; Prakash, G. K. S. Manganese-Catalyzed Sequential Hydrogenation of CO₂ to Methanol via Formamide. *ACS Catal.* **2017**, *7*, 6347–6351.
<https://doi.org/10.1021/acscatal.7b02066>.
- (24) Kothandaraman, J.; Goeppert, A.; Czaun, M.; Olah, G. A.; Prakash, G. K. S. Conversion of CO₂ from Air into Methanol Using a Polyamine and a Homogeneous Ruthenium Catalyst. *J. Am. Chem. Soc.* **2016**, *138*, 778–781. <https://doi.org/10.1021/jacs.5b12354>.
- (25) Rezayee, N. M.; Huff, C. A.; Sanford, M. S. Tandem Amine and Ruthenium-Catalyzed Hydrogenation of CO₂ to Methanol. *J. Am. Chem. Soc.* **2015**, *137*, 1028–1031.
<https://doi.org/10.1021/ja511329m>.
- (26) Kar, S.; Kothandaraman, J.; Goeppert, A.; Prakash, G. K. S. Advances in Catalytic Homogeneous Hydrogenation of Carbon Dioxide to Methanol. *J. CO₂ Util.* **2018**, *23*, 212–218.
<https://doi.org/10.1016/j.jcou.2017.10.023>.
- (27) Smith, A. M.; Whyman, R. Review of Methods for the Catalytic Hydrogenation of Carboxamides. *Chem. Rev.* **2014**, *114*, 5477–5510.
<https://doi.org/10.1021/cr400609m>.
- (28) Di Gioia, M. L.; Belsito, E. L.; Leggio, A.; Leotta, V.; Romio, E.; Siciliano, C.; Liguori, A. Reduction of Amide Carbonyl Group and Formation of Modified Amino Acids and Dipeptides. *Tetrahedron Lett.* **2015**, *56*, 2062–2066.
<https://doi.org/10.1016/j.tetlet.2015.02.074>.
- (29) Nystrom, R. F.; Brown, W. G. Reduction of Organic Compounds by Lithium Aluminum Hydride. III. Halides, Quinones, Miscellaneous Nitrogen Compounds. *J. Am. Chem. Soc.* **1948**, *70*, 3738–3740.
<https://doi.org/10.1021/ja01191a057>.
- (30) Weygand, F.; Eberhardt, G.; Linden, H.; Schäfer, F.; Eigen, I. Angewandte Chemie. *Angew. Chem.* **1962**, *53*, 525–531.
[https://doi.org/10.1016/0009-2509\(62\)87032-8](https://doi.org/10.1016/0009-2509(62)87032-8).
- (31) Jayaratne, U.; Zhang, Y.; Hazari, N.; Bernskoetter, W. H. Selective Iron-Catalyzed Deaminative Hydrogenation of Amides. *Organometallics* **2017**, *36*, 409–416.
<https://doi.org/10.1021/acs.organomet.6b00816>.

BIBLIOGRAPHY

- (32) Gusev, D. G. Rethinking the Dehydrogenative Amide Synthesis. *ACS Catal.* **2017**, *7*, 6656–6662. <https://doi.org/10.1021/acscatal.7b02415>.
- (33) Balaraman, E.; Gnanaprakasam, B.; Shimon, L. J. W.; Milstein, D. Direct Hydrogenation of Amides to Alcohols and Amines under Mild Conditions. *J. Am. Chem. Soc.* **2010**, *132*, 16756–16758. <https://doi.org/10.1002/chin.201116025>.
- (34) John, J. M.; Bergens, S. H. A Highly Active Catalyst for the Hydrogenation of Amides to Alcohols and Amines. *Angew. Chemie - Int. Ed.* **2011**, *50*, 10377–10380. <https://doi.org/10.1002/anie.201103137>.
- (35) Cabrero-Antonino, J. R.; Alberico, E.; Drexler, H.-J.; Baumann, W.; Junge, K.; Junge, H.; Beller, M. Efficient Base-Free Hydrogenation of Amides to Alcohols and Amines Catalyzed by Well-Defined Pincer Imidazolyl-Ruthenium Complexes. *ACS Catal.* **2016**, *6*, 47–54. <https://doi.org/10.1021/acscatal.5b01955>.
- (36) Garg, J. A.; Chakraborty, S.; Ben-David, Y.; Milstein, D. Unprecedented Iron-Catalyzed Selective Hydrogenation of Activated Amides to Amines and Alcohols. *Chem. Commun.* **2016**, *52*, 5285–5288. <https://doi.org/10.1039/C6CC01505K>.
- (37) Spletstosser, J. T.; White, J. M.; Tunoori, A. R.; Georg, G. I. Mild and Selective Hydrozirconation of Amides to Aldehydes Using Cp₂Zr(H)Cl: Scope and Mechanistic Insight. *J. Am. Chem. Soc.* **2007**, *129*, 3408–3419. <https://doi.org/10.1021/ja066362+>.
- (38) Jones, G.; Stanforth, S. P. The Vilsmeier Reaction of Non-Aromatic Compounds. *Organic Reactions*. 2000, pp 355–686. <https://doi.org/10.1002/0471264180.or056.02>.
- (39) Chardon, A.; Morisset, E.; Rouden, J.; Blanchet, J. Recent Advances in Amide Reductions. *Synthesis (Stuttg.)*. **2018**, *65*, 984–997. <https://doi.org/10.1055/s-0036-1589144>.
- (40) Amines, A.; Khalimon, A. Y.; Gudun, K. A.; Hayrapetyan, D. Base Metal Catalysts for Deoxygenative Reduction of Amides to Amines. *Catalysts* **2019**, *9*, 490–515.
- (41) Kilner, M.; Tyers, D. V.; Crabtree, S. P.; Wood, M. A. WO 03/093208 A1, 2003.
- (42) Vom Stein, T.; Meuresch, M.; Limper, D.; Schmitz, M.; Hölscher, M.; Coetzee, J.; Cole-Hamilton, D. J.; Klankermayer, J.; Leitner, W. Highly Versatile Catalytic Hydrogenation of Carboxylic and Carbonic

- Acid Derivatives Using a Ru-Triphos Complex: Molecular Control over Selectivity and Substrate Scope. *J. Am. Chem. Soc.* **2014**, *136*, 13217–13225. <https://doi.org/10.1021/ja506023f>.
- (43) Kita, Y.; Higuchi, T.; Mashima, K. Hydrogenation of Amides Catalyzed by a Combined Catalytic System of a Ru Complex with a Zinc Salt. *Chem. Commun.* **2014**, *50*, 11211–11213. <https://doi.org/10.1039/C4CC04481A>.
- (44) John, J. M.; Loorthuraja, R.; Antoniuk, E.; Bergens, S. H. Catalytic Hydrogenation of Functionalized Amides Under Basic and Neutral Conditions. *Catal. Sci. Technol.* **2015**, *5*, 1181–1186. <https://doi.org/10.1039/C4CY01227E>.
- (45) Miura, T.; Held, I. E.; Oishi, S.; Naruto, M.; Saito, S. Catalytic Hydrogenation of Unactivated Amides Enabled by Hydrogenation of Catalyst Precursor. *Tetrahedron Lett.* **2013**, *54*, 2674–2678. <https://doi.org/10.1016/j.tetlet.2013.03.047>.
- (46) Takada, Y.; Iida, M.; Iida, K.; Miura, T.; Saito, S. Versatile Ruthenium Complex “RuPCY” for Directed Catalytic Hydrogen Management in Organic Synthesis. *J. Synth. Org. Chem.* **2016**, *74*, 1078–1089. <https://doi.org/10.5059/yukigoseikyokaishi.74.1078>.
- (47) Zhang, L.; Han, Z.; Zhao, X.; Wang, Z.; Ding, K. Highly Efficient Ruthenium-Catalyzed N-Formylation of Amines with H₂ and CO₂. *Angew. Chemie - Int. Ed.* **2015**, *54*, 6186–6189. <https://doi.org/10.1002/anie.201500939>.
- (48) Schneck, F.; Assmann, M.; Balmer, M.; Harms, K.; Langer, R. Selective Hydrogenation of Amides to Amines and Alcohols Catalyzed by Improved Iron Pincer Complexes. *Organometallics* **2016**, *35*, 1931–1943. <https://doi.org/10.1021/acs.organomet.6b00251>.
- (49) Rezayee, N. M.; Samblanet, D. C.; Sanford, M. S. Iron-Catalyzed Hydrogenation of Amides to Alcohols and Amines. *ACS Catal.* **2016**, *6*, 6377–6383. <https://doi.org/10.1021/acscatal.6b01454>.
- (50) Shi, L.; Tan, X.; Long, J.; Xiong, X.; Yang, S.; Xue, P.; Lv, H.; Zhang, X. Direct Catalytic Hydrogenation of Simple Amides: A Highly Efficient Approach from Amides to Amines and Alcohols. *Chem. - A Eur. J.* **2017**, *23*, 546–548. <https://doi.org/10.1002/chem.201604904>.
- (51) Artús Suàrez, L.; Culakova, Z.; Balcells, D.; Bernskoetter, W. H.; Eisenstein, O.; Goldberg, K. I.; Hazari, N.; Tilset, M.; Nova, A. The Key Role of the Hemiaminal Intermediate in the Iron-Catalyzed

BIBLIOGRAPHY

- Deaminative Hydrogenation of Amides. *ACS Catal.* **2018**, *8*, 8751–8762. <https://doi.org/10.1021/acscatal.8b02184>.
- (52) Lane, E. M.; Zhang, Y.; Hazari, N.; Bernskoetter, W. H. Sequential Hydrogenation of CO₂ to Methanol Using a Pincer Iron Catalyst. *Organometallics* **2019**, *38*, 3084–3091. <https://doi.org/10.1021/acs.organomet.9b00413>.
- (53) Artús Suàrez, L.; Jayarathne, U.; Balcells, D.; Bernskoetter, W. H.; Hazari, N.; Jaraiz, M.; Nova, A. Rational Selection of Co-Catalysts for the Deaminative Hydrogenation of Amides. *Chem. Sci.* **2020**, *11*, 2225–2230. <https://doi.org/10.1039/C9SC03812D>.
- (54) Leischner, T.; Artús Suàrez, L.; Spannenberg, A.; Junge, K.; Nova, A.; Beller, M. Highly Selective Hydrogenation of Amides Catalysed by a Molybdenum Pincer Complex: Scope and Mechanism. *Chem. Sci.* **2019**, *10*, 10566–10576. <https://doi.org/10.1039/c9sc03453f>.
- (55) Papa, V.; Cabrero-Antonino, J. R.; Alberico, E.; Spanneberg, A.; Junge, K.; Junge, H.; Beller, M. Efficient and Selective Hydrogenation of Amides to Alcohols and Amines Using a Well-Defined Manganese-PNN Pincer Complex. *Chem. Sci.* **2017**, *8*, 3576–3585. <https://doi.org/10.1039/c7sc00138j>.
- (56) Alberico, E.; Sponholz, P.; Cordes, C.; Nielsen, M.; Drexler, H. J.; Baumann, W.; Junge, H.; Beller, M. Selective Hydrogen Production from Methanol with a Defined Iron Pincer Catalyst under Mild Conditions. *Angew. Chemie - Int. Ed.* **2013**, *52*, 14162–14166. <https://doi.org/10.1002/anie.201307224>.
- (57) Bornschein, C.; Werkmeister, S.; Wendt, B.; Jiao, H.; Alberico, E.; Baumann, W.; Junge, H.; Junge, K.; Beller, M. Mild and Selective Hydrogenation of Aromatic and Aliphatic (Di)Nitriles with a Well-Defined Iron Pincer Complex. *Nat. Commun.* **2014**, *5*, 4111–4121. <https://doi.org/10.1038/ncomms5111>.
- (58) Chakraborty, S.; Dai, H.; Bhattacharya, P.; Fairweather, N. T.; Gibson, M. S.; Krause, J. A.; Guan, H. Iron-Based Catalysts for the Hydrogenation of Esters to Alcohols. *J. Am. Chem. Soc.* **2014**, *136*, 7869–7872. <https://doi.org/10.1021/ja504034q>.
- (59) Werkmeister, S.; Junge, K.; Wendt, B.; Alberico, E.; Jiao, H.; Baumann, W.; Junge, H.; Gallou, F.; Beller, M. Hydrogenation of Esters to Alcohols with a Well-Defined Iron Complex. *Angew. Chemie - Int. Ed.* **2014**, No. 33, 8722–8726. <https://doi.org/10.1002/anie.201402542>.

BIBLIOGRAPHY

- (60) Zhang, Y.; MacIntosh, A. D.; Wong, J. L.; Bielinski, E. A.; Williard, P. G.; Mercado, B. Q.; Hazari, N.; Bernskoetter, W. H. Iron Catalyzed CO₂ Hydrogenation to Formate Enhanced by Lewis Acid Co-Catalysts. *Chem. Sci.* **2015**, *6*, 4291–4299. <https://doi.org/10.1039/C5SC01467K>.
- (61) Xu, R.; Chakraborty, S.; Bellows, S. M.; Yuan, H.; Cundari, T. R.; Jones, W. D. Iron-Catalyzed Homogeneous Hydrogenation of Alkenes under Mild Conditions by a Stepwise, Bifunctional Mechanism. *ACS Catal.* **2016**, *6*, 2127–2135. <https://doi.org/10.1021/acscatal.5b02674>.
- (62) Chakraborty, S.; Brennessel, W. W.; Jones, W. D. A Molecular Iron Catalyst for the Acceptorless Dehydrogenation and Hydrogenation of N-Heterocycles. *J. Am. Chem. Soc.* **2014**, *136*, 8564–8567. <https://doi.org/10.1021/ja504523b>.
- (63) Bielinski, E. A.; Förster, M.; Zhang, Y.; Bernskoetter, W. H.; Hazari, N.; Holthausen, M. C. Base-Free Methanol Dehydrogenation Using a Pincer-Supported Iron Compound and Lewis Acid Co-Catalyst. *ACS Catal.* **2015**, *5*, 2404–2415. <https://doi.org/10.1021/acscatal.5b00137>.
- (64) Lane, E. M.; Uttley, K. B.; Hazari, N.; Bernskoetter, W. Iron-Catalyzed Amide Formation from the Dehydrogenative Coupling of Alcohols and Secondary Amines. *Organometallics* **2017**, *36*, 2020–2025. <https://doi.org/10.1021/acs.organomet.7b00258>.
- (65) Leischner, T.; Spannenberg, A.; Junge, K.; Beller, M. Molecular Defined Molybdenum-Pincer Complexes and Their Application in Catalytic Hydrogenations. *Organometallics* **2018**, *37*, 4402–4408. <https://doi.org/10.1021/acs.organomet.8b00410>.
- (66) Hohenberg, P.; Kohn, W. Inhomogeneous Electron Gas. *Phys. Rev.* **1964**, *136*, B864–B871. <https://doi.org/10.1103/PhysRev.136.B864>.
- (67) Levy, M. Elementary Concepts in Density Functional Theory. In *Theoretical and Computational Chemistry*; Elsevier, 1996; Vol. 4, pp 3–24. [https://doi.org/10.1016/S1380-7323\(96\)80083-5](https://doi.org/10.1016/S1380-7323(96)80083-5).
- (68) Kohn, W.; Sham, L. J. Self-Consistent Equations Including Exchange and Correlation Effects. *Phys. Rev.* **1965**, *140*, A1133–A1138. <https://doi.org/http://dx.doi.org/10.1103/PhysRev.140.A1133>.
- (69) Zhao, Y.; Truhlar, D. G. The M06 Suite of Density Functionals for Main Group Thermochemistry, Thermochemical Kinetics, Noncovalent Interactions, Excited States, and Transition Elements: Two New Functionals and Systematic Testing of Four M06-Class Functionals and 12 Other Function. *Theor. Chem. Acc.* **2008**, *120*,

BIBLIOGRAPHY

- 215–241. <https://doi.org/10.1007/s00214-007-0310-x>.
- (70) Ramabhadran, R. O.; Raghavachari, K. Extrapolation to the Gold-Standard in Quantum Chemistry: Computationally Efficient and Accurate CCSD(T) Energies for Large Molecules Using an Automated Thermochemical Hierarchy. *J. Chem. Theory Comput.* **2013**, *9*, 3986–3994. <https://doi.org/10.1021/ct400465q>.
- (71) Balabanov, N. B.; Peterson, K. A. Systematically Convergent Basis Sets for Transition Metals. I. All-Electron Correlation Consistent Basis Sets for the 3d Elements Sc-Zn. *J. Chem. Phys.* **2005**, *123*, 064107–064123. <https://doi.org/10.1063/1.1998907>.
- (72) Marenich, A. V.; Cramer, C. J.; Truhlar, D. G. Universal Solvation Model Based on Solute Electron Density and on a Continuum Model of the Solvent Defined by the Bulk Dielectric Constant and Atomic Surface Tensions. *J. Phys. Chem. B* **2009**, *113*, 6378–6396. <https://doi.org/10.1021/jp810292n>.
- (73) Lewars, E. G. *Computational Chemistry. Introduction to the Theory and Applications of Molecular and Quantum Mechanics.*, 3rd ed.; Springer International Publishing: Peterborough, ON, Canada, 2016; Vol. 43. <https://doi.org/10.1007/978-3-319-30916-3>.
- (74) Cramer, C. J. *Essentials of Computational Chemistry*, 2nd ed.; John Wiley & Sons, Ltd: West Sussex, England, 2004; Vol. 69.
- (75) Miertuš, S.; Scrocco, E.; Tomasi, J. Electrostatic Interaction of a Solute with a Continuum. A Direct Utilizaion of AB Initio Molecular Potentials for the Prevision of Solvent Effects. *Chem. Phys.* **1981**, *55*, 117–129. [https://doi.org/10.1016/0301-0104\(81\)85090-2](https://doi.org/10.1016/0301-0104(81)85090-2).
- (76) Tomasi, J.; Mennucci, B.; Cancès, E. The IEF Version of the PCM Solvation Method : An Overview of a New Method Addressed to Study Molecular Solutes at the QM Ab Initio Level. *J. Mol. Struct.* **1999**, *464*, 211–226.
- (77) Marenich, A. V.; Cramer, C. J.; Truhlar, D. G. Generalized Born Solvation Model SM12. *J. Chem. Theory Comput.* **2013**, *9*, 609–620. <https://doi.org/10.1021/ct300900e>.
- (78) Klamt, A.; Schüürmann, G. COSMO: A New Approach to Dielectric Screening in Solvents with Explicit Expressions for the Screening Energy and Its Gradient. *J. Chem. Soc. Perkin Trans. 2* **1993**, No. 5, 799–805. <https://doi.org/10.1039/P29930000799>.
- (79) Mikkelsen, K. V.; Ågren, H.; Jensen, H. J. A.; Helgaker, T. A

BIBLIOGRAPHY

- Multiconfigurational Self-Consistent Reaction-Field Method. *J. Chem. Phys.* **1988**, *89*, 3086–3095. <https://doi.org/10.1063/1.454965>.
- (80) Cortis, C. M.; Langlois, J. M.; Beachy, M. D.; Friesner, R. A. Quantum Mechanical Geometry Optimization in Solution Using a Finite Element Continuum Electrostatics Method. *J. Chem. Phys.* **1996**, *105*, 5472–5484. <https://doi.org/10.1063/1.472388>.
- (81) Atkins, P.; de Paula, J.; Keller, J. *Atkins' Physical Chemistry*, 11th Editi.; Oxford University Press: Oxford, 2018.
- (82) Jensen, F. *Introduction to Computational Chemistry*, 3rd Editio.; John Wiley & Sons Inc: New York, United States, 2017.
- (83) Hoops, S.; Gauges, R.; Lee, C.; Pahle, J.; Simus, N.; Singhal, M.; Xu, L.; Mendes, P.; Kummer, U. COPASI - A Complex Pathway SImulator. *Bioinformatics* **2006**, *22*, 3067–3074. <https://doi.org/10.1093/bioinformatics/btl485>.
- (84) Hindmarsh, A. C. ODEPACK, a Systematized Collection of Ode Solvers. 1982, pp 427–429.
- (85) Hindmarsh, A. C. LSODE and LSODI, Two New Initial Value Ordinary Differential Equation Solvers. *ACM SIGNUM Newsl.* **1980**, *15*, 10–11. <https://doi.org/10.1017/CBO9781107415324.004>.
- (86) Hindmarsh, A. C. *ODE Solvers for Use with the Method of Lines*; Vichnevetsky, R., Stepleman, R. S., Eds.; IMACS: New Brunswick, 1981.
- (87) Petzold, L. Automatic Selection of Methods for Solving Stiff and Nonstiff Systems of Ordinary Differential Equations. *SIAM J Sci Stat Comput* **1983**, *4*, 136–148. <https://doi.org/10.1137/0904010>.
- (88) Qu, S.; Dai, H.; Dang, Y.; Song, C.; Wang, Z.-X. X.; Guan, H. Computational Mechanistic Study of Fe-Catalyzed Hydrogenation of Esters to Alcohols: Improving Catalysis by Accelerating Precatalyst Activation with a Lewis Base. *ACS Catal.* **2014**, *4*, 4377–4388. <https://doi.org/10.1021/cs501089h>.
- (89) Chakraborty, S.; Lagaditis, P. O.; Förster, M.; Bielinski, E. A.; Hazari, N.; Holthausen, M. C.; Jones, W. D.; Schneider, S. Well-Defined Iron Catalysts for the Acceptorless Reversible Dehydrogenation-Hydrogenation of Alcohols and Ketones. *ACS Catal.* **2014**, *4*, 3994–4003. <https://doi.org/10.1021/cs5009656>.
- (90) Chen, X.; Jing, Y.; Yang, X. Unexpected Direct Hydride Transfer Mechanism for the Hydrogenation of Ethyl Acetate to Ethanol

BIBLIOGRAPHY

- Catalyzed by SNS Pincer Ruthenium Complexes. *Chem. - A Eur. J.* **2016**, 22, 1950–1957. <https://doi.org/10.1002/chem.201504058>.
- (91) Nguyen, D. H.; Trivelli, X.; Capet, F.; Paul, J. F.; Dumeignil, F.; Gauvin, R. M. Manganese Pincer Complexes for the Base-Free, Acceptorless Dehydrogenative Coupling of Alcohols to Esters: Development, Scope, and Understanding. *ACS Catal.* **2017**, 7, 2022–2032. <https://doi.org/10.1021/acscatal.6b03554>.
- (92) Cabrero-Antonino, J. R.; Adam, R.; Papa, V.; Beller, M. Homogeneous and Heterogeneous Catalytic Reduction of Amides and Related Compounds Using Molecular Hydrogen. *Nat. Commun.* **2020**, 11, 1–18. <https://doi.org/10.1038/s41467-020-17588-5>.
- (93) Dub, P. A.; Gordon, J. C. The Role of the Metal-Bound N–H Functionality in Noyori-Type Molecular Catalysts. *Nat. Rev. Chem.* **2018**, 2, 396–408. <https://doi.org/10.1038/s41570-018-0049-z>.
- (94) Brunner, E. Solubility of Hydrogen in 10 Organic Solvents at 298.15, 323.15, and 373.15 K. *J. Chem. Eng. Data* **1985**, 30, 269–273. <https://doi.org/10.1021/je00041a010>.
- (95) Plata, R. E.; Singleton, D. A. A Case Study of the Mechanism of Alcohol-Mediated Morita Baylis-Hillman Reactions. the Importance of Experimental Observations. *J. Am. Chem. Soc.* **2015**, 137, 3811–3826. <https://doi.org/10.1021/ja5111392>.
- (96) Besora, M.; Vidossich, P.; Lledós, A.; Ujaque, G.; Maseras, F. Calculation of Reaction Free Energies in Solution: A Comparison of Current Approaches. *J. Phys. Chem. A* **2018**, 122, 1392–1399. <https://doi.org/10.1021/acs.jpca.7b11580>.
- (97) Becke, A. D. Density-Functional Thermochemistry. III. The Role of Exact Exchange. *J. Chem. Phys.* **1993**, 98, 5648–5652. <https://doi.org/10.1063/1.464913>.
- (98) Adamo, C.; Barone, V. Toward Reliable Density Functional Methods without Adjustable Parameters: The PBE0 Model. *J. Chem. Phys.* **1999**, 110, 6158–6170. <https://doi.org/10.1063/1.478522>.
- (99) Tao, J.; Perdew, J. P.; Staroverov, V. N.; Scuseria, G. E. Climbing the Density Functional Ladder: Nonempirical Meta-Generalized Gradient Approximation Designed for Molecules and Solids. *Phys. Rev. Lett.* **2003**, 91, 3–6. <https://doi.org/10.1103/PhysRevLett.91.146401>.
- (100) Chai, J.-D.; Head-Gordon, M. Long-Range Corrected Hybrid Density Functionals with Damped Atom–Atom Dispersion Corrections. *Phys.*

BIBLIOGRAPHY

- Chem. Chem. Phys.* **2008**, *10*, 6615–6620.
<https://doi.org/10.1039/b810189b>.
- (101) Becke, A. D. Density-Functional Exchange-Energy Approximation With Correct Asymptotic Behavior. *Phys. Rev. A* **1988**, *38*, 3098–3100. <https://doi.org/10.1103/PhysRevA.38.3098>.
- (102) Lee, C.; Yang, W.; Parr, R. G. Development of the Colle-Salvetti Correlation-Energy Formula into a Functional of the Electron Density. *Phys. Rev. B* **1988**, *37*, 785–789.
<https://doi.org/10.1103/PhysRevB.37.785>.
- (103) Miehlich, B.; Savin, A.; Stoll, H.; Preuss, H. Results Obtained with the Correlation Energy Density Functionals of Becke and Lee, Yang and Parr. *Chem. Phys. Lett.* **1989**, *157*, 200–206.
[https://doi.org/10.1016/0009-2614\(89\)87234-3](https://doi.org/10.1016/0009-2614(89)87234-3).
- (104) Perdew, J. P.; Burke, K.; Ernzerhof, M. Generalized Gradient Approximation Made Simple- ERRATA. *Phys. Rev. Lett.* **1996**, *77*, 3865–3868. <https://doi.org/10.1103/PhysRevLett.77.3865>.
- (105) Zhao, Y.; Truhlar, D. G. A New Local Density Functional for Main-Group Thermochemistry, Transition Metal Bonding, Thermochemical Kinetics, and Noncovalent Interactions. *J. Chem. Phys.* **2006**, *125*, 1–17. <https://doi.org/10.1063/1.2370993>.
- (106) Grimme, S.; Antony, J.; Ehrlich, S.; Krieg, H. A Consistent and Accurate Ab Initio Parametrization of Density Functional Dispersion Correction (DFT-D) for the 94 Elements H-Pu. *J. Chem. Phys.* **2010**, *132*, 1–18. <https://doi.org/10.1063/1.3382344>.
- (107) Hay, P. J.; Wadt, W. R. Ab Initio Effective Core Potentials for Molecular Calculations. Potentials for the Transition Metal Atoms Sc to Hg. *J. Chem. Phys.* **1985**, *82*, 270–283.
<https://doi.org/10.1063/1.448799>.
- (108) Hehre, W. J.; Ditchfield, R.; Pople, J. A. Self—Consistent Molecular Orbital Methods. XII. Further Extensions of Gaussian—Type Basis Sets for Use in Molecular Orbital Studies of Organic Molecules. *J. Chem. Phys.* **1972**, *56*, 2257–2261. <https://doi.org/10.1063/1.1677527>.
- (109) Krishnan, R.; Binkley, J. S.; Seeger, R.; Pople, J. A. Self-Consistent Molecular Orbital Methods. XX. A Basis Set For Correlated Wave Functions. *J. Chem. Phys.* **1980**, *72*, 650–654.
<https://doi.org/10.1063/1.438955>.
- (110) McLean, A. D.; Chandler, G. S. Contracted Gaussian Basis Sets for

BIBLIOGRAPHY

- Molecular Calculations. I. Second Row Atoms, Z=11-18. *J. Chem. Phys.* **1980**, 72, 5639–5648. <https://doi.org/10.1063/1.438980>.
- (111) Gaussian 09, Revision D.01, M. J. Frisch, G. W. Trucks, H. B. Schlegel, G. E. Scuseria, M. A. Robb, J. R. Cheeseman, G. Scalmani, V. Barone, B. Mennucci, G. A. Petersson, H. Nakatsuji, M. Caricato, X. Li, H. P. Hratchian, A. F. Izmaylov, J. Bloino, G. Zheng, J. L. Sonnenberg, M. Hada, M. Ehara, K. Toyota, R. Fukuda, J. Hasegawa, M. Ishida, T. Nakajima, Y. Honda, O. Kitao, H. Nakai, T. Vreven, J. A. Montgomery, Jr., J. E. Peralta, F. Ogliaro, M. Bearpark, J. J. Heyd, E. Brothers, K. N. Kudin, V. N. Staroverov, T. Keith, R. Kobayashi, J. Normand, K. Ragahavachari, A. Rendell, J. C. Burant, S. S. Iyengar, J. Tomasi, M. Cossi, N. Rega, J. M. Millam, M. Klene, J. E. Knox, J. B. Cross, V. Bakken, C. Adamo, J. Jaramillo, R. Gomperts, R. E. Stratmann, O. Yazyev, A. J. Austin, R. Cammi, C. Pomelli, J. W. Ochterski, R. L. Martin, K. Morokuma, V. G. Zakrzewski, G. A. Voth, P. Salvador, J. J. Dannenberg, S. Dapprich, A. D. Daniels, O. Farkas, J. B. Foresman, J. V. Ortiz, J. Cioslowski, and D. J. Fox, Gaussian, Inc., Wallingford CT, 2013.

Paper I

Artús Suàrez, L.; Culakova, Z.; Balcells, D; Bernskoetter, W. H.; Eisenstein, O.; Goldberg, K. I.; Hazari, N.; Tilset, M.; Nova, A. ACS Catal., **2018**, 8, 8751-8762

The Key Role of the Hemiaminal Intermediate in the Iron-Catalyzed Deaminative Hydrogenation of Amides

Lluís Artús Suàrez,[†] Zuzana Culakova,[#] David Balcells,[†] Wesley H. Bernskoetter,^{*,‡} Odile Eisenstein,^{†,¶} Karen I. Goldberg,^{#,||} Nilay Hazari,[§] Mats Tilset,[†] and Ainara Nova^{*,†}

[†]Hylleraas Centre for Quantum Molecular Sciences, Department of Chemistry, University of Oslo, P.O. Box 1033, Blindern, N-0315, Oslo, Norway

[‡]Department of Chemistry, University of Missouri, Columbia, Missouri 65211, United States

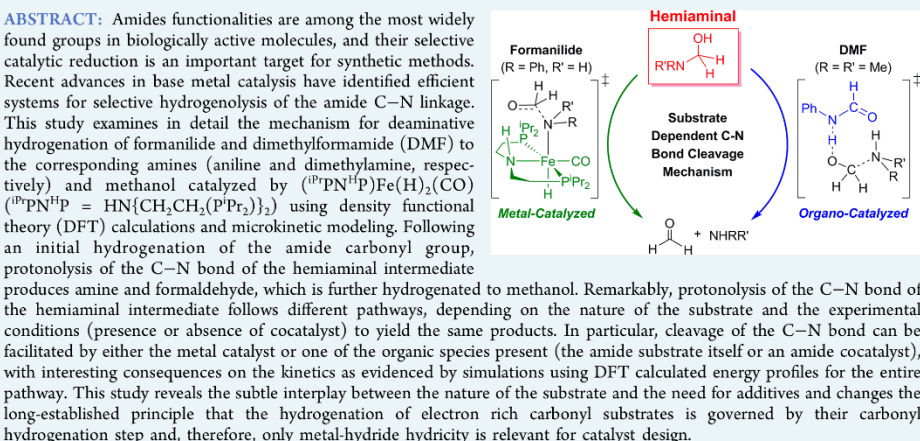
[§]Department of Chemistry, Yale University, P.O. Box 208107, New Haven, Connecticut 06520, United States

[#]Department of Chemistry, University of Washington, Seattle, Washington 98195, United States

^{||}Department of Chemistry, University of Pennsylvania, Philadelphia, Pennsylvania 19104, United States

[¶]Institut Charles Gerhardt, UMR 5253 CNRS-UM-ENSCM, cc 1501 Université de Montpellier, Montpellier 34095, France

Supporting Information



KEYWORDS: reaction mechanism, Fe, bifunctional catalysts, DFT, hemiaminal, amide, methanol, catalyst poisoning

INTRODUCTION

There are few organic functional groups which play as ubiquitous a role in chemical biology as amides.¹ The relative stability of amides compared to other carboxylic acid derivatives has made them ideal for use in peptide chains, and their unusual reactivity has proven critical in the development of pharmaceuticals and agrochemicals.^{2–4} Efficient and selective catalytic methods to reduce amides would provide a vast improvement over traditional synthetic techniques which utilize potent, stoichiometric metal-hydride reagents.⁵ Advances in transition metal catalyzed processes have led to the discovery of several systems, primarily based on precious metals, which can selectively reduce amides via C–O

bond hydrogenolysis (deoxygenative reduction) or C–N bond hydrogenolysis (deaminative reduction) (Scheme 1).^{6–14}

More recent catalyst development has provided the first examples of base-metal systems for the selective deaminative hydrohydrogenation of amides,¹⁵ including a collection of closely related catalysts based on the $[(^{1\text{P}}\text{PN}^{1\text{P}})\text{Fe}]$ ($^{1\text{P}}\text{PN}^{1\text{P}} = \text{HN}\{\text{CH}_2\text{CH}_2(\text{PPr}_2)\}_2$) fragment^{16–18} (Scheme 2). These “Noyori-type” bifunctional catalysts have proven to be effective for producing alcohols and amines from amides and are proposed to operate via a hemiaminal intermediate (Scheme

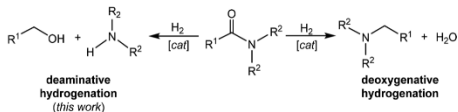
Received: June 5, 2018

Revised: August 3, 2018

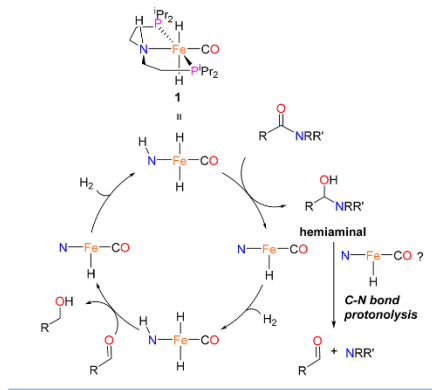
Published: August 7, 2018

DOI: 10.1021/acscatal.8b02184
ACS Catal. 2018, 8, 8751–8762

Scheme 1. Deaminative Hydrogenation vs Deoxygenative Hydrogenation of Amides



Scheme 2. Reaction Mechanism Investigated in This Work with a Schematic Representation of the Catalyst



2). The catalysts are particularly active for the reduction of formamides with turnover numbers (TONs) reaching >4000 within 3 h. Notably, some substrates gave increased TONs in the presence of secondary formamide additives (e.g., N-methylformanilide improved from a TON of 60 to 1300 in the presence of formanilide), but the exact reasons for the improvement were unclear.¹⁸

In this work, we present a computational study on the mechanism for amide hydrogenation using this “Noyori-type” bifunctional catalyst and elucidate several possible catalytic pathways that are consistent with the experimental results and describe the roles of the reaction additives. The mechanistic insight that is gained through the combination of density functional theory (DFT) calculations and microkinetic modeling will be relevant not only for the further optimization of the hydrogenation of amides but also for the rational design and development of cocatalysts in related hydrogenation processes.

COMPUTATIONAL DETAILS

DFT calculations were carried out with the Gaussian 09 software package.¹⁹ All chemical species were modeled in full without any simplification. The hybrid *meta*-GGA M06²⁰ functional was selected on the basis of geometry (Scheme S1 and Figure S1) and energy (Scheme S2 and Figure S2) benchmarks, using X-ray crystal structures²¹ and CCSD(T)²² (with basis set cc-PVTZ)^{23–25} energies as references. Structures were fully optimized without any geometry or symmetry constraints, combining the double- ζ LANL2DZ (on Fe, including relativistic effects)²⁶ and 6-31+G** (on all other elements)^{27,28} basis sets. Vibrational frequencies were computed at the same level of theory to classify all stationary points as either saddle points (transition states, with a single imaginary frequency) or energy minima (reactants, intermediates, and products, with only real frequencies). These calculations were also used to obtain the thermochemistry corrections (zero-point, thermal, and entropy energies) at the experimental $p = 30$ atm and $T = 373$ K, on the basis of the IGRRHO (ideal gas/rigid rotor/harmonic oscillator) approach. According to the ideal gas law, this pressure and temperature correspond to the 1 M concentration of the standard state used for species reacting in solution. No further corrections were thus introduced to account for the standard state. The experimental initial concentrations of the reactants were used in the microkinetic models to simulate conversion over time (vide infra). The energy of the optimized geometries was refined by single point calculations with triple- ζ quality basis sets, including the LANL2TZ²⁶ on Fe and the 6-311+G** on all other elements.^{29,30} The energies reported in the text were obtained by adding the thermochemistry corrections to the refined potential energies. The reference for all energies in the metal catalyzed cases are that of (³⁵PNH³⁵P)Fe(H₂)(CO) completed by the substrates needed for mass balance. A table with the enthalpy and entropy contributions to the Gibbs energy of all stationary points is given in Table S1. The solvation effects of THF were included in both the geometry optimizations and energy refinements using the continuum SMD model.³¹ The ultrafine (99 590) grid was used in all calculations to increase numerical accuracy and to facilitate convergence. A data set collection of input files and computational results is available in the ioChem-BD repository³² and can be accessed online via <http://dx.doi.org/10.19061/iochem-bd-6-10>. The complex reaction mechanisms inferred from the calculations were interpreted by means of quantitative microkinetic models (Figures S3 and S4), simulated with the COPASI software.³³ Time-course simulations were carried out with the LSODA algorithm.³⁴

	Step 1: Amide C=O Hydrogenation	Step 2: C–N bond protonolysis	Step 3: Formaldehyde C=O Hydrogenation
Formanilide	0.0	4.7	5.2
DMF	0.0	10.5	13.8

Gibbs energies in THF (SMD) at 30 atm and 373 K are given in kcal mol⁻¹.

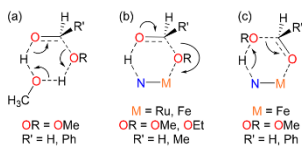
Figure 1. Reaction steps for the hydrogenation of formanilide ($R' = H$, $R'' = Ph$) and DMF ($R' = R'' = CH_3$) to amines and methanol. Gibbs energies in THF (SMD) at 30 atm and 373 K are given in kcal mol⁻¹.

■ RESULTS AND DISCUSSION

Elementary Steps in Amide Hydrogenation. The mechanism commonly proposed in the literature for amide hydrogenation involves the organic intermediates shown in Figure 1.¹⁷ This proposal is consistent with the ability of bifunctional catalysts to hydrogenate carbonyl groups, such as those in esters, ketones, and aldehydes.^{35,36} The first transformation (step 1), the hydrogenation of the amide carbonyl group to yield a hemiaminal intermediate, is followed by protonolysis of the C–N bond (step 2). The latter step yields amine and formaldehyde, which is reduced to methanol by further hydrogenation (step 3). Although the Fe catalyst is known to be involved in steps 1 and 3, which require the activation of H₂, its role in step 2 remains unclear.

In contrast with the hydrogenation of amides, which has not been studied extensively,³⁷ the related hydrogenation of esters has been thoroughly investigated for “Noyori-type” bifunctional catalysts. The proposed organic intermediates in ester hydrogenation are closely related to those shown in Figure 1, with the initial reduction of the ester resulting in the formation of a hemiacetal, which is similar to the hemiaminal intermediate in amide hydrogenation. Three different mechanisms have been explored for the formation of methanol and aldehyde from the hemiacetal intermediate (**Scheme 3**): (a)

Scheme 3. Transition States Proposed for the Conversion of a Hemiacetal into an Aldehyde and an Alcohol by (a) Methanol, (b) RO-Bound Metal (Fe and Ru), and (c) CO-Bound Metal (Fe)



methanol-catalyzed, (b) metal-catalyzed, with the metal bound to the oxygen of the OR group (M = Fe or Ru) and (c) metal-catalyzed, with the metal bound to the oxygen of the CO group (M = Fe).^{35,36,38} Calculations predict that in general the metal-catalyzed (b) and (c) mechanisms are the lowest in energy, with the optimal pathway depending on the nature of the system. In this work, these three mechanisms have been investigated for the C–N bond protonolysis of hemiaminal intermediates in amide hydrogenation (vide infra). In order to rationalize the dependence of the reaction outcome on the nature of the N-substituents, we have compared the computational results obtained with formanilide and dimethylformamide (DMF) as substrates. While experiments with formanilide yielded 99% conversion to methanol and aniline at 100 °C and 30 atm of H₂ using a precursor to **1** as the precatalyst, DMF was only reactive upon addition of formanilide as cocatalyst.¹⁸

To develop a clearer understanding of the effect of the N-substituents on the thermodynamics of the reaction, the Gibbs energies of the organic intermediates (Figure 1) were computed for both formanilide and DMF under the experimental conditions (*T* = 373.0 K, *p* = 30.0 atm).³⁹ With formanilide, the formation of hemiaminal is endoergic by ca. 5 kcal mol⁻¹ and its decomposition to amine and

formaldehyde is thermoneutral. In contrast, the last step, the hydrogenation of formaldehyde, is strongly exergonic ($\Delta G = -15.3$ kcal mol⁻¹), driving the reaction to the formation of the final products with an overall $\Delta G = -10.1$ kcal mol⁻¹. With DMF, both the formation of the hemiaminal and formaldehyde become more endoergic and the overall reaction is almost thermoneutral: $\Delta G = -1.5$ kcal mol⁻¹. These energies suggest that, while some reversibility would be expected with DMF, the hydrogenation of formanilide is likely irreversible.

In order to fully understand the mechanism and evaluate the kinetics of the hydrogenation of formanilide and DMF, the reaction pathways associated with the hydrogenation of the amide carbonyl group and the protonolysis of the C–N bond were studied computationally. The hydrogenation of formaldehyde was not considered in this study because it has already been investigated.³⁶ Further, the low barrier calculated for this process (ca. 6 kcal mol⁻¹) indicates that it is not the turnover limiting step.

H₂ Activation Across the Fe–N Bond. The formation of the *trans*-dihydride Fe complex (¹⁷PNP)²Fe(H)₂(CO) (**1**) from (¹⁷PNP)Fe(H)(CO) (**2**) and H₂ occurs at the outset of the reaction.¹⁸ This reaction also takes place twice in the proposed catalytic cycle, since it is required for catalyst regeneration, both after the reduction of the amide carbonyl group and after the reduction of formaldehyde (Scheme 1). In addition to the *trans* isomer, the *cis*-dihydride is also experimentally observed.⁴⁰ In line with this, calculations show that the *cis* isomer is only 2.4 kcal mol⁻¹ higher in energy than the *trans* isomer. However, the energy barrier for the hydrogenation of the amide carbonyl group (vide infra) is significantly higher with the *cis* isomer (Figure S6), and therefore, reaction of this isomer was not investigated any further.

In the absence of a proton relay such as the product (methanol³⁵) or the substrate (formanilide), the addition of H₂ (*p* = 30 atm) to **2** is concerted and has an energy barrier of 11.6 kcal mol⁻¹ (see Figure 2). In the presence of formanilide, the reaction becomes stepwise and the highest energy barrier drops to 4.0 kcal mol⁻¹. In this process, formanilide protonates the catalyst and deprotonates the dihydrogen complex in two consecutive steps (TS2–3 and TS4–1, respectively). The exergonic and low-barrier energy profile of **2** + H₂ → **1** ($\Delta G = -10.2$ and $\Delta G^\ddagger = 4.0$ kcal mol⁻¹) enables the recovery of the catalyst as **1** after both amide and formaldehyde carbonyl hydrogenation. In addition, the deprotonation of formanilide may also lead to its O- or N-coordination to Fe (isomers **5** and **6**, respectively). The formation of these off-cycle species is exergonic by -12.2 (**5**) and -10.7 (**6**) kcal mol⁻¹, which is consistent with the experimental observation that **1** reacts rapidly with formanilide at 23 °C to form **6**.¹⁸ In addition to the NMR characterization of **5** and **6**, the latter was also structurally characterized by single crystal X-ray diffraction analysis. The low energy barriers connecting **1**, **5**, and **6**, of ca. 13 kcal mol⁻¹, and the similar energies of these three species suggest that they are in equilibrium. The energy of **1** relative to **2** (-10.2 kcal mol⁻¹) shows that the hydrogenated form of the catalyst is the most stable under the reaction conditions.

Formanilide Hydrogenation to Hemiaminal. The energy profile for the hydrogenation of the carbonyl group of formanilide by **1** is shown in Figure 3. The hydrogenation of the carbonyl group of the amide is a stepwise process, in which the hydride transfer from Fe to the carbonyl C is followed by the proton transfer from the ligand NH to the carbonyl O. The

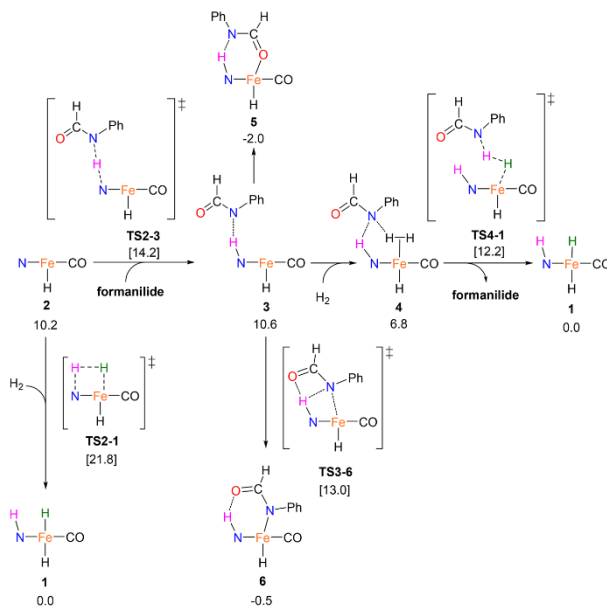


Figure 2. Reaction pathways for the hydrogenation of **2** to yield **1**. Gibbs energies in THF (SMD) at 30 atm and 373 K are given in kcal mol⁻¹. Cocatalysis by formanilide and formation of the off-cycle species (**5** and **6**) are also included. The reactive hydrogen atoms are highlighted in either purple (acidic) or green (hydridic).

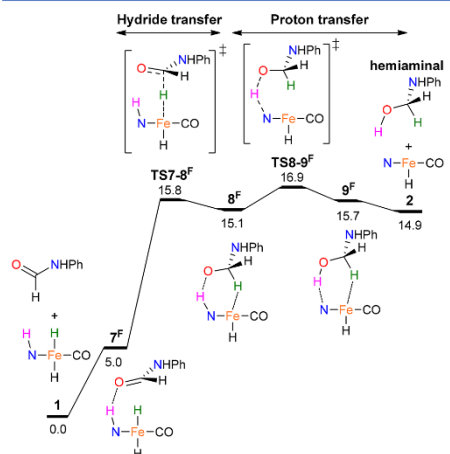


Figure 3. Reaction pathway for the hydrogenation of formanilide (labeled by a F superscript) to hemiaminal by **1**. Gibbs energies in THF (SMD) at 30 atm and 373 K are given in kcal mol⁻¹. The reactive hydrogen atoms are highlighted in either purple (acidic) or green (hydridic).

overall process is endergonic by 14.9 kcal mol⁻¹ and similar energies are obtained for both the hydride and proton transfer transition states (TS7-8^F and TS8-9^F, at 15.8 and 16.9 kcal mol⁻¹, respectively) and associated intermediates (8^F and 9^F, at 15.1 and 15.7 kcal mol⁻¹, respectively). In intermediate 9^F, the hemiaminal is interacting with the metal complex through a C–H···Fe agostic interaction, as shown by the short Fe···H contact (2.34 Å) and the elongated C–H bond distance (1.12 Å vs 1.10 Å in the free hemiaminal), and by an H-bond with the ^{iP}PNP ligand (N–H bond = 1.74 Å). These interactions account for the small thermodynamic preference for hemiaminal dissociation ($\Delta G = -0.8$ kcal mol⁻¹), despite the favorable entropy change associated with this reaction (see Supporting Information).

The stepwise mechanism proposed for the hydrogenation of formanilide to hemiaminal shown in Figure 3 is similar to the mechanism proposed for the hydrogenation of carbonyl groups in other substrates, including CO₂, aldehydes, ketones, and esters, catalyzed by similar Fe and Ru bifunctional catalysts.^{35,36,41,42}

Formanilide Protonolysis of the C–N Bond of the Hemiaminal. The formation of formaldehyde and aniline from the hemiaminal intermediate requires a proton transfer from the OH group to the N atom, as well as the cleavage of the C–N bond. In the isolated hemiaminal, the concerted O-to-N proton transfer has a prohibitively high energy barrier of 45.3 kcal mol⁻¹ (see Figure S7). Proton relays are needed as already proposed in the literature,^{17,35} and both the reactant

(formanilide) and the catalyst are candidates to assist the proton transfer, as described below.

The energy profile for the formanilide-catalyzed mechanism is shown in Figure 4. The proton transfer is a stepwise process

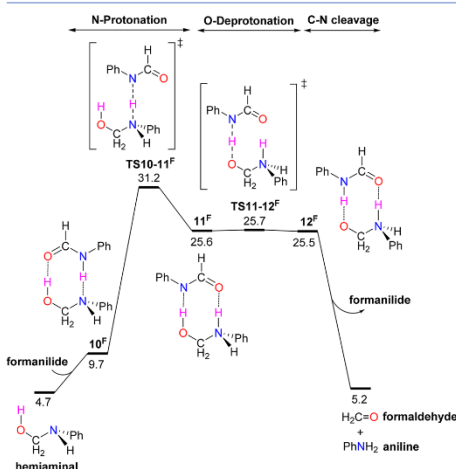


Figure 4. Reaction pathway for the protonolysis of the C–N bond of the hemiaminal catalyzed by formanilide (labeled by a F superscript). Gibbs energies in THF (SMD) at 30 atm and 373 K are given in kcal mol⁻¹.

starting with the protonation of the hemiaminal N by the NH group of formanilide, which involves the highest energy barrier (31.2 kcal mol⁻¹; $TS10-11^F$). In this reaction, the formanilide fragment rotates, exchanging whether the O or N of the formanilide is H-bound to the OH of the hemiaminal. In the following step, the resulting anionic N center abstracts the proton from the OH group ($TS11-12^F$). The zwitterionic intermediate (12^F , at 25.5 kcal mol⁻¹ above reactants) is stabilized by a double H-bond to formanilide. Upon dissociation of the latter, the C–N bond undergoes barrierless cleavage yielding formaldehyde and aniline in a strongly exergonic process (-20.3 kcal mol⁻¹).

The dehydrogenated form of the Fe catalyst (**2** in Figure 2) can participate in the C–N bond protonolysis of the hemiaminal by deprotonating the OH group. This reaction yields three different isomeric products; namely, 8^F , 14^F , and 15^F , in which the metal center is bound to a H, O, or N atom of the organic substrate, respectively (Figure 5). From 8^F , C–N bond protonolysis is achieved after the addition of H₂, yielding 13^F . The activation of H₂ within this intermediate triggers the proton transfer to N, the cleavage of the C–N bond, and the recovery of the hydrogenated form of the catalyst **1** in a single concerted step. Nonetheless, this reaction involves a high Gibbs energy barrier of 30.6 kcal mol⁻¹. In addition to 8^F , intermediates 14^F and 15^F , which are both kinetically accessible ($\Delta G^\ddagger = 21.0$ and 19.3 kcal mol⁻¹, respectively), can also facilitate C–N bond protonolysis pathways resembling those proposed for the hydrogenation of esters (Scheme 3).³⁵ From 14^F , the NH moiety of the catalyst ligand protonates the N of the hemiaminal, causing

cleavage of the C–N bond. This pathway also involves a high energy barrier (33.1 kcal mol⁻¹; $TS14-2^F$). 15^F yielded the lowest energy pathway, in which C–N bond cleavage occurs in a stepwise manner, yielding formaldehyde ($TS15-16^F$), followed by proton transfer to give aniline ($TS16-2^F$). The highest energy barrier, $\Delta G^\ddagger = 24.9$ kcal mol⁻¹, is associated with the C–N bond cleavage step. The overall process is almost thermoneutral, $\Delta G = 0.1$ kcal mol⁻¹, due to the exergonic (and fast) reduction of formaldehyde to methanol (Figure 1).

The hemiaminal O- and N-bound pathways shown in Figure 5 for the protonolysis of the C–N bond have a common feature: the protonation of the organic fragment by the NH moiety of the pincer ligand. This process can be assisted by a molecule of formanilide acting as a proton relay, as suggested by the mechanism shown in Figure 4. This hypothesis was confirmed by calculations (Figures S8 and 6), which showed that the $TS14-2^F$ (33.1 kcal mol⁻¹) and $TS16-2^F$ (12.4 kcal mol⁻¹) barriers are lowered to 25.5 and 0.6 kcal mol⁻¹, respectively, when formanilide assists the proton transfer. In the latter mechanism, which yielded the lowest energy profile, the C–N bond cleavage step remains associated with the highest energy barrier ($\Delta G^\ddagger = 24.9$ kcal mol⁻¹; Figure 6). Interestingly, this pathway leads to the exergonic formation of complex **6** ($\Delta G = -10.7$ kcal mol⁻¹), which was experimentally observed and characterized by NMR and X-ray crystallography.

Deaminative Hydrogenation of DMF. The reaction observed with formanilide, at 100 °C and 30 atm of H₂, is not observed with DMF under the same conditions.¹⁸ In this case, the formation of methanol and dimethylamine requires the addition of formanilide as cocatalyst. With the aim of rationalizing these observations, the reaction pathways determined for formanilide were evaluated for DMF.

The hydrogenation of the DMF carbonyl group by **1** follows the mechanism shown in Figure 3 but involves energy barriers of 23.1 ($TS7-8^{DMF}$) and 23.4 kcal mol⁻¹ ($TS8-9^{DMF}$; Figure 7), which are significantly higher than those found for formanilide. This is consistent with the lower electrophilicity of the carbonyl group, caused by the stronger donating effect of alkyl N substituents, which disfavors hydride addition. This is also consistent with the lower stability of the hemiaminal intermediate with DMF (10.5 kcal mol⁻¹), compared to formanilide (4.7 kcal mol⁻¹). Also in contrast to formanilide, the protonolysis of the C–N bond in the hemiaminal derived from DMF is stepwise rather than concerted. The common feature between the two organic substrates is the prohibitive barrier associated with the highest-energy transition state if there is no catalyst to facilitate this process. In the DMF-derived hemiaminal, this corresponds to the proton transfer step (42.7 kcal mol⁻¹ above reactants; TS_{HT}^{DMF} in Figure 8). The C–N cleavage takes place in the following step from a zwitterionic intermediate, which at 23.8 kcal mol⁻¹ above reactants, could be considered as accessible under the reaction conditions.

Using the information obtained in the case of formanilide (Figure 5), the C–N bond protonolysis pathways assisted by the dehydrogenated form of the catalyst, **2**, were explored for DMF. The calculations showed that the lowest-energy pathway obtained for DMF is different from that obtained for formanilide. The transition state for C–N bond cleavage ($TS15-16^{DMF}$), which with formanilide, yielded the lowest energy barrier, is too high with DMF to be experimentally

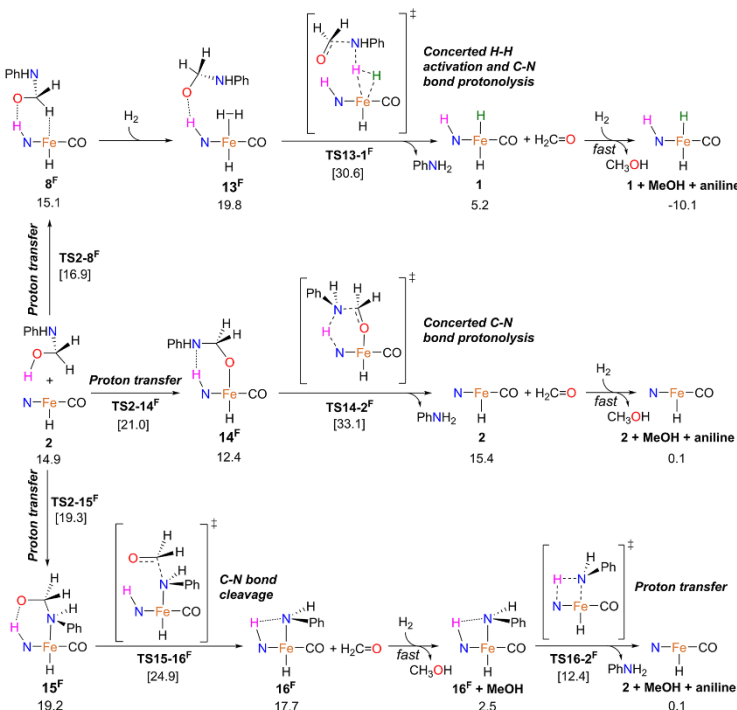


Figure 5. Reaction pathways for the protonolysis of the C–N bond of the formanilide-derived hemiaminal by **2**. In the labels, the F superscript accounts for formanilide. Gibbs energies in THF (SMD) at 30 atm and 373 K are given in kcal mol⁻¹. Three intermediates were considered, differing on the binding of the hemiaminal: CH-bound (top), O-bound (middle), and N-bound (bottom). The reactive hydrogen atoms are highlighted in either purple (acidic) or green (hydridic).

relevant (41.0 kcal mol⁻¹ above reactants; Figure 7). The **TS14–2^{DMF}** transition state also yielded a prohibitive energy barrier (39.9 kcal mol⁻¹). In contrast, the transition state involving molecular hydrogen (**TS13–1^{DMF}**) yielded the lowest energy barrier, 30.4 kcal mol⁻¹. However, this barrier is rather high and accounts for the lack of conversion in the absence of a cocatalyst, unless higher pressures of hydrogen (up to 60 atm) are used in the experiments.¹⁸ A reasonable alternative is to use formanilide to assist the hydrogenation of DMF for the protonolysis of the C–N bond. Calculations including formanilide in the model confirmed this hypothesis.

The protonolysis of the DMF-derived hemiaminal assisted by formanilide involves two steps (Figure 7), namely, N-to-N proton transfer (**TS10–11^{DMF}**) followed by O-to-N proton transfer (**TS11–12^{DMF}**). The formanilide-derived hemiaminal follows a similar pathway (Figure 4), but in the case of DMF, the highest barrier is much lower (19.1 vs 31.2 kcal mol⁻¹ for the N-to-N proton transfer), likely due to the increased basicity of the N proton acceptor. In line with this, the O-to-N proton transfer barrier is slightly higher, with **TS11–12^{DMF}** at 22.6 kcal mol⁻¹ above reactants. The relaxation of **TS11–12^{DMF}** toward products yielded the zwitterionic intermediate **18^{DMF}**, which undergoes C–N bond cleavage without

assistance over a barrier of 22.7 kcal mol⁻¹ (**TS_{CN}^{DMF}**, Figure 8). Alternative mechanisms in which the Fe catalyst acts in concert with formanilide were also explored, but they yielded higher energy profiles (Figure S8). Interestingly, in the hydrogenation of DMF and in contrast with that of formanilide, the energy barriers for C=O hydrogenation and C–N protonolysis are similar and the highest in the overall energy profile.

Microkinetic Models of the Global Mechanism. The calculations for the catalyzed hydrogenation of formanilide and DMF show that both amides follow the general catalytic cycle depicted in Scheme 2. Starting with the hydrogenation of the amide carbonyl, the reaction continues with the C–N bond protonolysis of the resulting hemiaminal and finishes with the hydrogenation of formaldehyde to methanol. Nonetheless, the protonolysis step, which involves the highest energy barriers, is facilitated by either an organic species (formanilide) or the Fe complex, depending on the amide substrate, as illustrated in Scheme 4.

With formanilide, the cleavage of the C–N bond is driven by the coordination of the resulting amido group to Fe and by the delocalization of the negative charge over the phenyl substituent. The final protonation of the amido group yielding

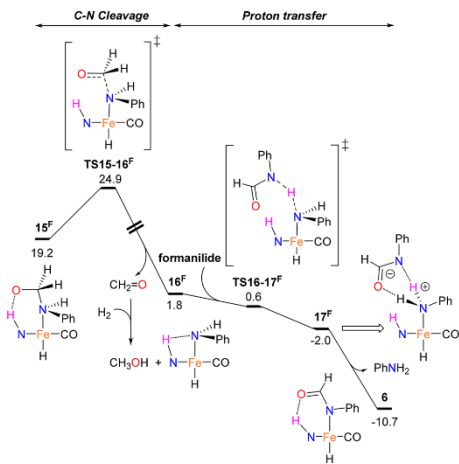


Figure 6. Reaction pathway for the protonolysis of the C–N bond of the N-bound hemiaminal with the assistance of formanilide (labeled with a F superscript). Gibbs energies in THF (SMD) at 30 atm and 373 K are given in kcal mol^{-1} .

the amine does not require cocatalysis. In contrast, with DMF, this pathway becomes unfeasible ($\Delta G^\ddagger = 41.0 \text{ kcal mol}^{-1}$), presumably because the methyl substituents cannot stabilize the negative charge of the resulting amido species. In this case, the protonation of the hemiaminal N, yielding a zwitterionic intermediate, is required to force the cleavage of the C–N bond. This proton transfer requires a cocatalyst with an acidic X–H bond (e.g., formanilide). In the absence of such species, dihydrogen may play this role but it requires high pressure and activation by Fe, still yielding a rather high energy barrier ($\Delta G^\ddagger = 30.4 \text{ kcal mol}^{-1}$). With formanilide acting as cocatalyst, the zwitterion, which undergoes barrier-less C–N cleavage, is readily accessible by fast proton transfer ($\Delta G^\ddagger = 19.1 \text{ kcal mol}^{-1}$).

In contrast with its cocatalytic effect in the protonolysis of the hemiaminal C–N bond, formanilide can also have a detrimental influence by deactivating the dehydrogenated form of the catalyst (2) through the formation of a stable off-cycle species (5), as shown in Scheme 5. Further, formanilide plays different roles in the mechanism depending on whether it is the substrate itself or the cocatalyst in the hydrogenation of DMF. With the aim of achieving a deeper understanding of these mechanisms, microkinetic models were constructed by using the rate constants for each individual step calculated from the Gibbs energy profiles.^{43–46} These models facilitate the interpretation of complex reaction networks, like the interconnected (and thus competing) cycles shown in Scheme 5. Further, they include the interplay between energy barriers and concentrations in a quantitative manner. The concentration vs time plots shown in Figure 9 were computed by using the DFT-optimized energies⁴⁷ and the initial experimental conditions, including molar concentrations. Interestingly, these microkinetic models revealed that, beyond the critical C–N protonolysis step, other factors, like the

competition between hydrogen and formanilide to form either 1 or 5 from 2, also play a key role (vide infra).

In the case of formanilide, the microkinetic model predicted a very low conversion to aniline and methanol (i.e., 0.2%, as shown in Figure 9a) after 4 h (experimental reaction time, which gave a conversion of 99%), when only the Fe complex was considered as catalyst in the protonolysis of the C–N bond (pathway P2a in Scheme 5). This result originated from the low concentration of complex 2 relative to 5 (only 0.8%), which is due to the large concentration of formanilide poisoning the catalyst, compared to that of H_2 (1.4 vs 0.162 M, respectively). The inclusion of the formanilide cocatalytic effect (pathway P2b in Scheme 5) caused a minor increase of the conversion, reaching 1.5% after the same reaction time. In order to assess the influence of catalyst deactivation by formation of adduct 5, the equilibrium between this species and 2 + formanilide (P4) was removed from the microkinetic model. The resulting simulations yielded a significant increase in conversion to 25.8% showing the major effect that the formation of 5 has on the overall efficiency of this reaction. In this scenario, most of the conversion results from the Fe catalyzed protonolysis of the C–N bond (pathway P2a). A clear conclusion from Figure 9 is that the productive effect of formanilide as cocatalyst is far from compensating its detrimental effect as catalyst poison. This effect is also apparent in Figure 10, which shows how conversion increases by destabilizing adduct 5; a shift in the energy of this species relative to reactants by $\Delta\Delta G = +2 \text{ kcal mol}^{-1}$ can quadruple the overall conversion. Thus, the stability of 5 has a dramatic influence on the yield of the overall reaction.

Even small variations in the energy barriers associated with TS15–16^F and TS10–11^F (i.e., the highest-energy transition states in the Fe- and formanilide-catalyzed C–N protonolysis pathways, respectively; Figure 7) have a strong impact on conversion (Figure 10). According to the microkinetic models, an energy barrier decrease of only $\Delta\Delta G^\ddagger = -1 \text{ kcal mol}^{-1}$ can double the conversion. However, the most dramatic results were observed upon combining the destabilization of adduct 5 (Figure 2) by $\Delta\Delta G = +2 \text{ kcal mol}^{-1}$ with a lowering of the energy of TS15–16^F by $\Delta\Delta G^\ddagger = -3 \text{ kcal mol}^{-1}$, which raised the conversion predicted from ca. 1% to the experimental 99%. This result does not significantly change by including the mechanism where the protonolysis of the C–N bond is assisted by the Fe complex and formanilide (TS20–21^F; see the Supporting Information).

The mechanism inferred from the DFT calculations and drawn in Scheme 5 accounts for the experimental observations, since the energy deviations derived from the fit are within the error range expected for calculated Gibbs energies. These errors can be introduced by the inaccuracy of the DFT method (see benchmarks in the Supporting Information) and the approaches used in the calculation of the solvent, entropy, and thermal effects.^{50,51} Lowering the TS10–11^F barrier with similar energy shifts had similar but much milder effects. Even if adduct 5 is considered as not stable enough to accumulate ($\Delta\Delta G^\ddagger$ and $\Delta\Delta G$ adduct of -3 and $+3 \text{ kcal mol}^{-1}$, respectively), the conversion does not increase over 60% (Figure 10). These results suggest that the design of a catalyst yielding higher conversions under milder conditions should focus on both accelerating the cleavage of the C–N bond and excluding catalyst poisoning. Efficient strategies would include increasing the acceptor character of the ancillary ligands (i.e., to stabilize the amido product) and their steric bulk (i.e., to

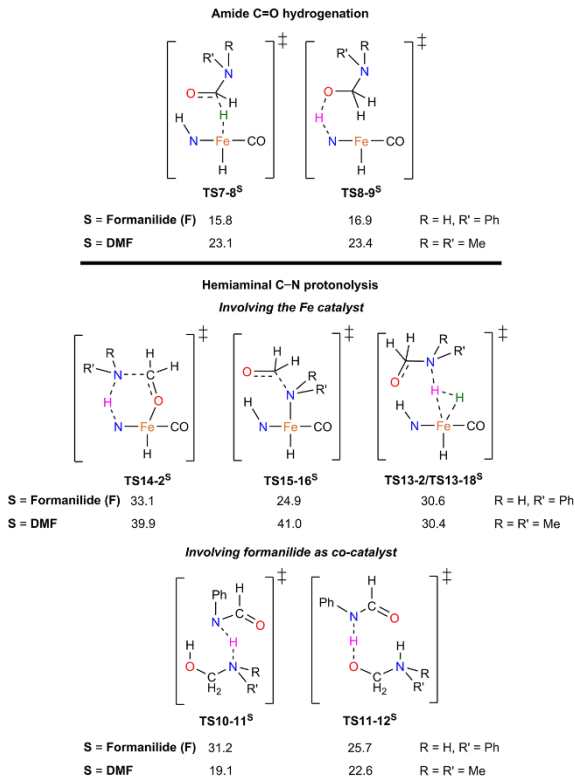


Figure 7. Key transition states and energy barriers in the hydrogenation of formanilide (F) and DMF (DMF). Gibbs energies in THF (SMD) at 30 atm and 373 K are given in kcal mol⁻¹. The reactive hydrogen atoms are highlighted in either purple (acidic) or green (hydridic).

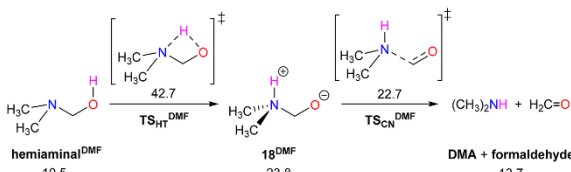


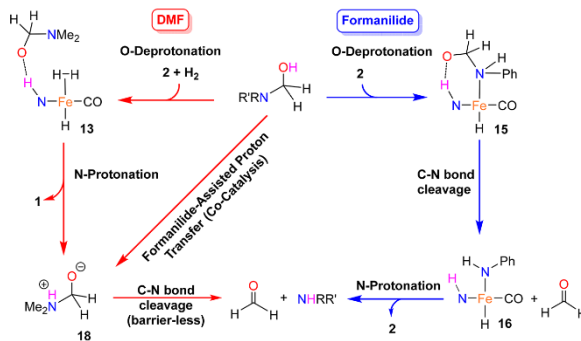
Figure 8. Nonassisted intramolecular protonolysis of the C–N bond of the DMF-derived hemiaminal (labeled by a DMF superscript). Gibbs energies in THF (SMD) at 30 atm and 373 K are given in kcal mol⁻¹.

disfavor formanilide binding to the metal center), taking into account that these may have an impact on the stability of the catalyst¹⁶ or on the amide C=O hydrogenation step.⁵²

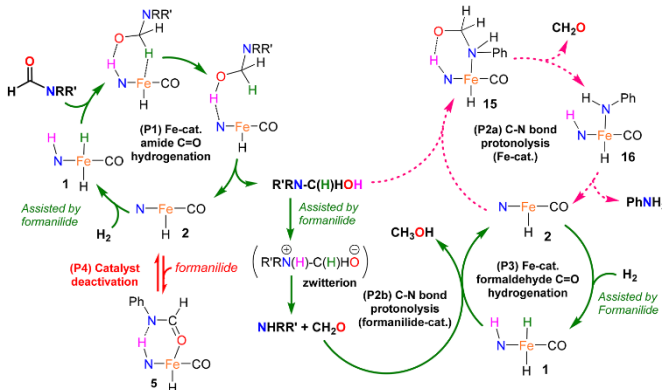
In the case of DMF, conversion to methanol after 4 h taking into account the cocatalytic effect of formanilide in C–N bond protonolysis is 25.9% (Figure 9b), significantly higher than the experimental (13.6%). However, in this case, the microkinetic model was simplified by ignoring the consumption of formanilide, which also undergoes hydrogenation under these conditions. When including the consumption of formanilide by

hydrogenation in the model,⁵³ the simulations predicted a lower conversion of 11.6%, in line with the experiments. This simulation also showed that some formanilide can assist the C–N bond protonolysis before being consumed, probably because of the small difference in energy between the rate limiting step for formanilide and DMF hydrogenation of ca. 1 kcal mol⁻¹ (TS8-9^{DMF} vs TS15-16^F) and the lower concentration of formanilide compared to DMF. In contrast, conversion increased to 31.3% when the formation of adduct 5 (Figure 2) was excluded from the microkinetic model. The

Scheme 4. Three Pathways for the Protonolysis of the C–N Bond of the Hemiaminal Intermediates Derived from Formanilide and DMF



Scheme 5. Reaction Mechanisms Used in the Microkinetic Models of the Formanilide ($R = H, R' = Ph$) and DMF ($R = R' = Me$) Hydrogenation^a



^aThe productive pathways involving both amides are in solid green arrows (P1, P2b and P3), those involving just formanilide are in dashed pink arrows (P2a) and those leading to catalyst deactivation are in solid red double arrows (P4).⁴⁸

concentration of the Fe catalyst **1** available thus also plays a key role in the deaminative hydrogenation of DMF. This can be ascribed to the contribution of **1** to the C=O hydrogenation step (pathway P1 in Scheme 5), which in the case of DMF, has a similar energy barrier to that of the C–N bond protonolysis (23.4 and 23.8 kcal mol⁻¹, respectively). A rational strategy toward increasing the conversion of DMF would be to use a different proton relay cocatalyst, which in contrast to formanilide, would not undergo hydrogenation nor poison the catalyst. However, the maximum conversion is limited to 31.8% in the case of DMF, due to the less favorable thermodynamics of the overall reaction ($\Delta G = -1.5$ kcal mol⁻¹ vs -10.1 kcal mol⁻¹ with formanilide; Figure 1). In line with this, the microkinetic models reached equilibrium at conversions of 31.8%⁵⁴ and 99.9% for DMF and formanilide, respectively.

CONCLUSIONS

This computational study reveals the complex reaction network underlying the mechanism of the deaminative hydrogenation of amides catalyzed by $Fe(^{19}PN^H_2P)(H)_2(CO)$ ($^{19}PN^H_2P = HN\{CH_2CH_2(P^*Pr_2)\}_2$). Despite the different nature and substrate performance of the two amides considered, i.e., formanilide and DMF, as examples of secondary aryl and tertiary alkyl amides, both substrates follow mechanisms with common steps. These include the hydrogenation of the C=O groups of the amide and formaldehyde (in both cases catalyzed by the Fe complex) and the protonolysis of the C–N bond of the hemiaminal intermediate assisted by formanilide (which is either the reactant itself or the cocatalyst used in the case of DMF). However, there are also relevant differences; in the case of formanilide, the C–N bond protonolysis can be catalyzed by the Fe complex, which in this case, provides the lowest energy pathway. Regardless of the mechanism and the substrate, the kinetic bottleneck of the

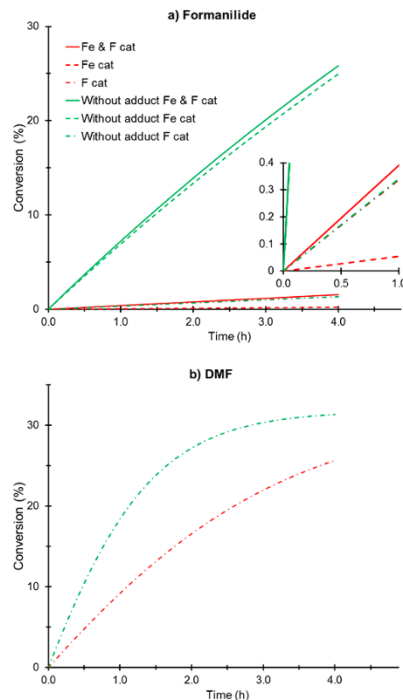


Figure 9. Amide conversion over time for the hydrogenation of formanilide (labeled by a F, top) and DMF (bottom). The simulations were based on the reaction mechanism shown in Scheme 5. The initial conditions, reaction time, temperature, and pressure were the same as those used in the experiments;¹⁸ i.e., 1.4 M of amide, 0.162 M of H₂,⁴⁹ 1 mM of catalyst 1, and 0.02 M of formanilide cocatalyst (DMF). H₂ concentration was kept constant throughout the kinetic simulations, consistent with the effectively constant pressure of H₂ used in the experiments.

overall reaction involves the cleavage of the C–N bond of the hemiaminal, showing the key role played by this organic intermediate. Remarkably, this result changes the long-established principle that the hydrogenation of electron rich carbonyl substrates, such as amides and esters, are governed by their carbonyl hydrogenation step and, therefore, only metal-hydride hydricity is relevant for catalyst design.

Furthermore, the interpretation of the DFT results by means of microkinetic models reveals the critical effect introduced by the formation of stable adducts in which formanilide binds strongly to the dehydrogenated form of the catalyst. The rational design of improved catalysts and cocatalysts should thus aim to both accelerate the cleavage of the C–N bond and prevent the poisoning of the catalyst. According to the mechanistic model derived from this study, in the case of formanilide, these goals should be pursued by focusing on the Fe catalyst, whereas in the case of DMF, the focus should be on the organic cocatalyst.

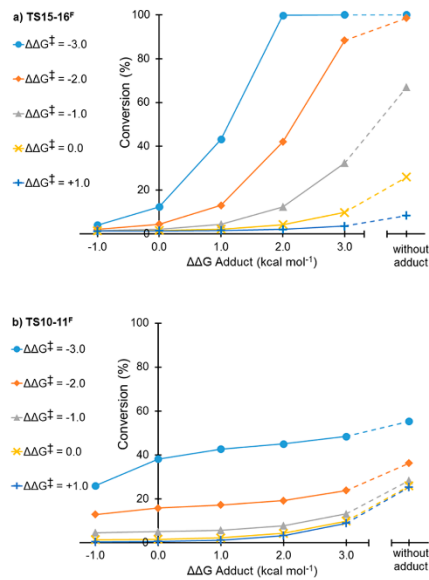


Figure 10. Amide conversion (after 4 h) vs $\Delta\Delta G$ (shift applied to the energy of adduct 5) and $\Delta\Delta G^\ddagger$ (shift applied to the energy of transition states TS15–16^F and TS10–11^F).

ASSOCIATED CONTENT

Supporting Information

The Supporting Information is available free of charge on the ACS Publications website at DOI: 10.1021/acscatal.8b02184.

Computational details, comparison of experimental and calculated ΔH_f^o , additional computed energy pathways for formanilide hydrogenation and hemiaminal proton transfer, DMF calculated maximum conversion, table with G, H, and $-TS$ energy components, and optimized coordinates (PDF)

AUTHOR INFORMATION

Corresponding Authors

*E-mail: bernskoetterwh@missouri.edu.

*E-mail: ainara.nova@kjemi.uio.no.

ORCID

Lluís Artús Suárez: 0000-0002-8814-9410

David Balcells: 0000-0002-3389-0543

Wesley H. Bernskoetter: 0000-0003-0738-5946

Odile Eisenstein: 0000-0001-5056-0311

Karen I. Goldberg: 0000-0002-0124-1709

Nilay Hazari: 0000-0001-8337-198X

Mats Tilset: 0000-0001-8766-6910

Ainara Nova: 0000-0003-3368-7702

Notes

The authors declare no competing financial interest.

■ ACKNOWLEDGMENTS

L.A.S., D.B., and A.N. acknowledge the support from the Research Council of Norway through its FRINATEK (No. 250044) and Center of Excellence schemes (No. 262695) and the Norwegian Metacenter for Computational Science (NOTUR, nn4654k). W.H.B. and N.H. acknowledge support from the U.S. Department of Energy, Office of Science, Basic Energy Sciences, Catalysis Science Program, under Award DE-SC0018222. Z.C. acknowledges support from the Office for Science and Technology of the Embassy of France in the United States in the form of a Chateaubriand Fellowship, as well as the National Science Foundation Graduate Research Fellowship Program under Grant No. DGE-1256082. K.I.G. and Z.C. also acknowledge support from NSF through the CCI Center for Enabling New Technologies through Catalysis (CENTC) Phase II Renewal, CHE-1205189. The authors thank Prof. Martin Jaraiz (University of Valladolid) for helpful discussions about the microkinetic models. Z.C. thanks Dr. Eric Clot for useful discussions during her stay at the University of Montpellier, France.

■ REFERENCES

- (1) Arthur, G. *The Amide Linkage: Selected Structural Aspects in Chemistry, Biochemistry, and Materials Science*, 1st ed.; Wiley-Interscience: Hoboken, 2000.
- (2) Constable, D. J. C.; Dunn, P. J.; Hayler, J. D.; Humphrey, G. R.; Leazer, J. L., Jr.; Linderman, R. J.; Lorenz, K.; Manley, J.; Pearlman, B. A.; Wells, A.; et al. Key Green Chemistry Research Areas—a Perspective from Pharmaceutical Manufacturers. *Green Chem.* **2007**, 9, 411–420.
- (3) Wieland, T.; Bodanszky, M. *The World of Peptides: A Brief History of Peptide Chemistry*, 1st ed.; Springer-Verlag: Berlin, 1991.
- (4) Zabicky, J.; Patai, S. *The Chemistry of Amides*, 1st ed.; John Wiley & Sons: London, 1970.
- (5) Smith, A. M.; Whyman, R. Review of Methods for the Catalytic Hydrogenation of Carboxamides. *Chem. Rev.* **2014**, 114, 5477–5510.
- (6) Ito, M.; Ootsuka, T.; Watari, R.; Shibusaki, A.; Himizu, A.; Ikariya, T. Catalytic Hydrogenation of Carboxamides and Esters by Well-Defined Cp⁺Ru Complexes Bearing a Protic Amine Ligand. *J. Am. Chem. Soc.* **2011**, 133, 4240–4242.
- (7) John, J. M.; Bergens, S. H. A Highly Active Catalyst for the Hydrogenation of Amides to Alcohols and Amines. *Angew. Chem., Int. Ed.* **2011**, 50, 10377–10380.
- (8) Miura, T.; Held, I. E.; Oishi, S.; Naruto, M.; Saito, S. Catalytic Hydrogenation of Unactivated Amides Enabled by Hydrogenation of Catalyst Precursor. *Tetrahedron Lett.* **2013**, 54, 2674–2678.
- (9) Kita, Y.; Higuchi, T.; Mashima, K. Hydrogenation of Amides Catalyzed by a Combined Catalytic System of a Ru Complex with a Zinc Salt. *Chem. Commun.* **2014**, 50, 11211–11213.
- (10) Rezayee, N. M.; Huff, C. A.; Sanford, M. S. Tandem Amine and Ruthenium-Catalyzed Hydrogenation of CO₂ to Methanol. *J. Am. Chem. Soc.* **2015**, 137, 1028–1031.
- (11) John, J. M.; Loorthuraja, R.; Antoniuk, E.; Bergens, S. H. Catalytic Hydrogenation of Functionalized Amides Under Basic and Neutral Conditions. *Catal. Sci. Technol.* **2015**, 5, 1181–1186.
- (12) Balaraman, E.; Gnanaprakasam, B.; Shimoni, L. J. W.; Milstein, D. Direct Hydrogenation of Amides to Alcohols and Amines Under Mild Conditions. *J. Am. Chem. Soc.* **2010**, 132, 16756–16758.
- (13) Cabrero-Antonino, J. R.; Alberico, E.; Drexler, H. J.; Baumann, W.; Junge, K.; Junge, H.; Beller, M. Efficient Base-Free Hydrogenation of Amides to Alcohols and Amines Catalyzed by Well-Defined Pincer Imidazolyl-Ruthenium Complexes. *ACS Catal.* **2016**, 6, 47–54.
- (14) Zhang, L.; Han, Z.; Zhao, X.; Wang, Z.; Ding, K. Highly Efficient Ruthenium-Catalyzed N-Formylation of Amines with H₂ and CO₂. *Angew. Chem., Int. Ed.* **2015**, 54, 6186–6189.
- (15) Garg, J.; Chakraborty, S.; Ben-David, Y.; Milstein, D. Unprecedented Iron-Catalyzed Selective Hydrogenation of Activated Amides to Amines and Alcohols. *Chem. Commun.* **2016**, 52, 5285–5288.
- (16) Schneek, F.; Assmann, M.; Balmer, M.; Harms, K.; Langer, R. Selective Hydrogenation of Amides to Amines and Alcohols Catalyzed by Improved Iron Pincer Complexes. *Organometallics* **2016**, 35, 1931–1943.
- (17) Rezayee, N. M.; Samblanet, D. C.; Sanford, M. S. Iron-Catalyzed Hydrogenation of Amides to Alcohols and Amines. *ACS Catal.* **2016**, 6, 6377–6383.
- (18) Jayaratne, U.; Zhang, Y.; Hazari, N.; Bernskoetter, W. H. Selective Iron-Catalyzed Deaminative Hydrogenation of Amides. *Organometallics* **2017**, 36, 409–416.
- (19) Frisch, M. J.; Trucks, G. W.; Schlegel, H. B.; Scuseria, G. E.; Robb, M. A.; Cheeseman, J. R.; Scalmani, G.; Barone, V.; Mennucci, B.; Petersson, G. A.; Nakatsuji, H.; Caricato, M.; Li, X.; Hratchian, H. P.; Izmaylov, A. F.; Bloino, J.; Zheng, G.; Sonnenberg, J. L.; Hada, M.; Ehara, M.; Toyota, K.; Fukuda, R.; Hasegawa, J.; Ishida, M.; Nakajima, T.; Honda, Y.; Kitao, O.; Nakai, H.; Vreven, T.; Montgomery, J. A., Jr.; Peralta, J. E.; Ogliaro, F.; Bearpark, M.; Heyd, J. J.; Brothers, E.; Kudin, K. N.; Staroverov, V. N.; Keith, T.; Kobayashi, R.; Normand, J.; Raghuvaran, K.; Rendell, A.; Burant, J. C.; Iyengar, S. S.; Tomasi, J.; Cossi, M.; Rega, N.; Millam, J. M.; Klene, M.; Knox, J. E.; Cross, J. B.; Bakken, V.; Adamo, C.; Jaramillo, J.; Gomperts, R.; Stratmann, R. E.; Yazyev, O.; Austin, A. J.; Cammi, R.; Pomelli, C.; Ochterski, J. W.; Martin, R. L.; Morokuma, K.; Zakrzewski, V. G.; Voth, G. A.; Salvador, P.; Dannenberg, J. J.; Dapprich, S.; Daniels, A. D.; Farkas, O.; Foresman, J. B.; Ortiz, J. V.; Cioslowski, J.; Fox, D. J. *Gaussian 09*, Revision D.01; Gaussian, Inc.: Wallingford CT, 2013.
- (20) Zhao, Y.; Truhlar, D. G. The M06 Suite of Density Functionals for Main Group Thermochemistry, Thermochemical Kinetics, Noncovalent Interactions, Excited States, and Transition Elements: Two New Functionals and Systematic Testing of Four M06-Class Functionals and 12 other Function. *Theor. Chem. Acc.* **2008**, 120, 215–241.
- (21) Zhang, Y.; MacIntosh, A. D.; Wong, J. L.; Bielinski, E. A.; Williard, P. G.; Mercado, B. Q.; Hazari, N.; Bernskoetter, W. H. Iron Catalyzed CO₂ Hydrogenation to Formate Enhanced by Lewis Acid Co-Catalysts. *Chem. Sci.* **2015**, 6, 4291–4299.
- (22) Purvis, G. D.; Bartlett, R. J. A Full Coupled-Cluster Singles and Doubles Model: The Inclusion of Disconnected Triples. *J. Chem. Phys.* **1982**, 76, 1910–1918.
- (23) Dunning, T. H. Gaussian Basis Sets For Use in Correlated Molecular Calculations. I. The Atoms Boron Through Neon and Hydrogen. *J. Chem. Phys.* **1989**, 90, 1007–1023.
- (24) Woon, D. E.; Dunning, T. H. Gaussian Basis Sets For Use in Correlated Molecular Calculations. III. The Atoms Aluminum Through Argon. *J. Chem. Phys.* **1993**, 98, 1358–1371.
- (25) Balabanov, N. B.; Peterson, K. A. Systematically Convergent Basis Sets for Transition Metals. I. All-Electron Correlation Consistent Basis Sets for the 3d Elements Sc-Zn. *J. Chem. Phys.* **2005**, 123, 064107–064123.
- (26) Hay, P. J.; Wadt, W. R. Ab Initio Effective Core Potentials for Molecular Calculations. Potentials for the Transition Metal Atoms Sc to Hg. *J. Chem. Phys.* **1985**, 82, 270–283.
- (27) Hehre, W. J.; Ditchfield, R.; Pople, J. A. Self—Consistent Molecular Orbital Methods. XII. Further Extensions of Gaussian—Type Basis Sets For Use in Molecular Orbital Studies of Organic Molecules. *J. Chem. Phys.* **1972**, 56, 2257–2261.
- (28) Kohn, W.; Becke, A. D.; Parr, R. G. Density Functional Theory of Electronic Structure. *J. Phys. Chem.* **1996**, 100, 12974–12980.
- (29) Wei, Y.; Zeng, X. Catalytic Strategies toward Selective Hydrogenation of Aromatic Ketones and Phenols: Facile Synthesis of Cyclohexyl Ketones. *Synlett* **2016**, 27, 650–655.
- (30) McLean, A. D.; Chandler, G. S. Contracted Gaussian Basis Sets for Molecular Calculations. I. Second Row Atoms, Z = 11–18. *J. Chem. Phys.* **1980**, 72, 5639–5648.

- (31) Marenich, A. V.; Cramer, C. J.; Truhlar, D. G. Universal Solvation Model Based on Solute Electron Density and on a Continuum Model of the Solvent Defined by the Bulk Dielectric Constant and Atomic Surface Tensions. *J. Phys. Chem. B* **2009**, *113*, 6378–6396.
- (32) Alvarez-Moreno, M.; De Graaf, C.; López, N.; Maseras, F.; Poblet, J. M.; Bo, C. Managing the Computational Chemistry Big Data Problem: The ioChem-BD Platform. *J. Chem. Inf. Model.* **2015**, *55*, 95–103.
- (33) Hoops, S.; Sahle, S.; Gauges, R.; Lee, C.; Pahle, J.; Simus, N.; Singhal, M.; Xu, L.; Mendes, P.; Kummer, U. COPASI – A Complex Pathway Simulator. *Bioinformatics* **2006**, *22*, 3067–3074.
- (34) Petzold, L. Automatic Selection of Methods for Solving Stiff and Nonstiff Systems of Ordinary Differential Equations. *SIAM J. Sci. Stat. Comput.* **1983**, *4*, 136–148.
- (35) Qu, S.; Dai, H.; Dang, Y.; Song, C.; Wang, Z. X.; Guan, H. Computational Cechanistic Study of Fe-Catalyzed Hydrogenation of Esters to Alcohols: Improving Catalysis by Accelerating Precatalyst Activation with a Lewis Base. *ACS Catal.* **2014**, *4*, 4377–4388.
- (36) Chakraborty, S.; Lagaditis, P. O.; Förster, M.; Bielinski, E. A.; Hazari, N.; Holthausen, M. C.; Jones, W. D.; Schneider, S. Well-Defined Iron Catalysts for the Acceptorless Reversible Dehydrogenation-Hydrogenation of Alcohols and Ketones. *ACS Catal.* **2014**, *4*, 3994–4003.
- (37) Zhang, H. A DFT Study on Direct Hydrogenation of Amide Catalyzed by a PNN Ru(II) Pincer Complex. *Comput. Theor. Chem.* **2015**, *1066*, 1–6.
- (38) Chen, X.; Jing, Y.; Yang, X. Unexpected Direct Hydride Transfer Mechanism for the Hydrogenation of Ethyl Acetate to Ethanol Catalyzed by SNS Pincer Ruthenium Complexes. *Chem. - Eur. J.* **2016**, *22*, 1950–1957.
- (39) The computed ΔH_f° for Step 2 (with DMF) and Step 3 in gas phase are in agreement with the experimental values from NIST (see the Supporting Information); <https://webbook.nist.gov/chemistry/>.
- (40) Bielinski, E. A.; Lagaditis, P. O.; Zhang, Y.; Mercado, B. Q.; Würtele, C.; Bernskoetter, W. H.; Hazari, N.; Schneider, S. Lewis Acid-Assisted Formic Acid Dehydrogenation Using a Pincer-Supported Iron Catalyst. *J. Am. Chem. Soc.* **2014**, *136*, 10234–10237.
- (41) Fan, T.; Chen, X.; Lin, Z. Theoretical Studies of Reactions of Carbon Dioxide Mediated and Catalysed by Transition Metal Complexes. *Chem. Commun.* **2012**, *48*, 10808–10828.
- (42) Dub, P. A.; Gordon, J. C. Metal-Ligand Bifunctional Catalysis: The “Accepted” Mechanism, the Issue of Concertedness, and the Function of the Ligand in Catalytic Cycles Involving Hydrogen Atoms. *ACS Catal.* **2017**, *7*, 6635–6655.
- (43) Besora, M.; Maseras, F. Microkinetic Modeling in Homogeneous Catalysis. *WIREs Comput. Mol. Sci.* **2018**, e1372.
- (44) Jaraíz, M.; Enriquez, L.; Pinacho, R.; Rubio, J. E.; Lesarri, A.; López-Pérez, J. L. A DFT-Based Computational-Experimental Methodology for Synthetic Chemistry: Example of Application to the Catalytic Opening of Epoxides by Titanocene. *J. Org. Chem.* **2017**, *82*, 3760–3766.
- (45) Rush, L. E.; Pringle, P. G.; Harvey, J. N. Computational Kinetics of Cobalt-Catalyzed Alkene Hydroformylation. *Angew. Chem., Int. Ed.* **2014**, *53*, 8672–8676.
- (46) Kaled, M.; Himo, F. Mechanism and Selectivity of Cooperatively Catalyzed Meyer-Schuster Rearrangement/Tsuji-Trost Allylic Substitution. Evaluation of Synergistic Catalysis by Means of Combined DFT and Kinetics Simulations. *J. Am. Chem. Soc.* **2017**, *139*, 10250–10266.
- (47) The energy barrier for the hydrogenation of formaldehyde was taken from the literature.³⁶
- (48) Even though both adducts **5** and **6** can be formed (Figure 2), only **5**, which is the most stable, was considered for the sake of simplicity.
- (49) The concentration used for H_2 was estimated using the solubility of this gas in pure THF at $p = 33.4$ atm and $T = 100$ °C (0.01461 H_2 mol/solution mol) which was measured experimentally;
- Brunner, E. Solubility of Hydrogen in 10 Organic Solvents at 298.15, 323.15, and 373.15 K. *J. Chem. Eng. Data* **1985**, *30*, 269–273.
- (50) Plata, R. E.; Singleton, D. A. A Case Study of the Mechanism of Alcohol-Mediated Morita Baylis-Hillman Reactions. The Importance of Experimental Observations. *J. Am. Chem. Soc.* **2015**, *137*, 3811–3826.
- (51) Besora, M.; Vidossich, P.; Lledós, A.; Ujaque, G.; Maseras, F. Calculation of Reaction Free Energies in Solution: A Comparison of Current Approaches. *J. Phys. Chem. A* **2018**, *122*, 1392–1399.
- (52) Jayaratne, U.; Hazari, N.; Bernskoetter, W. H. Selective Iron-Catalyzed N-Formylation of Amines Using Dihydrogen and Carbon Dioxide. *ACS Catal.* **2018**, *8*, 1338–1345.
- (53) The consumption of formamide was included as a one-step reaction yielding formaldehyde using an energy barrier of 21.9 kcal mol⁻¹ ($TS15-16^b$, $\Delta\Delta G^\ddagger = -3$ kcal mol⁻¹).
- (54) This conversion is also consistent with the equilibrium constant ($K_{eq} = 7.8$) derived from the computed ΔG (see the Supporting Information).

Supporting Information

The Key Role of the Hemiaminal Intermediate in the Iron-Catalyzed Deaminative Hydrogenation of Amides

Lluís Artús Suàrez,[†] Zuzana Culakova,[#] David Balcells,[†] Wesley H. Bernskoetter,^{*,‡} Odile Eisenstein,[†] Karen I. Goldberg,^{#,§} Nilay Hazari,[§] Mats Tilset,[†] Ainara Nova^{*,†}

[†]Hylleraas Centre for Quantum Molecular Sciences, Department of Chemistry, University of Oslo, P.O. Box 1033, Blindern, N-0315 Oslo, Norway

[‡]Department of Chemistry, University of Missouri, Columbia, Missouri, 65211, USA

[#]Department of Chemistry, Yale University, P.O. Box 208107, New Haven, Connecticut, 06520, USA

[§]Department of Chemistry, University of Washington, Seattle, Washington, 98195, USA

[¶]Department of Chemistry, University of Pennsylvania, Philadelphia, Pennsylvania, 19104, USA

E-mail: bernskoetterwh@missouri.edu, ainara.nova@kjemi.uio.no.

Table of Contents:

Computational Details

DFT functional benchmarks **S2**

Selected methodology **S5**

Microkinetic models **S5**

Comparison of experimental and calculated standard reaction enthalpies **S8**

Formanilide hydrogenation by the trans- and cis-dihydride Fe complex **S8**

Hemiaminal intramolecular proton transfer **S9**

Formanilide assisted protonolysis of the C–N bond of the O-bound hemiaminal **S9**

DMF calculated maximum conversion **S10**

G, H and -TS energies **S11**

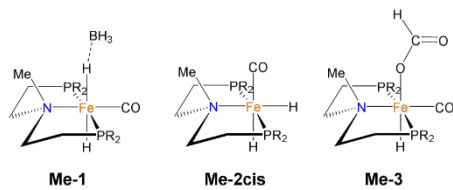
Cartesian coordinates of optimized geometries, and corresponding corrected Gibbs energies **S13**

S1

Computational Details

DFT functional benchmarks

Eight different functionals, including both hybrid (B3LYP+GD3,¹ PBE0+GD3,² TPSSh,³ M06⁴ and ωB97XD⁵) and pure (BLYP+GD3,^{6–8} PBE+GD3,⁹ TPSS³ and M06L¹⁰) flavors, were benchmarked in the structural optimization of complexes **Me-1**, **Me-2cis** and **Me-3** (Scheme S1).¹¹ These structures were selected because they contain the same [ⁱPrPN^XP)Fe(CO)H] fragment (ⁱPrPN^XP = XN{CH₂CH₂(PⁱPr₂)₂}, X=H and Me) found in the Fe intermediates involved in the reaction under study. X=Me was included because we are interested in comparing systems with X=H and Me in future studies. Structures were fully optimized without any geometry or symmetry constraint and using a double-ζ quality basis set combining the LANL2DZ^{12,13} on iron (including relativistic effects) and the 6-31+G**^{14,15} for all other elements. The X-Ray crystal structures of **Me-1**, **Me-2cis** and **Me-3** complexes were used as experimental reference to assess the accuracy of the functionals tested.¹¹ The root-mean-square deviation (RMSD) over all metal-ligand distances, plus that of the carbonyl (reflecting the π-backdonation interaction with the metal center), was used to quantify accuracy. Only in this case, and for the purpose of comparison to the crystal structures, geometries were optimized in gas phase (vide infra). In general, all functionals yielded high quality structures with an average RMSD < 0.05 Å (Figure S1). In particular, the PBE0+GD3, TPSS, TPSSh and M06 functionals provided the best agreement with the crystal structures, with an average RMSD < 0.02 Å.



Scheme S1. Iron complexes used in the structural benchmark (R = ⁱPr).

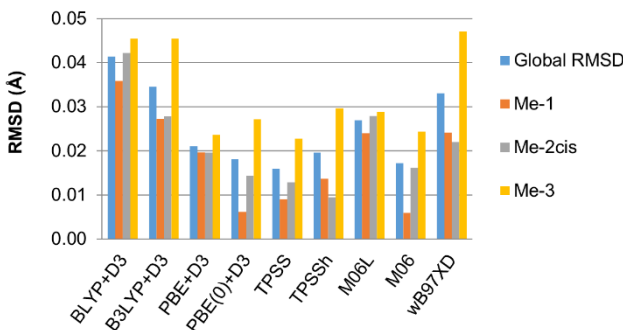
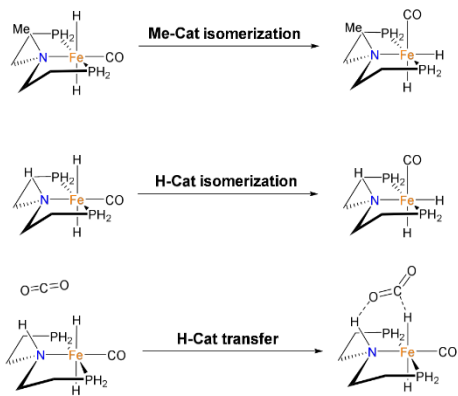


Figure S1. Quantitative deviation (\AA) of the DFT-optimized geometries relative to the experimental X-Ray crystal structures.

With the aim of assessing the accuracy in the calculation of the energies, we computed the potential energy changes upon going from reactants to products ($\Delta_r E$) for the three model reactions shown in Scheme S2. For the hydride transfer reaction, the potential energy barrier (ΔE^\ddagger) was also computed. Two different functionals, namely the PBE0+GD3 and the M06, chosen on the basis of their low RMSD values (Figure S1), were used for full geometry optimization with the double- ζ basis set (vide supra). The energy was refined by means of single-point calculations with three different functionals (TPSSh, PBE0+GD3 and M06; *i.e.* the hybrids that yielded the lowest RMSDs), expanding the basis set to triple- ζ quality (LANL2TZ^{12,13} on Fe, 6-311+G**^{16,17} on the rest). For the sake of benchmarking these DFT energies, the $\Delta_r E$ values were recomputed by means of single point CCSD(T)¹⁸ calculations with the correlation-consistent cc-pVTZ basis set.^{19–21} The data in Figure S2, including the deviation of the DFT energies relative to the CCSD(T) ($\Delta \Delta E$), clearly shows that the M06 functional provides the most accurate energies, with all deviations $\leq 1.0 \text{ kcal mol}^{-1}$ for both the $\Delta_r E$ and ΔE^\ddagger values and a $0.8 \text{ kcal mol}^{-1}$ RMSD.



Scheme S2. Reactions used in the energy benchmarks. The R substituents of the phosphine were replaced by hydrogens to make the CCSD(T) calculations feasible.

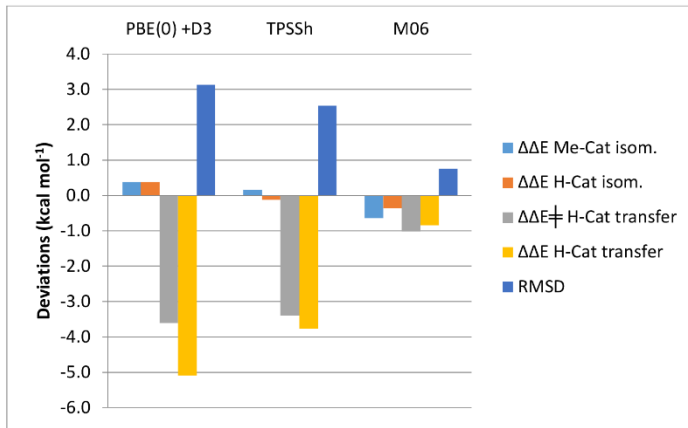


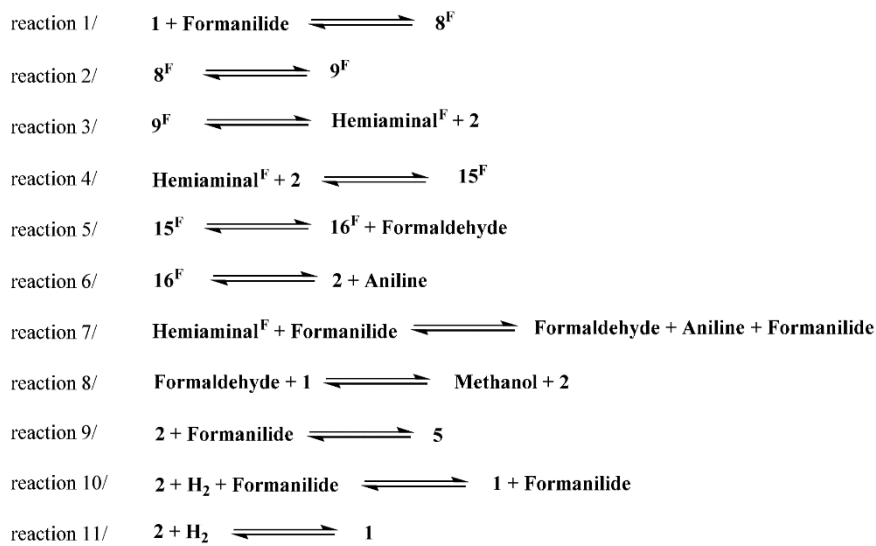
Figure S2. Quantitative deviation of the DFT $\Delta_r E$ and ΔE^\ddagger relative to the CCSD(T).

Selected methodology

In view of the results shown in Figures S1 and S2, the M06 functional was used in both the geometry optimizations, with the double- ζ basis set, and energy refinements, with the triple- ζ basis set.^{16,17} Once converged, the geometry optimizations were complemented with the analytic calculation of the frequencies with the double- ζ basis set. Frequencies were used to classify all stationary points as either energy minima (i.e. reactants, intermediates and products, with only real frequencies) or saddle points (i.e. transition states, with a single imaginary frequency vibrating along the reaction pathway connecting reactants to products). These calculations were also used to derive the thermochemistry (zero-point, thermal and entropy energies) at the experimental pressure (30 atm) and temperature (373 K). Solvent effects of THF were introduced both in the geometry optimizations and energy refinements by means of the continuum SMD model.²² The ultrafine (99,590) grid was used in all calculations for higher numerical accuracy. All calculations were carried out with the Gaussian09 (RevD.01) software package.²³

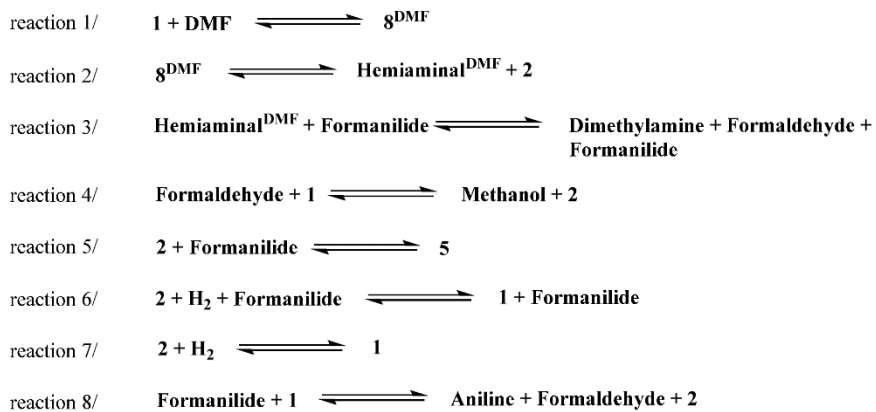
Microkinetic models

Microkinetic models were constructed with the COPASI software²⁴ (version 4.22). Association reactions were assumed to have low Gibbs energy barriers ($\Delta G^\ddagger \leq 5 \text{ kcal mol}^{-1}$), thus having no impact on the global kinetics of the reaction. The initial concentrations used in the simulations were those reported in the experiments²⁵ (1.4 M of amide, 1mM of catalyst, 0.162 M of hydrogen and 20 mM of co-catalyst). The concentration of hydrogen was kept constant, in line with the effectively constant pressure of hydrogen used in the reactor (30 atm). H₂ concentration was approximate using the molar fraction of H₂ in a saturated solution of H₂ in THF at 33.4 atm and 100 °C (0.01461 H₂ mol / solution mol) asuming incompresibility of THF and that [H₂] << [THF].²⁶ Also following the experiments, simulations were carried out for a total time of 4 hours at T = 373 K. The models were based on deterministic time course simulations with the LSODA algorithm.²⁷ The elementary steps of the mechanism underlying the microkinetic models are given in Figures S3 (formanilide) and S4 (DMF), together with the ΔG^\ddagger values derived from the DFT calculations.



	ΔG^\ddagger Forward (kcal mol ⁻¹)	ΔG^\ddagger Backwards (kcal mol ⁻¹)
reaction 1	15.8	0.7
reaction 2	1.8	1.2
reaction 3	4.2	5.0
reaction 4	4.4	0.2
reaction 5	5.8	7.2
reaction 6	10.0	12.3
reaction 7	26.5	26.0
reaction 8	5.0	10.1
reaction 9	4.0	16.2
reaction 10	4.0	14.2
reaction 11	11.6	21.8

Figure S3. Reactions and corresponding Gibbs energies (kcal mol⁻¹) used in the microkinetic model of the deaminative hydrogenation of formanilide.



	ΔG^\ddagger Forward (kcal mol ⁻¹)	ΔG^\ddagger Backwards (kcal mol ⁻¹)
reaction 1	23.1	0.6
reaction 2	0.9	2.8
reaction 3	13.5	10.3
reaction 4	6.0	11.1
reaction 5	4.0	16.2
reaction 6	4.0	14.2
reaction 7	11.6	21.8
reaction 8	24.9	9.5

Figure S4. Reactions and corresponding Gibbs energies (kcal mol⁻¹) used in the microkinetic model of the deaminative hydrogenation of DMF.

Comparison of experimental and calculated standard reaction enthalpies

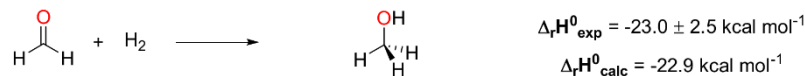
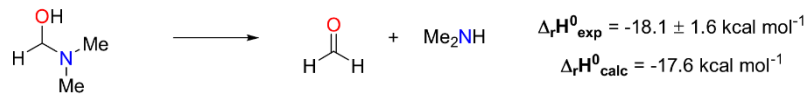


Figure S5. Experimental and calculated standard reaction enthalpies in gas phase (kcal mol^{-1}). Experimental energies obtained from the national institute of standards and technology (NIST).²⁸ Calculated Gibbs energies in gas phase at 1 atm and 273 K.

Formanilide hydrogenation by the trans- and cis-dihydride Fe complex

The carbonyl hydrogenation of formanilide by cis-dihydride Fe complex (${}^t\text{PrPN}^{\text{H}}\text{P}\text{Fe}(\text{H})_2(\text{CO})$) is *ca* 9 kcal mol⁻¹ higher than by the trans isomer **1** (Figure S6). Based on this result, the cis-isomer was not investigated further.

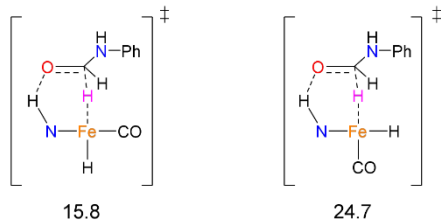


Figure S6. Transition states for the carbonyl hydrogenation of formanilide by the trans- and cis-dihydride of ${}^t\text{PrPN}^{\text{H}}\text{P}\text{Fe}(\text{H})_2(\text{CO})$. Gibbs energies in THF (SMD) at 30 atm and 373 K are given in kcal mol^{-1} . **1 + amide** is used as zero of energies.

Hemiaminal intramolecular proton transfer

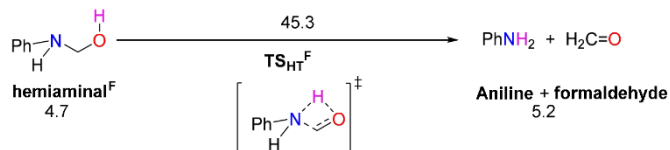


Figure S7. Non-assisted intramolecular protonolysis of the C–N bond of the formanilide-derived hemiaminal (labeled by a superscript F). Gibbs energies in THF (SMD) at 30 atm and 373 K are given in kcal mol⁻¹. Formanilide + H₂ is used as zero of energies.

Formanilide assisted protonolysis of the C–N bond of the O-bound hemiaminal

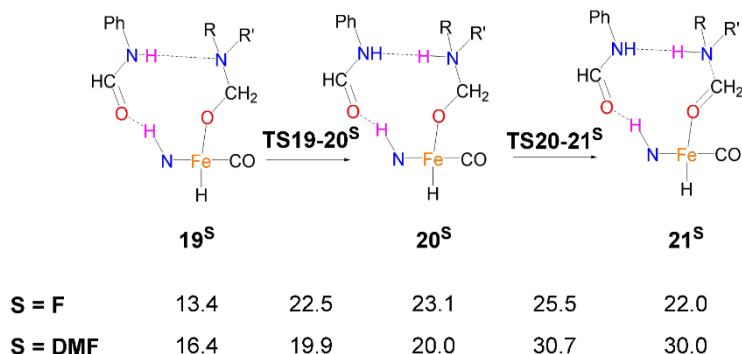


Figure S8. Reaction pathway for the protonolysis of the C–N bond of the O-bound hemiaminal with the assistance of formanilide in THF (SMD) at 30 atm and 373 K, Gibbs energies in kcal mol⁻¹. R = Ph and R' = H for F, R = R' = Me for DMF.

Inclusion of this mechanism in the microkinetic model of formanilide, in addition to the pathways showed in Scheme 5, increases conversion by only 0.2 % (from 1.5% to 1.7%) and by 9.9 % when removing adduct formation (from 25.8% to 35.7%). Including energy corrections in **TS20-21^F** and in the adduct formation, as done for **TS15-16^F**, does not increase conversion to 99% (8.5% by decreasing the energy of **TS20-21^F** to 22.5 kcal mol⁻¹, and 63.1 % by also increasing the energy of the adduct by 2 kcal mol⁻¹).

DMF calculated maximum conversion.

The maximum conversion of DMF was obtained from x , which is the final concentration of methanol at the equilibrium. x was derived from the equilibrium constant (K_{eq}), which was calculated from the ΔG of the reaction (-1.52 kcal mol⁻¹). As in the microkinetic model, we assumed a constant concentration of $[H_2] = 0.162$ M.

$$\frac{[Amine][Methanol]}{[H_2]^2[Amide]} = K_{eq}$$

$$\frac{x \cdot x}{0.162^2 \cdot (1.4 - x)} = 7.767$$

$$x^2 + 0.204 - 0.285 = 0$$

$$x = 0.442$$

$$\Delta G = -R \cdot T \cdot \ln K_{eq}$$

$$-1.52 \text{ kcal mol}^{-1} = -1.9872 \cdot 10 \text{ kcal mol}^{-1} \cdot K^{-1} \cdot 373.15 \text{ K} \cdot \ln K_{eq}$$

$$\ln K_{eq} = 2.050$$

$$K_{eq} = 7.767$$

$$\text{Conv.} = \frac{[Methanol]_f}{[Amide]_0} \cdot 100$$

$$\text{Conv.} = \frac{0.442}{1.4} \cdot 100$$

$$\text{Conv.} = 31.57 \%$$

G, H, and -TS energies.

Table S1. Relative energies of all stationary points in kcal mol⁻¹.

Label	G	H	-TS	Comments
1	0	0	0	
H₂	0	0	0	
Formanilide	0	0	0	
DMF	0	0	0	
2	10.2	21.5	-11.4	
3	10.6	6.7	3.8	
4	6.8	-5.0	11.9	
5	-2.0	-5.1	3.1	

6	-0.5	-7.1	6.5	
7F	5.0	-7.9	12.8	
8F	15.1	1.3	13.8	
9F	15.7	4.2	11.6	
10F	9.7	-11.1	20.8	
11F	25.6	3.6	22.0	
12F	25.5	4.5	21.0	
13F	19.8	-2.3	22.1	
14F	12.4	-1.3	13.7	
15F	19.2	2.6	16.6	
16F	17.7	15.6	2.1	(16F + Formaldehyde)
	2.5	-7.3	9.8	(16F + MeOH)
17F	13.3	-3.8	17.1	(17F + Formaldehyde)
	-2.0	-26.7	24.8	(17F + MeOH)
19F	13.4	-12.1	25.6	
20F	23.1	-4.0	27.1	
21F	22.0	-2.2	24.2	
7DMF	3.9	-8.0	11.9	
8DMF	22.5	8.6	13.9	
9DMF	21.8	9.2	12.7	
10DMF	12.5	-8.7	21.2	
11DMF	20.8	-0.6	21.4	
12DMF	23.2	1.8	21.4	
13DMF	24.3	4.5	19.8	
14DMF	16.5	2.4	14.1	
15DMF	24.6	8.4	16.1	
18DMF	23.8	15.5	8.3	
19DMF	16.4	-9.9	26.3	
20DMF	22.7	-4.3	27.0	
21DMF	30.0	6.7	23.4	
TS2-1	21.8	24.2	-2.5	
TS2-3	14.2	9.0	5.2	
TS3-6	13.0	7.6	5.4	
TS4-1	12.2	-0.8	13.0	
TS7-8F	15.8	1.1	14.7	
TS8-9F	16.9	1.9	15.1	
TS10-11F	31.2	8.7	22.5	
TS11-12F	25.7	3.4	22.3	
TS13-1F	30.6	8.1	22.5	
TS14-2F	33.1	20.1	13.0	
TS15-16F	24.9	11.0	13.9	
TS16-2F	27.7	24.3	3.4	(TS + Formaldehyde)
	12.4	1.4	11.1	(TS + MeOH)
TS16-17F	15.8	-1.2	17.0	(TS + Formaldehyde)
	0.6	-24.1	24.7	(TS + MeOH)

TS19-20F	22.5	-6.1	28.6	
TS20-21F	25.5	-1.2	26.7	
TS7-8DMF	23.1	9.1	14.0	
TS8-9DMF	23.4	8.4	15.1	
TS10-11DMF	19.1	-4.0	23.0	
TS11-12DMF	22.6	0.1	22.5	
TS13-18DMF	30.4	9.3	21.1	
TS14-2DMF	39.9	29.8	10.1	
TS15-16DMF	41.0	26.2	14.7	
TS19-20DMF	19.9	-8.5	28.4	
TS20-21DMF	30.7	7.0	23.7	
TSHTF	45.3	35.9	9.4	
TSHTDMF	42.7	33.2	9.4	
TSCNDMF	22.7	14.3	8.3	
HemiaminalF	14.9	18.0	-3.1	(HemiaminalF + 2)
	4.7	-3.6	8.3	
HemiaminalDMF	20.6	22.9	-2.3	(HemiaminalDMF + 2)
	10.5	1.4	9.1	
Formaldehyde				
Aniline	5.2	8.5	-3.3	(Aniline + Formaldehyde)
	15.4	30.1	-14.7	(Aniline + Formaldehyde + 2)
Dimethylamine	13.7	17.1	-3.4	(Dimethylamine + Formaldehyde)
	23.9	38.7	-14.7	(Dimethylamine + Formaldehyde + 2)
MeOH	-10.1	-14.4	4.3	(MeOH + Aniline)
	-1.5	-5.8	4.3	(MeOH + Dimethylamine)

References

- (1) Becke, A. D. Density-Functional Thermochemistry. III. The Role of Exact Exchange. *J. Chem. Phys.* **1993**, *98*, 5648–5652.
- (2) Adamo, C.; Barone, V. Toward Reliable Density Functional Methods without Adjustable Parameters: The PBE0 Model. *J. Chem. Phys.* **1999**, *110*, 6158–6170.
- (3) Tao, J.; Perdew, J. P.; Staroverov, V. N.; Scuseria, G. E. Climbing the Density Functional Ladder: Nonempirical Meta-generalized Gradient Approximation Designed for Molecules and Solids. *Phys. Rev. Lett.* **2003**, *91*, 3–6.
- (4) Zhao, Y.; Truhlar, D. G. The M06 Suite of Density Functionals for Main Group Thermochemistry, Thermochemical Kinetics, Noncovalent Interactions, Excited States, and Transition Elements: Two New Functionals and Systematic Testing of Four M06-Class Functionals and 12 Other Function. *Theor. Chem. Acc.* **2008**, *120*, 215–241.
- (5) Chai, J.-D.; Head-Gordon, M. Long-Range Corrected Hybrid Density Functionals with Damped Atom–atom Dispersion Corrections. *Phys. Chem. Chem. Phys.* **2008**, *10*, 6615.
- (6) Becke, A. D. Density-Functional Exchange-Energy Approximation with Correct Asymptotic Behavior. *Phys. Rev. A* **1988**, *38*, 3098–3100.
- (7) Lee, C.; Yang, W.; Parr, R. G. Development of the Colle-Salvetti Correlation-Energy Formula into a Functional of the Electron Density. *Phys. Rev. B* **1988**, *37*, 785–789.
- (8) Miehlich, B.; Savin, A.; Stoll, H.; Preuss, H. Results Obtained with the Correlation Energy Density Functionals of Becke and Lee, Yang and Parr. *Chem. Phys. Lett.* **1989**, *157*, 200–206.
- (9) Perdew, J. P.; Burke, K.; Ernzerhof, M. Generalized Gradient Approximation Made Simple. *Phys. Rev. Lett.* **1996**, *77*, 3865–3868.
- (10) Zhao, Y.; Truhlar, D. G. A New Local Density Functional for Main-Group Thermochemistry, Transition Metal Bonding, Thermochemical Kinetics, and Noncovalent Interactions. *J. Chem. Phys.* **2006**, *125*.
- (11) Zhang, Y.; MacIntosh, A. D.; Wong, J. L.; Bielinski, E. A.; Williard, P. G.; Mercado, B. Q.; Hazari, N.; Bernskoetter, W. H. Iron Catalyzed CO₂ Hydrogenation to Formate Enhanced by Lewis Acid Co-Catalysts. *Chem. Sci.* **2015**, *6*, 4291–4299.
- (12) Hay, P. J.; Wadt, W. R. Ab Initio Effective Core Potentials for Molecular Calculations. Potentials for the Transition Metal Atoms Sc to Hg. *J. Chem. Phys.* **1985**, *82*, 270–283.
- (13) Wadt, W. R.; Hay, P. J. Ab Initio Effective Core Potentials for Molecular Calculations. Potentials for Main Group Elements Na to Bi. *J. Chem. Phys.* **1985**, *82*, 284–298.
- (14) Hehre, W. J.; Ditchfield, R.; Pople, J. a. Self—Consistent Molecular Orbital Methods. XII. Further Extensions of Gaussian—Type Basis Sets for Use in Molecular Orbital Studies of Organic Molecules. *J. Chem. Phys.* **1972**, *56*, 2257–2261.
- (15) Francil, M. M.; Pietro, W. J.; Hehre, W. J.; Binkley, J. S.; Gordon, M. S.; DeFrees, D. J.; Pople, J. A.

- Self-Consistent Molecular Orbital Methods. XXIII. A Polarization-Type Basis Set for Second-Row Elements. *J. Chem. Phys.* **1982**, *77*, 3654–3665.
- (16) Krishnan, R.; Binkley, J. S.; Seeger, R.; Pople, J. A. Self-Consistent Molecular Orbital Methods. XX. A Basis Set for Correlated Wave Functions. *J. Chem. Phys.* **1980**, *72*, 650–654.
- (17) McLean, A. D.; Chandler, G. S. Contracted Gaussian Basis Sets for Molecular Calculations. I. Second Row Atoms, Z=11-18. *J. Chem. Phys.* **1980**, *72*, 5639–5648.
- (18) Purvis, G. D.; Bartlett, R. J. A Full Coupled-Cluster Singles and Doubles Model: The Inclusion of Disconnected Triples. *J. Chem. Phys.* **1982**, *76*, 1910–1918.
- (19) Dunning, T. H. Gaussian Basis Sets for Use in Correlated Molecular Calculations. I. The Atoms Boron through Neon and Hydrogen. *J. Chem. Phys.* **1989**, *90*, 1007–1023.
- (20) Woon, D. E.; Dunning, T. H. Gaussian Basis Sets for Use in Correlated Molecular Calculations. III. The Atoms Aluminum through Argon. *J. Chem. Phys.* **1993**, *98*, 1358–1371.
- (21) Balabanov, N. B.; Peterson, K. A. Systematically Convergent Basis Sets for Transition Metals. I. All-Electron Correlation Consistent Basis Sets for the 3d Elements Sc-Zn. *J. Chem. Phys.* **2005**, *123*.
- (22) Marenich, A. V.; Cramer, C. J.; Truhlar, D. G. Universal Solvation Model Based on Solute Electron Density and on a Continuum Model of the Solvent Defined by the Bulk Dielectric Constant and Atomic Surface Tensions. *J. Phys. Chem. B* **2009**, *113*, 6378–6396.
- (23) Gaussian 09 2.
- (24) Hoops, S.; Gauges, R.; Lee, C.; Pahle, J.; Simus, N.; Singhal, M.; Xu, L.; Mendes, P.; Kummer, U. COPASI - A COMplex PAthway SIMulator. *Bioinformatics* **2006**, *22*, 3067–3074.
- (25) Jayaratne, U.; Zhang, Y.; Hazari, N.; Bernskoetter, W. H. Selective Iron-Catalyzed Deaminative Hydrogenation of Amides. *Organometallics* **2017**, *36*, 409–416.
- (26) Brunner, E. Solubility of Hydrogen in 10 Organic Solvents at 298.15, 323.15, and 373.15 K. *J. Chem. Eng. Data* **1985**, *30*, 269–273.
- (27) Petzold, L. Automatic Selection of Methods for Solving Stiff and Nonstiff Systems of Ordinary Differential Equations. *SIAM J Sci Stat Comput* **1983**, *4*, 136–148.
- (28) NIST <https://webbook.nist.gov/chemistry/>.

Paper II

Artús Suàrez, L.; Jayarathne, U.; Balcells, D; Bernskoetter, W. H.; Hazari, N.; Jaraiz, M.; Nova, A. *Chem. Sci.*, **2020**, *11*, 2225-2230

EDGE ARTICLE

[View Article Online](#)
[View Journal](#) | [View Issue](#)


Cite this: *Chem. Sci.*, 2020, **11**, 2225

All publication charges for this article have been paid for by the Royal Society of Chemistry

Received 25th July 2019
 Accepted 17th January 2020
 DOI: 10.1039/c9sc03812d
rsc.li/chemical-science



Rational selection of co-catalysts for the deaminative hydrogenation of amides[†]

Lluís Artús Suàrez,^a Upul Jayarathne,^{‡b} David Balcells,^a Wesley H. Bernskoetter,^b Nilay Hazari,^c Martín Jaraiz,^{d,e} and Ainara Nova^{a,f,*af}

The catalytic hydrogenation of amides is an atom economical method to synthesize amines. Previously, it was serendipitously discovered that the combination of a secondary amide co-catalyst with (ⁱPr²PNP)Fe(H)(CO) (ⁱPr²PNP = NICH₂CH₂(P*i*Pr₂)₂⁻), results in a highly active base metal system for deaminative amide hydrogenation. Here, we use DFT to develop an improved co-catalyst for amide hydrogenation. Initially, we computationally evaluated the ability of a series of co-catalysts to accelerate the turnover-limiting proton transfer during C–N bond cleavage and poison the (ⁱPr²PNP)Fe(H)(CO) catalyst through a side reaction. TBD (triazbicyclodecene) was identified as the leading co-catalyst. It was experimentally confirmed that when TBD is combined with (ⁱPr²PNP)Fe(H)(CO) a remarkably active system for amide hydrogenation is generated. TBD also enhances the activity of other catalysts for amide hydrogenation and our results provide guidelines for the rational design of future co-catalysts.

Introduction

The selective hydrogenation of carbonyl complexes is one of the most important and widely used catalytic reactions in organic synthesis.^{1–3} However, the reduction of electron rich carboxylic acid derivatives, such as amides, is still difficult.^{4,5} The ubiquity of the amide functional group in biological systems, pharmaceuticals, and industrial chemicals⁶ has spurred considerable effort to create efficient catalytic systems for amide hydrogenation. Nevertheless, amides are still typically reduced using waste generating stoichiometric reagents, such as LiAlH₄, and to date only a small number of homogenous catalysts can

directly hydrogenate amides to amines.^{5,7–12} These catalysts, which include both precious and base metal systems, provide proof-of-principle that this atom economic transformation is possible, but can still be improved.¹

Current mechanistic models for transition metal catalyzed amide reduction, in particular deaminative hydrogenation to produce an amine and an alcohol, propose a sequential reduction of the amide to an intermediate hemiaminal (step 1, Scheme 1), which then undergoes C–N bond cleavage to yield an amine and an aldehyde (step 2). Subsequent hydrogenation of the aldehyde affords the corresponding alcohol (step 3).^{13,14}

Most well-defined catalysts for deaminative hydrogenation rely on a Noyori-type,^{14,15} bifunctional pathway whereby a metal-hydride and adjacent ligand based proton are delivered to the carbonyl C=O moiety (Scheme 1). Intriguingly, recent mechanistic studies indicate that while the Noyori-type catalyst structure is essential for facilitating the dihydrogen addition steps of the process (1 and 3, in Scheme 1), the proton transfer between the O- and N-ends of the hemiaminal (step 2), which

^aHylleraas Centre for Quantum Molecular Sciences, Department of Chemistry, University of Oslo, P. O. Box 1033, Blindern, N-0315 Oslo, Norway. E-mail: ainara.nova@kjemi.uio.no

^bDepartment of Chemistry, University of Missouri, Columbia, Missouri, 65211, USA

^cDepartment of Chemistry, Yale University, P. O. Box 208107, New Haven, Connecticut, 06520, USA

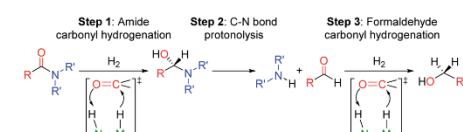
^dDepartment of Electronics, ETSIT, University of Valladolid, Paseo Belén 15, 47011 Valladolid, Spain

^eIU CINQUIMA, University of Valladolid, Paseo de Belén 7, 47011 Valladolid, Spain

^fDepartment of Chemistry, UiT-The Arctic University of Norway, N-9037 Tromsø, Norway

[†] Electronic supplementary information (ESI) available: Experimental details (including procedure for co-catalyst screening and synthesis of (ⁱPr²PNP)RuH(CO)(HCONPh)) and computational details (including information on the microkinetic models with DMF and 4-formylmorpholine, results obtained with diphenylformanilide, and optimized coordinates). CCDC 1943231. For ESI and crystallographic data in CIF or other electronic format see DOI: 10.1039/c9sc03812d

[‡] These authors contributed equally to this study.



Scheme 1 Proposed reaction steps for the deaminative hydrogenation of amides to amines and methanol catalyzed by Noyori type catalysts represented as N(H)–M(H).

triggers the cleavage of the C–N bond, does not involve necessarily the metal catalyst.¹³ In addition, step 2 is the turnover-limiting step, indicating that novel methods to facilitate hemiaminal cleavage are required to improve catalytic amide hydrogenation.

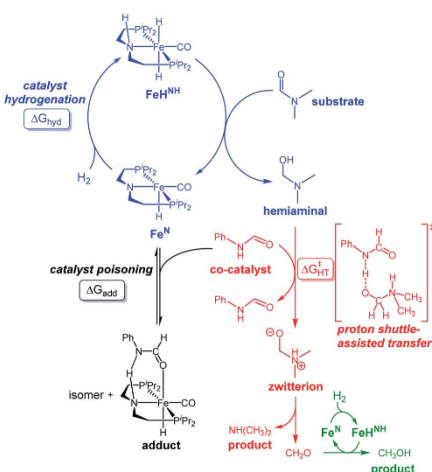
Our laboratories have previously investigated amide hydrogenation catalyzed by the iron(II) complex, (¹⁸PNP)Fe(H)(CO) (¹⁸PNP = N[CH₂CH₂(P*i*Pr)₂]₂⁻) (Fe^N) using both computational and experimental methods (Scheme 2).^{5,13} In deaminative amide hydrogenation using Fe^N, a key serendipitous finding was that the reaction is promoted by a co-catalytic amount of a secondary amide (formamide in Scheme 2). This effect was particularly pronounced in the hydrogenation of tertiary alkyl amides, such as DMF, which are important because they are key intermediates in the homogeneous hydrogenation of CO₂ to methanol mediated by amines.^{16,17} The interplay of the two amide equivalents (*i.e.* one reactant and one co-catalyst) adds complexity to the mechanism. Computational studies indicate that the secondary amide lowers the barrier to the proton transfer that occurs in hemiaminal C–N bond cleavage ($\Delta G_{\text{HT}}^{\ddagger}$, in Scheme 2) because the NH moiety acts as a proton-shuttle.¹³ However, the use of a secondary amide as a co-catalyst has two major pitfalls: (1) secondary amides can form stable adducts with Fe^N (ΔG_{add} , in Scheme 2) *via* 1,2-addition across the iron–amide bond, which lowers the concentration of the active species in catalysis; and (2) the amide co-catalyst can be consumed during the reaction, which undermines its contribution as a co-catalyst and introduces a product separation problem.⁵ Here, we use a rational approach involving DFT

calculations to design co-catalysts tailored for the deaminative hydrogenation of tertiary amides. Our best co-catalyst, triazabicyclodecene (TBD), acts as push-pull proton shuttle for C–N bond cleavage, and leads to significant improvement in iron catalyzed deaminative amide hydrogenation. Importantly, the improvement from TBD also occurs for a number of other transition metal catalysts for deaminative amide hydrogenation, suggesting that the addition of co-catalysts of this type is a general strategy for improving amide reduction.

Results and discussion

Computational co-catalyst design

On the basis of the mechanism shown in Scheme 2, DFT calculations were performed on a series of potential organic co-catalysts for the hydrogenation of DMF using Fe^N (Table 1; see ES[†] for computational details). The co-catalysts assessed included molecules with either single site hydrogen bond donors (entries 4–7 and 10) or with both hydrogen bond donor and acceptor sites which could act as push–pull proton shuttles (entries 1–3, 8 and 11). Various aryl and alkyl substituents (*i.e.* H, Me, ¹Pr, ²Bu, Ph) were introduced into the pool of co-catalysts, to sample a wide range of stereoelectronic effects. In molecules with C=O or C=N functional groups, only electron-rich systems were chosen to minimize the hydrogenation of the co-catalyst. Although there are co-catalysts that are hydrogenated when used as reactants (*e.g.* formanilide and acetamide),⁵ when they are used in catalytic concentrations their consumption is slower than that of the reactants, enabling their co-catalytic effect.¹³ The ability of each potential co-catalyst to assist with the hemiaminal proton transfer^{5,18,19} involved in the C–N bond cleavage (step 2 in Scheme 1) was quantified by computing the transition state(s) associated with this process ($\Delta G_{\text{HT}}^{\ddagger}$; Scheme 2 and Fig. 1), which can be either concerted (with TBD, methanol and morpholine) or step-wise (all other co-catalysts). In the latter, the N-protonation of the hemiaminal is followed by its O-deprotonation, which is rate-limiting for all co-catalysts except urea. The thermodynamic preference of the co-catalyst to trap the iron complex was quantified by computing the free energy for the formation of the off-cycle adducts from Fe^N (ΔG_{add} ; Scheme 2 and Fig. 1). In this framework, all co-catalysts were screened with the aim of finding an optimal balance between a low $\Delta G_{\text{HT}}^{\ddagger}$ and a thermoneutral or endergonic value of ΔG_{add} . Catalyst hydrogenation (ΔG_{hyd} ; Scheme 2) competes with adduct formation and, thus, there is an interplay between the free energies of both reactions. In the case of Fe^N, ΔG_{hyd} (which will depend on the nature of the catalyst) was calculated to be $-10.2 \text{ kcal mol}^{-1}$ under the experimental conditions.¹³ The value of $\Delta G_{\text{add}} - \Delta G_{\text{hyd}}$ (ΔG_p , in Table 1) is therefore a measure of how adduct formation may limit the reaction by catalyst poisoning (*i.e.* a more positive value is indicative of less deactivation). For example, the production of methanol may be expected to inhibit catalysis by adduct formation with Fe^N (entry 7; $\Delta G_{\text{add}} = -6.9 \text{ kcal mol}^{-1}$). However, catalyst hydrogenation is even more favorable ($\Delta G_{\text{hyd}} = -10.2 \text{ kcal mol}^{-1}$) making the FeH^{NH} the likely preferred species ($\Delta G_p = 3.3 \text{ kcal mol}^{-1}$).



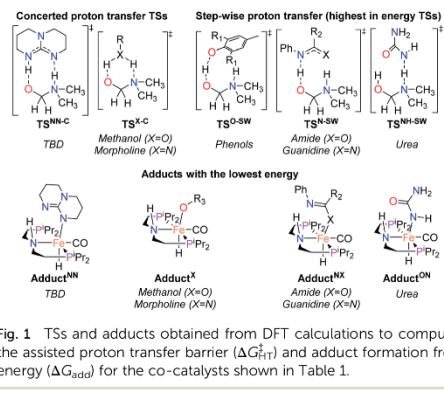
Scheme 2 Reaction mechanism for the deaminative hydrogenation of amides by Noyori-type catalysts. Isomer = Fe N-bound form of the adduct. Color code: hemiaminal formation (blue), C–N cleavage by proton transfer (red), formaldehyde hydrogenation (green) and adduct formation (black).

Table 1 Evaluation of co-catalysts for the hydrogenation of tertiary amides with Fe^{N}

Entry	Co-catalyst	$\Delta G_{\text{HT}}^{\ddagger}$ ^a	ΔG_{add}^b	ΔG_{P}^c	TON ^d	Conv. ^d
1	TBD	21.3	-1.5	8.7	830	59%
2	<chem>*N(*)C(=O)C</chem>	25.3	-8.3	1.9	780	55%
3	<chem>*N(*)C(=O)C</chem>	22.6	-12.2	-2.0	630	45%
4	<chem>*c1ccc(O)c(C)c1</chem>	24.3	-11.5	-1.3	—	—
5	<chem>*c1ccc(O)c(C)c1</chem>	21.8	-11.4	-1.2	—	—
6	<chem>*c1ccc(O)c(C)c1</chem>	25.5	4.4	14.6	560	40%
7	<chem>CH3OH</chem>	29.6	-6.9	3.3	510	37%
8	<chem>*N(*)N(*)C(=O)C</chem>	22.3	-9.3	1.4	440	31%
9	No additive	—	—	—	320	22%
10	<chem>*N1CCOC1</chem>	34.6	8.0	18.2	320	22%
11	<chem>NH2NH2C(=O)NH2</chem>	35.3	-8.8	1.4	90	6%

^a $\Delta G_{\text{HT}}^{\ddagger}$ (in kcal mol⁻¹) corresponds to the calculated energy of the proton-transfer transition state with the highest energy for DMF assisted by the co-catalysts (Scheme 2, Fig. 1). ^b ΔG_{add} (in kcal mol⁻¹) corresponds to the calculated energy for the formation of the adduct (isomer with the lowest energy) formed by $[\text{Fe}^{\text{N}}]$ with the co-catalysts (Scheme 2, Fig. 1). ^c $\Delta G_{\text{P}} = \Delta G_{\text{add}} - \Delta G_{\text{hyd}}$ (-10.2 kcal mol⁻¹ for all co-catalysts). ^d Experimental reaction conditions: 30 atm H₂, 5 μmol of $[\text{Fe}^{\text{N}}]$ (0.07 mol%), (1.75 mol%) of each additive and 7 mmol of 4-formylmorpholine in 5 mL of THF at 100 °C for 2 h. TON and conv. were determined by GC-FID analysis of the products and remaining starting material. Each entry is the average of two or more trials.

The DFT calculations using DMF as a model substrate yielded optimal results for TBD (triazabicyclodecene) as a co-catalyst (Table 1, entry 1). The basic and rigid character of the guanidine scaffold provides a low proton transfer barrier ($\Delta G_{\text{HT}}^{\ddagger} = 21.3$ kcal mol⁻¹), facilitating the C–N bond cleavage of the hemiaminal intermediate. Additionally, TBD yielded a ΔG_{add} close to zero (-1.5 kcal mol⁻¹) and the second largest $\Delta G_{\text{add}} - \Delta G_{\text{hyd}}$ (8.7 kcal mol⁻¹), suggesting that the formation of the adduct does not compete with the hydrogenation of the amide. 1,2,3-Triphenylguanidine (entry 8) yielded a similar $\Delta G_{\text{HT}}^{\ddagger}$ barrier, but with a more negative ΔG_{add} value

**Fig. 1** TSs and adducts obtained from DFT calculations to compute the assisted proton transfer barrier ($\Delta G_{\text{HT}}^{\ddagger}$) and adduct formation free energy (ΔG_{add}) for the co-catalysts shown in Table 1.

(-9.3 kcal mol⁻¹), likely due to its lower basicity compared to TBD. Acetanilide (entry 2) also afforded promising results, in this case showing that replacement of H by Me in the originally reported formanilide co-catalyst (entry 3) changes $\Delta G_{\text{add}} - \Delta G_{\text{hyd}}$ from negative to positive, meaning lower competition of the adduct formation towards amide hydrogenation. Among single site hydrogen bond donors, phenols (entries 4–6) exhibited some promise as a proton shuttle, although sterically large substituents were required to alleviate formation of iron adducts (**Adduct^{NN}**, Fig. 1). Interestingly, morpholine and urea yield the largest energy barrier of all of the co-catalysts (34.6 and 35.3 kcal mol⁻¹, respectively). This result suggests that a purely basic co-catalyst, although beneficial to prevent adduct formation, does not assist with the hemiaminal proton transfer. Overall, the computational results indicate that the best co-catalysts are those which provide spatially separated hydrogen bond donor and acceptor sites which can act as push-pull proton shuttles, together with a basic character and/or steric bulky groups to prevent the formation of adducts.

The high co-catalytic activity predicted for TBD (entry 1) was further analyzed by performing microkinetic modelling^{20–22} using the complex reaction network we previously found for amide hydrogenation (see ESI†).¹³ Under the conditions typically used experimentally (1.4 M of DMF, 0.02 M of TBD, 1 mM of Fe^{N} and fixed concentration of 0.162 M of H₂, at 100 °C),⁵ the microkinetic model yielded a high conversion of 27% over a short reaction time of 2 hours. This conversion is substantially higher than the conversion with formanilide as co-catalyst (12%). The same trend was observed by using 4-formylmorpholine as the substrate (see ESI†),²³ a benchmark tertiary amide used in our prior studies on Fe^{N} -catalyzed catalyzed deaminative hydrogenation. In this case, the conversions with TBD and formanilide were 56% and 46%, respectively.

Experimental co-catalyst and catalyst testing

The computational predictions of co-catalyst efficacy were examined experimentally using 4-formylmorpholine (Table 1).

Each potential co-catalyst was tested in catalytic trials with a 1.75 mol% loading, along with 0.07 mol% Fe^N under previously optimized conditions.⁵ Due to the high activity of the catalyst, the variable amount of time required to manipulate the pressure vessel between trials, and the need to equilibrate the vessel at the reaction temperature, it was not possible to acquire reliable initial rate measurements (conversions < 10%). Instead, reaction times were limited to 2 hours to minimize conversion and provide kinetically relevant comparisons. The reaction progress was monitored by amide conversion because of chromatographic issues in quantifying the morpholine product. However, no signals other than starting materials, morpholine and methanol were observed by GC-FID. As predicted by DFT, TBD proved a remarkable co-catalyst, affording a greater than two fold enhancement in TON (compare entries 1 and 9) over the short reaction time. Examination of the influence of TBD loading from 0 to 250 μmol (see ESI; Fig. S7†) indicated a strong correlation between TON and [TBD], saturating at approximately 200 μmol . The computational results also successfully predicted the relative ability of the other co-catalysts. For additives in which ΔG_p is positive, the best co-catalysts should be those which lower the ΔG_{Hf} involved in the hemiaminal C–N bond cleavage, as illustrated in entries 1, 2, 6 and 7. In cases where iron deactivation is problematic due to a large negative ΔG_{add} , then the key barrier to amide hydrogenation is approximated by the total energy difference between $\Delta G_{\text{add}} - \Delta G_{\text{hyd}}$ and ΔG_{Hf} , which explains the superior performance of acetanilide over formanilide (entries 2 and 3). The only discernable variation from this trend is the unexpectedly poor performance of 1,2,3-triphenylguanidine (entry 8), which may react in a different manner as indicated by an immediate color change upon treatment with Fe^N . The use of urea in the reaction appeared to inhibit the reaction (lower conversion than without additive), which is likely due to other irreversible reactions with the iron species or difficulties in drying the very hydroscopic parent amide. Still, our rational co-catalyst design has led to the identification of a remarkably active catalytic system for selective amide hydrogenation.

The few homogenous transition metal catalysts reported for deaminative hydrogenation are all proposed to follow similar pathways (Scheme 1), with Noyori-type bifunctional mechanisms being prominent.^{14,15} Given the importance of non-metal mediated hemiaminal cleavage in our computed mechanism, we hypothesized that the co-catalytic enhancements observed here with Fe^N should be generalizable to other systems. Indeed, highly active ruthenium catalysts recently reported by Beller and Sanford^{24–26} also exhibit substantial enhancement in activity upon co-catalytic addition of TBD or formanilide (Table 2). The (¹⁰ $\text{P}\text{N}^{\text{H}}\text{P}$) $\text{Ru}(\text{H})(\text{CO})(\text{BH}_4)$ ($\text{RuBH}_4^{\text{NH}}$) precatalyst (¹⁰ $\text{P}\text{N}^{\text{H}}\text{P}$ = $\text{HN}[\text{CH}_2\text{CH}_2(\text{PPh}_2)]_2$) exhibited a near 4-fold increase in TON for 4-formylmorpholine hydrogenation over a short 2 hour reaction time in the presence of TBD, making it one of the most active systems for hydrogenation of this benchmark substrate. In this case, formanilide inhibits the reaction by forming a stable ruthenium adduct (Fig. S6†). In contrast, with the (PNN) $\text{Ru}(\text{H})(\text{CO})(\text{BH}_4)$ (Ru^{PNN}) (PNN = 3-(di-*tert*-butylphosphino)-*N*-(1-methyl-1*H*-imidazol-2-*I*)methyl]propylamine)

Table 2 Comparison of co-catalysts for amide hydrogenation with pincer supported group 8 catalysts^a

Catalyst	Co-catalyst	TON ^b	Conv. ^b
Fe^N	None	320	23%
	TBD	830	59%
	HCONHPh	630	45%
$\text{RuBH}_4^{\text{NH}}$	None	310	22%
	TBD	1200	86%
	HCONHPh	0 ^c	0 ^c
Ru^{PNN}	None	440	31%
	TBD	1170	84%
	HCONHPh	1040	74%

^a Reaction conditions: 30 atm H_2 , 5 μmol of [Fe or Ru] (0.07 mol%), 125 μmol of co-catalyst, and 7 mmol of 4-formylmorpholine in 5 mL of THF at 100 °C for 2 h. For [Ru] co-catalysts 10 μmol of NEt_3 was added to activate the catalyst. ^b Determined by GC-FID analysis of the products and remaining starting material. Each entry is the average of two or more trials. ^c Formanilide reacts irreversibly with this Ru catalyst to form an adduct, see ESI for details.

precatalyst, the relative difference in performance between TBD and formanilide is not as large, likely because the steric bulk of the *tert*-butyl substituents on the phosphine donors lowers the stability of a formanilide adduct.

The co-catalytic effect of TBD with Fe^N across different classes of amides was also investigated experimentally (Table 3). Examples of dialkyl and diaryl formamides (entries 1 and 2) exhibited significant enhancement in TON in the presence of TBD compared to the reaction without co-catalyst. *N*-Phenylacetamide (entry 3), a substrate that previously proved challenging for Fe^N , was also hydrogenated with greater productivity in the presence of TBD. However, no enhancement was observed upon TBD treatment of the corresponding benzamide (entry 4). This may be due to steric limitation at the carbonyl moiety created by the larger phenyl substituent. In this case, substituting TBD for a smaller co-catalyst provided a modest increase in TON. These results suggest the co-catalytic effect of TBD and related shuttles may be effective with more diverse amides. Admittedly, the enhancement observed with diphenylformanilide was initially unexpected because a mechanism involving the iron-catalyst instead of formanilide, was previously proposed for the hemiaminal C–N bond cleavage using aryl amide substrates.¹³ However, the calculated ΔG_{Hf} using the



Table 3 Co-catalytic enhancement of amide hydrogenations using TBD^a

Entry	Substrate	[TBD]	TON ^b
1		0 1.75	50 300
2		0 0.45	1150 5180
3		0 1.75	140 230
4		0 1.75 1.75 ^c	120 120 250 ^c

^a Reaction conditions: 60 atm H₂, 5 µmol of [Fe] (0.07 mol%), x µmol of TBD, and 7 mmol of substrate in 5 mL of THF at 120 °C for 16 h. ^b TON was determined by GC-FID and NMR analysis of the products and remaining starting material. Each entry is the average of three or more trials. ^c TBD was substituted by N-phenylacetamide (Table 1; entry 2).

understanding provide new opportunities for the catalytic hydrogenation of challenging electron-rich carbonyl compounds.

Conflicts of interest

There are no conflicts to declare.

Acknowledgements

LL. A., D. B. and A. N. thank the support from the Research Council of Norway (FRINATEK Grant No. 250044 and Center of Excellence Grand No. 262695), the Norwegian Metacenter for Computational Science (NOTUR, nn4654k) and NordForsk, (Grand No. 85378). U. J., W. B. and N. H. acknowledge support from the U.S. Department of Energy, Office of Science, Basic Energy Sciences, Catalysis Science Program (DE-SC0018222).

Notes and references

- J. Magano and J. R. Dunetz, *Org. Process Res. Dev.*, 2012, **16**, 1156–1184.
- G. Zhang and S. K. Hanson, *Chem. Commun.*, 2013, **49**, 10151–10153.
- G. Zhang, B. L. Scott and S. K. Hanson, *Angew. Chem., Int. Ed.*, 2012, **51**, 12102–12106.
- A. M. Smith and R. Whyman, *Chem. Rev.*, 2014, **114**, 5477–5510.
- U. Jayarathne, Y. Zhang, N. Hazari and W. H. Bernskoetter, *Organometallics*, 2017, **36**, 409–416.
- G. Arthur, *The Amide Linkage: Selected Structural Aspects in Chemistry, Biochemistry, and Materials Science*, Wiley-Interscience, Hoboken, 1st edn, 2000.
- S. Kar, A. Goepert, J. Kothandaraman and G. K. S. Prakash, *ACS Catal.*, 2017, **7**, 6347–6351.
- D. G. Gusev, *ACS Catal.*, 2017, **7**, 6656–6662.
- E. Balaraman, B. Gnanaprakasam, L. J. W. Shimon and D. Milstein, *J. Am. Chem. Soc.*, 2010, **132**, 16756–16758.
- J. M. John and S. H. Bergens, *Angew. Chem., Int. Ed.*, 2011, **50**, 10377–10380.
- M. Beller, W. Baumann, E. Alberico, H.-J. J. Drexler, J. R. Cabrero-Antonino, H. Junge, K. Junge, E. Alberico, H.-J. J. Drexler, W. Baumann, K. Junge, H. Junge and M. Beller, *ACS Catal.*, 2016, **6**, 47–54.
- J. A. Garg, S. Chakraborty, Y. Ben-David and D. Milstein, *Chem. Commun.*, 2016, **52**, 5285–5288.
- L. Artú Suárez, Z. Culakova, D. Balcells, W. H. Bernskoetter, O. Eisenstein, K. I. K. Goldberg, N. Hazari, M. Tilset and A. Nova, *ACS Catal.*, 2018, **8**, 8751–8762.
- P. A. Dub and J. C. Gordon, *Nat. Rev. Chem.*, 2018, **2**, 396–408.
- L. Alig, M. Fritz and S. Schneider, *Chem. Rev.*, 2018, **119**, 2681–2751.
- S. Kar, J. Kothandaraman, A. Goepert and G. K. S. Prakash, *J. CO₂ Util.*, 2018, **23**, 212–218.
- C. Tang, K. Sordakis, H. Junge, M. Beller, L. K. Vogt, G. Laurenczy and P. J. Dyson, *Chem. Rev.*, 2017, **118**, 372–433.

Fig. 2 Gibbs energies associated with the C–N bond cleavage TSs for diphenylformamide assisted by Fe^N and the TBD co-catalyst.

diphenylformanilide hemiaminal intermediate and TBD is lower ($\Delta G^\ddagger = 21.8 \text{ kcal mol}^{-1}$) than the barrier for the iron-assisted mechanism ($\Delta G^\ddagger = 28.6 \text{ kcal mol}^{-1}$, see Fig. 2). This result is in agreement with the enhanced reactivity observed for the hydrogenation of diphenylformanilide using TBD as co-catalyst (see Fig. 2).

Conclusions

In conclusion, this work establishes the basis for co-catalyst optimization in amide deaminative hydrogenation reactions using Noyori-type catalysts. Key factors in the co-catalyst design include a push-pull motif of hydrogen bonding sites to assist the C–N bond cleavage of the hemiaminal and controlled acidity and steric hindrance to prevent catalyst poisoning. Notably, these design principles yielded co-catalysts enhancing the activity of systems based on different transition metals. The generality of the co-catalyst effect and its mechanistic

- 18 A. Wakatsuki, Y. Kabe, M. Matsumoto, N. Watanabe and H. K. Ijuin, *Tetrahedron Lett.*, 2018, **59**, 971–977.
- 19 B. Yuan, R. He, W. Shen, Y. Xu, X. Liu and M. Li, *ChemistrySelect*, 2016, **1**, 2971–2978.
- 20 The microkinetic model was performed using COPASI 4.22 software.
- 21 S. Hoops, R. Gauges, C. Lee, J. Pahle, N. Simus, M. Singhal, L. Xu, P. Mendes and U. Kummer, *Bioinformatics*, 2006, **22**, 3067–3074.
- 22 M. Besora and F. Maseras, *Wiley Interdiscip. Rev.: Comput. Mol. Sci.*, 2018, **1372**, 1–13.
- 23 Microkinetic models show that 4-formylmorpholine reacts in a similar manner than DMF (see ESI†).
- 24 C. Bornschein, K. P. J. Gustafson, O. Verho, M. Beller and J. E. Bäckvall, *Chem.-Eur. J.*, 2016, **22**, 11583–11586.
- 25 R. Adam, E. Alberico, W. Baumann, H. J. Drexler, R. Jackstell, H. Junge and M. Beller, *Chem.-Eur. J.*, 2016, **22**, 4991–5002.
- 26 N. M. Rezayee, C. A. Huff and M. S. Sanford, *J. Am. Chem. Soc.*, 2015, **137**, 1028–1031.

Electronic Supplementary Information

**Rational Selection of Co-Catalysts for the Deaminative Hydrogenation of
Amides**

Lluís Artús Suàrez, Upul Jayarathne, David Balcells, Wesley Bernskoetter,* Nilay Hazari,
Martín Jaraiz, Ainara Nova*

Table of Contents:

Experimental Details

<i>General procedure and sample spectra for screening the co-catalytic effect</i>	S2
<i>Synthesis of $(^3\text{h}PNP)\text{RuH}(\text{CO})(\text{HCONPh})$</i>	S4
<i>Comparative influence of base activator and co-catalysts</i>	S6
<i>Discussion of aldehyde hydrogenation</i>	S7
<i>Influence of [TBD] on Catlaysis</i>	S7

Computational Details

<i>Microkinetic models</i>	S9
<i>Gibbs energies of organic reaction intermediates</i>	S13
<i>Amide influence in ΔG_{HT}^\ddagger</i>	S13
<i>Cartesian coordinates of optimized geometries, and corresponding corrected Gibbs energies</i>	S14

References

S45

S1

Experimental Details

All manipulations were carried out using standard vacuum, Schlenk line, canula or glovebox techniques. Hydrogen was purchased from Airgas and used as received. The catalysts **Fe^N** and **Ru^{PNN}** were prepared as previously described.^{1,2} All other chemicals including **RuBH₄^{NH}** were purchased from Aldrich, Fisher, VWR, Strem or Cambridge Isotope Laboratories. Amide substrates and additives were purified by sublimation and distillation or vacuum transfer after drying over appropriate drying agents.³ All other non-volatile solids were dried under vacuum at 50 °C. Solvents were dried and deoxygenated using literature procedures.³ ¹H, ¹³C and ³¹P NMR spectra were recorded on Bruker 300 MHz DRX, 500 MHz DRX or 600 MHz spectrometers at ambient temperature, unless otherwise noted. ¹H and ¹³C chemical shifts are referenced to residual solvent signals; ³¹P chemical shifts are referenced to an external standard of H₃PO₄. Probe temperatures were calibrated using ethylene glycol and methanol as previously described.⁴ High pressure catalytic hydrogenation reactions were performed using a Parr 5500 series compact reactor with glass insert.

General procedure and sample spectra for screening the co-catalytic effect

Inside a glovebox, the catalyst (5 µmol) was added as a solution to a glass reactor liner (50 mL). Then amide (7 mmol) and 5 mL of THF were added in succession using a micro syringe. Subsequently, the relevant additive (25 µmol) was added and the Parr reactor sealed and removed from the glovebox. The reactor was pressurized with Commercial grade hydrogen at ambient temperature (450 psi) and heated (100 °C) with mechanical stirring. After 2h heating was stopped, and the reactor was immediately immersed in to a cold ice bath and the H₂ was slowly vented. The products and the remaining reactants were analysed by ¹H NMR spectroscopy or GC FID using mesitylene as an internal standard. GC Method: 0.418 mL of mesitylene was added to the reaction solution and the final volume was adjusted to 10 mL by adding THF. An aliquot of 0.02 mL from this mixture was diluted to 0.2 mL and analyzed using a Thermo Fisher GC (Trace 1300; Column – TG 5MS AMINE 30m x 0.25 mm x 0.25 µm; start at 40 °C, ramp 25 °C. hold 2 min). Response factors were calculated using standards. NMR Method: The reaction solution was diluted either to 10 mL or 9 mL. An aliquot of 0.1 mL was mixed with 0.05 mL of 1M mesitylene to prepare the NMR sample.

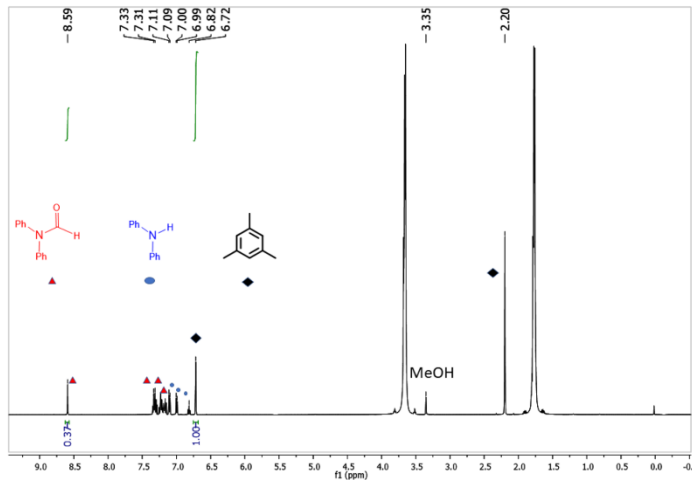
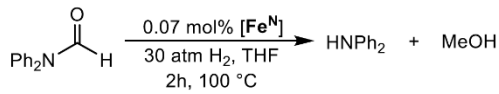


Figure S1: Sample ¹H NMR spectrum of product solution from hydrogenation of diphenylformamide using **Fe^N** with no additives. The labelled peaks identify the species present. Two large solvent peaks for residual THF are also observed.

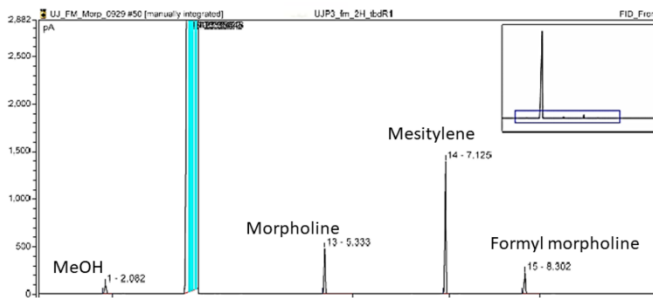
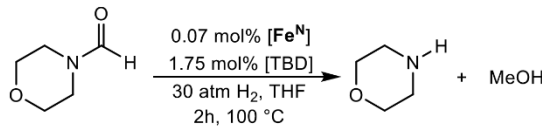


Figure S2: Sample GC-FID chromatogram of product solution from the hydrogenation of formylmorpholine using **Fe^N** in the presence of TBD. The labelled peaks identify the species present along with the off scale solvent signal.

Synthesis of (^{P_b}PN^HP)RuH(CO)(HCONPh)

Inside the glovebox, a sample of **RuBH₄NH** (0.023 g, 0.039 mmol) was transferred to a J-Young tube using 1 mL of THF. Then a solution of NEt₃ in THF (1M, 0.117 mL, 0.117 mmol) was added to the reaction mixture, followed by HCONHPh in THF (1M, 0.043 mL, 0.043 mmol). A drop of deuterated benzene was added, and the tube was tightly closed before it was removed from the glovebox. This mixture was heated at 50 °C and the reaction monitored using ³¹P NMR spectroscopy until it reached completion. After that, the tube was taken back in to the glovebox and all the volatiles were evaporated under reduced pressure. A near colorless solid was obtained and crystals suitable for X-ray diffraction were obtained by slow diffusion of pentane into a concentrated THF solution of the product. Yield: 0.013 g (40 %). ¹H NMR (THF-*d*₈; 50 MHz, 23 °C) (two isomers observed): major isomer: 10.98 (s, 1H, N-H), 8.02 (s, 1H, HCO, overlap with PhH), 8.02(s, 4H, PhH), 7.41(m 10H, PhH), 7.32(br 1H, PhH), 7.26(q,t, 6H, PhH), 6.43(m 2H, PhH), 5.55(d, 2H, PhH), 3.35 (m, 2H, CH₂), 3.02 (t, 2H, CH₂), 2.87 (d, 2H, CH₂), 2.16 (m, 2H, CH₂), -14.24 (t, 1H, Fe-H); ³¹P{¹H} NMR (THF-*d*₈): 58.955; ¹³C{¹H} NMR (THF-*d*₈): δ 174.07 (s, HCO), 137.69-137.43 (m, PhH), 135.14 (s, PhH), 132.39 (s, PhH), 130.67 (s, PhH), 129.47-128.75 (m, PhH), 127.22 (s, PhH), 125.67 (s, PhH), 121.34 (s, PhH), 52.17 (t, CH₂), 32.89 (t, CH₂).

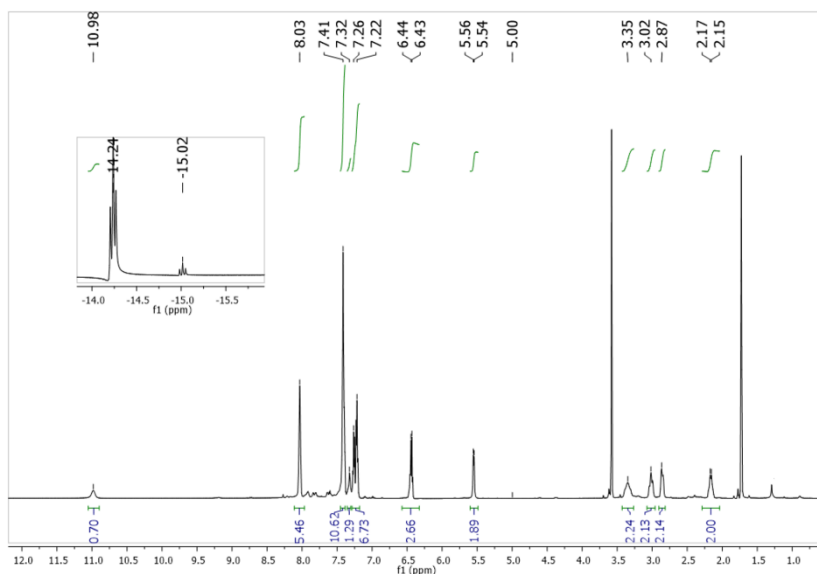


Figure S3: ¹H NMR of (^{P_b}PN^HP)RuH(CO)(HCONPh) (two isomers observed) in THF-*d*₈.

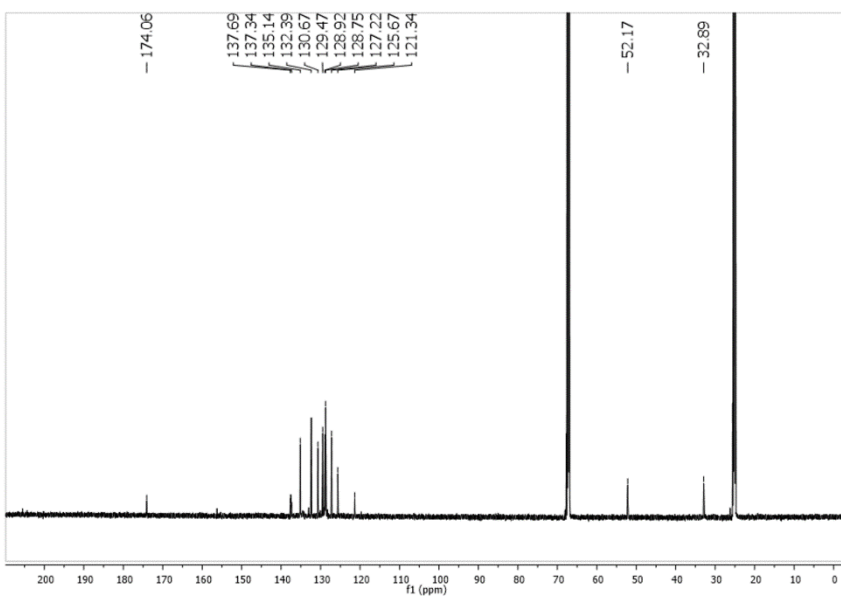


Figure S4: $^{13}\text{C}\{\text{H}\}$ NMR of $(^{\text{Ph}}\text{P}\text{N}^{\text{H}}\text{P})\text{RuH}(\text{CO})(\text{HCONPh})$ in $\text{THF}-d_8$.

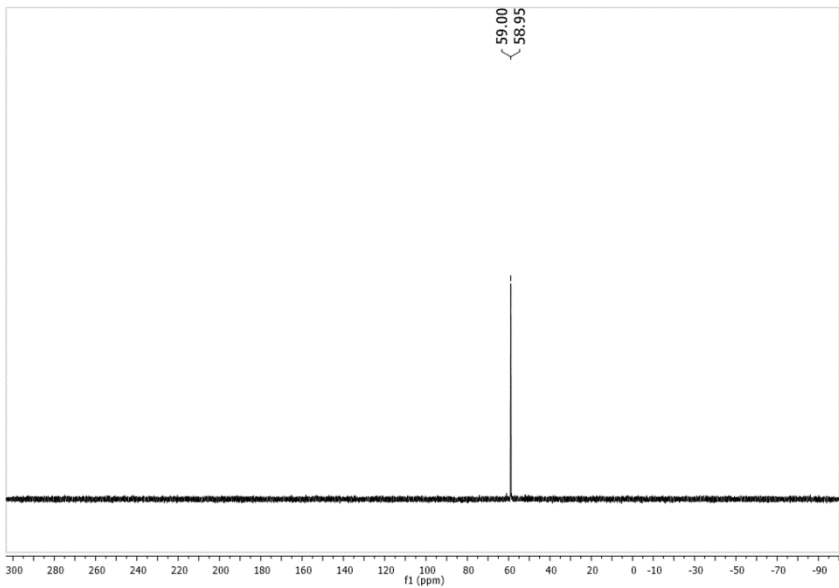


Figure S5: $^{31}\text{P}\{\text{H}\}$ NMR of $(^{\text{Ph}}\text{P}\text{N}^{\text{H}}\text{P})\text{RuH}(\text{CO})(\text{HCONPh})$ (two isomers observed) in $\text{THF}-d_8$.

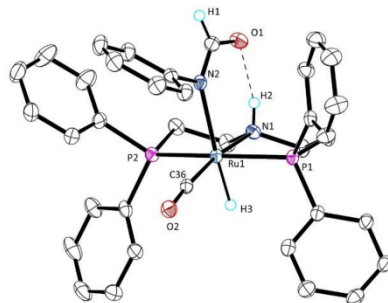
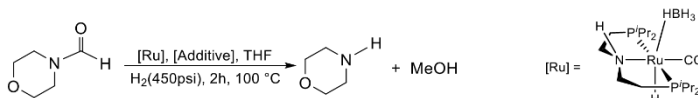


Figure S6: Molecular structure of (^{Ph}PNH₂P)RuH(CO)(HCONPh) with thermal ellipsoids at 50% probability. Hydrogen atoms and an additional formanilide molecule, co-crystallized with the complex, have been removed for clarity. Selected bond lengths (Å) and angles (deg): Ru(1)–N(2) 2.236(2), Ru(1)–P(2) 2.3082(8), Ru(1)–P(1) 2.3203(8), Ru(1)–N(1) 1.195 (2); P(1)–Ru(1)–P(2) 163.64(3), N(2)–Ru(1)–N(1) 93.01 (9).

Comparative influence of base activator and co-catalysts

Table S1 distinguished the possible roles of the co-catalyst in promoting C–N scission and acting as a base activator. Entries 1 and 2 suggest that TBD can work as an activator, presumably by scavenging BH₃ from (^{Ph}PNH₂P)RuH(CO)(BH₄). Significantly, comparison of the entries 2, 4, 5 and 6 suggest that the effect of a base catalyst activator saturates at 2 eq per metal and that the influence of TBD as a co-catalyst for C–N bond scission far exceeds any potential influence from acting as a simple catalyst activator.

Table S1: Influence of base activator and co-catalysts on 4-formylmorpholine hydrogenation using (^{Ph}PNH₂P)RuH(CO)(BH₄).^a



Entry	NEt ₃	TBD	HCONHPh	2,6-diisopropyl-4-methylphenol	TON ^b (Con %)
1	2 eq	25 eq	-----	-----	1200 (86%)
2	-----	25 eq	-----	-----	1040 (74%)
3	2 eq	-----	-----	25 eq	822 (59%)
4	2 eq	-----	-----	-----	310 (22%)
5	25 eq	-----	-----	-----	290 (21%)
6	-----	-----	-----	-----	210 (15%)
7	2 eq	-----	25 eq	-----	NR (0%)

^a Reaction conditions: 30 atm H₂(~ 450 psi), 5 μmol of [Ru] (0.018 mol %), 125 μmol of each additive, 10 or 125 μmol of NEt₃ and 7 mmol of formyl morpholine in 5 mL of THF at 100 °C for 2 h. ^b Determined using GC-FID analysis of the products and remaining starting material. Each entry is average of two or more trials.

Discussion of aldehyde hydrogenation

The microkinetic modeling of the catalytic reaction suggests that the intermediate aldehyde is hydrogenated rapidly under the reaction conditions and plays little or no role in the reaction rate (See Reaction 4; Table S2). In the case of formylmorpholine hydrogenation, the intermediate aldehyde is formaldehyde. Given the difficulty in obtaining dry formaldehyde in a non-polymer form we have substituted benzaldehyde for a comparison of the hydrogenation of aldehydes and formamides. Using 0.07 mol% of Fe^{N} , 100 °C, and 30 atm H₂ in THF, both formylmorpholine and benzaldehyde are hydrogenated to nearly full conversion (>96%). However, although both reactions give high conversion, the uptake of hydrogen gas is noticeably different. The benzaldehyde reaction ceased uptake of hydrogen after *ca* 30 mintues while formylmorpholine continued to consume hydrogen for *ca* 90 minutes. While these observations are insufficient to establish reliable rate measurements they confirm the computational conclusions that aldehyde hydrogenation is a viable intermediate step in catalysis and that it is facile relative to formamide hydrogenation.

Influence of [TBD] on Catalysis

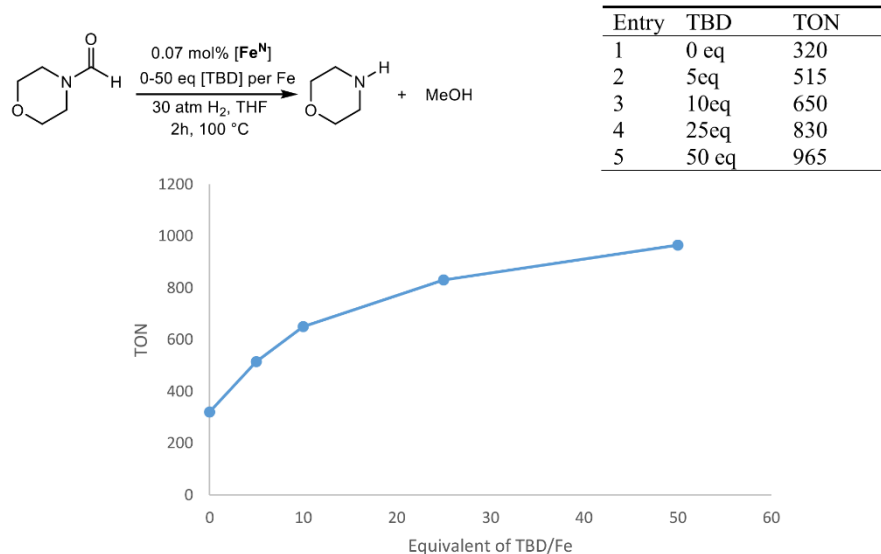


Figure S7: Correlation between TBD loading and TON for formylmorpholine hydrogenation. Experimental conditions: 30 atm H₂ (~450 psi), 5 μmol of Fe^{N} (0.07 mol %), 0-250 μmol of TBD, and 7 mmol of formyl morpholine in 5 mL of THF at 100 °C for 2h. TON determined using GC-FID analysis of the products and remaining starting material. Each point is average of two or more trials.

Computational Details

DFT calculations were carried out with the Gaussian09 software package.⁵ The hybrid meta-GGA M06⁶ functional was selected on the basis of geometry and energy benchmarks.⁷ Structures were fully optimized without any geometry or symmetry constraints, combining the double-z LANL2DZ (on Fe and Ru, including relativistic effects)^{8,9} and 6-31+G** (on all other elements)^{10,11} basis sets. Vibrational frequencies were computed at the same level of theory to classify all stationary points as either saddle points (transition states, with a single imaginary frequency) or energy minima (reactants, intermediates and products, with only real frequencies). These calculations were also used to obtain the thermochemistry corrections (zero-point, thermal and entropy energies) at the experimental p = 30 atm and T = 373 K conditions. The energy of the optimized geometries was refined by single point calculations with triple-z quality basis sets, including the LANL2TZ^{8,9} on Fe and the 6-311+G** on all other elements.¹² The energies reported in the text were obtained by adding the thermochemistry corrections to the refined potential energies. The solvation effects of THF were included in both the geometry optimizations and energy refinements using the continuum SMD model.¹³ The ultrafine (99,590) grid was used in all calculations to increase numerical accuracy and to facilitate convergence. Microkinetic models were carried out with the COPASI 4.22 software.¹⁴ A data set collection of input files and computational results is available in the ioChem-BD repository¹⁵ and can be accessed online via <https://dx.doi.org/10.19061/iochem-bd-6-14>.

The mechanism proposed in Scheme 2 is the result of a thorough mechanistic investigation of the deaminative hydrogenation of DMF by Fe^N .⁷ In this study several mechanisms proposed for the hydrogenation of esters were investigated with fomanilide and DMF. The conclusion of this study was that the mechanism for the hemiaminal C–N bond protonolysis (Step 2 in Scheme 1) depends on the substrate (formanilide or DMF) and the presence of reagents able to assist the proton transfer. In the case of DMF, formanilide could act as a co-catalyst to assist in protonolysis. In contrast, when formanilide is the reactant, the protonolysis is assisted by Fe^N . This difference originates from the basicity of the $-\text{NMe}_2$ group in DMF, which deprotonates formanilide, while NPhH is difficult to protonate but can form an imido intermediate with the Fe-catalyst.

Microkinetic models:

Microkinetic models were constructed to: (1) predict catalytic activity upon using TBD as co-catalyst instead of formanilide, with (¹⁰PNP)Fe(H)(CO) (**Fe^N**) and DMF, and (2) account for the experimental conversions observed with 4-formylmorpholine as substrate.

Microkinetic models were constructed with the COPASI software¹⁴ (version 4.22). Association reactions were assumed to have low energy barriers ($\Delta G^\ddagger \leq 5$ kcal mol⁻¹), and thus have no impact on the global kinetics of the reaction. The initial concentrations used in the simulations were those reported in the corresponding experiments¹⁶ (1.4 M of amide, 1mM of catalyst, 0.162 M of hydrogen and 25 mM of co-catalyst). The concentration of hydrogen was kept constant, in line with the effectively constant pressure of hydrogen used in the reactor (30 atm). H₂ concentration was approximated using the molar fraction of H₂ in a saturated solution of H₂ in THF at 33.4 atm and 100 °C (0.01461 H₂ mol / solution mol) assuming incompressibility of THF and that [H₂] << [THF].¹⁷ As in the experiments, simulations were carried out for a total time of 2 hours at T = 373 K. The models were based on deterministic time course simulations with the LSODA algorithm.¹⁸

1) DMF with formanilide and TBD as co-catalysts

The DMF conversion vs time traces using **Fe^N** and formanilide or TBD as co-catalysts were obtained by running a microkinetic model based on the mechanism reported in our previous work⁷ (Figure S8). The elementary steps of the mechanism underlying the microkinetic model are given in Figure S9, together with the ΔG^\ddagger values derived from the DFT calculations published in our previous work⁷ and presented in Table S2. This model predicts conversions of 12 and 27% for the formanilide and TBD-assisted reactions respectively. The formation of the 1,2-addition adduct with between **Fe^N** and the product MeOH (reaction 11) was included in the microkinetic model to evaluate the influence of this reaction on DMF conversion. However, the % conversion with and without this reaction were the same, suggesting that the adduct formation with MeOH is not relevant in this process.

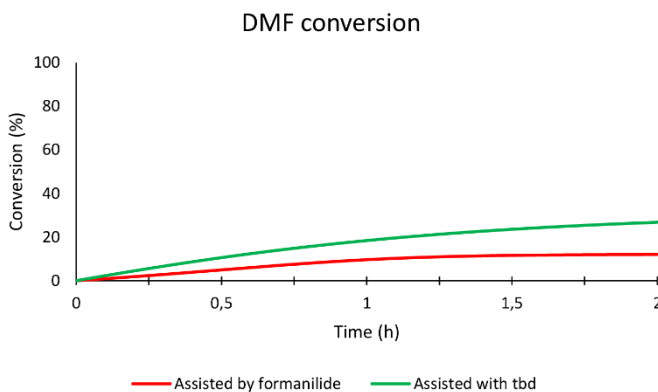


Figure S8: Microkinetic simulations of assisted DMF deaminative hydrogenation.

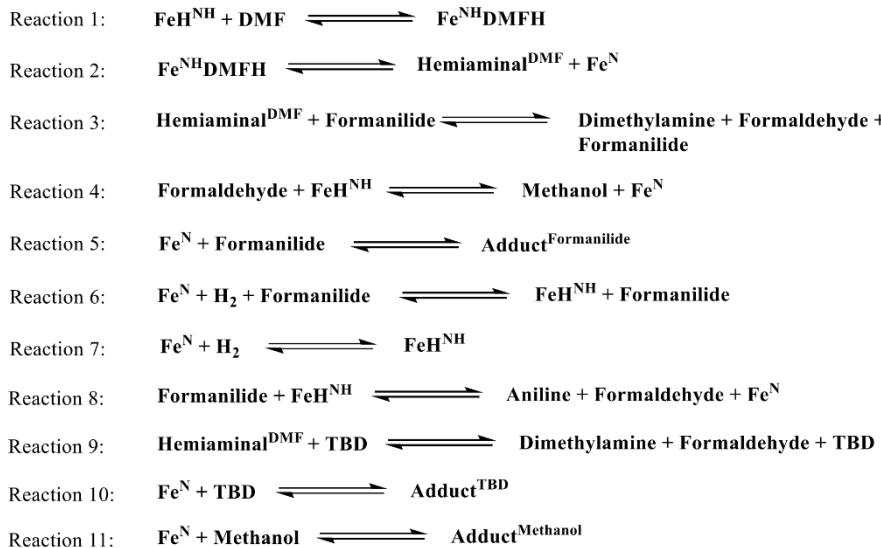


Figure S9: Implemented reactions in the DMF microkinetic simulations.

	ΔG^\ddagger Forward (kcal mol ⁻¹)	ΔG^\ddagger Backwards (kcal mol ⁻¹)
Reaction 1	23.1	0.6
Reaction 2	0.9	2.8
Reaction 3	13.5	10.3
Reaction 4	6.0	11.1
Reaction 5	4.0	16.2
Reaction 6	4.0	14.2
Reaction 7	11.6	21.8
Reaction 8	21.9	6.5
Reaction 9	13.5	10.3
Reaction 10	4.0	5.4
Reaction 11	5.0	11.9

Table S2: Reactions and corresponding Gibbs energies (kcal mol⁻¹) used in the microkinetic model of the deaminative hydrogenation of DMF.

2) 4-formylmorpholine with formanilide and TBD as co-catalyst

The conversions of 4-formylmorpholine *vs* time catalyzed by Fe^N and using formanilide and TBD as co-catalysts (Figure S10), were obtained by running the microkinetic model shown in Figure S6. In this case, the energies of reactions 1, 2, 3 and 9 were replaced by reactions 12, 13, 14 and 15 (Figure S11), in which 4-formylmorpholine is used instead of DMF (see Table S3). This model predicts conversions of 46 and 56% for the formanilide and TBD-assisted reactions respectively. Experimental conversions of 4-formylmorpholine hydrogenation with 25 eq of formanilide or TBD as co-catalyst could be fitted by correcting the energy of methanol by \pm 0.2 kcal mol⁻¹. The similar energies obtained for the reactions 1, 2, 3 and 9 using DMF and 11, 12, 13 and 14 using morpholidine indicate that the same mechanism is expected for the two substrates.

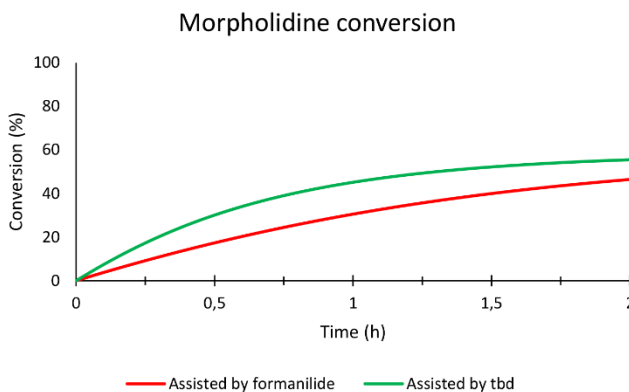


Figure S10: Microkinetic simulations of assisted 4-formylmorpholine deaminative hydrogenation



Figure S11: Reactions used together with 4, 5, 6, 7, 8, 10 and 11 to perform the 4-formylmorpholine microkinetic simulations.

	ΔG^\ddagger Forward (kcal mol ⁻¹)	ΔG^\ddagger Backwards (kcal mol ⁻¹)
Reaction 12	22.5	1.5
Reaction 13	0.5	2.5
Reaction 14	14.6	11.0
Reaction 15	14.6	11.0

Table S3: Reactions and corresponding Gibbs energies (kcal mol⁻¹) used in the microkinetic model of the deaminative hydrogenation of DMF.

Gibbs energies of organic reaction intermediates

The formation of hemiaminal and formaldehyde intermediates from DMF and 4-formylmorpholine is endergonic in both cases by ca 10 kcal/mol (see Figure S12). Therefore their concentration in solution is expected to be very low (eg: 0.1 μ M of hemiaminal according to the microkinetic model). This may explain why these species are not observed in the crude ^1H NMR spectrum.

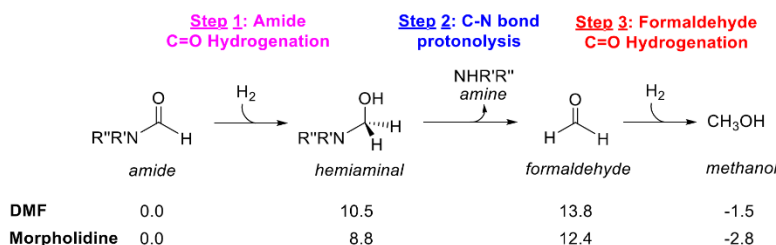


Figure S12: Gibbs energies (in kcal mol^{-1}) for the hydrogenation of DMF ($R' = \text{Me}$, $R'' = \text{Me}$) and morpholidine ($R'R'' = \text{O}(\text{CH}_2)_4$) to amines and methanol calculated in THF solvent (SMD) at 30 atm and 373 K.

Amide influence on $\Delta G_{\text{HT}}^\ddagger$

The $\Delta G_{\text{HT}}^\ddagger$ barriers obtained for DMF and 4-formylmorpholine using different co-catalysts were computed to determine the influence of the substrate. As shown in Table S4, similar values were obtained for the three co-catalysts, indicating that DMF can be used as a model for morpholine.

$\Delta G_{\text{HT}}^\ddagger (\text{kcal mol}^{-1})$	TBD	Triphenylguanidine	Methanol
DMF	21.3	22.3	29.6
4-Formylmorpholine	22.6	21.4	28.1
$\Delta G_{\text{HT}}^\ddagger$	N-methylformanilide	Formanilide	
DMF	25.3	22.6	
4-Formylmorpholine	25.4	21.7	

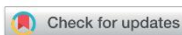
Table S4: Comparison between DMF and 4-formylmorpholine of $\Delta G_{\text{HT}}^\ddagger$ (kcal mol $^{-1}$).

References

- 1 E. A. Bielinski, P. O. Lagaditis, Y. Zhang, B. Q. Mercado, C. Würtele, W. H. Bernskoetter, N. Hazari and S. Schneider, *J. Am. Chem. Soc.*, 2014, **136**, 10234–10237.
- 2 M. Beller, W. Baumann, E. Alberico, H.-J. J. Drexler, J. R. Cabrero-Antonino, H. Junge, K. Junge, E. Alberico, H.-J. J. Drexler, W. Baumann, K. Junge, H. Junge and M. Beller, *ACS Catal.*, 2016, **6**, 47–54.
- 3 M. A. Giardello, R. K. Rosen, R. H. Grubbs, F. J. Timmers and A. B. Pangborn, *Organometallics*, 2002, **15**, 1518–1520.
- 4 J. Sandström, *Dynamic NMR Spectroscopy*, Academic Press, New York, 1982.
- 5 Gaussian 09, Revision D.01, M. J. Frisch, G. W. Trucks, H. B. Schlegel, G. E. Scuseria, M. A. Robb, J. R. Cheeseman, G. Scalmani, V. Barone, B. Mennucci, G. A. Petersson, H. Nakatsuji, M. Caricato, X. Li, H. P. Hratchian, A. F. Izmaylov, J. Bloino, G. Zheng, J. L. Sonnenberg, M. Hada, M. Ehara, K. Toyota, R. Fukuda, J. Hasegawa, M. Ishida, T. Nakajima, Y. Honda, O. Kitao, H. Nakai, T. Vreven, J. A. Montgomery, Jr., J. E. Peralta, F. Ogliaro, M. Bearpark, J. J. Heyd, E. Brothers, K. N. Kudin, V. N. Staroverov, T. Keith, R. Kobayashi, J. Normand, K. Raghavachari, A. Rendell, J. C. Burant, S. S. Iyengar, J. Tomasi, M. Cossi, N. Rega, J. M. Millam, M. Klene, J. E. Knox, J. B. Cross, V. Bakken, C. Adamo, J. Jaramillo, R. Gomperts, R. E. Stratmann, O. Yazev, A. J. Austin, R. Cammi, C. Pomelli, J. W. Ochterski, R. L. Martin, K. Morokuma, V. G. Zakrzewski, G. A. Voth, P. Salvador, J. J. Dannenberg, S. Dapprich, A. D. Daniels, O. Farkas, J. B. Foresman, J. V. Ortiz, J. Cioslowski, and D. J. Fox, Gaussian, Inc., Wallingford CT, 2013., .
- 6 Y. Zhao and D. G. Truhlar, *Theor. Chem. Acc.*, 2008, **120**, 215–241.
- 7 L. Artús Suàrez, Z. Culakova, D. Balcells, W. H. Bernskoetter, O. Eisenstein, K. I. Goldberg, N. Hazari, M. Tilset and A. Nova, *ACS Catal.*, 2018, **8**, 8751–8762.
- 8 P. J. Hay and W. R. Wadt, *J. Chem. Phys.*, 1985, **82**, 270–283.
- 9 W. R. Wadt and P. J. Hay, *J. Chem. Phys.*, 1985, **82**, 284–298.
- 10 W. J. Hehre, R. Ditchfield and J. A. Pople, *J. Chem. Phys.*, 1972, **56**, 2257–2261.
- 11 W. Kohn, A. D. Becke and R. G. Parr, *J. Phys. Chem.*, 1996, **1**, 12974–12980.
- 12 A. D. McLean and G. S. Chandler, *J. Chem. Phys.*, 1980, **72**, 5639–5648.
- 13 A. V. Marenich, C. J. Cramer and D. G. Truhlar, *J. Phys. Chem. B*, 2009, **113**, 6378–6396.
- 14 S. Hoops, R. Gauges, C. Lee, J. Pahle, N. Simus, M. Singhal, L. Xu, P. Mendes and U. Kummer, *Bioinformatics*, 2006, **22**, 3067–3074.
- 15 M. Álvarez-Moreno, C. De Graaf, N. López, F. Maseras, J. M. Poblet and C. Bo, *J. Chem. Inf. Model.*, 2015, **55**, 95–103.
- 16 U. Jayarathne, Y. Zhang, N. Hazari and W. H. Bernskoetter, *Organometallics*, 2017, **36**, 409–416.
- 17 E. Brunner, *J. Chem. Eng. Data*, 1985, **30**, 269–273.
- 18 L. Petzold, *SIAM J Sci Stat Comput*, 1983, **4**, 136–148.

Paper III

Leischner, T.; Artús Suàrez, L.; Spannenberg, A.; Junge, K.; Nova, A.; Beller, M. *Chem. Sci.*, **2019**, *10*, 10566-10576

Cite this: *Chem. Sci.*, 2019, **10**, 10566

All publication charges for this article have been paid for by the Royal Society of Chemistry

Received 12th July 2019
 Accepted 21st September 2019
 DOI: 10.1039/c9sc03453f
rsc.li/chemical-science

Highly selective hydrogenation of amides catalysed by a molybdenum pincer complex: scope and mechanism†

Thomas Leischner,^a Lluís Artús Suárez,^b Anke Spannenberg,^a Kathrin Junge,^a Ainara Nova^{b*} and Matthias Beller^{a*}

A series of molybdenum pincer complexes has been shown for the first time to be active in the catalytic hydrogenation of amides. Among the tested catalysts, Mo-1a proved to be particularly well suited for the selective C–N hydrogenolysis of *N*-methylated formanilides. Notably, high chemoselectivity was observed in the presence of certain reducible groups including even other amides. The general catalytic performance as well as selectivity issues could be rationalized taking an anionic Mo(0) as the active species. The interplay between the amide C=O reduction and the catalyst poisoning by primary amides accounts for the selective hydrogenation of *N*-methylated formanilides. The catalyst resting state was found to be a Mo-alkoxo complex formed by reaction with the alcohol product. This species plays two opposed roles – it facilitates the protolytic cleavage of the C–N bond but it encumbers the activation of hydrogen.

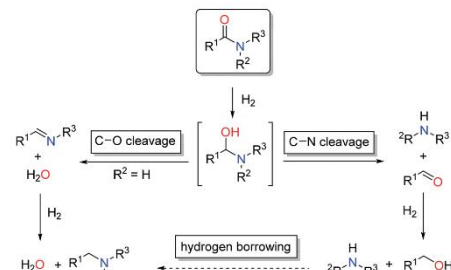
Introduction

The reduction of carboxylic acid derivatives *via* catalytic homogeneous hydrogenation represents an attractive atom-economic and environmentally benign methodology.^{1,2} To date, the vast majority of homogeneous catalysts for these transformations rely on noble metals.³ The limited availability of these elements along with their toxicity and pollutive nature initiated efforts for their replacement. Significant progress in this direction has been achieved in the past decade, in particular with respect to iron,⁴ manganese⁵ and cobalt⁶ based systems. Thus, several examples of base metal catalysed hydrogenations of aldehydes, ketones, carboxylic acids, esters and nitriles have been reported in recent years, some of them with remarkable activities and selectivities.^{2a,7} On the contrary, hydrogenation of amides is known to a much less extent.⁸ The latter can be attributed to the extremely low electrophilicity of the carbonyl group, which renders their hydrogenation particularly challenging.

In general, catalytic hydrogenation of amides can proceed *via* either C–N (hydrogenolysis) or C–O (hydrogenation) bond cleavage of the intermediate hemiaminal (Scheme 1). While the

C–O bond scission results in the formation of the alkylated/benzylated amine with H₂O as the only by-product, the C–N bond cleavage leads to the free amine and the corresponding alcohol. Recently, an additional amide hydrogenation pathway was demonstrated, where the alkylated/benzylated amine is produced by a hydrogen borrowing/autotransfer mechanism from the initially formed alcohol and amine under specific acidic reaction conditions.⁹ Until today, the development of catalytic systems that enable these chemoselective transformations continues to be challenging and therefore are subject of ongoing research.

Initial efforts in this direction mainly focused on homogeneous ruthenium catalysts.¹⁰ Since the inspiring report by Cole-



Scheme 1 Pathways for amide reduction.

^aLeibniz Institut für Katalyse e. V., Albert-Einstein-Straße 29a, Rostock, 18059, Germany. E-mail: Matthias.Beller@catalysis.de

^bHylleraas Centre for Quantum Molecular Sciences, Department of Chemistry, University of Oslo, P.O. Box 1033, Blindern, N-0315, Oslo, Norway. E-mail: Ainara.nova@kjemi.uio.no

† Electronic supplementary information (ESI) available. See DOI: 10.1039/c9sc03453f

Hamilton and co-workers in 2012, various Ru-based systems for the highly selective scission of either the C–N or the C–O bond have been described.¹⁰

In sharp contrast, reports on homogeneous base metal catalysts for this important reaction are particularly scarce. Pioneering work in this area was published by the groups of Milstein, Langer and Sanford only as late as 2016.^{11–13} For the first time, they could demonstrate the ability of certain iron PNP pincer complexes (**Fe-1** as well as **Fe-2a/b**, Scheme 2) to promote the C–N bond cleavage in a number of different amides.

More specifically, Milstein and co-workers reported, that **Fe-1**, after activation with KHMDS, induced the hydrogenolysis of activated aliphatic and aromatic 2,2,2-trifluoroacetamides. However, no reaction was observed, with more common substrates such as *N*-phenylacetamide and *N*-phenylbenzamide.¹¹ The protocols described by Sanford (**Fe-2a**) and Langer (**Fe-2b**) showed more general substrate scopes and obtained notable conversions and yields also for unactivated amides.^{12,13}

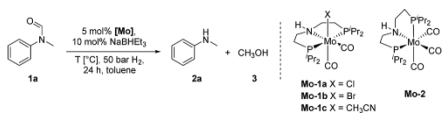
Additionally, Bernskoetter and co-workers showed that the pentavalent iron PNP-pincer complex **Fe-3** is particularly active for the hydrogenolysis of a number of secondary formanilides and *N*-formylmorpholine (Scheme 2). The system stands out due to its extremely low catalyst loading (0.018–0.07 mol%) and notably operates under base-free conditions. Interestingly, the group of Bernskoetter demonstrated that an addition of 20 equivalents of formanilide resulted in a significantly improved activity of the system towards otherwise almost unreactive *N*-methylformanilide. Based on NMR experiments, the authors concluded that the catalyst adopts a different resting state in the presence of the additive (**Fe-4**, Scheme 2) and thus is less prone towards deactivating side reactions.¹⁴ The computational study of this reaction also suggested that the formanilide additive is involved in the C–N bond cleavage of the hemiaminal intermediate, which is the rate limiting step.¹⁵

Recently, our group reported the very first example of a manganese catalysed deaminative hydrogenation of amides

under relatively mild conditions.¹⁶ After activation with exogenous base, the PNN pincer complex **Mn-1** (Scheme 2) exhibits remarkable activity for the hydrogenation of a broad scope of secondary and tertiary amides to the corresponding alcohols and amines. Notably, also more challenging primary amides were successfully cleaved in modest yields, though more forcing conditions were shown to be necessary. The generality of the system was finally highlighted by the cleavage of the amide bond in the herbicide diflufenican. To date, **Mn-1** represents one of the most active and broadly applicable non-noble metal catalysts for amide hydrogenation. In a related study, Prakash and co-workers demonstrated that the manganese PNP pincer complex **Mn-2** is a suitable catalyst for the hydrogenation of formamides. The reaction proceeds *via* cleavage of the C–N bond to produce methanol and the corresponding amine.¹⁷

In 2018, we published the synthesis of a number of structurally related molybdenum PNP pincer complexes. Among the described complexes, **Mo-1a** (Table 1) was shown to be active in the catalytic hydrogenation of different acetophenones and styrenes.¹⁸ Similar Mo-systems have also been used for the hydrogenation of CO₂, imines and nitriles.¹⁹ Based on these reports and our previous work, we became interested in the behaviour of such base-metal catalysts for the reductive cleavage of amides. Herein, we demonstrate its suitability for the hydrogenation of *N*-methylated formanilides under relatively mild conditions. To the best of our knowledge, PNP pincer supported molybdenum complexes have not been described for such transformations. Interestingly, the optimal catalyst

Table 1 Hydrogenation of *N*-methylformanilide **1a** to *N*-methylaniline **2a** and methanol **3** using Mo catalysts **Mo-1a–c** and **Mo-2**



Entry ^{a,b}	[Mo]	T [°C]	Conv. ^c [%]	2a ^c [%]
1	Mo-1a	130	>99	99
2	Mo-1b	130	>99	99
3	Mo-1c	130	>99	99
4	Mo-2	130	10	9
5 ^d	—	130	10	8
6	Mo-1a	100	>99	98
7	Mo-1b	100	>99	99
8	Mo-1c	100	76	73
9	Mo-1a	80	89%	86%
10 ^e	Mo-1b	80	87%	84%
11 ^e	Mo-1a	80	49	47
12 ^e	Mo-1b	80	46	46

^a Standard reaction conditions: *N*-methylformanilide **1a** (67.6 mg, 0.5 mmol), NaBH4 (50 µL, 0.05 mmol, 10 mol%), 2 mL toluene, 50 bar H₂, 24 h. ^b Yield of **3** was not determined. ^c Conversion of **1a** and yield of **2a** were determined by GC using hexadecane as internal standard. ^d No catalyst was used. ^e Reaction was performed with 2.5 mol% of Mo catalyst.

Scheme 2 Base metal catalysts reported for the hydrogenolysis (C–N bond cleavage) of amides.



exhibits a high selectivity for formamides. This preference has been rationalized by means of DFT calculations, which suggest that the produced MeOH reacts with the catalyst and changes the mechanism and rate limiting step of the reaction. This result, which is not observed in related Fe-catalysts, indicates that the catalyst design strategy should be adapted to the nature of the metal centre.

Results and discussion

Catalytic hydrogenation of amides using molybdenum pincer complexes

At the outset of our study, we explored molybdenum-based PNP pincer complexes **Mo-1a–c** and **Mo-2** (Table 1), recently synthesised by our group, as potential catalysts for the hydrogenation of amides. Using *N*-methylformanilide **1a** as benchmark substrate, preliminary experiments were conducted using 5 mol% of Mo catalyst in toluene at 50 bar H₂ and 130 °C, in the presence of 10 mol% of NaBH₃E₃. The reaction proceeded smoothly for complexes **Mo-1a–c** to afford *N*-methylaniline **2a** in quantitative yield along with methanol as the only by-product (Table 1, entries 1–3). However, complex **Mo-2** failed to display any catalytic activity (Table 1, entry 4). Next, the activity of the complexes was tested at reduced temperatures (Table 1, entries 6–10). It was found, that complexes **Mo-1a** as well as **Mo-1b** were equally efficient, when the reaction was conducted at 100 °C. Catalyst **Mo-1c**, however, gave a somewhat lower conversion and yield. Further reduction of the reaction temperature to 80 °C resulted once again in similar conversions and yields for **Mo-1a** and **Mo-1b**, respectively. Based on these observations, the catalyst loading was reduced to 2.5 mol% under otherwise identical reaction conditions (Table 1, entries 11 and 12). It turned out, that changing this parameter also led to almost identical outcomes for both catalytic systems. Therefore we concluded that, under reaction conditions, **Mo-1a** and **Mo-1b** very likely form the same active species. On the basis of the obtained results and due to the more challenging synthesis of **Mo-1b**, we decided to focus on catalyst **Mo-1a** in the due course of the study.

Selecting 80 °C reaction temperature and 5 mol% of **Mo-1a** (Table 1, entry 8) as the optimal setting for further optimization, we tested several different solvents. In contrast to previous work on manganese catalysed hydrogenolysis of amides, toluene was found to give the best results. Cyclohexane yielded slightly lower activities, while *n*-heptane as well as polar solvents, were shown to be significantly less suitable for the attempted transformation (Fig. 1).

Subsequently, we studied the influence of dihydrogen pressure, catalyst loading as well as the amount of additive used on the reaction outcome (Table 1, see ESI†). Lowering the pressure to 30 bar H₂ resulted in a sharp drop in activity. However, no loss of reactivity was observed when the amount of NaBH₃E₃ was decreased to 5 mol%. A rise of the reaction temperature to 100 °C resulted in full conversion of the benchmark substrate to *N*-methylaniline in the presence of 5 mol% NaBH₃E₃ and **Mo-1a**, respectively. Further mitigation of the catalyst loading as well as

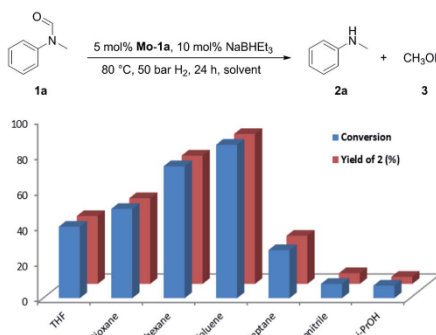


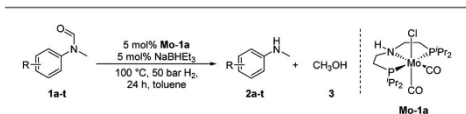
Fig. 1 Study of the solvent effect in the hydrogenation of *N*-methylformanilide **1a** to *N*-methylaniline **2a** and methanol **3** catalysed by **Mo-1a**.

the amount of NaBH₃E₃, however, had negative effects on the catalytic performance of the system.

Having optimised conditions in hand, we proceeded to the application of **Mo-1a** in the hydrogenation of a variety of different *N*-methylformanilides to the corresponding anilines and methanol (Table 2).

Most substrates were hydrogenated in good to excellent yields under optimised conditions at 100 °C and 50 bar H₂ over 24 h, using toluene as solvent. In general, *meta*- and *para*-substitution were well tolerated, while substituents in *ortho*-position (Table 2, entries 19 and 20) appeared to be troublesome, probably due to steric hindrance. Amides containing electron donating groups were less reactive under standard conditions as compared to the benchmark substrate. In some cases higher reaction temperatures were required, in order to achieve good conversions (Table 2, entries 2, 6, 7). Notably, the thiomethyl substituted derivative (Table 2, entry 3) was fully hydrogenated and no catalyst poisoning effect was observed. Moreover, the system tolerated fluoro-substituents (Table 2, entries 8, 17, 20) and no dehalogenation products were detected. Interestingly, the system showed a good functional group tolerance towards substrates containing other reducible moieties such as benzyl ethers, C=C double bonds and esters (Table 2, entries 6, 12, 13). Noteworthy, no double bond isomerisation occurred during the reduction of a stilbene derivative (Table 2, entry 12). Additionally, pyridines, nitriles and nitro arenes remained unaffected under our reaction conditions; however, only poor to modest conversions were observed when the reaction was carried out at 130 °C (Table 2, entries 11, 14, 15). Presumably, this effect originates from substrate coordination to the metal centre and subsequent catalyst deactivation. The system turned out to be sensitive towards halides other than fluorine. Hence, during one of the hydrogenations, small amounts of the dehalogenation product were detected (Table 2, entry 9).

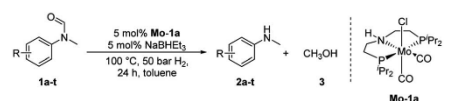
Table 2 Substrate scope in the hydrogenation of *N*-methyl-formanilides to *N*-methylanilines **2** and methanol **3** catalysed by Mo-**1a**



Entry^{a,b} Formamide Conv.^c. (%) Yield^d of **2** (%)

Entry ^{a,b}	Formamide	Conv. ^c . (%)	Yield ^d of 2 (%)
1	1a	>99	94
2 ^e	1b	>99	96
3	1c	>99	95
4	1d	83	80
5	1e	87	84
6 ^e	1f	56	52
7 ^{fg}	1g	46	43
8	1h	98	93
9	1i	40	34 ^f

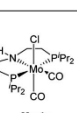
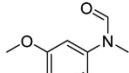
Table 2 (Contd.)



Entry^{a,b} Formamide Conv.^c. (%) Yield^d of **2** (%)

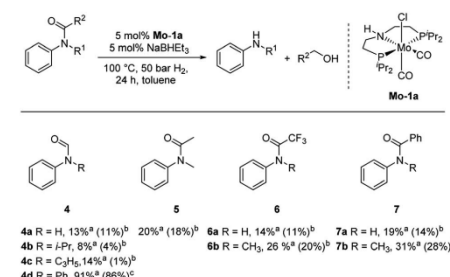
Entry ^{a,b}	Formamide	Conv. ^c . (%)	Yield ^d of 2 (%)
10	1j	>99	>99
11 ^e	1k	52	50
12	1l	95	92
13	1m	>99	97
14 ^e	1n	14	12 ^f
15 ^e	1o	8	6 ^f
16	1p	>99	97
17	1q	>99	98

Table 2 (Contd.)

Entry ^{a,b}	Formamide	Conv. ^c (%)	Yield ^d of 2 (%)	
18		>99	93	
19 ^e		12	9 ^f	
20 ^e		18	15 ^f	

^a Standard reaction conditions: *N*-methylformamide (0.5 mmol), **Mo-1a** (12.5 mg, 5 mol%), NaBH₄Et₃ (50 μL, stock solution 0.5 M in THF, 5 mol%), 2 mL toluene, 50 bar H₂, 24 h. ^b Yield of 3 was not determined. ^c Conversions of *N*-methylformamides were determined by GC using hexadecane as internal standard. ^d Isolated yields. ^e Reaction was carried out at 130 °C. ^f Yields were determined by GC using hexadecane as internal standard. ^g Yield was determined based on the hydrochloride salt.

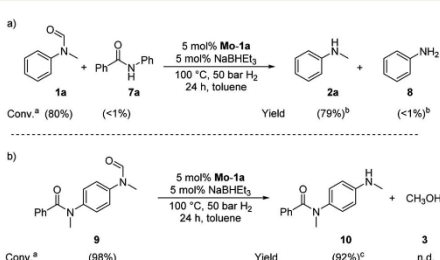
Subsequently, we investigated the more general applicability of our PNP pincer complex **Mo-1a** in the hydrogenation of other amides. Initial experiments focussed on the role of the nitrogen



Scheme 3 Hydrogenation of different amides (4–7) to the corresponding amines and alcohols catalysed by **Mo-1a**. ^aConversions were determined by GC using hexadecane as internal standard. ^bYields were determined by GC using hexadecane as internal standard and refer to anilines, yields of alcohols were not determined. ^cIsolated yields of anilines.

substitution on the reaction outcome. For this purpose, a series of different secondary and tertiary formanilides were subjected to our protocol (Scheme 3). The presence of an NH moiety turned out to be detrimental, as was observed for the parental formanilide (**4a**). This is in sharp contrast with the results obtained with Fe pincer complexes, in which formanilide derivatives give the highest conversion.¹⁴ In order to further validate this, 2,2,2-trifluoroacetanilide (**6a**) and simple benzamidine (**7a**) were employed and results comparable to formanilide (**4a**) were obtained. Likewise, only low conversions and yields were obtained in the case of *N*-iPr- (**4b**) and *N*-allylformanilide (**4c**), respectively. Surprisingly, when *N*-allylformanilide was tested as substrate, the formation of *N*-allylaniline was only observed in traces. The main product was identified to be aniline, thus hinting at a deallylation pathway that additionally takes place to the envisaged hydrogenolysis. In contrast, *N,N*-diphenylformanilide (**4d**) was reduced smoothly and *N,N*-diphenylamine was isolated in excellent yield. Next, the hydrogenation of *N*-methylacetanilide (**5**) and the more activated 2,2,2-N-methyltrifluoroacetanilide (**6b**), respectively, were attempted. In either case, only poor conversions were determined demonstrating the high preference of this complex for specific formanilides. This was further supported by the low reactivity of *N*-methylbenzamidine (**7b**) and some aliphatic formamides (see Table 2, ESI†).

Based on these observations, we were curious to demonstrate selective formamide reduction in the presence of other amide moieties. In a proof of concept experiment, the hydrogenation of the benchmark amide in the presence of benzamide **7a** was conducted (Scheme 4, eqn (a)). It could be shown that **Mo-1a** was capable to cleave *N*-methylformamide (**1a**) with extremely high preference. Notably, the reaction still proceeded with 80% conversion with respect to *N*-methylformamide (**1a**). To further highlight the scope of our system, we designed model substrate **9** combining two amide functionalities in one structure. After 24 h reaction, the intended hydrogenolysis of



Scheme 4 Selective hydrogenations of (a) *N*-methylformamide **1a** in the presence of benzamide **7a** and (b) *N*-methyl-*N*-(4-(*N*-methylformamide)phenyl)benzamide **9**. Standard conditions: substrate(s) 0.5 mmol (each), **Mo-1a** (12.5 mg, 0.025 mmol, 5 mol%), NaBH₄Et₃ (50 μL, 0.5 M stock solution in THF, 0.025 mmol, 5 mol%), toluene (2 mL), 50 bar H₂, 100 °C, 24 h. ^aConversions determined by GC using hexadecane as internal standard. ^bYields determined by GC using hexadecane as internal standard. ^cIsolated yield.



the formamide moiety in **9** had occurred smoothly and the target molecule **10** was isolated in a very high yield (92%). Notably, no cleavage of the benzamide was observed.

We believe these results could pave the way towards new and selective deprotection strategies in organic synthesis mediated by this base metal PNP pincer complex.

Reaction mechanism

In order to understand the general reactivity of **Mo-1a** and its performance with different amides, DFT calculations and supporting experiments were conducted. Scheme 5 shows the experiments performed to determine the active catalyst species. Treatment of **Mo-1a** with NaBHET₃ resulted in rapid hydrogen evolution. The nature of the gas was determined in a scale up experiment (100 µmol of **Mo-1a**) using GC-analysis. This observation prompted us to assume that the obtained reaction product was likely to be a pincer amido species such as **Mo-3**, in which Mo(i) has been reduced to Mo(0). This conclusion was further supported by HR-ESI mass spectrometry of the corresponding reaction mixture. When the distinct reactivity of the catalyst towards formanilide was studied, we isolated **Mo-4** in form of colorless needles from the reaction mixture (Fig. 2; for detailed experimental procedure see ESIf).

Notably, the crystal structure of **Mo-4** (Fig. 2 and Scheme 5) features two anionic Mo(0) complexes neutralized by two Na⁺ cations interacting with the CO ligands. In order to investigate, whether **Mo-4** is involved in the catalytic cycle, the reduction of *N*-methylformanilide was carried out using 2.5 mol% of **Mo-4** under conditions optimized for **Mo-1a**. In fact, we observed full conversion of the substrate and isolated *N*-methylaniline in 92% yield. Thus, we conclude, that the catalytically active species contains a Mo(0) center. This is also consistent with the EPR-silent nature of the product formed in the activation of **Mo-1a** by NaBHET₃.

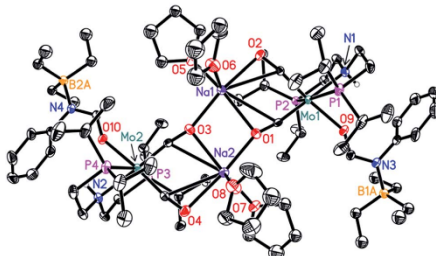


Fig. 2 Molecular structure of **Mo-4** in the crystal (see Scheme 5 for a graphical representation). Displacement ellipsoids correspond to 30% probability. Hydrogen atoms except the N-bound are omitted for clarity.

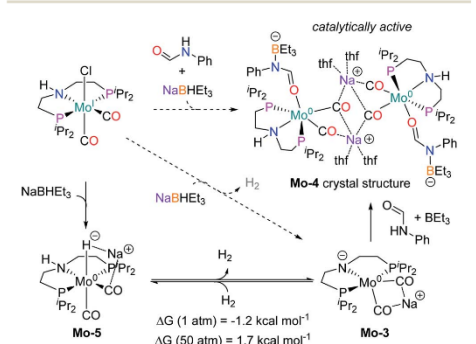
The observed activity of **Mo-4** suggests that the Mo(0)-complexes **Mo-3** and **Mo-5**, shown in Scheme 5, are presumably the main catalytic intermediates. Similar species have been proposed for the isoelectronic Fe(II)-complexes **Fe-2**, **Fe-3** and the Mn(I)-complex **Mn-2** (Scheme 2).²⁰

Based on these results, DFT calculations, with the M06 functional, including toluene solvation with the SMD model, were used to get further insights into the reaction mechanism (see computational details and ESI for details†). The hydrogeneration of **Mo-3** to yield **Mo-5**, was found to be almost isoenergetic, with a small preference for **Mo-3** at 1 bar and **Mo-5** at 50 bar (Scheme 5). These energies agree with the bubbling of H₂ observed experimentally during the catalyst activation reaction.

As represented in Scheme 1, amide hydrogenation is proposed to consist in three steps: amide C=O reduction, C–N bond protonolysis of the formed hemiaminal, and aldehyde C=O reduction. These steps were computed for *N*-methylformanilide and the energy profiles for the preferred pathways are given in Fig. 3 and 5, and the ESI.†

The mechanism for the amide C=O hydrogenation by **Mo-5** consists of the hydride transfer from Mo to the amide carbonyl group (**Mo-ts-6-7**), followed by proton transfer from the ligand nitrogen to the amide oxygen (**Mo-ts-7-8**). This pathway was computed for formanilide (**Mo-ts-6-7-NH** in Fig. 3) and *N*-methylformanilide. With both substrates, the hydride transfer has the highest energy barrier (10.6 kcal mol⁻¹ with formanilide and 13.1 kcal mol⁻¹ with *N*-methylformanilide). Interestingly, these energies are lower than those reported by us for the analogous Fe catalyst with formanilide (15.8 kcal mol⁻¹, **Fe-ts-6-7** in Fig. 3).¹⁵

The mechanism for the C–N bond cleavage from the formed hemiaminal (Scheme 1) was also investigated. In the case of **Fe-3**, this step was reported to proceed via the transition state **Fe-ts-C^H-N^H** (Fig. 4).¹⁵ With Mo and *N*-methylformanilide, the same pathway involves a Gibbs energy barrier of 22.9 kcal mol⁻¹ (**Mo-ts-C^H-N^{Me}**). An increase of less than 1 kcal mol⁻¹ is observed by changing the substrate to *N*-methyacetanilide (**Mo-ts-C^M-N^M**).



Scheme 5 Reactions performed to get insight on the active catalytic species (in dashed arrows) with the experimental observed products (H₂ and the crystal structure of **Mo-4**, in color) and the intermediates proposed (**Mo-3** and **Mo-5**). Gibbs energies calculated for the dehydrogenation of **Mo-5** at different pressure.

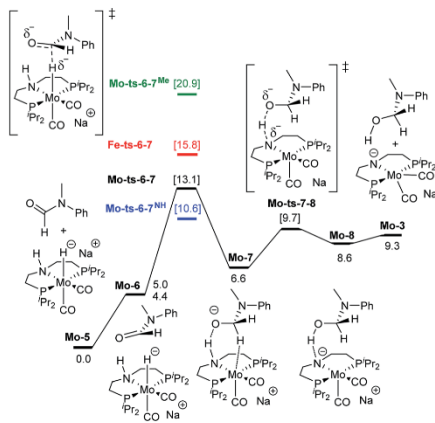


Fig. 3 Reaction pathway for the hemiaminal formation from the *N*-methyl formanilide with Mo-5. Gibbs energies in toluene (SMD) at 50 atm and 373 K are given in kcal mol⁻¹. In blue and green, energies for the hydride transfer using formanilide and *N*-methylacetanilide, respectively. In red, energy for the hydride transfer using the reported Fe-3 complex at 30 atm (Scheme 2).¹⁵

The similar energy barriers obtained with these substrates did not account for the large differences in yield observed experimentally (99% Conv. in *N*-methylformanilide vs. 20% Conv. in *N*-methylacetanilide). In addition, the lower energy barriers obtained with Mo compared to Fe are inconsistent with the higher H₂ pressure and time required to accomplish amide hydrogenation with Mo-1a compared to Fe-3.¹⁴

These discrepancies were explained by considering the reaction of Mo-3 with methanol leading to the Mo-methoxy intermediate Mo-9a (Fig. 5). This reaction, which involves the deprotonation of MeOH by the amido ligand (Mo-ts-3-9a), has a low energy barrier ($\Delta G^\ddagger = 2.8$ kcal mol⁻¹) and is highly exergonic ($\Delta G = -11.4$ kcal mol⁻¹). The formation of related M-methoxy species have been observed for similar Fe, Ru, Os and Mn PNP-pincer complexes.^{20,21,22} This species can promote the protonolysis of the C–N bond by assisting the OH-deprotonation and N-protonation of the hemiaminal

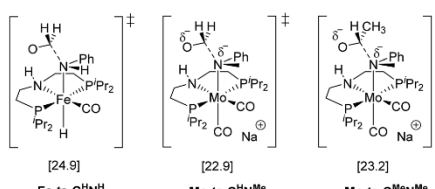


Fig. 4 TSs for the C–N bond cleavage step via the mechanism previously reported for Fe-3.¹⁵

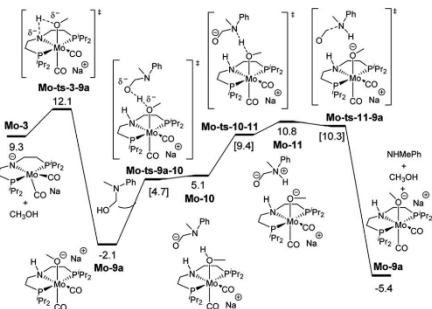
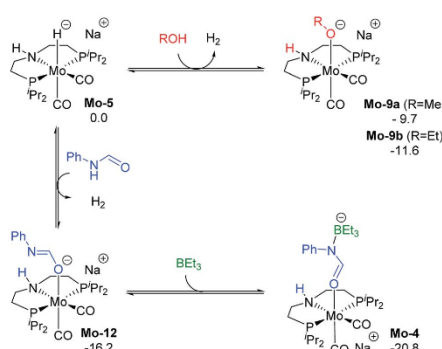


Fig. 5 Reaction pathway of the MeOH assisted hemiaminal proton transfer and posterior C–N bond cleavage. Gibbs energies in toluene (SMD) at 50 atm and 373 K are given in kcal mol⁻¹.

intermediate (Mo-11-9a). The highest energy of this process is 10.8 kcal mol⁻¹, which corresponds to the zwitterion hemiaminal intermediate interacting with the methoxide–Mo complex (Mo-11). This energy is lower than the energy barrier for the hydride transfer (13.1 kcal mol⁻¹), indicating that the C–N bond cleavage is not the rate limiting step once MeOH is formed (note: for a comparison of this mechanism with Mo and Fe-systems see ESI†).

The reaction of Mo-5 with MeOH yields hydrogen and is exergonic ($\Delta G = -9.7$ kcal mol⁻¹, Scheme 6). The methoxy intermediate Mo-9a is thus the resting state of the catalyst.

Formanilide, and other secondary amides, can also displace H₂ from the catalyst (Mo-12 in Scheme 6). This reaction is even more exergonic ($\Delta G = -16.2$ kcal mol⁻¹) than with MeOH increasing the global energy barrier for the hydride transfer from 10.6 to 26.8 kcal mol⁻¹ with formanilide. This energy may increase to 31.4 kcal mol⁻¹ by reaction with BEt₃ (Mo-4). In



Scheme 6 Calculated Gibbs energies (kcal mol⁻¹) for the substitution of H₂ in Mo-5 by methanol, ethanol, formanilide and BEt₃ yielding Mo-9a, b, Mo-10 and Mo-4, respectively.



contrast, with *N*-methylformanilide, the only penalty to pay is the addition of MeOH. Therefore, the energy barrier for the hydride transfer increases from 13.1 to 22.9 kcal mol⁻¹, which is lower than the barrier for formanilide, consistent with the larger conversion obtained with *N*-methylformanilide. In the case of *N*-methylacetanilide, the addition of ethanol instead of methanol is expected. The higher stability of the ethoxide complex **Mo-9b** compared to **Mo-9a** by ca. 2 kcal mol⁻¹ (Scheme 6), together with the higher energy barrier for the hydride transfer with this substrate ($\Delta G = 20.9$ kcal mol⁻¹, Fig. 3), is consistent with the low yields obtained experimentally with *N*-methylacetanilide.

The mechanism of catalyst recovery by addition of H₂ to the methoxide complex **Mo-9a** is shown in Fig. S3.[†] In this pathway, methanol assists the activation of the Mo–H₂ complex (**Mo-14**) by acting as a proton-shuttle with a global energy barrier of 23.0 kcal mol⁻¹. Similar mechanisms have been proposed with Ru–N and Fe–N complexes (see ESI[†]).^{21b,23}

The results from the computational study can be summarized in the catalytic cycle represented in Fig. 6. In the absence of alcohol, the Mo-catalyst is involved in the hemiaminal C–N bond cleavage after the amide C=O reduction (blue cycle). This reaction yields amine and formaldehyde, which is reduced to alcohol by the catalyst **Mo-5** in a subsequent reaction (in red). In the presence of alcohol, a Mo-alkoxo intermediate is formed, **Mo-9a**. This species, which becomes the catalyst resting state, is involved in the hemiaminal C–N bond cleavage. Finally, the

N-methylformanilide conversion

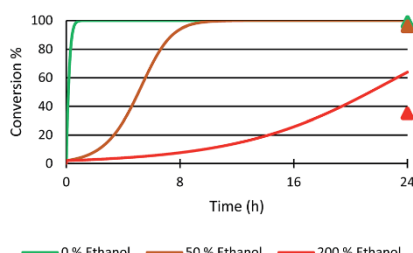


Fig. 7 Microkinetic simulation of *N*-methylformanilide **1a** conversion with 0% (green), 50% (brown) and 200% (red) ethanol in solution. The initial concentration of reactants were the same as those used in the experiments; i.e. 0.25 M *N*-methylformanilide **1a**, 0.207 M of dihydrogen and 12.5 mM of **Mo-5**. Experimental values at 24 hours represented with triangles.

catalyst recovery takes place by the displacement of alcohol by H₂. The nature of the catalyst resting state may change with secondary amides, which reacts with the catalyst forming an adduct (**Mo-4**, in green) that hampers the reaction.

In order to validate this mechanism and the nature of Mo(0) active species, the role of the counter-cation in this reaction was explored computationally and experimentally by using LiHBET₃, NaHBET₃, and KBHET₃. Carrying out the benchmark reaction at 80 °C, 5 mol% of the alkali metal hydrides were added to activate **Mo-1a**. It could be shown, that for NaBHET₃ and KBHET₃ similar conversions of *N*-methylformanilide (**1a**) (76% and 77%, respectively) and yields of **2a** (75% and 73%, respectively) were obtained. However, when LiBHET₃ was used, only 10% conversion of **1a** and 9% yield of *N*-methylaniline **2a** was obtained. These results were in agreement with the trends on the energy barriers obtained for the amide C=O reduction step, which are 22.9, 23.0 and 28.8 kcal mol⁻¹ with Na⁺, K⁺ and Li⁺, respectively, taking **Mo-9a** as energy reference. The stronger electrostatic interaction of Li⁺ with the methoxide intermediate (**Mo-9aLi⁺**), accounts for the highest energy barrier predicted for this system (see ESI[†]).

Next, the role of the alcohol was explored by adding different amounts of ethanol to the benchmark system. In the presence of 50 mol% of EtOH, 96% conversion of *N*-methylformanilide (**1a**) and 93% product yield were obtained. However, the addition of 200 mol% resulted in a sharp decrease in conversion and yield (35% conversion, 32% yield). Thus, it was concluded that ethanol has a detrimental effect on the performance of the catalytic system. Notably, these trends were reproduced with a microkinetic model based on the general mechanism represented in Fig. 6 (in Fig. 7). This model predicted 100% conversion after 24 h of reaction for both 0% and 50% concentrations of ethanol. In contrast, and in line with the experiments, the same model predicted a significant decrease of conversion to 64% with an ethanol concentration of 200% (see ESI for further details[†]).

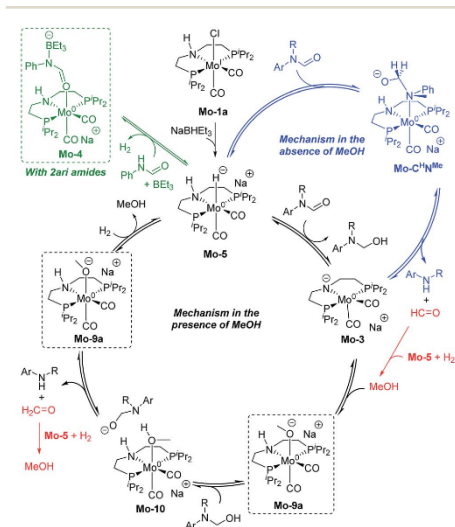


Fig. 6 General mechanism for the amide hydrogenation in the absence (in blue) and presence (in black) of methanol with the formaldehyde hydrogenation in red. Dashed squares indicate the catalyst resting state in the presence of MeOH and Zari amides (in green).

Conclusions

Well-defined molybdenum-PNP pincer complexes have been used for the first time in the hydrogenation of a range of amides to the corresponding alcohols and amines. *N*-Alkylated and *N*-arylated formamides can be hydrogenated to the corresponding products in good to high yields. Applying complex **Mo-1a** high selectivity for the hydrogenation of formamides was observed in the presence of other reducible groups. These results pave the way for potential applications of this type of complexes in synthetic methodologies.

The DFT study shows that the active Mo(0) species (**Mo-5**) reduces the C=O group of the amide through low-energy barriers, compared to Fe-based systems. However, the alcohol product and secondary amides react with the catalyst forming stable adducts encumbering catalyst recovery and increasing the overall barrier for the reduction of the C=O group. These results suggest that further catalyst design should focus on preventing the formation of these adducts, while keeping the high hydricity of the complex.

Experimental details

General experimental information

All hydrogenation reactions were set up under Ar in a 300 mL autoclave (PARR Instrument Company). In order to avoid unspecific reductions, all catalytic experiments were carried out in 4 mL glass vials, which were set up in an alloy plate and placed inside the autoclave.

In a glove box, a 4 mL glass vial containing a stirring bar was charged with complex **Mo-1a** (12.5 mg; 5 mol%). Toluene (2 mL) was added and the corresponding brown suspension was treated with NaBH₄ (0.5 M in THF; 50 μL; 10 mol%). The reaction mixture was stirred for 10 minutes and the corresponding substrate was subsequently added. Afterwards, the vial was capped and transferred into an autoclave. Once sealed, the autoclave was purged three times with 10 bar of hydrogen, then pressurized to the desired hydrogen pressure (50 bar), and placed into an aluminum block that was preheated to the desired temperature (100 °C). After 24 h, the autoclave was cooled in an ice bath and the remaining gas was released carefully. The solution was subsequently diluted with ethyl acetate and filtered through a small pad of Celite (1 cm in a Pasteur pipette). The Celite was washed with methanol (2 mL) and the combined filtrates were subsequently evaporated to dryness. The remaining residue was purified by column chromatography (SiO₂, heptane/EtOAc, gradient 100 : 0 → 0 : 100). In the case of substrate 7, the purified product was dissolved in 5 mL of Et₂O and subsequently treated with 1 mL of HCl (2 M in Et₂O). The reddish precipitate was filtered off, washed three times with 5 mL of Et₂O and finally dried *in vacuo*. For the characterization of the products of the catalysis, see ESI.[†]

Computational details

DFT calculations were carried out with Gaussian 09²⁴ with the M06²⁵ functional and the double-z LANL2DZ (on Mo, including

relativistic effects)²⁶ and 6-31+G** (on all other elements)²⁷ basis sets. Calculations were done using the full system. The location of the Na⁺ cation was evaluated in some of the intermediates, and the preferred position is represented in figures and schemes of the manuscript (see ESI[†]). The geometry optimization and energies of the possible spin states of **Mo-1a** and **Mo-4** were consistent with a doublet and singlet ground state, respectively (see ESI[†]). Vibrational frequencies were computed at the same level of theory to obtain the thermochemistry corrections (zero-point, thermal and entropy energies) at the experimental *p* = 50 atm and *T* = 373.15 K. The energy of the optimized geometries was refined by single point calculations with triple-z quality basis sets, including the LANL2TZ²⁶ on Mo and the 6-31+G** on all other elements.²⁸ The energies reported in the text were obtained by adding the thermochemistry corrections to the refined potential energies. The solvation effects of toluene were included in both the geometry optimizations and energy refinements using the continuum SMD model.²⁹ The ultrafine (99 590) grid was used in all calculations for higher numerical accuracy. A repository containing all input and output files is available on-line from ioChem BD at <https://iochem-bd.bsc.es/browse/handle/100/193698>.³⁰ Microkinetic models were simulated with the COPASI software³¹ using the LSODA algorithm. See ESI for further details.[†]

Conflicts of interest

There are no conflicts to declare.

Acknowledgements

T. Leischner, K. Junge and M. Beller thank the analytical department (S. Schareina, S. Buchholz, A. Lehmann) of the Leibniz-Institute for Catalysis, Rostock. Ll. A. and A. N. thank the support from the Research Council of Norway (FINATEK Grant No. 250044 and Center of Excellence Grant No 262695), the Norwegian Metacenter for Computational Science (NOTUR, nn4654k) and the 'Nordic Consortium for CO₂ Conversion' (NordForsk project no 85378, <http://site.uit.no/nordco2>).

Notes and references

- (a) P. Roose, K. Eller, E. Henkes, R. Rossbacher and H. Hönke, *Ullmann's Encyclopedia of Industrial Chemistry*, Germany, 2000; (b) P. G. Jessop, *The Handbook of Homogeneous Hydrogenation*, Germany, 2006.
- For selected examples of carboxylic acid derivatives hydrogenation, see: (a) S. Werkmeister, K. Junge, B. Wendt, E. Alberico, H. J. Jiao, W. Baumann, H. Junge, F. Gallou and M. Beller, *Angew. Chem., Int. Ed.*, 2014, **53**, 8722–8726; (b) T. vom Stein, M. Meureusch, D. Limper, M. Schmitz, M. Holscher, J. Coetze, D. J. Cole-Hamilton, J. Klankermayer and W. Leitner, *J. Am. Chem. Soc.*, 2014, **136**, 13217–13225; (c) D. Srimani, A. Mukherjee, A. F. G. Goldberg, G. Leitus, Y. Diskin-Posner, L. J. W. Shimon, Y. Ben David and D. Milstein, *Angew. Chem., Int. Ed.*, 2015, **54**, 12357–12360; (d) X. J. Cui,

- Y. H. Li, C. Topf, K. Junge and M. Beller, *Angew. Chem., Int. Ed.*, 2015, **54**, 10596–10599; (e) T. J. Korstanje, J. I. van der Vlugt, C. J. Elsevier and B. de Bruin, *Science*, 2015, **350**, 298–301; (f) M. Naruto and S. Saito, *Nat. Commun.*, 2015, **6**, 8140; (g) J. R. Cabrero-Antonino, I. Sorribes, K. Junge and M. Beller, *Angew. Chem., Int. Ed.*, 2016, **55**, 387–391.
- 3 (a) B. Cornile and W. A. Herrmann, *Applied Homogenous Catalysis with Organometallic Compounds: A Comprehensive Handbook in Two Volumes*, Germany, 1996; (b) D. L. Dodds and D. L. Cole-Hamilton, *Sustainable Catalysis*, United States of America, 2013.
- 4 D. Wie, C. Netkaew and C. Darcel, *Eur. J. Inorg. Chem.*, 2019, 2471–2487.
- 5 M. Garbe, K. Junge and M. Beller, *Eur. J. Org. Chem.*, 2017, **30**, 4344–4362.
- 6 G. A. Filonenko, R. van Putten, E. J. M. Jensen and E. A. Pidko, *Chem. Soc. Rev.*, 2018, **47**, 1459–1483.
- 7 For selected examples see: (a) R. Langer, G. Leitus, Y. Ben-David and D. Milstein, *Angew. Chem., Int. Ed.*, 2011, **50**, 2120–2124; (b) N. Gargas, B. Stöger, L. F. Veiros, E. Pittenauer, G. Allmaier and K. Kirchner, *Organometallics*, 2014, **33**, 6905–6914; (c) T. Zell, Y. Ben-David and D. Milstein, *Catal. Sci. Technol.*, 2015, **5**, 822–826; (d) N. Gargas, B. Stöger, L. F. Veiros and K. Kirchner, *ACS Catal.*, 2016, **6**, 2664–2672; (e) S. Elangovan, B. Wendt, C. Topf, S. Bachmann, M. Sealone, A. Spannenberg, H. Jiao, W. Baumann, K. Junge and M. Beller, *Adv. Synth. Catal.*, 2016, **358**, 820–825; (f) S. Lange, S. Elangovan, C. Cordes, A. Spannenberg, H. Jiao, H. Junge, S. Bachmann, M. Sealone, C. Topf, K. Junge and M. Beller, *Catal. Sci. Technol.*, 2016, **6**, 4768–4772; (g) S. Elangovan, C. Topf, S. Fischer, H. Jiao, A. Spannenberg, W. Baumann, R. Ludwig, K. Junge and M. Beller, *J. Am. Chem. Soc.*, 2016, **138**, 8809–8814.
- 8 (a) P. M. Rylander, *Hydrogenation Methods*, Academic Press, London, 1985; (b) J. Hartwig, *Organotransition Metal Chemistry*, University Science Books, 2010.
- 9 (a) D. Cantillo, *Eur. J. Inorg. Chem.*, 2011, **19**, 3008–3013; (b) P. A. Dub and T. Ikariya, *ACS Catal.*, 2012, **2**, 1718–1741; (c) A. M. Smith and R. Whyman, *Chem. Rev.*, 2014, **114**, 5477–5510.
- 10 (a) A. A. Nunez Magro, G. R. Eastham and D. J. Cole-Hamilton, *Chem. Commun.*, 2007, **30**, 3154–3156; (b) E. Balaraman, B. Gnanaprakasam, L. J. W. Shimon and D. Milstein, *J. Am. Chem. Soc.*, 2010, **132**, 16756–16758; (c) J. M. John and S. H. Bergens, *Angew. Chem., Int. Ed.*, 2011, **50**, 10377–10380; (d) J. Coetze, D. L. Dodds, J. Klankermayer, S. Brosinski, W. Leitner, A. M. Z. Slawin and D. J. Cole-Hamilton, *Chem.-Eur. J.*, 2013, **19**, 11039–11050; (e) T. Miura, I. E. Held, S. Oishi, M. Naruto and S. Saito, *Tetrahedron Lett.*, 2013, **54**, 2674–2678; (f) T. von Stein, M. Meureusch, D. Limper, M. Schmitz, M. Hölscher, J. Coetze, D. J. Cole-Hamilton, J. Klankermayer and W. Leitner, *J. Am. Chem. Soc.*, 2014, **136**, 13217–13225; (g) J. R. Cabrero-Antonino, E. Alberico, H. J. Drexler, W. Baumann, K. Junge, H. Junge and M. Beller, *ACS Catal.*, 2016, **6**, 47–54; (h) L. Shi, X. Tan, J. Long, X. Xiong, S. Yang, P. Xue, H. Lv and X. Zhang, *Chem.-Eur. J.*, 2017, **23**, 546–548.
- 11 J. A. Garg, S. Chakraborty, Y. Ben-David and D. Milstein, *Chem. Commun.*, 2016, **52**, 5285–5288.
- 12 N. M. Rezayee, D. C. Samblanet and M. S. Sanford, *ACS Catal.*, 2016, **6**, 6377–6383.
- 13 F. Schneck, M. Assmann, M. Balmer, K. Harms and R. Langer, *Organometallics*, 2016, **35**, 1931–1943.
- 14 U. Jayaranthe, Y. Zhang, N. Hazari and W. Bernskoetter, *Organometallics*, 2017, **36**, 409–416.
- 15 L. A. Suarez, Z. Culacova, D. Balcels, W. H. Bernskoetter, O. Eisenstein, K. I. Goldberg, N. Hazari, M. Tilset and A. Nova, *ACS Catal.*, 2018, **8**, 8751–8762.
- 16 V. Papa, J. R. Cabrero-Antonino, E. Alberico, A. Spannenberg, K. Junge, H. Junge and M. Beller, *Chem. Sci.*, 2017, **8**, 3576–3585.
- 17 S. Kar, A. Goeppert, J. Kothandaraman and J. K. S. Prakash, *ACS Catal.*, 2017, **7**, 6347–6351.
- 18 T. Leischner, A. Spannenberg, K. Junge and M. Beller, *Organometallics*, 2018, **37**, 4402–4408.
- 19 (a) S. Chakraborty, O. Blacque, T. Fox and H. Berke, *Chem.-Asian J.*, 2014, **9**, 328–337; (b) S. Chakraborty, O. Blacque and H. Berke, *Dalton Trans.*, 2015, **44**, 6560–6570; (c) S. Chakraborty and H. Berke, *ACS Catal.*, 2014, **4**, 2191–2194; (d) Y. Zhang, P. G. Williard and W. H. Bernskoetter, *Organometallics*, 2016, **35**, 860–865.
- 20 (a) S. Chakraborty, P. Lagaditis, M. Förster, E. A. Bielinski, N. Hazari, M. C. Holthausen, W. D. Jones and S. Schneider, *ACS Catal.*, 2014, **4**, 3994–4003; (b) E. A. Bielinski, P. Lagaditis, Y. Zhang, B. Q. Mercado, C. Würtele, W. H. Bernskoetter, N. Hazari, S. Schneider and P. O. Lagaditis, *J. Am. Chem. Soc.*, 2014, **136**, 10234–10237; (c) D. Nguyen, X. Trivelli, F. Capet, J. F. Paul, F. Dumeignil and R. M. Gauvin, *ACS Catal.*, 2017, **7**, 2022–2032.
- 21 (a) Z. Shao, Y. Wang, Y. Liu, Q. Wang, X. Fu and Q. Liu, *Org. Chem. Front.*, 2018, **5**, 1248–1256; (b) X. Chen, Y. Jing and X. Yang, *Chem.-Eur. J.*, 2016, **22**, 1950–1957; (c) E. Bielinski, M. Förster, Y. Zhang, W. H. Bernskoetter, N. Hazari and M. Holthausen, *ACS Catal.*, 2015, **5**, 2404–2415.
- 22 D. Gusev, *ACS Catal.*, 2017, **7**, 6656–6662.
- 23 (a) G. Zhang and S. Hanson, *Chem. Commun.*, 2013, **49**, 10151–10153; (b) Z. Wie, A. De Aguirre, K. Junge, M. Beller and H. Jiao, *Catal. Sci. Technol.*, 2018, **8**, 3649–3665.
- 24 M. J. Frisch, G. W. Trucks, H. B. Schlegel, G. E. Scuseria, M. A. Robb, J. R. Cheeseman, G. Scalmani, V. Barone, B. Mennucci, G. A. Petersson, N. Nakatsuji, M. Caricato, X. Li, H. P. Hratchian, A. F. Izmaylov, J. Bloino, G. Zheng, J. L. Sonnenberg, M. Hada, M. Ehara, K. Toyota, R. Fukuda, J. Hasegawa, M. Ishida, T. Nakajima, Y. Honda, O. Kitao, H. Nakai, T. Vrete, J. A. Montgomery, J. E. Peralta, F. Ogliare, M. Bearpark, J. J. Heyd, E. Brothers, K. N. Kudin, V. N. Staroverov, T. Keith, R. Kobayashi, J. Normand, K. Raghavachari, A. Rendell, J. C. Burant, S. S. Iyengar, J. Tomasi, M. Cossi, N. Rega, J. M. Millam, M. Klene, J. E. Knox, J. B. Cross, V. Bakken,



- C. Adamo, J. Jaramillo, R. Gomperts, R. E. Stratmann, O. Yazyev, A. J. Austin, R. Cammi, C. Pomelli, J. W. Ochterski, R. L. Martin, K. Morokuma, V. G. Zakrzewski, G. A. Voth, P. Salvador, J. J. Dannenberg, S. Dapprich, A. D. Daniels, O. Fakas, J. B. Foresman, J. V. Ortiz, J. Cioslowski and D. J. Fox, *Gaussian 09, Revision D.01*, Gaussian, Inc., Wallingford CT, 2013.
- 25 Y. Zhao and D. Truhlar, *Theor. Chem. Acc.*, 2008, **120**, 215–241.
- 26 (a) P. Hay and W. Wadt, *J. Chem. Phys.*, 1985, **82**, 270–283; (b) W. Wadt and P. Hay, *J. Chem. Phys.*, 1985, **82**, 284–298.
- 27 (a) W. J. Hehre, R. Ditchfield and J. A. Pople, *J. Chem. Phys.*, 1972, **56**, 2257–2261; (b) W. Kohn, A. D. Becke and R. G. Parr, *J. Phys. Chem.*, 1996, **1**, 12974–12980.
- 28 A. McLean and G. Chandler, *J. Chem. Phys.*, 1980, **72**, 5639–5648.
- 29 A. Marenich, C. Cramer and D. Truhlar, *J. Phys. Chem. B*, 2009, **113**, 6378–6396.
- 30 M. Álvarez-Moreno, C. De Graaf, N. López, F. Maseras, J. M. Poblet and C. Bo, *J. Chem. Inf. Model.*, 2015, **55**, 95–103.
- 31 S. Hoops, R. Gauges, C. Lee, J. Pahle, N. Simus, M. Singh, L. Xu, P. Mendes and U. Kummer, *Bioinformatics*, 2006, **22**, 3067–3074.

Computational Details

General Computational Information.

DFT calculations were carried out with the Gaussian09 software package.¹⁰ The hybrid meta-GGA M06¹¹ functional was selected on the basis of geometry (Figure S1 Table S1) benchmark, using X-Ray crystal structures as references. Structures were fully optimized without any geometry or symmetry constraints, combining the double-z LANL2DZ (on Mo, including relativistic effects)¹² and 6-31+G** (on all other elements)¹³ basis sets. Vibrational frequencies were computed at the same level of theory to classify all stationary points as either saddle points (transition states, with a single imaginary frequency) or energy minima (reactants, intermediates and products, with only real frequencies). These calculations were also used to obtain the thermochemistry corrections (zero-point, thermal and entropy energies) at the experimental p = 50 atm and T = 373 K. The energy of the optimized geometries was refined by single point calculations with triple-z quality basis sets, including the LANL2TZ¹² on Mo and the 6-311+G** on all other elements.¹⁴ The energies reported in the text were obtained by adding the thermochemistry corrections to the refined potential energies. The solvation effects of toluene were included in both the geometry optimizations and energy refinements using the continuum SMD model.¹⁵ The ultrafine (99,590) grid was used in all calculations to increase numerical accuracy and to facilitate convergence. A data set collection of input files and computational results is available in the ioChem-BD repository and can be accessed online via <https://iochem-bd.bsc.es/browse/handle/100/193698>.¹⁶ The complex reaction mechanisms inferred from the calculations were interpreted by means of quantitative microkinetic models (Figure S4, Figure S5 and Table S2), simulated with the COPASI software.¹⁷ Time course simulation were carried with the LSODA algorithm.

DFT functional benchmark

In a previous work of the group, the hydrogenation of amides by an iron (II) Noyori-type bifunctional catalyst was studied by using the M06 functional.⁶ This method was selected based on a method benchmark using X-ray geometries and CCSD(T) energies. In order to obtain comparable results, the same functional was initially chosen for this study. This functional was found to give geometries in good agreement with those experimentally obtained for complexes Mo-1a (RMSD = 0.037 Å), Mo-1c (RMSD = 0.031 Å), and Mo-4 (RMSD = 0.030 Å) and therefore was selected for this study. The geometry optimization and energies of the possible spin states for these species were consistent with a doublet for Mo-1a, and a singlet ground state for Mo-1c and Mo-4, respectively.

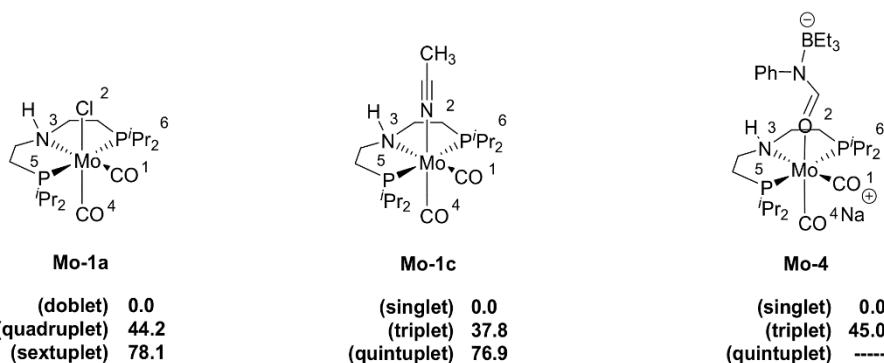


Figure S1. Mo-complexes used for the geometry benchmark using M06 with the labels used in Table S1, and the corresponding free energies for the first and second excited states. Mo-4 quintuplet did not converge.

Mo-1a

	Mo-CO ¹	Mo-Cl ²	Mo-NH ³	Mo-CO ⁴	Mo-P ⁵	Mo-P ⁶	RMSD
<u>Experimental</u>	1.9536	2.5817	2.3029	1.9118	2.5002	2.4878	
<u>M06</u>							
(doublet)	1.9785	2.5814	2.3754	1.9549	2.5099	2.5099	0.0373
(quadruplet)	2.2574	2.6006	2.5649	1.9931	2.5313	2.5314	0.1687
(sextuplet)	2.2645	2.5904	2.5645	2.2881	2.6643	2.5793	0.2388

Mo-1c

	Mo-CO ¹	Mo-NCCH ₃ ²	Mo-NH ³	Mo-CO ⁴	Mo-P ⁵	Mo-P ⁶	RMSD
<u>Experimental</u>	1.9203	2.2274	2.3227	1.9155	2.4389	2.4296	
<u>M06</u>							
(singlet)	1.9496	2.2247	2.3793	1.9490	2.4485	2.4485	0.0307
(triplet)	1.9775	2.2606	2.3677	1.9873	2.5054	2.5083	0.0608
(quintuplet)	2.3050	2.2898	3.2786	2.0528	2.6364	2.6682	0.4436

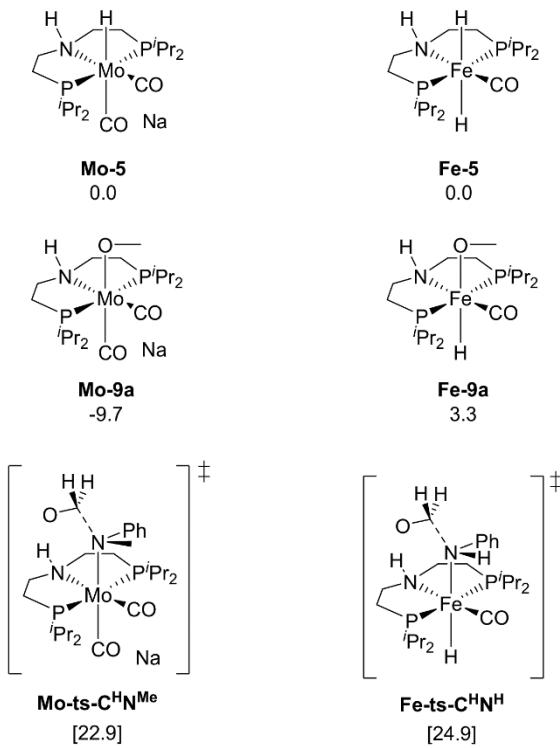
Mo-4

	Mo-CO ¹	Mo-OR ²	Mo-NH ³	Mo-CO ⁴	Mo-P ⁵	Mo-P ⁶	RMSD
<u>Experimental</u>	1.8893	2.2391	2.3230	1.8893	2.4406	2.4421	
<u>M06</u>							
(singlet)	1.9116	2.2477	2.3694	1.8967	2.4777	2.4794	0.0304
(triplet)	2.0950	2.2919	2.4984	1.8675	2.5240	2.5271	0.1229

Table S1. Root mean square deviation of distances (in Å) of optimized geometries with respect experimental single crystal X-ray diffraction geometries, for Mo-1a, Mo-1c and Mo-4 molecules.

Comparison Iron system vs Molybdenum system.

In this work, a mechanism in which a methoxide intermediate is involved in the hemiaminal C-N bond cleavage (Mo-ts-12-13) has been proposed with Mo. This mechanism differs from the one previously proposed with Fe, in which the N of the hemiaminal is coordinated to Fe during the C-N bond cleavage (Fe-ts-CH^HN^H). We have calculated ts-12-13 with Fe (see Figure S2) and has a higher energy than ts-CH^HN^H, indicating that the methoxide mechanism is not preferred with Fe. The higher stability of the methoxide intermediate with Mo (Mo-9a) compared with (Fe-9a) may explain this difference in reactivity.



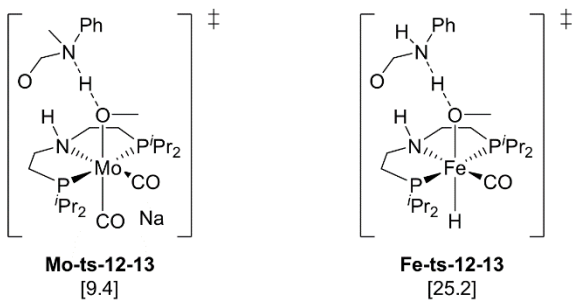


Figure S2. Computed free energies, in kcal mol⁻¹, for selected TSs and minima involved in the hemiaminal C-N bond cleavage step with Mo and Fe-systems.

Catalyst recovery mechanism.

The mechanism of catalyst recovery by addition of H₂ to the methoxide complex Mo-9a is shown in Fig. S3. In this pathway, methanol assists the activation of the Mo-H₂ complex (Mo-14) by acting as a proton-shuttle. The global energy barrier for the catalyst recovery mechanism is 23.0 kcal mol⁻¹, which is similar to the global barrier for the hydride transfer with *N*-methylformanilide (5) (22.8 kcal mol⁻¹). This result suggests that both hydride transfer and catalyst recovery should be considered as rate limiting processes in the hydrogenation of amides catalyzed by Mo.

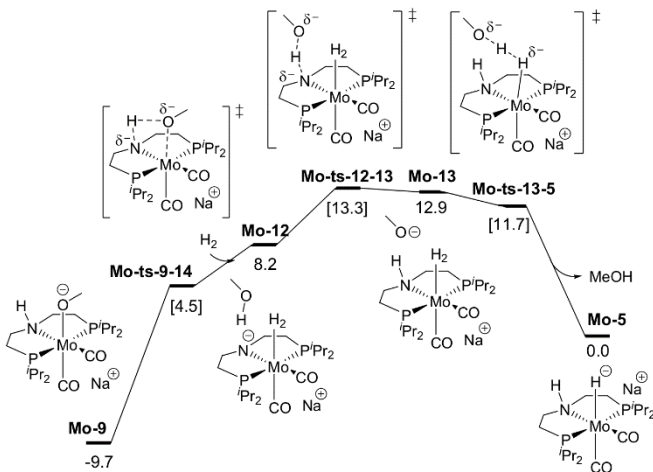


Figure. S3 Reaction pathway of the MeOH assisted hemiaminal proton transfer and posterior C–N bond cleavage. Gibbs energies in toluene (SMD) at 50 bar and 373 K are given in kcal mol⁻¹.

Hydrogenation of formaldehyde

The free energy profile for the formaldehyde reduction is represented in Figure S4.

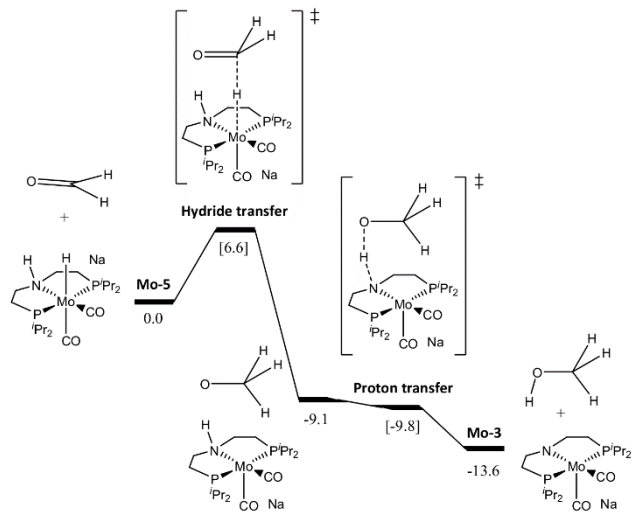
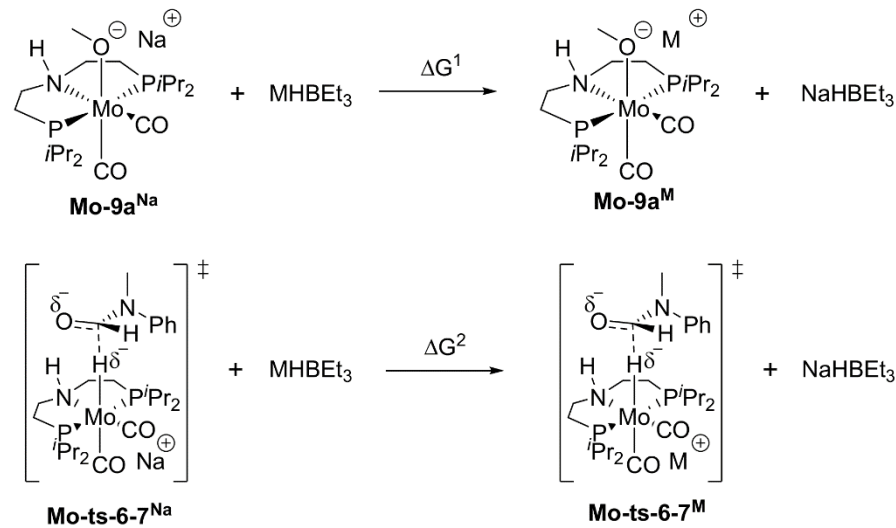


Figure S4 Free energy profile in kcal mol⁻¹ for the formaldehyde hydrogenation to methanol by Mo-5.

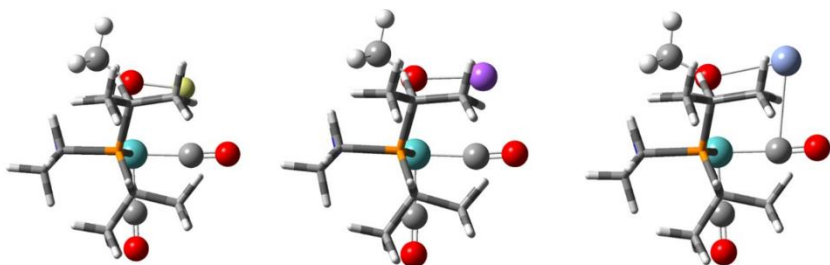
Mo-9a and Mo-ts-6-7 with Li⁺, Na⁺ and K⁺

The energy barrier for the hydride transfer involves Mo-ts-6-7 and the methoxy intermediate Mo-9a, which is the ground state. The energy barriers computed for Na⁺, K⁺ and Li⁺ is 22.9, 23.0, and 28.8 kcal/mol, respectively. Therefore, the difference in energy barrier for Li⁺ and K⁺ is 5.8 kcal/mol instead of 9 kcal/mol. In order to analyse these differences in energy barrier, the stability of Mo-9a and Mo-ts-6-7 with the different cations have been evaluated using isodesmic reactions (Figures S5). The energies of these reactions and the geometrical analysis of Mo-9a and Mo-ts-6-7 (Figures S6) suggest that the higher energy barrier for Li⁺ is due to a higher stabilization of the ground state (Mo-9a) with this cation, probably due to stronger electrostatic interaction of Li⁺ with the OMe group.



M	ΔG ¹ (kcal mol ⁻¹)	ΔG ² (kcal mol ⁻¹)
Li ⁺	- 4.6	1.4
K ⁺	- 0.9	-0.7

Figure S5. Free energies (kcal mol⁻¹) for the comparative isodesmic reaction between Li⁺, Na⁺ and K⁺ in Mo-9a and Mo-ts-6-7



Mo-9a^{Li}

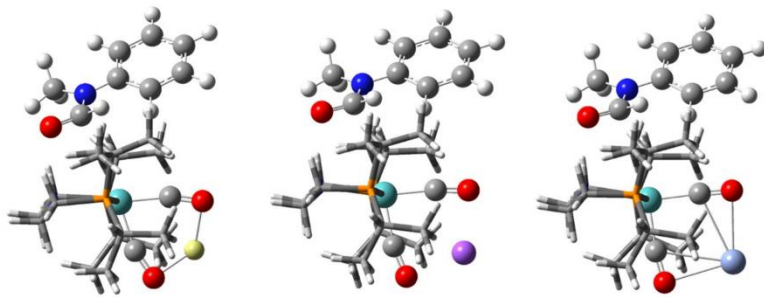
Mo-9a^{Na}

Mo-9a^K

Distances O-Li 1.74 Å
 O-Mo 2.36 Å

O-Na 2.14 Å
O-Mo 2.36 Å

O-K 2.48 Å
O-Mo 2.35 Å



Mo-ts-6-7^{Li}

Mo-ts-6-7^{Na}

Mo-ts-6-7^K

Angles C-Mo-C 78.5

C-Mo-C 84.7

C-Mo-C 89.2

Figure S6. Optimized geometries for Mo-9a and Mo-ts-6-7 with selected distances and angles in Å. PNP ligand depicted in tubes/wireframes for visual clarity. Mo (turquoise), C (grey), O (red), N (blue), H (white), P (orange), Li (Lithium), Na (purple), K (lithium).

Microkinetic model

Microkinetic models were constructed with the COPASI software (version 4.22).⁷ The initial concentrations used in the simulations were those reported in the experiments (0.25 M of N-methylformanilide, 0.207 M of hydrogen and 0, 0.125 and 0.5 M of ethanol). The concentration of hydrogen was kept constant, in line with the effectively constant pressure of hydrogen used in the reactor (50 atm). H₂ concentration was approximated using the molar fraction of H₂ in a saturated solution of H₂ in toluene at 50 atm and 100 °C assuming incompressibility of THF and that [H₂] << [toluene].⁸ As in the experiments, simulations were carried out for a total time of 24 hours at T = 373 K. The models were based on deterministic time course simulations with the LSODA algorithm.⁹

Two microkinetic models were constructed: 1) assuming a barrierless catalyst activation; 2) including a catalyst activation process with an energy barrier estimated to fit the experimental conversions. We have not studied computationally the catalyst activation process due to the complexity and little experimental information obtained for this reaction.

1) N-methylformanilide with EtOH poisoning assuming barrierless catalyst activation.

The N-methylformanilide conversion vs time traces using Mo-5 as catalyst were obtained by running a microkinetic model described below. A concentration of 12.5 mM of Mo-5 was used. The elementary steps of the mechanism underlying the microkinetic model are given in Figure S7 and Figure S8, together with the ΔG[‡] values derived from the DFT calculations in Table S2.

2) N-methylformanilide with EtOH poisoning assuming a catalyst activation.

The N-methylformanilide conversion vs time traces using Mo-1a as catalyst were obtained by running a microkinetic model described below. A concentration of 12.5 mM of Mo-1a and 12.5 mM of NaHB₃Et were used. The elementary steps of the mechanism underlying the microkinetic model are given in Figure S7 and Figure S8, together with the ΔG[‡] values

derived from the DFT calculations in Table S2. Mo-ts-6-7, was optimized to 25.1 kcal mol⁻¹ to fit experimental conversions.

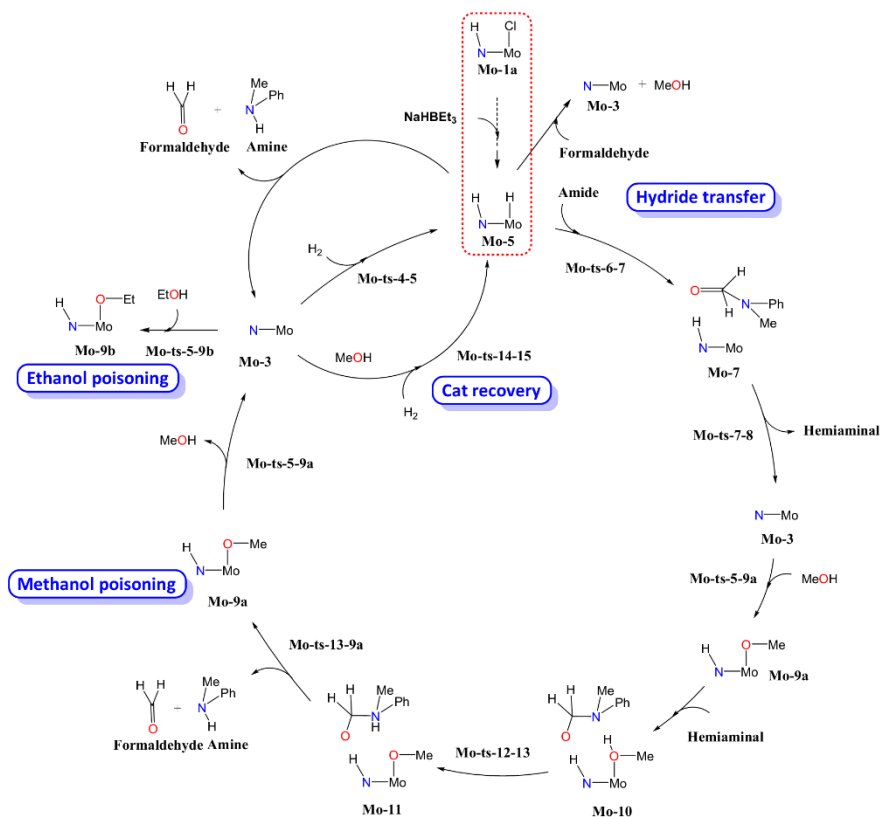


Figure S7. Reactions included in the microkinetic model of N-methylformanilide deaminative hydrogenation. In red dotted square, catalyst activation reaction.

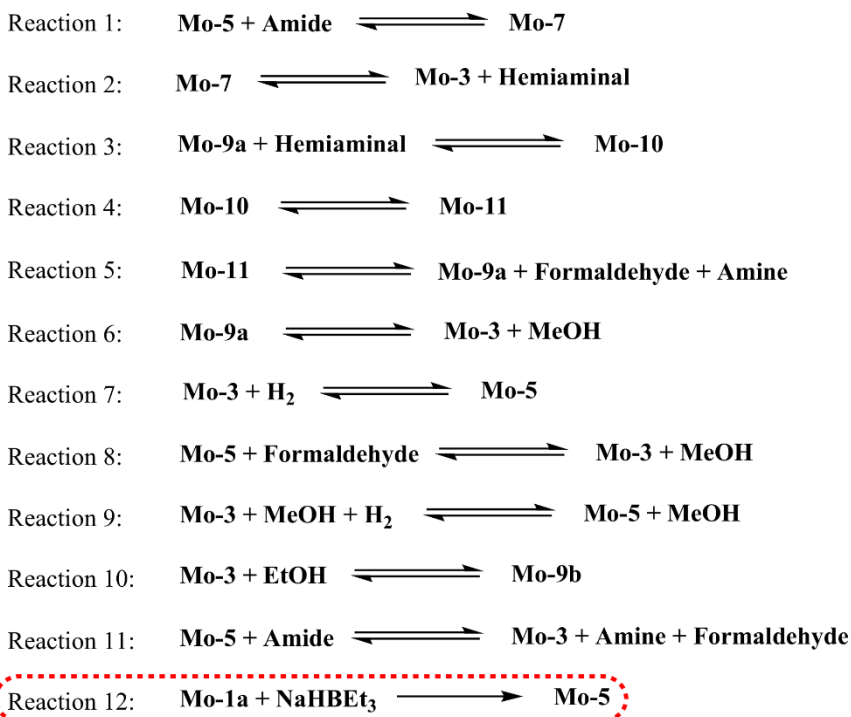


Figure S8 Reactions used in the microkinetic simulations. In red dotted square, reaction included in the model to estimate the catalyst activation.

	ΔG^\ddagger Forward (kcal mol ⁻¹)	ΔG^\ddagger Backwards (kcal mol ⁻¹)
Reaction 1	13.1	6.5
Reaction 2	3.1	0.4
Reaction 3	7.4	0.1 ^a
Reaction 4	5.9	0.2 ^b
Reaction 5	0.2 ^b	13.9
Reaction 6	14.2 ^c	2.8
Reaction 7	18.6	20.3
Reaction 8	6.6	20.2
Reaction 9	11.6	13.3
Reaction 10	5.0 ^c	18.3
Reaction 11	22.9	14.4

Table S2. Reactions and corresponding Gibbs energies (kcal mol⁻¹) used in the microkinetic model of the deaminative hydrogenation of DMF. In red, reaction included to fit the experimental conversions. ^aTS raised to 5.2 to get positive energies. ^bTSs raised to 11 kcal mol⁻¹ to get positive energies. ^cEstimated low energy barrier.

Evaluation of the position of the Na cation

The cation location was determined by computing the energy of selected species (Mo-3, Mo-4, Mo-5, and Mo-9a) with the cation in different positions (interacting with two CO ligands, P_{2CO}; or interacting with CO and a lone pair, P_{CO/LP}; see scheme S9). The location yielding the lowest energy was the one used in the energy profiles, and is the one represented in the Schemes of the manuscript. In most cases, small energy differences (<2 kcal/mol) are obtained when comparing P_{2CO} and P_{CO/LP} structures.

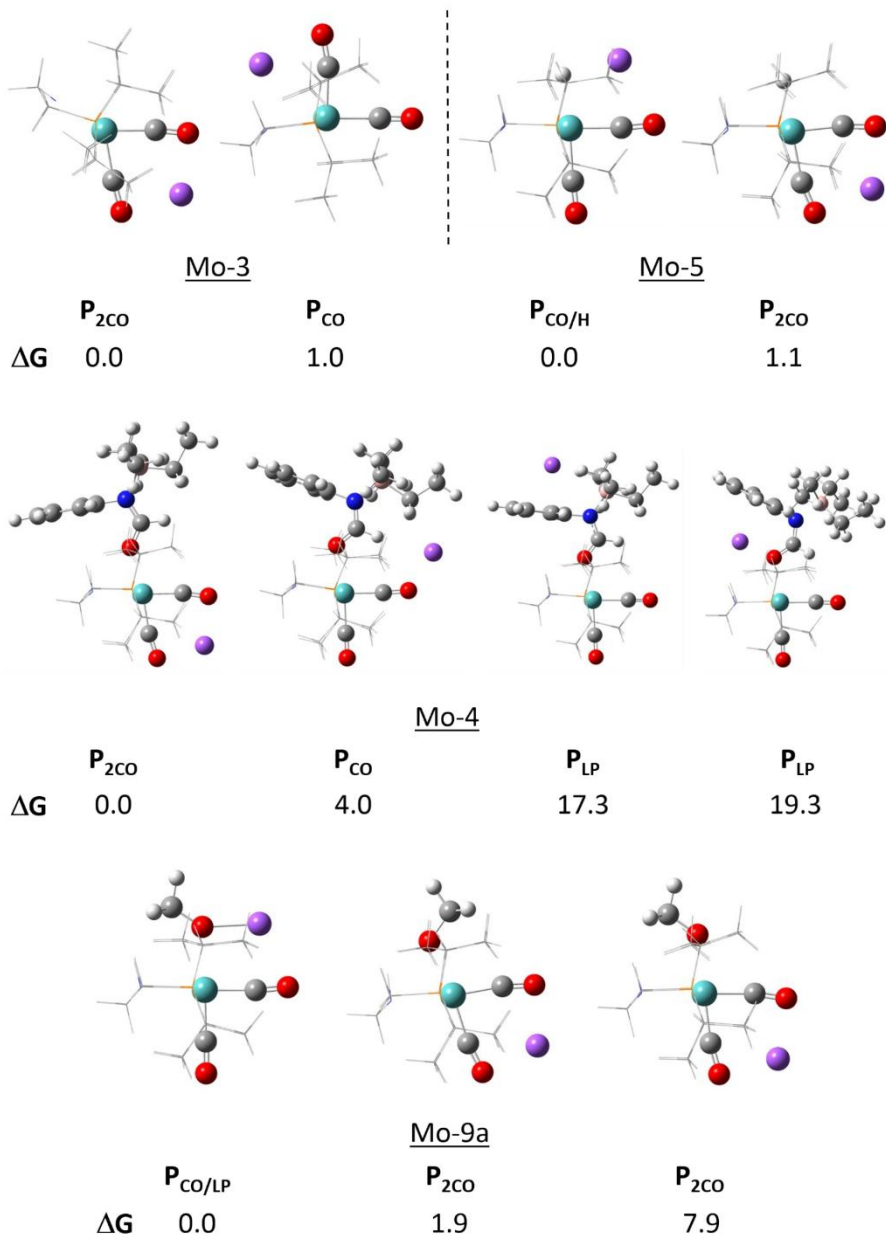


Figure S9. Evaluation of multiple Na^+ positions and their relative free energies ($kcal\ mol^{-1}$). PNP ligand depicted in a wireframe representation for more clarity. Legend: Mo (turquoise), C (grey), O (red), N (blue), H (white), Na (purple), P (orange)

- ¹T. Leischner, A. Spannenberg, K. Junge, M. Beller, *Organometallics*, 2018, 37, 4332-4335.
- ²J. Chen, W. Long, S. Fang, Y. Yang, X. Wan, *Chem. Commun.*, 2017, 53, 13256-13259.
- ³R. Bisht, M. E. Hoque, B. Chatopadhyay, *Angew. Chem. Int. Ed.*, 2018, 57, 15726-15766.
- ⁴P. V. Ilyin, A. S. Pankova, M. A. Kuznetsov, *Synthesis*, 2012, 44, 1353-1358.
- ⁵H. Taneda, K. Inamoto, Y. Kondo, *Chem. Commun.*, 2014, 50, 6523-6525.
- ⁶L. Artús Suàrez, Z. Culakova, D. Balcells, W. H. Bernskoetter, O. Eisenstein, K. I. Goldberg, N. Hazari, M. Tilset, A. Nova, *ACS Catal.*, 2018, 8, 8751-8762.
- ⁷S. Hoops, S. Sahle, R. Gauges, C. Lee, J. Pahle, N. Simus, M. Singhal, L. Xu, M. Pedro, U. Kummer, *Bioinformatics*, 2006, 22, 3067-3074.
- ⁸E. Brunner, *J. Chem. Eng. Data*, 1985, 30, 269-273.
- ⁹L. Petzold, *SIAM J. Sci. and Stat. Comput.* 1983, 4, 136-148.
- ¹⁰M. J. Frisch, G. W. Trucks, H. B. Schlegel, G. E. Scuseria, M. A. Robb, J. R. Cheeseman, G. Scalmani, V. Barone, B. Mennucci, G. A. Petersson, H. Nakatsuji, M. Caricato, X. Li, H. P. Hratchian, A. F. Izmaylov, J. Bloino, G. Zheng, J. L. Sonnenberg, M. Hada, M. Ehara, K. Toyota, R. Fukuda, J. Hasegawa, M. Ishida, T. Nakajima, Y. Honda, O. Kitao, H. Nakai, T. Verve, J. A. Montgomery, J. E. Peralta, F. Ogliare, M. Bearpark, J. J. Heyd, E. Brothers, K. N. Kudin, V. N. Staroverov, T. Keith, R. Kobayashi, J. Normand, K. Raghavachari, A. Rendell, J. C. Burant, S. S. Iyengar, J. Tomasi, M. Cossi, N. Rega, J. M. Millam, M. Klene, J. E. Knox, J. B. Cross, V. Bakken, C. Adamo, J. Jaramillo, R. Gomperts, R. E. Stratmann, O. Yazev, A. J. Austin, R. Cammi, C. Pomelli, J. W. Ochterski, R. L. Martin, K. Morokuma, V. G. Zakrzewski, G. A. Voth, P. Salvador, J. J. Dannenberg, S. Dapprich, A. D. Daniels, O. Fakas, J. B. Foresman, J. V. Ortiz, J. Cioslowski, G. A. Voth, *Gaussian 09*, Revision D.01; Gaussian, Inc.: Wallingford CT, 2013.
- ¹¹Y. Zhao, D. Truhlar, *Theor. Chem. Acc.*, 2008, 120, 215-241.
- ¹²(a) P. Hay, W. Wadt, *J. Chem. Phys.*, 1985, 82, 270-283 (b) W. Wadt, P. Hay, *J. Chem. Phys.*, 1985, 82, 284-298.
- ¹³(a) W. J. Hehre, R. Ditchfield, J. A. Pople, *J. Chem. Phys.*, 1972, 56, 2257-2261 (b) W. Kohn, A. D. Becke, R. G. Parr, *J. Phys. Chem.*, 1996, 1, 12974-12980.
- ¹⁴A. McLean, G. Chandler, *J. Chem. Phys.*, 1980, 72, 5639-5648.
- ¹⁵A. Marenich, C. Cramer, D. Truhlar, *J. Phys. Chem. B.*, 2009, 113, 6378-6396.
- ¹⁶M. Álvarez-Moreno, C. De Graaf, N. López, F. Maseras, J. M. Poblet, C. Bo, *J. Chem. Inf. Model.*, 2015, 55, 95-103.
- ¹⁷S. Hoops, R. Gauges, C. Lee, J. Pahle, N. Simus, M. Singhal, L. Xu, P. Mendes, U. Kummer, *Bioinformatics*, 2006, 22, 3067-3074.